ELASTIC PLASTIC DAMAGE LAWS FOR CORTICAL BONE

THÈSE N^{O} 3435 (2006)

PRÉSENTÉE À LA FACULTÉ SCIENCES ET TECHNIQUES DE L'INGÉNIEUR

Institut d'ingénierie des systèmes

SECTION DE GÉNIE MÉCANIQUE

ÉCOLE POLYTECHNIQUE FÉDÉRALE DE LAUSANNE

POUR L'OBTENTION DU GRADE DE DOCTEUR ÈS SCIENCES

PAR

David GARCIA

ingénieur physicien diplômé EPF
de nationalité suisse et originaire de Lausanne (VD)

acceptée sur proposition du jury:

Prof. A. Curnier, Prof. Ph. Zysset, directeurs de thèse
Prof. M. Jirásek, rapporteur
Prof. L. Rakotomanana, rapporteur
Prof. L. Vuillet, rapporteur

Lausanne, EPFL
2006

A mes parents et à mon épouse Bertha

Acknowledgements

First of all I would like to acknowledge sincerely Pénélope Leyland without whom this thesis would never have started. I thank her for putting me in good hands with very talented people.

Next, I would like to express my sincere gratitude to both professors Philippe Zysset and Alain Curnier who trusted me and gave me the opportunity to realize this thesis. I acknowledge them for their continuous supervision, availability, patience, and support. I was given the benefit of their high competence, experience and innovative ideas in the field of biomechanics and continuum mechanics throughout all fruitful discussions we had together. They gave me many useful advices and introduced me to the biomechanical community. I would specially thank Alain Curnier for his careful reading of this thesis.

I am very grateful to professors Milan Jirásek, Lalaonirina Rakotomanana and Laurent Vulliet to have accepted to be part of the jury and for evaluating my thesis work. I thanks further Prof. Jacques Giovanola for being the president of the jury.

I wish to express my thank Prof. John Botsis for allowing me to use all the facilities at his lab. Furthermore, I acknowledge all the staff of the workshop, specially Gino Crivellari, Marc Jeanneret and Nicolas Favre. They provided a technical support of high quality for the realization of the traction specimens and the customized grips.

I also wish to acknowledge Romain Balet for having done his master project on bone biomechanics, for carrying out valuable experiments on bovine cortical bone and for providing me the data of his experimental results. I greatly acknowledge Thomas Kitzler for providing me the finite element model of the lumbar vertebral body.

I further would like to thank for their friendship all the colleagues I have met during those four years, namely Aleksandar Sekulic, Larissa Sorensen, Laurent Humbert, Gabriel Dunkel, Fabiano Colpo, Marzio Bergomi, Joël Cugnoni, Jörn Justiz, Colin Sanctuary, Stefan Hengsberger, Liliana Rincón, Sébastien Barrault and Laurent Rappillard.

Last but not least, I would like to thank my family and my wife for always supporting me and believing in me.

Abstract

Motivated by applications in orthopaedic and maxillo-facial surgery, the mechanical behaviour of cortical bone tissue in cyclic overloads at physiological strain rates is investigated. The emphasis is on the development of appropriate constitutive laws that faithfully reproduce the loading, unloading, and reloading sequence observed during experimental *in vitro* uniaxial testing. To this end, the models include three distinct modes of evolution, namely a linear elastic mode due to bone cohesion, a damage mode where microcracks are generated and a plastic mode corresponding to sliding at the microcracks.

The proposed models use the internal state variable approach common in continuum damage mechanics and allow a straightforward interpretation of the constitutive behaviour of cortical bone. They are derived within the generalized standard materials formalism and are thus thermodynamically consistent. The mathematical formulation of the models is based on the definition of two internal state variables: a damage variable that represents the microcrack density reducing the tissue stiffness, and a plastic strain variable representing the deformation associated with these microcracks.

Firstly, two one-dimensional models describing the uniaxial quasistatic behaviour of cortical bone are developed. The first one includes a single scalar damage variable, whereas the second one is based on tensile and compressive damage variables, which improves the simulation results. Both models are then extended into rate-dependent alternatives by relating the rate of damage accumulation to some high power of the damage threshold stress. All four models consider different tensile and compressive damage threshold stresses as it is the case for cortical bone.

Secondly, the material constants characterizing the one-dimensional models are identified on experimental grounds. To this end, a series of *in vitro* uniaxial overloading tests were carried out on bovine cortical bone. Reliable measurements were obtained in tension using dumbbell specimens, avoiding thus undesirable boundary effects.

Thirdly, a three-dimensional rate-independent constitutive law inspired by the one-dimensional models is formulated and implemented in a finite element code. It includes porous fabric-based orthotropic elasticity and rate-independent plasticity with damage. The onset of damage is characterized by an orthotropic stress-based damage criterion described by porosity and fabric, which takes into account distinct tensile and compressive damage threshold stresses.

Finally, the potential of the new three-dimensional elastic plastic damage constitutive law for cortical bone is demonstrated by means of a finite element analysis of the compression of a vertebra.

Version abrégée

Motivé par des applications en chirurgie orthopédique et maxillo-faciale, le comportement de l'os cortical en situation d'endommagement à des taux de déformation physiologiques est étudié. L'accent est mis sur le développement de lois constitutives appropriées qui reproduisent fidèlement les séquences de charge, décharge et recharge observées lors d'expériences uniaxiales *in vitro*. A cette fin, elles comprennent trois modes d'évolution: un mode linéaire élastique dû à la cohésion de l'os, un mode d'endommagement dans lequel des microfissures sont générées et un mode plastique correspondant au glissement à leur interface.

Les modèles proposés utilisent l'approche des variables internes courante en mécanique des milieux continus et permettent une interprétation aisée du comportement mécanique de l'os cortical. Ils sont établis dans le cadre des matériaux standards généralisés donc thermodynamiquement consistants. Leur formulation est basée sur la définition de deux variables internes: une variable d'endommagement qui représente la densité de microfissures et une déformation plastique associée à leur déformation.

Premièrement, deux modèles unidimensionnels décrivant le comportement uniaxial quasistatique de l'os cortical sont développés. Le premier est à une seule variable d'endommagement scalaire alors que le deuxième est basé sur deux variables, une en tension et une autre en compression, ce qui améliore le résultat des simulations. Les deux modèles sont ensuite étendus en alternatives dépendantes du temps en reliant le taux d'accumulation de l'endommagement à une haute puissance du seuil d'endommagement. Les quatre modèles considèrent des seuils d'endommagement différents en tension et en compression.

Deuxièmement, les constantes matérielles qui caractérisent les modèles unidimensionnels sont identifiées expérimentalement. A cette fin, une série de tests uniaxiaux *in vitro* furent effectués sur de l'os cortical bovin. Des mesures fiables purent être obtenues en tension à l'aide d'éprouvettes de traction en forme d'haltères, évitant ainsi des effets de bords indésirables.

Troisièmement, une loi constitutive tridimensionnelle indépendante des taux inspirée des modèles unidimensionnels est formulée puis implémentée dans un code d'éléments finis. Elle comprend une élasticité orthotrope basée sur la porosité et le tenseur de fabrique, et une plasticité avec endommagement indépendante des taux. Ce dernier est caractérisé par un critère orthotrope formulé en contrainte et décrit par la porosité et le tenseur de fabrique. Il tient compte de seuils d'endommagement différents en tension et en compression.

Finalement, le potentiel de la nouvelle loi constitutive tridimensionnelle élastique, plastique avec endommagement de l'os cortical est démontré à l'aide d'une analyse par éléments finis de la compression d'une vertèbre.

Contents

Chapter 1

Introduction

The skeleton is the bearing structure of the human body. Its integrity is essential to human health. The human skeleton is made of a couple hundred bones with various shapes and sizes. Each bone is constituted of bone tissue. Understanding and modeling the mechanical behaviour of bone tissue is important. This is the main objective of this thesis. In this introduction, we will substantiate the current need to develop a more realistic behaviour law for bone starting from a detailed description of this tissue and its function, in order to motivate our thesis achievement: an elastic plastic damage law for bone.

1.1 Cortical and trabecular bone

Bone tissue is traditionally subdivided into two types: *cortical* (compact) bone and *trabecular* (porous) bone, although the interface between the two is somewhat fuzzy. This distinction comes from the macroscopic appearance of bone tissue. At this level, the outer shell of a bone which is made of cortical or compact bone can be clearly discerned from the inner core of the bone made of trabecular or cancellous bone (Figure 1.1). These two types of bones are identified by their porosity and exhibit distinct material properties. On the one hand, cortical bone has a dense microstructure (a porosity of about 5-10%) and accounts for approximately 80% of the total mass of the skeleton. On the other hand, trabecular bone has a porosity in the range of 45-95% and represents 20% of the skeleton mass. It consists of a meshwork in which the *trabeculae* (i.e. struts and plates) are roughly arranged along the principal stresses in the bone.

Figure 1.1: Cross-section of a femur showing a dense tissue, namely cortical bone on its periphery and a porous tissue which is called trabecular bone in its interior.

1.2 Bone: an optimized material

Bone tissue, like other biological microstructures, is the result of a long-term optimization controlled by the selection processes of evolution. Therefore, the microstructure and composition of bone is well adapted to its function. Beside the structural functions of bone such as protecting vital organs and serving as an articulated framework that supports soft tissues and allows for muscular activity, it has also important metabolic functions. It regulates ionic concentrations in the fluids of the body (homeostasis), serves as calcium repository and plays a major role in the formation of blood cells (hematopoiesis).

The human skeleton contains 206 bones which vary in size from the almost microscopic ossicles of the inner ear to femora which may exceed $45\,cm$ in length. This large variation in size is accompanied by similar variations in shape and function which results in a broad range of mechanical properties.

Being a highly specialized tissue, the relevant properties of bone are particularly well adapted and outstanding in comparison to other inert materials. Following the ideas of Ashby et al. [Ashby, 1992, Ashby et al., 1995] developed in their concept of materials property charts, it is helpful to evaluate and compare the mechanical behaviour of bone and other materials on the basis of so-called performance indices (Figure 1.2). If maximizing a combination of properties such as Young's modulus ϵ to density ρ ratio, some aspect of the performance of the material will be optimized. For example, the stiffness of a lightweight beam with respect to bending is optimized with a maximum value for ϵ/ρ. Bone tissue resists particularly well to fracture,

better than any synthetic ceramic. It is characterized by a high fracture toughness. Motivated by this observation, it is of primary importance to characterize bone tissue on solid grounds and to develop constitutive laws which can be very helpful to optimize many clinical procedures and the requisite medic

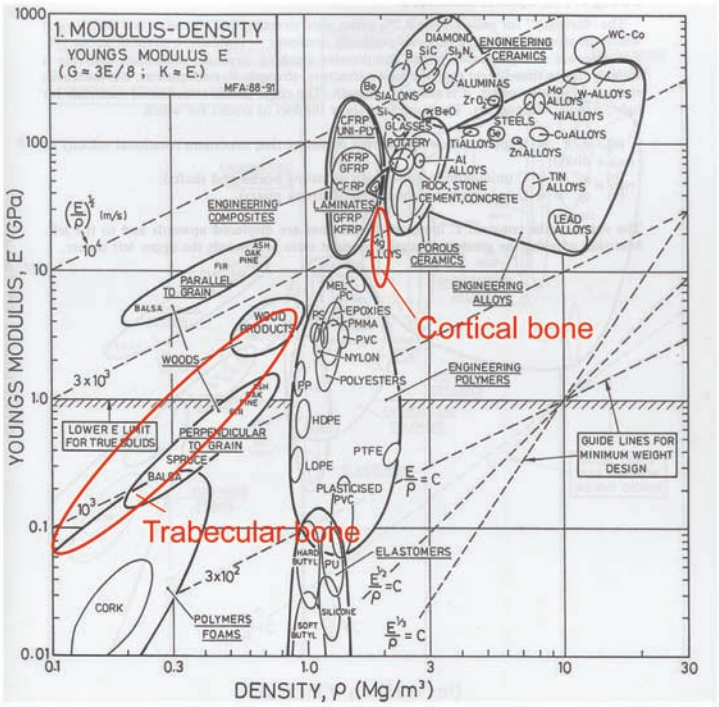

Figure 1.2: A material property chart for bone tissue and engineering materials, plotting Young's modulus against density. Guidelines identify efficient materials with minimum weight design (adapted from [Ashby, 1992]).

1.3 Degradation of bone

1.3.1 Osteoporotic fractures

Many life (biological) factors can be associated to an alteration of the mechanical properties of bone. Some of them are intense physical activity, malnutrition, growth, aging, and diseases. *Osteoporosis* is a disease characterized by a decrease of bone mass and a degradation of bone architecture, which leads to an increased bone fracture risk (Figure 1.3). This metabolic disease affects mostly elderly people and in particular women.

Past the age of 50, approximately one woman of three is victim of an osteoporotic fracture and one men of five. Hence, osteoporosis has become a major public health problem with significant socio-economic consequences all over the world. In year 2000, the costs for the treatment of all osteoporotic fractures in Europe exceeded 24.6 billions euros (newspaper 'Le Temps', 2005). One frequent location of osteoporotic fractures is the vertebral body ([Lippuner et al., 1997]). Vertebral fractures result in back pain, increase the risk of subsequent vertebral fractures and mortality. Other frequent osteoporotic fractures include hip and wrist fractures.

Figure 1.3: Differences between an osteoporotic (left) and a normal (right) femur. Osteoporotic bone shows a markedly lower density, degraded microstructure and bone fracture (from Medisave UK, Ltd.).

1.3.2 Clinical treatments

The current clinical treatment of vertebral fractures consists of high dose analgesia and initial bed rest (no more than a few days), followed by physical therapy to prevent further fractures. Patients who do not respond to conservative treatment or who continue to have severe pain may be candidates for *percutaneous vertebroplasty*. Percutaneous vertebroplasty involves injecting a biomaterial (a bone cement) into the collapsed vertebra to stabilize and strengthen the fracture and vertebral body ([Predey et al., 2002]).

Beside many biological and clinical requirements for a biomaterial such as biocompatibility or setting time, its mechanical properties must be well understood and characterized. It is of primary importance to have an accurate knowledge of elasticity, ultimate stresses, amount and distribution of the biomaterial injected in the vertebral body. This is critical to recover the stiffness, prevent further crushing of the treated vertebra and avoid fracture in the adjacent vertebral bodies.

Hip fractures are currently treated by a total joint replacement of the hip. The choice of the biomaterial constituting the prosthesis determine its reliability. Hence, failure predictions in bone and bone-implant stability must be thoroughly investigated on numerical and experimental grounds.

1.4 Motivation for a damage law of bone

In order to find an adequate bone substitute material intended for use in percutaneous vertebroplasty, it is essential to have a thorough understanding of the mechanical behaviour of bone tissue. Similarly, in view of optimizing the reliability of a bone-implant structure or predicting bone fracture, an accurate model of the mechanical behaviour of bone is required. Hence, orthopaedic research has an *important need* for realistic constitutive laws for bone tissue including heterogeneities, anisotropic elasticity and damage behaviour i.e. progressive degradation of its elastic properties.

To date, little has been accomplished in describing the mechanical behaviour of cortical bone tissue in cyclic overloading (i.e. damaging) situations ([Fondrk et al., 1999a], Section 2.3). This is why we decided to develop an elastic plastic law for cortical bone including damage.

To this end, the general methodology proposed by [Humphrey, 2003] was available to us. It includes five basic steps which are followed throughout this thesis:

(i) 'delineation of general characteristics of interest;

(ii) establishing an appropriate theoretical framework for quantification;

(iii) identification of specific functional forms of the constitutive relations;

(iv) calculation of the values of the associated material parameters; and

(v) evaluation of the predictive capability of the final relation.'

Regarding the framework, continuum damage mechanics has shown to be appropriate for modeling and quantifying damage processes at a macroscopic level ([Krajcinovic, 1989]).

In addition to these guidelines, let us mention that solving complex problems like the ones involved in orthopaedic biomechanics requires a combination of specific computational techniques such as the finite element method (spatial discretization), the linear iteration method (solution of nonlinearities) and the finite difference method (time discretization). Therefore, in order to be useful, the constitutive laws must be developed in a form which is compatible with these computational methods.

1.5 Thesis postulate

For all the reasons given in the previous Section, the main objective of the present thesis can be stated as follows.

> *In this thesis, we address the effect of single and cyclic overloads on the mechanical behaviour of cortical bone tissue at physiological strain rates. New thermodynamically consistent rate-independent and rate-dependent constitutive relations for cortical bone tissue which combine elasticity, plasticity and damage are presented. The laws are first formulated in one dimension and subsequently identified experimentally. One of them is then generalized in three dimensions and provides the basis for a biomechanical application.*

More precisely, the *four original contributions of the thesis* are:

- Firstly, new one- and three-dimensional constitutive laws for cortical bone that combine elasticity, plasticity and damage are formulated in the framework of continuum mechanics and thermostatics of irreversible processes.
- Secondly, the material constants of the uniaxial laws are identified through a series of *in vitro* mechanical tests carried out on bovine cortical bone.
- Thirdly, the three-dimensional law is discretized in time mainly with the help of implicit projection algorithms, and implemented in a commercial software for finite element mechanical analysis (ABAQUS).
- Finally, the potential of the resulting law and model is demonstrated via a biomechanical application simulating the axial compression of a vertebra.

1.6 Outline

According to these objectives, the thesis is organized in the following eight chapters.

- Chapter 2 begins with a brief histological description of bone tissue going from the macrostructural to the sub-nanostructural level. Then, the principal macroscopic mechanical properties of cortical bone are reviewed and existing models for its constitutive behaviour are exposed.

- Chapter 3 defines the theoretical solid mechanics framework used throughout this thesis. Firstly, we present the notions of continuum mechanics necessary to understand the models. Secondly, the thermostatics framework used to formulate the constitutive laws is exposed. Thirdly, we describe progressively the basic rheological models and behaviours upon which our models are based on.

- Chapter 4 consists in the conception, design and formulation of innovative one-dimensional constitutive laws for cortical bone tissue. We begin by modeling its quasistatic behaviour with help of two rate-independent models. Rate-dependent damage accumulation mechanisms are then taken into account by relating the rate of damage accumulation to some high power of the damage threshold stress. The resulting two rate-dependent models are shown to be an intuitive generalization of the rate-independent ones.

- Chapter 5 presents the methods, results and discussion of original *in vitro* uniaxial mechanical tests carried out on bovine femoral cortical bone. The tests were specially elaborated to highlight the cyclic overloading behaviour of bone at physiological strain rates. They allowed for a successful identification of the material constants and thus the validation of the one-dimensional constitutive laws.

- Chapter 6 details a straightforward three-dimensional generalization of the simplest one-dimensional constitutive law for cortical bone. It includes its theoretical formulation, followed by a description of its numerical implementation. Implicit projection algorithms are presented and consistent tangent operators are derived. Then, the numerical methods traditionally employed in computational solid mechanics are presented, namely the finite element method, the iterative linearization method and the finite difference method. Finally, the implementation of the three-dimensional law is validated simulating some elementary test problems.

- Chapter 7 is the application of the developed three-dimensional law to a concrete biomechanical example. Damage of a lumbar vertebra under compressive load is analyzed and visualized by means of a finite element model. The chapter begins with a description of the mesh, the material properties and boundary conditions. Then, stress and damage distributions in the vertebra are visualized and discussed.

- Chapter 8 summarizes the main features and limitations of the developed one- and three-dimensional constitutive laws and concludes on their potential utility in orthopaedic biomechanics.

Chapter 2

Histological and biomechanical background

In this Chapter, we begin with a brief description of the complex hierarchical structure of bone tissue (Section 2.1). We distinguish mainly five degrees of organization going from the macroscopic level (up to several millimetres) to the sub-nanostructural level (below a few hundred nanometers). These structures are adapted to the variety of mechanical, biological and chemical functions that bone fulfills. Then, as the mechanical properties of bone vary considerably at different structural levels, we focus our attention on the mechanical properties of bone at the macroscopic level (Section 2.2). The description covers elastic and viscoelastic properties, damage thresholds, and damaged behaviour, with an emphasis on cortical bone. Finally, some constitutive models of bone tissue are presented and criticized in Section 2.3.

2.1 Bone structure and composition

2.1.1 Bone structure

The main function of the musculoskeletal system (bone, cartilage, tendons, ligaments and muscles) is to transmit forces from one part of the body to another in order to effect its motion and locomotion and to support vital organs (e.g. brain, heart, lungs) and protect them from accidental damaging loads. Beside the mechanical functions of structural support and protection, bone tissue has important biological and chemical roles. It stores stem cells and carries out the mineral ion homeostasis serving as mineral reservoir (calcium and phosphate needed for metabolism).

Being a living tissue, bone has the remarkable property to adapt its

structure to its function. As a result, bones of various shapes and structure are found in the body, but the architecture of a vertebrate skeleton is fairly the same from one species to another. The ability of bone to modify its structure to specific loadings is known as *Wolff's law* ([Wolff, 1892]). At the macroscopic level (millimetre lengthscale) bone is heterogeneous, porous and anisotropic. Although porosity can vary continuously from 5 to 95%, most bones are either very dense or very porous. Thus, at this level, bone tissue is divided into two types (Figure 2.1). The first type is *cortical* or *compact* bone. Its porosity of 5 to 10% is characterized by different types of pores ([Cowin, 1999]).

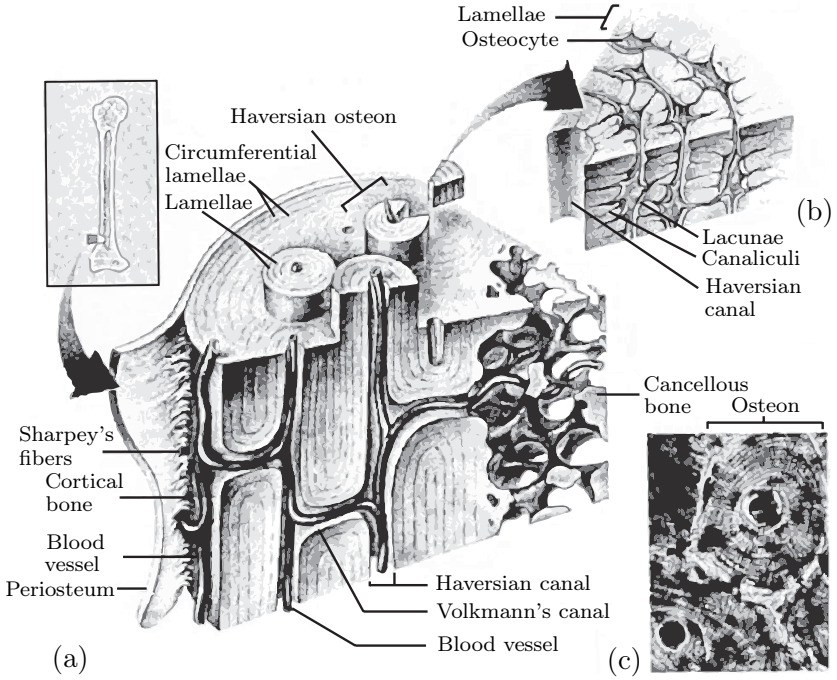

Figure 2.1: Microscopical structure of cortical bone (a) sketch of cortical bone, (b) cut of Haversian system, (c) photomicrograph of a Haversian system (from [Fridez, 1996]).

The *Haversian canals* are approximately aligned along the long axis of the bone. They contain capillaries and nerves, forming thus a vascular type of porosity. They are about $50\,\mu m$ in diameter. The Haversian canals are connected to each other by the shorter and transverse *Volkmann's canals*. Another class of porosity is formed by the *resorption cavities* which are about $200\,\mu m$ in diameter. They are an integral part of the bone remodelling process.

The second type of bone is *trabecular* or *cancellous* bone. Its porosity varies from 50 to 95%. The pores are interconnected and filled with marrow.

Their size is on the order of $1\,mm$. The main function of the marrow is to produce the blood cells. The bony matrix is constituted of plates and struts called *trabeculae*, with a thickness of about 100-200 μm (Figure 2.1). Their arrangement is variable but has a preferential orientation in highly mechanically loaded bones ([Burr et al., 1998]). There is a "grain" direction along which mechanical stiffness and strength are greatest.

In a cross-section of a long bone such as the femur, cortical bone is found in the periphery of the shaft (diaphysis) and the extremities (epiphysis) where it surrounds a porous trabecular core. Trabecular bone is found at the ends of all long bones and within flat and irregular bones. It is enclosed by a dense cortical shell.

The microstructure of cortical bone is composed of regular, cylindrically shaped *lamellae* (Figures 2.1 and 2.2). In contrast, the microstructure resulting from compaction of trabecular bone is composed of an irregular superposition of lamellae. Some investigators ([Carter and Hayes, 1977b, Zysset, 1994, Roy et al., 1999]) consider, for mechanical purposes, cortical and trabecular bone as a single constitutive material with variable porosity. Others ([Choi et al., 1990, Rho et al., 1993]) think that the two types of bone must be considered as two different materials. As they share a similar chemical composition and show a similar mechanical behaviour over a wide range of deformations (Section 2.2), we think that a single constitutive law can be used locally for both types of bone.

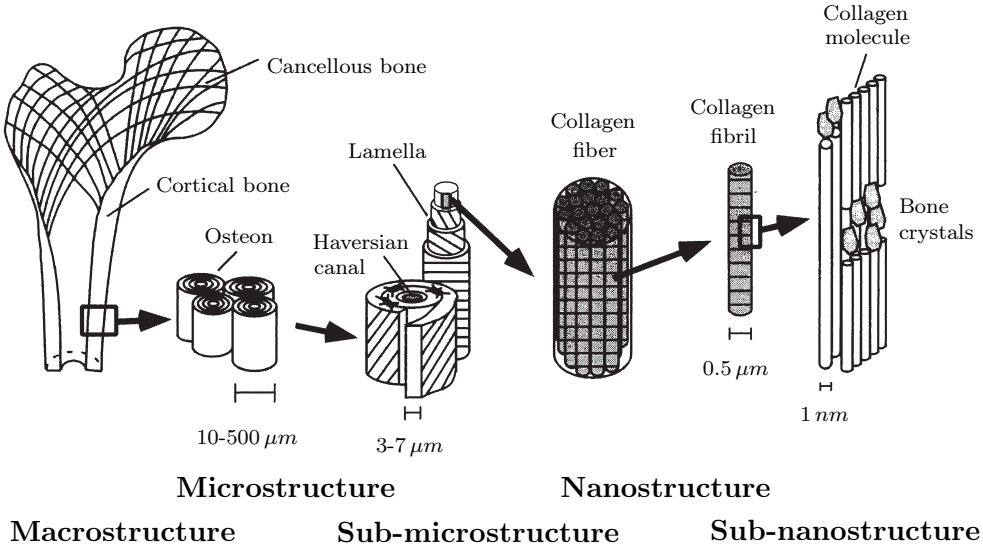

Figure 2.2: Hierarchical structural organization of bone: macro) cortical and cancellous bone; micro) osteons with Haversian systems; sub-micro) lamellae; nano) collagen fiber assemblies of collagen fibrils; sub-nano) bone mineral crystals, collagen molecules, and non-collagenous proteins (from [Rho et al., 1998]).

At the microstructural level, cylindrical structures known as *osteons* or *Harversian systems* are found in cortical bone (Figures 2.1 and 2.2 micro)). They are roughly parallel to the long axis of the bone and have a diameter of about $200\,\mu m$. They are formed by concentric lamellae and surround the Haversian canal. The boundary between the osteon and the surrounding cortical bone is known as the *cement line*.

A single lamella (3-7 μm wide) is formed by a planar arrangement of mineralized collagen fibers (Figure 2.2 micro)). Beside the osteons, cortical bone exhibits other forms of architectures. The tissue where the mineralized collagen fibers are poorly organized and no pattern can be distinguished are called *woven* bone. This type of bone is quickly formed and appears during the healing process after fracture (e.g. [Doblaré et al., 2004]). Highly organized bone consisting of parallel layers or lamellae is called *lamellar* bone. This type of bone is slowly formed and stronger than woven bone due to its architecture. The skeletal embryo consists of woven bone, which is later replaced by lamellar bone.

Within a single lamella, the arrangement and orientation of the substance of a lamella is not well known. At the sub-microstructural level (Figure 2.2 sub-micro)), the classical view of a twisted "plywood" lamellar structure is due to [Giraud-Guilles, 1988]. In this representation, the collagen fibers of a lamella in an osteon lie in parallel in each lamella, with a change of orientation of fibrils from one lamella to the next. Transmission electron microscope studies suggest a rotated plywood structure within each lamella ([Weiner et al., 1999]). However, precision acoustic microscopy measurements indicate that the structure of collagen in bone is, as yet, not fully understood ([Turner et al., 1995]). Thus, a single lamella cannot be considered to contain individual, highly oriented collagen bundles, but the fibers form a continuum both within a single lamella and between lamellae ([Rho et al., 1998]).

The nanoindentation technique provides an interesting tool to investigate the mechanical properties of microstructural components of bone tissue (e.g. [Rho et al., 1999a, Hengsberger et al., 2001]). The elastic properties of individual human bone lamellae have been investigated by [Hengsberger, 2002, Hengsberger et al., 2002] for example. The variations of the nanoindentation properties have been studied as a function of the locus of indentation within a single osteon by [Rho et al., 1999b], and as a function of age and gender by [Hoffler et al., 2000b].

2.1.2 Bone composition

At the nanostructural level, bone is composed of collagen, water, hydroxyapatite mineral, and small amounts of proteoglycans and noncollagenous proteins, exhibiting thus a composite structure. Being a dynamic porous structure, its porosity and composition varies with species, age, sex, the specific bone, and may change as a result of a pathologic condition or in a normal adaptive response to a mechanical or physiological stimulus.

The *collagen*, mainly of *type I* in bone, is a structural triple helix protein which can organize itself into strong fibers. It gives bone flexibility and tensile strength. It is also found in tendons, ligaments and skin. The bone mineral crystals grow within the collagen fibrils and between the collagen molecules (Figure 2.2 sub-nano)). These are the *hydroxyapatite* crystals, $Ca_{10}(PO_4)_6(OH_2)$. They have a plate-like shape with hexagonal symmetry and are mainly responsible for the stiffness of the bone. The average lengths and widths of the plates are $50 \times 25\,nm$ and the crystal thickness is 2-3 nm. The periodic arrangement of the collagen molecules and the bone crystals form the mineralized collagen fibril.

Other ground substances are found in bone tissue. The *proteoglycans* may modulate the collagen fibril assembly and control the location or rate of mineralization ([Burr et al., 1998]). Other *noncollagenous proteins*, such as *osteocalcin*, play an important role in the mineralization of new bone.

Finally, *water* is found in its free form in the calcified bone matrix but also bound to other molecules.

In summary, bone tissue has a highly hierarchized material structure, which is complex, multiphasic, heterogeneous and anisotropic. Depending on the scale level of interest, it can be observed in various forms and each of them depends on the local degree of maturation of the tissue. At the macroscopic level, which is the level of interest in this study, bone is classified into cortical and trabecular bone. Both undergo continuous changes in their structure, shape and composition, as a response to an adaptative process known as *bone remodelling*. Four types of bone cells are responsible for this adaptation. They allow for efficient repair and help to prevent fractures. The basic bone cells and their functions are briefly described in the following Subsection.

2.1.3 Bone cells and bone remodelling

During bone growth, like during our childhood, bones adapt their shapes as a response to physiological needs or repeated physiological loads. This process is referred to as *bone modelling*. It can be formative or resorp-

tive ([Burr et al., 1998]). The ability of bone tissue to continuously renew itself is called *remodelling*. It plays a fundamental role in microdamage repair removing a portion of older bone and replacing it with newly formed bone. This process prevents accumulation of fatigue damage that could lead to fatigue fracture. *Fracture healing* only occurs during fracture repair (e.g. [Doblaré et al., 2004]).

Bone remodelling usually takes place in Haversian systems of cortical bone or on the surfaces of single trabeculae in trabecular bone. It is accomplished antagonistically by two types of bone cells: the *osteoclasts* and *osteoblasts*. They work together in *basic multicellular units*, or *BMUs* (e.g. [Frost, 1963]). A BMU is formed by about 10 osteoclasts and several hundreds osteoblasts (Figure 2.3).

The osteoclasts, originating from the marrow, remove bone by demineralizing it with acid and cleaving collagen with enzymes. The osteoblasts, partly created at the periostum layer, produce new bone.

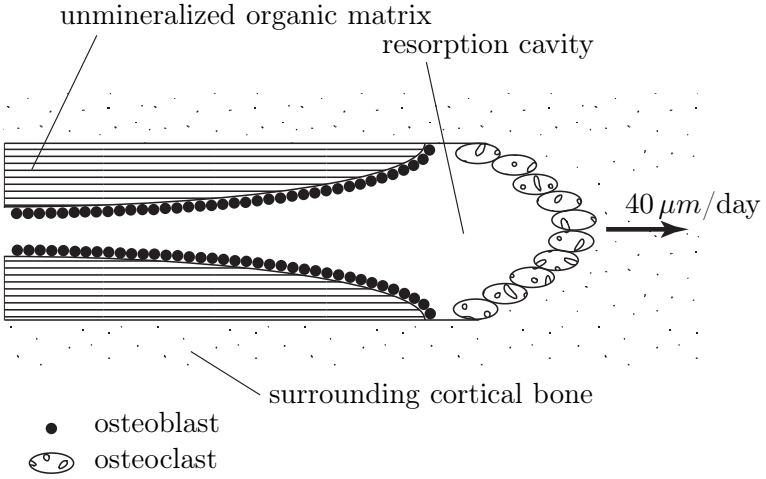

Figure 2.3: Schematic diagram of the osteonal bone remodeling process (not to scale). The osteoclasts remove bone followed by the osteoblasts which produce new unmineralized bone. The cells complex is referred to as BMU.

The BMUs follow a well defined sequence, known as the *activation*, *resorption*, and *formation* sequence (ARF). Firstly, a biochemical or mechanical signal causes the osteoclasts to migrate. Secondly, they begin to remove bone somewhere on the bone surface. In compact bone, they dig tunnels of about $200\,\mu m$ in diameter through the cortex at a velocity of about $40\,\mu m$/day. When working on bone surfaces, they simply progress and remove bone material along these surfaces. Finally, once the osteoclasts have

resorbed a certain amount of bone, the much smaller osteoblasts follow them, replacing the removed tissue by an unmineralized organic matrix. They lay down concentric lamellae at an average radial closure rate of 1-2 μm/day. In humans, the resorption period is about 3 weeks and the formation or refilling period is about 3 months. Thus, the total remodelling period is about 4 months.

The *mineralization* phase follows the ARF sequence, namely mineral is deposited within and between the collagen fibers of the newly formed unmineralized tissue ([Landis, 1995]).

Two others types of bone cells, which result from the bone remodelling process, must be mentioned. The *bone lining cells* are inactive osteoblasts that remain on the surface of the bone once the formation period has stopped. If needed, they can be reactivated by a biochemical or mechanical stimulus and initiate a new ARF sequence. The *osteocytes* are former osteoblasts that are buried in the bony matrix. Located in the resorption cavities and interconnected with each other by the canaliculi, they form a dense network which acts as a mechanical sensor that may control bone remodelling (Figure 2.1 b)).

The continuously renewed heterogeneous anisotropic composite structure of bone tissue confers it very interesting mechanical properties. They are described in the following Section, with a focus on cortical bone.

2.2 Macroscopic mechanical properties of cortical bone

It has been shown that the mechanical properties of bone tissue depend strongly on the structural level of interest. For example [Reilly and Burstein, 1975], measured a femoral tensile longitudinal elastic modulus in the 17 GPa range (cortical bone). Microbending experiments carried out on cortical bone specimens provided a modulus of 5.4 GPa ([Choi et al., 1990]). Ascenzi and Bonucci examined the tensile properties of single osteons. For osteons with a majority of fibers aligned with the long axis of the bone, they measured a tensile elastic modulus of 12 GPa, whereas 5.5 GPa were found for osteons with alternating lamellar orientations ([Ascenzi and Bonucci, 1967]). More recently, nanoindentation experiments done on single lamellae of cortical bone reflected an elastic modulus in the 22 GPa range close to the macroscopic value ([Rho et al., 1997, Zysset et al., 1999, Hengsberger et al., 2001]). Similar experiments carried out on human trabecular bone lamellae reflected an elastic modulus in the 11 GPa range ([Zysset et al., 1998]).

Going much deeper into the structure of bone, the elastic modulus of the apatite crystals is about $80\,GPa$ and about $1.5\,GPa$ for the collagen.

In order to understand the mechanical behaviour of bone tissue, it is important to combine various experimental techniques, each having its own resolution. The difficult task to reconcile the different material structures and properties at the many different length scales still is to be done (e.g. [Hengsberger et al., 2003]).

Much of the finite element studies to date (Chapter 7) still consider bone tissue as a linear elastic material (e.g. [Crawford et al., 2003]).

In view of the scarcity of a satisfactory macroscopic constitutive model for bone and adequate cyclic overloading experiments, this work is concerned with a *macroscopic* description, formulation and identification of bone. The emphasis is on cortical bone but we are confident the same model can be used for trabecular bone.

2.2.1 Constitutive behaviour of cortical bone

The macroscopic mechanical properties of cortical bone vary greatly with porosity, mineralization level and organization of the solid matrix. Their values differ from one bone to another as well as within different regions of the same bone ([Goldstein et al., 1983, Rho et al., 1995]).

[Currey, 2004] lists five important mechanical properties on which natural selection may be acting. The first is bone *stiffness*, which is directly related to its *elastic* behaviour. The second is *resilience* or ability to absorb energy beyond the elastic limit or damage threshold and before rupture. Within this range, bone will not necessarily break but undergo *damage*, which leads to *stiffness reduction* and *permanent strains*. The third is *damage threshold stress*, an important property defining the onset of damage accumulation. It is usually determined in tension, compression or bending. The fourth property which is directly related to the second one is *toughness* or ability to prevent the formation and propagation of cracks. The fifth is *fatigue resistance*, a particularly important requisite for all biological tissues of the musculoskeletal system.

The most classical way to analyze and characterize the macroscopic constitutive behaviour of cortical bone is to examine a *typical* uniaxial *quasistatic* cyclic stress-strain curve. Figure 2.4 shows the typical *tensile* behaviour of cortical bone during cyclic loading. The experiment was carried out under load control at a low stress rate and was provided by [Zioupos, 2002].

Just looking at Figure 2.4, we retained *three principal deformation modes* in this thesis which should be included in any macroscopic quasistatic

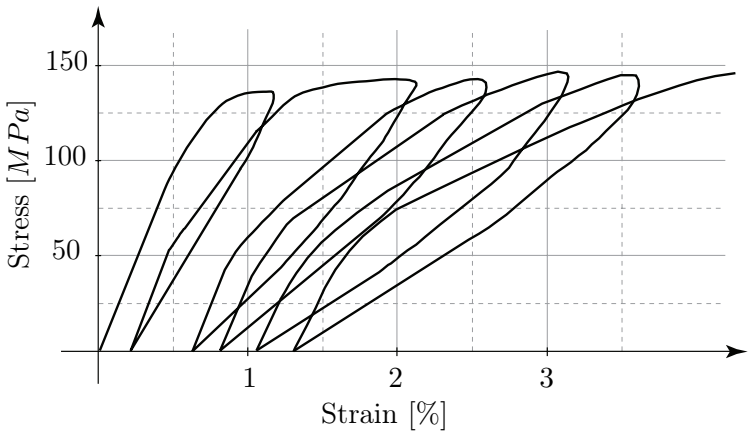

Figure 2.4: Typical quasistatic cyclic tensile stress-strain curve of cortical bone (from [Zioupos, 2002]).

constitutive model for cortical bone.

The first mode is *intact linear elasticity*, abbreviated by (E). This mode is clearly seen at the beginning of each new cycle and to a lower extent during the initial unloading phase (Figure 2.5). Bone cohesion may be responsible for this mode.

The second mode is the *damaging mode*, abbreviated by (D). This phase corresponds to the generation of microcracks (which leads to the stiffness reduction seen in the reloading curves), to an energy dissipation (hysteresis loop area), and to permanent strains (loop feet strains) (Figure 2.5). The observed permanent strains suggest that this mode is a plastic damaging mode in addition to elastic damage.

The third mode, called *plastic mode*, is abbreviated by (P). It corresponds to the damaged unloading and reloading curves and may be interpreted as a sliding with friction at the microcracks. A striking feature visible in Figure 2.5 is that all damaged reloading curves are collinear with the origin. To our knowledge, no other material possesses this remarkable property. Its physiological or biomechanical consequence remains to be explained. The piecewise linear behaviour of damaged bone has also been observed by [Kotha and Guzelsu, 2003] and contrasted with the behaviour of undamaged bone. [Keaveny et al., 1999] also pointed out similar features on their load-unload-reload curves.

Applying this classification, these three deformation modes will constitute the major ingredients of our constitutive laws for bone tissue.

A very similar behaviour is obtained with trabecular bone suggesting that damage occurs at the nanometer scale of the collagen and hydroxyapa-

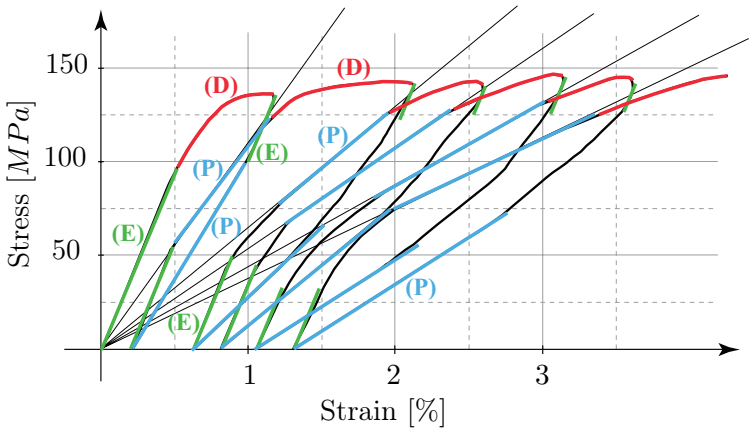

Figure 2.5: Three hypothesized modes of deformation of cortical bone: (E) intact linear elastic mode (D) damage mode (P) plastic mode. Note that all damaged reloading curves are collinear with the origin.

tite ([Keaveny et al., 2001]). Damage in bone may be caused by shear failure of the organic matrix, namely sliding of the collagen molecules or microfibrils on each other. Figure 2.6 shows the uniaxial compressive behaviour of trabecular bone in a cyclic overloading situation. The main difference between the two types of bone lies in the damage mode. Due to pore collapse, a softening of the stress occurs in the damaging mode. Furthermore, once damage has been accumulated, the damage threshold is decreased as can be seen in the subsequent cycle.

Suspecting similar microdamage mechanisms responsible for the damaged behaviour of both compact and trabecular bone, we will use the same damage model for both types of bone in our finite element simulations (Chapter 7).

Only in a second step, *viscous* effects may be investigated. Even though the mechanical properties of bone show differences from person to person and from bone to bone, the *qualitative* aspect of a stress-strain curve remains unchanged, keeping its characteristic features. We now briefly review the principal mechanical properties of bone.

Densities

Bone is composed approximately of 43% of mineral phase, 32% of organic phase and 25% of water. Being a porous material, various densities can be defined. *Volume fraction* or *structural density* ρ_s is defined as the volume of the bony matrix per unit of volume. Complementarily, *porosity* is defined as $(1-\rho_s)$. Cortical and trabecular bone tissue *densities* (mass per unit volume)

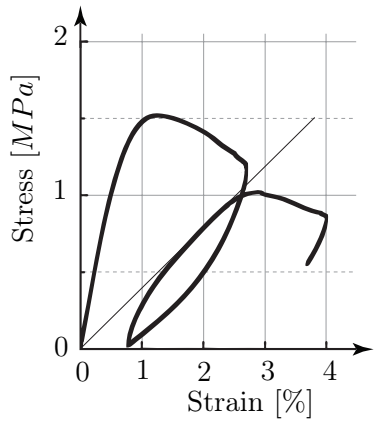

Figure 2.6: Uniaxial compressive cyclic behaviour of trabecular bone (adapted from [Keaveny et al., 1999]). Note that the damaged reloading is also collinear with the origin.

are essentially constant at about $2\,g/cm^3$. The *apparent density* ρ_a is defined as the product of volume fraction and tissue density (or equivalently total mass per unit volume of bone). A measure of the degree of mineralization is given by the *ash density*. It reflects the concentration of the mineral phase of the bone (weight of ash per unit volume).

Elastic properties

The elasticity of bone is its ability to fully and instantaneously recover its initial shape after release of an applied load that did not exceed the elastic limit. Various experimental techniques have been used to investigate the elastic properties of cortical bone tissue. Beside the traditional mechanical techniques such as uniaxial tensile or compressive testing (e.g. [Reilly and Burstein, 1975]), torsion tests (e.g. [Jepsen and Davy, 1997]), biaxial testing (e.g. [Lakes et al., 1979]), or bending (e.g. [Currey, 1965]), ultrasonic technique is a useful method in measuring elastic properties of cortical bone (e.g. [Lang, 1970, van Buskirk et al., 1981]). The advantage of this method is the determination of the fully anisotropic elastic constants within the same specimen. Microstructural heterogeneities and anisotropic elastic properties can be measured with the nanoindentation technique (e.g. [Hoffler et al., 2000a, Fan et al., 2001]). However, several concerns are raised regarding nanoindentation tests. Indeed, the commonly used model of deformation of an elastic half space by a rigid punch ([Sneddon, 1965, Oliver and Pharr, 1992]) assumes an isotropic targeted material and must be adapted in consequence ([Stroh, 1962, Lothe and Barnett, 1976, Vlassak and Nix, 1993, Hay et al., 1999, Swadener and Pharr, 2001]).

At the macroscopic level, the anisotropic elasticity of cortical bone tissue is well approximated by transverse isotropic or orthotropic constitutive relations ([van Buskirk and Ashman, 1981, Piekarski et al., 2004]). The longitudinal elastic modulus of long bones is about $17.4\,GPa$ for human bone ($20.4\,GPa$ for bovine bone), whereas the transverse elastic modulus is about $9.6\,GPa$ (and $11.7\,GPa$ for bovine bone)([Cowin, 1989]). These values are the same in tension and compression.

The effect of porosity and mineral content on the longitudinal elastic modulus of compact bone has been studied, among others, by [Currey, 1988b]. He found that over 80% of the total variation in the elastic modulus is explained by these two variables and that the dependence is roughly cubic on both volume fraction and calcium content. [Carter and Hayes, 1977b] found that the elastic modulus of both compact *and* trabecular bone are closely related to the cube of the apparent wet bone density. The ash density probably proportional to mineral content seems also to be a representative compositional variable of bone tissue. A review of the different correlation relations can be found in [Doblaré et al., 2004].

The role of collagen on the elastic properties of bone has been investigated by [Wang et al., 2001], by heating the bone, thus denaturating the collagen within the bone. Their results indicate that the toughness and strength of bone decrease significantly with increasing collagen denaturation, whereas its elastic modulus is almost constant irrespective of collagen denaturation.

The elastic properties of trabecular bone tissue are more difficult to measure than those of cortical bone. The extremely small dimensions of individual trabeculae set numerous technical difficulties. The apparent elastic modulus of trabecular bone can vary over a wide range (roughly speaking from 0.1 to $2000\,MPa$) ([Keaveny et al., 2001]). By the term apparent we mean defined at the continuum (macroscopic) level. At this level, a representative volume element containing a large number of trabeculae must be tested (typically around $5\times5\times5\,mm^3$). As for cortical bone, there are no differences between the tensile and compressive elastic constants of trabecular bone ([Rohl et al., 1991]). Structural density relationships also hold for the elasticity of trabecular bone. Approximating the longitudinal elastic modulus by the general form $\epsilon = c\rho_a^p$, [Hodgskinson and Currey, 1992] found that the power p between the modulus and the apparent density is close to two. Other structural relationships can be found in [Cowin, 2001]. Relationships between the elastic constants and a fabric tensor that represents the anisotropy of trabecular bone have been investigated by [Cowin, 1985]. An alternative and attractive model that requires less independent parameters was developed by [Zysset, 1994, Zysset and Curnier, 1995].

Viscous properties

The viscous part of the mechanical viscoelastic behaviour of bone is responsible for the dependency of stiffness on strain rate, the ability to dissipate energy within the elastic range of deformation, and for phenomena such as stress relaxation and creep behaviour found in both compact and trabecular bone. It has been shown that, at physiological strain rates, i.e. rates as they occur during normal daily activities ($\sim 1\,Hz$), bone tissue has a weak dependence on strain rates ([McElhaney, 1966, Fondrk et al., 1988, Fondrk et al., 1999b]). Elastic moduli are approximately proportional to the strain rate raised to the 0.06 power ([Carter and Hayes, 1977b]). In the same study, the stiffening effect due to the water content in compact bone or marrow in trabecular bone was shown to be small, except for high strain rates.

Various creep-fracture tests have been carried out on cortical bone ([Carter and Caler, 1983, Caler and Carter, 1989, Mauch et al., 1992]). The three characteristic stages of creep exhibited by many materials are also observed for bone (in tensile and compressive loadings). The effect of temperature, stress and microstructure on the creep behaviour of compact bovine bone was investigated by [Rimnac et al., 1993]. The viscoelastic and creep properties of trabecular bone are similar to those of cortical bone ([Bowman et al., 1994]).

In conclusion, viscoelastic effects of bone are of secondary importance at physiological strain rates. Our constitutive model for cortical bone tissue will thus consider a linear behaviour in the elastic range of deformation (it may not be appropriate for impacts).

Overloading and failure properties

The damaged behaviour of cortical bone corresponds to the generation of microcracks, (which leads to stiffness reduction), an energy dissipation, permanent strains and may result in its failure. The *damage threshold stress* which coincides with the *elastic limit* or *yield stress* quantifies the onset of damage behaviour. As in standard plasticity, the damage threshold or yield point is mostly taken as the point where the stress-strain curve deviates by a strain of 0.2% from the straight line describing the initial part of the curve (e.g. [Currey, 1990]). Numerous studies show that damage threshold stresses of compact bone tissue are different in tension and compression (e.g. [Reilly and Burstein, 1975, Currey, 1990, Kotha and Guzelsu, 2003]). Their mean values vary considerably from one author to another, but let us mention the values of [Cowin, 1989] for an order of magnitude. For human femoral cor-

tical bone, the tensile longitudinal damage threshold stress is about 115 MPa and the compressive one about 182 MPa. For bovine femoral cortical bone, the mentioned damage threshold stress values are 141 MPa in tension and 196 MPa in compression. Distinct tensile and compressive thresholds also hold for trabecular bone (e.g. [Keaveny et al., 1999, Keaveny et al., 2001, Rincón, 2003]). The recent study of [Bayraktar et al., 2004] indicates that the elastic and the tensile and compressive yield properties of trabecular bone at the tissue (microscopic) level are similar to those of cortical tissue.

Similar structural relations linking the apparent density to the elastic modulus were found between the apparent density and the longitudinal damage threshold stresses. The power law relating these two variables is characterized by an exponent close to two ([Reilly and Burstein, 1975, Currey, 1990]). However, these trends depend on the loading direction.

The maximal stress reached before failure in a monotonic loading, also known as *ultimate stress*, is mostly slightly higher than the damage threshold stress ([Currey, 1990]). This is mainly due to the damaged behaviour of cortical bone which shows only a small hardening in that region, in tension as well as in compression. The tensile longitudinal *ultimate strains* for femoral human cortical bone are in the range of 3% (and 1.6% for bovine cortical bone). The compressive longitudinal values are about 2.2% for human bone and 2.5% for bovine bone ([Cowin, 1989]).

Fatigue properties

Another type of damage occurring in bone tissue and which results in a degradation of its mechanical properties is fatigue damage (e.g. [Carter and Hayes, 1977a, Pattin et al., 1996]). When periodically loaded in the laboratory, bone experiences fatigue damage and may fail from it like any other composite material (e.g. [Carter et al., 1976]). This behaviour can be attributed to cumulative microcracking, debonding, void growth, and fiber breakage. In living bone, fatigue damage accumulation has been postulated as a stimulus to the bone remodelling response ([Martin and Burr, 1982, Ramtani and Zidi, 2002]).

Fractures induced by fatigue damage accumulation are clinically called *stress fractures*. They mostly occur in persons who have repetitive physical activities such as soldiers, ballet dancers or joggers (e.g. [Burckhardt, 2004]). It also occurs at lower activity levels in bones weakened by osteoporosis. If the remodelling process is not sufficient to repair the accumulation of fatigue microcracks, they can result in macrocracks leading to fracture.

Many experimental studies have investigated the fatigue strength behaviour of cortical bone (e.g. [Caler and Carter, 1989, Zioupos et al., 1996,

Zioupos and Casinos, 1998, George and Vashishth, 2003]). The fracture mechanisms in bone tissue were recently examined by [Ritchie et al., 2004]. The fatigue behaviour of trabecular bone shows similarities with that of cortical bone ([Choi and Goldstein, 1992]). Therefore, it is plausible that cortical bone properties can be used to predict the behaviour of trabecular bone ([Taylor et al., 2002]).

In this study, we do not consider damage accumulation mechanisms due to fatigue. For modeling the mechanical behaviour of cortical bone tissue, the accent is put on typical overloading situations including a low number of tensile and/or compressive cycles. Nevertheless, we expect bone tissue to exhibit similar mechanical properties degradations due to fatigue damage and overloading damage.

2.2.2 Human and bovine cortical bone

Many of the forequoted biomechanical studies have been carried out on bovine bone tissue. The main reason for this is that bovine bones are larger and much more accessible than human bones. Therefore, it is quite justified to ask if the corresponding results can be applied to human bone tissue and if some useful conclusions or predictions can be drawn from those studies.

From a structural standpoint, the differences between bovine and human cortical bone are primarily attributable to differences in maturation rates (e.g. [Carter et al., 1976]). A bovine bone grows much faster than a human bone. Indeed, in humans, full growth is not achieved until the age of about $16\,yr$ but cows are fully grown in only two years. In consequence, the structure of bovine bone is fibrolamellar whereas that of human bone is lamellar ([Currey, 2002]).

The compositions of human and bovine bones are similar. Different degrees of mineralization can lead to slightly different shapes of the overloading part of the stress-strain diagrams. By testing a wide variety of animals, [Currey, 1990] showed that in highly mineralized specimens the stress-strain curve is almost flat in the overloading region. The less mineralized specimens were characterized by a quite marked hardening in that region.

By comparing the studies of human and bovine bone, we conclude that even if the microstructure and composition may vary between human and bovine bones, the mechanical behaviour of these tissues is *qualitatively* similar. In consequence, as bovine bone tissue is of easy access, it is reasonable to investigate it first and to model its constitutive behaviour. In a second step, the model should be adjusted to human bone tissue, based on novel tests with human bone specimens.

2.2.3 Age-related and disease effects

When the balance between bone apposition and bone resorption is no longer respected (due to age, sex hormone deficiency in women, other hormonal disorders, calcium or vitamin D deficiency), the quantity of bone is substantially reduced. It may result in a net loss of bone substance and a deterioration of its microarchitecture. As a consequence, the mechanical properties of pathologic bones are greatly altered ([Seeman, 2002]).

There is a large number of diseases affecting bone quality. One of them is osteoporosis which results in a significant bone loss. Osteoporotic bone is much more porous and thus more fragile and subject to fractures than normal (healthy) bone. Another pathology affecting bone tissue is osteopetrosis. It is a disease caused by an inability to produce sufficient osteoclasts. Thus, normal resorption and remodelling cannot occur, resulting in much harder and denser bones than usual.

Age-related changes in the mechanical properties of bone are of great importance in understanding bone fragility and age-related fractures. Both cortical and trabecular bone from young adults show significantly higher elastic moduli than the tissues from older adults ([Guo, 2001]). The strength and the modulus of elasticity decrease after maturation by approximately 2% per decade ([Burstein et al., 1976]). The mechanical properties of bone tissue were explored at the lamellar level by [Hoffler et al., 2000b]. Their results suggest that the elastic modulus and hardness of bone lamellae are independent of age and gender. Therefore, the age and gender-related decrease in mechanical integrity observed at the macroscopic level may not involve necessarily alterations at the microstructural level.

Age-related and disease effects on the quality of bone tissue are currently the object of intensive investigations. Biomechanical testing is an essential tool for assessing bone quality. For example, it proves to be specially useful for all drug therapy investigations which intend to prevent bone fractures (e.g. [Hengsberger, 2002]).

2.3 Constitutive models for bone tissue

As described in the previous Section, damage accumulation is a critical component of the fracture process in bone under monotonic, cyclic, creep, and fatigue loading conditions. However, our understanding of damage is incomplete. A wide range of constitutive damage models have been developed for different classes of materials (e.g. [Lemaitre and Chaboche, 1985, Simo and Ju, 1987, Lubarda and Krajcinovic, 2000, Carol et al., 2001b]).

One important issue when modeling a damageable material is the choice of the damage variable quantifying its alteration ([Krajcinovic, 1998]). The most common estimate of damage accumulation is to measure its stiffness degradation. The elastic moduli of a cracked solid have been determined by [Budiansky and O'Connell, 1976]. Alternative measures of the damage process in cortical bone were investigated by [Jepsen and Davy, 1997]. Their results suggest that the reduction in torsional properties are better measures of the damage process than reduction in either damage threshold stress or modulus in traction.

The problem of finding an appropriate damage measure is not simple, even for isotropic materials. Indeed, materials which show an isotropic material response in the elastic regime often exhibit anisotropic characteristics in the inelastic regime. The development and growth of cracks and voids can undoubtly induce anisotropy in the mechanical behaviour of the material. To describe this effect realistically, the underlying model must be able to reproduce these anisotropies. In the context of continuum damage mechanics, this leads to the introduction of high order tensorial damage variables (e.g. second-order or even fourth-order damage tensors). Even if it is not very realistic, only "isotropic" damage will be considered in this study for simplicity. It will be formulated in its simplest form, namely in terms of a single scalar variable representing the stiffness reduction of cortical bone tissue (e.g. [Lemaitre, 1996]).

Let us now describe some constitutive models which have been developed and which could or have been applied to cortical bone tissue.

2.3.1 Composite models

In an early attempt to model bone tissue, [Piekarski, 1973] viewed it as a composite material. He applied the underlying theory to bone with various contents of mineral and organic phases. However, this model could not satisfactorily explain the elasticity and the anisotropy of bone.

Damage mechanics, incorporating anisotropic elasto-plasticity and anisotropic elastic degradation, was applied to the composite nature of concrete by [Ortiz, 1985]. Interestingly, it delivered a very similar constitutive behaviour to that of bone tissue. Damage mechanics was also applied to composite laminates ([Allix et al., 1987]) and several elastic plastic damage constitutive models were more recently developed for composite materials (e.g. [Matzenmiller et al., 1995, Oller et al., 1996, Voyiadjis and Deliktas, 2000, Chaboche et al., 2001]). Recently, a simplified hierarchical model of biocomposites including mineral platelets and a protein matrix was developed ([Jäger and Fratzl, 2000, Gao et al., 2003]). They showed that the nanome-

ter size of the mineral platelets in bone may be the result of fracture strength optimization. However, the composition of bone tissue is more complex than most engineering composites. Thus, none of these models could satisfactorily explain the nonlinear macroscopic mechanical behaviour of bone for arbitrary loading conditions.

2.3.2 Microplane models

An interesting alternative to describe the anisotropic behaviour of a material is given by the microplane theory (e.g. [Carol and Bazant, 1997]). In that framework, the constitutive equations between single stress and strain components are formulated on individual microplanes at a material point. Most microplane models are based on the formulation of phenomenological microplane constitutive laws with parameters which are difficult to identify experimentally. The microplane model was formulated in a thermodynamically consistent way by [Carol et al., 2001a]. In addition, [Kuhl et al., 2001] presented a technique to derive microplane constitutive equations in a thermodynamically consistent way. In an attempt to link the micro and macro material scales, the microplane damage parameters have been adjusted to macroscopic damage laws by [Leukart and Ramm, 2003]. To our knowledge, microplane theory has not yet been applied to bone tissue, but deserves our attention.

2.3.3 Specific models

One of the most successful model to date in describing the mechanical behaviour of cortical bone tissue in cyclic overloading conditions is due to [Fondrk et al., 1999a]. The model is based on two internal state variables and successfully reproduces the tensile behaviour of compact bone under arbitrary loading conditions. However, the interpretation and experimental identification of the internal state variables is delicate. Furthermore, it includes only the axial tensile behaviour of bone and is unable to take into account a distinct compressive behaviour. A three-dimensional generalization of the model, specially useful for any finite element analysis, is also missing.

Another interesting attempt in modelling bone tissue is due to [Krajcinovic et al., 1987]. In their simple microstructural model, damage is quantified by the ratio between the number of pulled-out osteons and the total number of osteons. This model allows for some useful insights into microdamage mechanisms.

The cumulative damage model for bone fracture proposed by [Carter and Caler, 1985] is derived from tests in cyclic fatigue loading, and also in

monotonic tensile loading. In this model, a certain amount of damage is necessary to fracture bone, and the rate of damage accumulation is related to some high power of the damage threshold stress. The predictions of the model deliver fairly good results for creep and strain rate experiments. However, it is unable to describe correctly the loading, unloading and reloading sequence observed in overloading experiments.

Further one-dimensional models for bone tissue are proposed by [Rincón et al., 2001] and [Zysset, 2002]. Both models combine linear viscoelasticity with plasticity and damage but do not describe satisfactorily the damaged behaviour of bone.

A damage constitutive law based on the generalized standard materials formalism has been developed for trabecular bone by [Zysset, 1994]. In the same work, the law is successfully generalized in 3D, using a model based on fabric tensors characterizing the local trabecular morphology. The model may be applied to cortical bone tissue but it does not take into account an anisotropic damage surface with different properties in tension and compression. Furthermore, the piecewise linear behaviour observed in damaged bone is not included in this model (Subsection 2.2.1).

A three-dimensional model for brittle elastic solids with unequal tensile and compressive strengths has been developed by [Lubarda et al., 1994]. The different response in tension and compression of a brittle material is modeled by introducing positive and negative stress and strain operators. However, bone is not a completely brittle material. The damaged deformation mode following the nearly linear elastic part of a tensile stress-strain curve (Figure 2.4) exhibits rather a ductile behaviour.

Bone damage criteria

Various criteria have been developed in modeling the constitutive behaviour of different classes of materials. Let us mention some important criteria which may be applied to cortical bone.

The *Tresca* and *von Mises* criteria are isotropic criteria traditionally used to predict yielding of ductile materials like metals. If used as damage threshold criteria, they also assume equal damage threshold stresses in tension and compression, which is not very realistic for bone tissue.

An anisotropic generalization of the Mises criterion is due to [Hill, 1950]. Unfortunately, the quadratic *Hill* criterion also assumes equal tensile and compressive strengths. Further criteria applied in the field of anisotropic plasticity have been studied by [Rogers, 1987] and by [Spencer, 1993, Voyiadjis and Thiagarajan, 1995] for the case of fibre-reinforced materials.

The *Mohr-Coulomb* conical criterion is an isotropic damage criterion

which is commonly used for materials with different behaviour in tension and compression. It depends on the mean stress and has been applied to soils, rocks, and concrete. [Hoffman, 1967] proposed a fracture criterion for brittle materials that also takes into account different strengths in tension and compression. Nevertheless, *Hoffman*'s criterion is also an isotropic criterion and thus unsuitable for bone tissue. More recently, [Ferrari and Granik, 1995] developed a more general criterion with also distinct tensile and compressive thresholds. Unfortunately, it is not convex a priori and may be not thermodynamically consistent. Recently, a method for defining general implicit orthotropic yield criterion has been formulated by [Oller et al., 2003].

The *Tsai-Wu* quadratic criterion was originally developed for fibre-reinforced composite materials by [Tsai and Wu, 1971]. It is a generalization of Hill's anisotropic criterion and accounts for different tensile and compressive damage threshold stresses, as well as interactions between the strengths under different loading conditions. The criterion is expressed in terms of the stress tensor and two material dependent tensors. The different behaviour in tension and compression is mainly achieved by translating Hill's anisotropic damage surface in stress space. Unfortunately, the Tsai-Wu criterion is defined by a high number of material constants. In particular, three interaction coefficients between normal stresses are difficult to identify on experimental grounds (i.e. biaxial testing, e.g. [Rincón, 2003]).

In order to reduce the number of constants of the Tsai-Wu criterion, [Cowin, 1986] proposed a fracture criterion applicable to porous and/or composite materials. *Cowin*'s criterion is formulated in stress space and is based on the properties of the homogenized microstructure. It depends on the stress state, the porosity of the underlying material, and on the fabric tensor reflecting the microstructural morphology. The main drawback of this criterion is the difficulty of determining all parameters involved.

An alternative criterion for bone tissue also based on fabric and porosity is due to [Pietruszczak et al., 1999]. It is formulated in terms of the first, second, and third stress invariant. Unfortunately, it does not predict failure of bone under hydrostatic compression.

Recently, an interesting multiaxial yield and failure criterion has been successfully identified for human trabecular bone ([Rincón, 2003, Zysset and Rincón, 2005])). The criterion is expressed in terms of the stress tensor. It combines an halfspacewise definition of Hill's criterion for anisotropy ([Curnier et al., 1995]) and an alternative porosity and fabric dependence of the criterion for reducing the number of necessary constants ([Zysset, 1994, Zysset and Curnier, 1995]). If we assume a similar constitutive behaviour for trabecular and cortical bone, this makes it an attractive candidate for an anisotropic damage criterion for cortical bone tissue.

In spite of the large number of models and the lack of agreement between different studies on bone biomechanics, priorities must be set in any modelling process. Let us now describe some important ingredients which should be included in a constitutive law for bone tissue.

Requirements for a constitutive law for cortical bone

We retained four basic requirements for a constitutive law for cortical bone.

1. *It should be based on simple mechanical principles and formulated in a thermodynamically consistent way.* Doing so, it should provide a coherent and comprehensive interpretation of the observed behaviours. Effects such as mechanical properties degradation, increased energy dissipation, and damage accumulation processes should be clarified this way.

2. *It should reproduce with accuracy a broad sample of experimental records.* By the word broad we do not mean *all* types of experiments. The model should predict only the effects it is accounting for. For example, a constitutive model intended to describe the quasistatic behaviour of cortical bone can hardly be applied to impact studies involving high strain rates. In our case, the model is intended to explain the overloading behaviour of bone at physiological strain rates for arbitrary proportional loading conditions. It should be able to reproduce the elastic degradation and development of permanent residual strains after overloading. Furthermore, in cyclic overloading experiments, the reloading stress-strain curve should have a short initial nonlinear region with a tangent modulus similar to that of the undamaged material (Figure 2.4). This should be followed by an approximately linear region with a reduced or damaged modulus (collinear with the origin). The reloading curve should approach the extrapolated envelope of the original loading curve. The model should display elements of both metal-type plasticity and brittle-type damage.

3. *Its material constants should be measurable and identifiable on experimental grounds.* The model should be as simple as possible and based on a minimal set of material parameters. The determination of the constants should imply a minimal set of mutually independent feasible mechanical experiments.

4. *It should be suitable in any computational implementation.* In particular, its implementation in a finite element code must be efficient and computationally inexpensive.

Chapter 3

Theoretical solid mechanics background

The objective of this Chapter is to define the theoretical framework and to recall the general concepts used throughout this work. First, a brief review of continuum mechanics is given. Then, the methods of thermostatics and the formalism of generalized standard materials are presented. Finally, basic rheological behaviours and their underlying mathematical models are explicited. They will serve as a basis for the new constitutive laws for cortical bone.

3.1 Continuum mechanics framework

The motion of macroscopic deformable bodies can be described in the framework of continuum mechanics. The main assumption is to consider sufficiently large bodies with respect to their microscopic structure. Then, the fundamental law of dynamics governing the motion of the body can be deduced from the principle of virtual power (e.g. [Germain, 1995, Curnier, 2005]).

In this Section, we first define the strain and stress measures used in this study. Then the principle of virtual power and the formulation of a general problem in continuum mechanics are stated.

3.1.1 Strain measures

Let $\mathbb{B}$ be a solid body formed by a set of particles which occupy a portion $\boldsymbol{\Omega}$ of the space $\mathbb{R}^3$ at time $t = 0$. If each particle composing the solid is labelled by a vector $\boldsymbol{x}$ expressed in a *reference frame* $\{\mathbf{e}_1, \mathbf{e}_2, \mathbf{e}_3\}$ (Figure

3.1), then a body is defined as:

$$\mathbb{B} \equiv \boldsymbol{\Omega} := \{\boldsymbol{x} = x_i \mathbf{e}_i,\ i = 1,2,3 \mid \textit{conditions defining the body}\} \subset \mathbb{R}^3$$

The *deformed* or *present configuration* of the solid, denoted as $\boldsymbol{\Omega}_t$, is defined by:

$$\boldsymbol{\Omega}_t := \{\mathbf{y} = y_i \mathbf{e}_i,\ i = 1,2,3\} \subset \mathbb{R}^3$$

The function $\mathbf{y} : \boldsymbol{\Omega} \times \mathbb{R}_+ \to \boldsymbol{\Omega}_t$

$$\mathbf{y} = \mathbf{y}(\boldsymbol{x}, t) \quad \text{with} \quad \mathbf{y}(\boldsymbol{x}, 0) = \boldsymbol{x} \tag{3.1}$$

is the *motion* or *deformation* of the body (Lagrangian description). Thus, the *displacement* of the particle $\boldsymbol{x}$ at time t is given by:

$$\mathbf{u} = \mathbf{u}(\boldsymbol{x}, t) := \mathbf{y}(\boldsymbol{x}, t) - \boldsymbol{x} \tag{3.2}$$

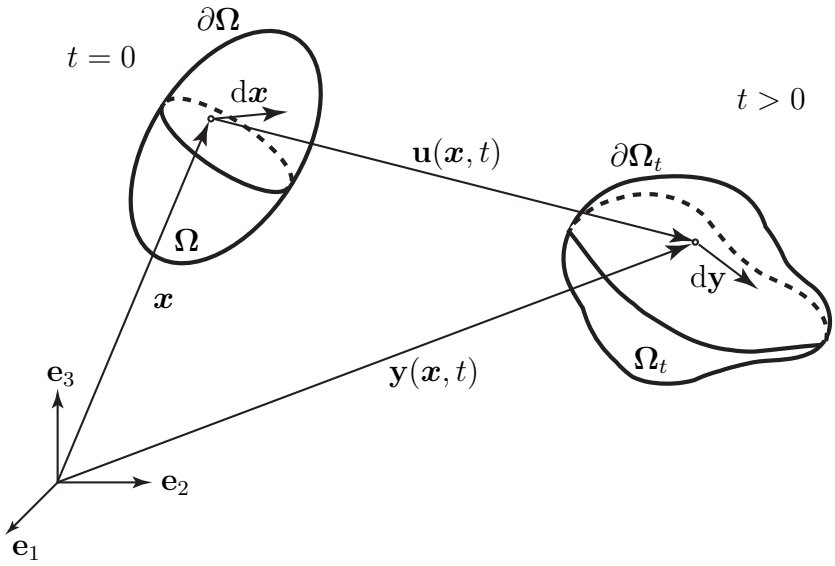

Figure 3.1: Reference and present configuration used in the Lagrangian description.

The transformation of an original material fiber $\mathrm{d}\boldsymbol{x}$ is determined by the *deformation gradient* $\mathbf{F}$:

$$\mathrm{d}\mathbf{y} = \mathbf{F}\,\mathrm{d}\boldsymbol{x} \quad \Longleftrightarrow \quad \mathbf{F} = \mathbf{F}(\boldsymbol{x}, t) := \nabla_{\boldsymbol{x}}\,\mathbf{y} = \frac{\partial \mathbf{y}}{\partial \boldsymbol{x}}\,(\boldsymbol{x}, t) \tag{3.3}$$

Therefore, $\mathbf{F}$ is a measure of local transformations (rotations and deformations) in the solid.
Local changes of volume are given by the *jacobian* of the transformation:

$$J = J(\boldsymbol{x}, t) := \det \mathbf{F} \tag{3.4}$$

In order to avoid a collapse of the body or its explosion, we impose the restrictions

$$0 < J < +\infty$$

The *displacement gradient* is defined by:

$$\mathbf{H} = \mathbf{H}(\boldsymbol{x}, t) := \frac{\partial \mathbf{u}}{\partial \boldsymbol{x}}(\boldsymbol{x}, t) = \mathbf{F} - \mathbf{I} \tag{3.5}$$

The (right Cauchy-Green) material *metric tensor* $\mathbf{C} = \mathbf{F}^{\mathrm{T}}\mathbf{F}$ allows to compute the changes of angle and length between material fibers:

$$\mathrm{d}\mathbf{y}' \cdot \mathrm{d}\mathbf{y} = \mathrm{d}\boldsymbol{x}' \cdot \mathbf{C}\,\mathrm{d}\boldsymbol{x} \tag{3.6}$$

with $(\cdot)$ the usual vector scalar product.
As $\mathbf{C} \equiv \mathbf{I}$ in a rigid body motion (implying no deformation of the body), we define an adequate measure of deformation, the symmetric Green-St Venant (Lagrangian) *material strain tensor*:

$$\mathbf{E} = \mathbf{E}(\boldsymbol{x}, t) := \frac{1}{2}(\mathbf{C} - \mathbf{I}) \tag{3.7}$$

It has the advantage of being objective (invariant in a rigid body motion) and to vanish when $\mathbf{F} \equiv \mathbf{I}$.
For small transformations ($\mathbf{F} \simeq \mathbf{I}$), we have:

$$\mathbf{E} \simeq \frac{1}{2}(\mathbf{H}^{\mathrm{T}} + \mathbf{H}) \tag{3.8}$$

3.1.2 Stress measures

Let us assume that the body $\mathbb{B}$ is subject to only two types of external forces: body forces and contact forces.
In the material nominal description, we define the resultant *body force* $\overline{\mathbf{g}^t}$ acting on the solid at time t by:

$$\overline{\mathbf{g}^t}(\boldsymbol{\Omega}, t) := \int_{\boldsymbol{\Omega}} \mathbf{g}^t(\boldsymbol{x}, t)\,\mathrm{d}V \tag{3.9}$$

and the resultant *contact force* $\overline{\mathbf{p}}$ by:

$$\overline{\mathbf{p}}(\partial\boldsymbol{\Omega}, t) := \int_{\partial\boldsymbol{\Omega}} \mathbf{p}(\boldsymbol{x}, t, \mathbf{n}(\boldsymbol{x}))\, \mathrm{d}A \tag{3.10}$$

where $\mathbf{p}(\boldsymbol{x}, t, \mathbf{n}(\boldsymbol{x}))$ is the *nominal stress* vector acting on the element surface $\mathrm{d}A$ of outward normal $\mathbf{n}(\boldsymbol{x})$. Finally, we define the *inertial forces* associated to the body:

$$\overline{\ddot{\mathbf{m}}^t}(\boldsymbol{\Omega}, t) := \int_{\boldsymbol{\Omega}} \ddot{\mathbf{y}}(\boldsymbol{x}, t)\rho(\boldsymbol{x}, t)\, \mathrm{d}V \tag{3.11}$$

with $\rho(\boldsymbol{x}, t)$ the density of the solid.
Thus, the equilibrium of the forces acting on the solid can be written as:

$$\overline{\ddot{\mathbf{m}}^t}(\boldsymbol{\Omega}, t) = \overline{\mathbf{g}^t}(\boldsymbol{\Omega}, t) + \overline{\mathbf{p}}(\partial\boldsymbol{\Omega}, t)$$

The equilibrium remains satisfied for any portion $\boldsymbol{\omega} \subseteq \boldsymbol{\Omega}$:

$$\overline{\ddot{\mathbf{m}}^t}(\boldsymbol{\omega}, t) = \overline{\mathbf{g}^t}(\boldsymbol{\omega}, t) + \overline{\mathbf{p}}(\partial\boldsymbol{\omega}, t) \tag{3.12}$$

Cauchy's theorem, (e.g. [Curnier, 2005]), states that for any particle of the solid there exists a *first nominal Piola-Kirchhoff stress tensor* $\mathbf{P}$, implicitly defined by:

$$\mathbf{p}(\boldsymbol{x}, t, \mathbf{n}(\boldsymbol{x})) =: \mathbf{P}(\boldsymbol{x}, t)\, \mathbf{n}(\boldsymbol{x}) \tag{3.13}$$

Thus, the forces equilibrium can be expressed in local form:

$$\rho(\boldsymbol{x}, t)\ddot{\mathbf{y}}(\boldsymbol{x}, t) = \mathbf{div}\, \mathbf{P}(\boldsymbol{x}, t) + \mathbf{g}^t(\boldsymbol{x}, t) \quad \forall\, \boldsymbol{x} \in \boldsymbol{\Omega} \tag{3.14}$$

The equilibrium of the moments around the origin associated to the inertial forces, body forces and contact forces is satisfied for any portion $\boldsymbol{\omega} \subseteq \boldsymbol{\Omega}$:

$$\begin{aligned} \int_{\boldsymbol{\omega}} \mathbf{y}(\boldsymbol{x}, t) \times \ddot{\mathbf{y}}(\boldsymbol{x}, t)\rho(\boldsymbol{x}, t)\, \mathrm{d}V = \\ \int_{\boldsymbol{\omega}} \mathbf{y}(\boldsymbol{x}, t) \times \mathbf{g}^t(\boldsymbol{x}, t)\, \mathrm{d}V + \int_{\partial\boldsymbol{\omega}} \mathbf{y}(\boldsymbol{x}, t) \times \mathbf{p}(\boldsymbol{x}, t, \mathbf{n}(\boldsymbol{x}))\, \mathrm{d}A \end{aligned} \tag{3.15}$$

and in local form:

$$\mathbf{P}(\boldsymbol{x}, t)\, \mathbf{F}^{\mathrm{T}}(\boldsymbol{x}, t) = \mathbf{P}^T(\boldsymbol{x}, t)\, \mathbf{F}(\mathbf{x}, t) \quad \forall\, \boldsymbol{x} \in \boldsymbol{\Omega} \tag{3.16}$$

The symmetric and objective *second material Piola-Kirchhoff stress tensor* $\mathbf{S}$ is defined by:

$$\mathbf{S} = \mathbf{S}(\boldsymbol{x}, t) := \mathbf{F}^{-1}(\boldsymbol{x}, t)\, \mathbf{P}(\boldsymbol{x}, t) \tag{3.17}$$

The local moment equilibrium (3.16) corresponds to the symmetry of $\mathbf{S}$:

$$\mathbf{S}(\boldsymbol{x},t) = \mathbf{S}^{\mathrm{T}}(\boldsymbol{x},t) \quad \forall\, \boldsymbol{x} \in \boldsymbol{\Omega} \tag{3.18}$$

Finally, we define the symmetric *spatial Cauchy stress tensor* $\mathbf{T}$ in the actual configuration by:

$$\mathbf{T} = \mathbf{T}(\mathbf{y},t) := J^{-1}(\mathbf{y},t)\mathbf{P}(\mathbf{y}^{-1}(\mathbf{y},t),t)\,\mathbf{F}^{\mathrm{T}}(\mathbf{y},t) \tag{3.19}$$

For small transformations ($\mathbf{F} \simeq \mathbf{I}$), the three measures of stress coincide:

$$\mathbf{P}(\boldsymbol{x},t) \simeq \mathbf{S}(\boldsymbol{x},t) \simeq \mathbf{T}(\mathbf{y}(\boldsymbol{x},t),t)$$

3.1.3 Principle of virtual power

It can be shown (e.g. [Curnier, 2005]), that the *internal power of deformation* $\overline{P}^{\,int}$ associated to the internal efforts acting on an arbitrary portion $\boldsymbol{\omega} \subseteq \boldsymbol{\Omega}$ is given by:

$$\overline{P}^{\,int} = \int_{\boldsymbol{\omega}} \mathbf{P} : \dot{\mathbf{F}}\,\mathrm{d}V = \int_{\boldsymbol{\omega}} \mathbf{S} : \dot{\mathbf{E}}\,\mathrm{d}V = \int_{\boldsymbol{\omega}} J\mathbf{T} : \mathbf{D}\,\mathrm{d}V \tag{3.20}$$

with $\mathbf{D} = \frac{1}{2}\left(\dot{\mathbf{F}}\mathbf{F}^{-1} + \mathbf{F}^{-\mathrm{T}}\dot{\mathbf{F}}^{\mathrm{T}}\right)$ and (:) the second-order tensor scalar product defined in Appendix A. The stress $\mathbf{P}$ is said *conjugate* (or *dual*) to the strain $\mathbf{F}$ (or $\mathbf{H}$) in the sense that the product $\mathbf{P} : \dot{\mathbf{F}}$ (or $\mathbf{P} : \dot{\mathbf{H}}$) represents the stress power at the strain rate $\dot{\mathbf{F}}$ (or $\dot{\mathbf{H}}$). The same statement holds between the variables $\mathbf{S}$, $\mathbf{E}$ and $J\mathbf{T}$, $\int \mathbf{D}\,\mathrm{d}t$, respectively.

The *principle of virtual power* ([Germain, 1973, Germain, 1995]) states that

i) the internal power of deformation vanishes for any rigid body motion

ii) for any virtual motion, we have:

$$\overset{\circ}{\overline{P}}{}^{\,inertia}(t) + \overset{\circ}{\overline{P}}{}^{\,int}(t) = \overset{\circ}{\overline{P}}{}^{\,ext}(t) \tag{3.21}$$

where $\overline{P}^{\,inertia}$ and $\overline{P}^{\,ext}$ are the inertial and external powers of deformation, respectively, and the circle denotes a power developed along a virtual motion.

The two fundamental laws of solid dynamics can then be derived from this principle.

3.1.4 Vector notation

The second-order strain tensor $\mathbf{E}$ and the material stress tensor $\mathbf{S}$ are symmetric. Therefore, they consist of only six independent components and can be represented as vectors of $\mathbb{R}^6$, using the following convention:

$$\mathbf{E} = \begin{pmatrix} E_{11} \\ E_{22} \\ E_{33} \\ \sqrt{2}E_{23} \\ \sqrt{2}E_{31} \\ \sqrt{2}E_{12} \end{pmatrix} \qquad \text{and} \qquad \mathbf{S} = \begin{pmatrix} S_{11} \\ S_{22} \\ S_{33} \\ \sqrt{2}S_{23} \\ \sqrt{2}S_{31} \\ \sqrt{2}S_{12} \end{pmatrix} \tag{3.22}$$

The coefficients $\sqrt{2}$ ensure that the scalar product and the dyadic product are preserved in this new notation.
The fourth-order elasticity (or tangent inelasticity) tensors having major and minor symmetries are represented by symmetric 6×6 matrices with 21 independent components. Later on, the elasticity tensors of an hyperelastic material will be represented in this way.

3.1.5 Problem statement

In summary, we can formulate a general problem of continuum mechanics in the following way.
Given the initial configuration of a solid body

$$\boldsymbol{\Omega} \subset \mathbb{R}^3 \quad , \quad \partial\boldsymbol{\Omega} \equiv \boldsymbol{\Gamma}_{\mathbf{y}} \cup \boldsymbol{\Gamma}_{\mathbf{p}}$$

the functions

$$\rho(\boldsymbol{x}),\, \mathbf{P}(\boldsymbol{x},t),\, \mathbf{g}^t(\boldsymbol{x},t) \qquad \forall\, \boldsymbol{x} \in \boldsymbol{\Omega}$$

the initial and boundary conditions

$$\begin{array}{ll} \mathbf{y}(\boldsymbol{x},0) = \boldsymbol{x} & \forall\, \boldsymbol{x} \in \boldsymbol{\Omega} \\ \dot{\mathbf{y}}(\boldsymbol{x},0) = \mathbf{v}_0(\boldsymbol{x}) & \forall\, \boldsymbol{x} \in \boldsymbol{\Omega} \\ \mathbf{y}(\boldsymbol{x},t) = \bar{\mathbf{y}}(\boldsymbol{x},t) & \forall\, \boldsymbol{x} \in \boldsymbol{\Gamma}_{\mathbf{y}} \\ \mathbf{P}(\boldsymbol{x},t)\,\mathbf{n}(\boldsymbol{x}) = \bar{\mathbf{p}}(\boldsymbol{x},t) & \forall\, \boldsymbol{x} \in \boldsymbol{\Gamma}_{\mathbf{p}} \end{array}$$

find the motion $\mathbf{y} : (\boldsymbol{x},t) \mapsto \mathbf{y}(\boldsymbol{x},t)$ such that

$$\begin{aligned} \int_{\boldsymbol{\Omega}} \mathring{\mathbf{y}}(\boldsymbol{x},t) \cdot \big(\rho(\boldsymbol{x})\ddot{\mathbf{y}}(\boldsymbol{x},t) - \mathbf{g}^t(\boldsymbol{x},t)\big)\, \mathrm{d}V + \\ + \int_{\boldsymbol{\Omega}} \nabla\mathring{\mathbf{y}}(\boldsymbol{x},t) : \mathbf{P}(\boldsymbol{x},t)\, \mathrm{d}V = \int_{\boldsymbol{\Gamma}_{\mathbf{p}}} \mathring{\mathbf{y}}(\boldsymbol{x},t) \cdot \bar{\mathbf{p}}(\boldsymbol{x},t)\, \mathrm{d}A \end{aligned} \tag{3.23}$$

for any virtual velocity $\mathring{\mathbf{y}}$ such that $\mathring{\mathbf{y}} = \mathbf{0}$ on $\mathbf{\Gamma}_{\mathbf{y}}$.
Equation (3.23) is the weak form of the differential dynamic equation (3.14) or the principle of virtual power.

Assumed to be given, the functions $\rho(\boldsymbol{x})$ and $\mathbf{P}(\boldsymbol{x}, t)$ characterize the actual state of the constituent material. The major goal of this study is to develop an adequate *constitutive law* for cortical bone. Such a law relates the current stress state in the body $\mathbf{P}(\boldsymbol{x}, t)$ to other quantities such as the strain $\mathbf{F}(\boldsymbol{x}, t)$ and its rate $\dot{\mathbf{F}}(\boldsymbol{x}, t)$ known as the state variables. If necessary, these variables must take into account the past history of the mechanical state of the body.
It is important to formulate a constitutive law which is objective (invariant under any change of reference frame). That is the reason why we privilege a formulation of the law in terms of $\mathbf{S}(\mathbf{E})$ rather than $\mathbf{P}(\mathbf{F})$ for example.

In the next Section, we present how to formulate a realistic constitutive law with help of the two principles of thermodynamics. It will serve as a basis for the development of the constitutive laws for cortical bone.

3.2 Thermostatics framework

In contrast with statistical mechanics, thermodynamics is a phenomenological theory that tries to find the relations between observed *macroscopic* properties, without trying to find their microscopic origin. These measurable properties arise from averages done over of a very large number of identical microsystems (typically 10^{10} for a solid). To simplify the discussion, we consider only *thermomechanical* properties and not chemical or electrical properties. The axioms, rules and methods of thermodynamics are justified by the agreement between its theoretical predictions and the experimentally observed results.

Only a few macroscopic quantities like strains survive after this spatio-temporal averaging process. We call them *mechanical variables*. Conversely, most of the microscopic quantities have no effect on the macroscopic description of the system. However, these microscopic quantities that are occulted during the average process may have an influence at the macroscopic level through new macroscopic measurable quantities such as the temperature for example. They are called *thermodynamical variables*.

In order to describe the constitutive behaviour of a certain class of materials, let us focus on one representative element system of a continuum medium, assumed to be so small that, within it, the state variables (mechan-

ical and thermodynamical) may be considered to be uniform although they differ from element to element. Furthermore, let us assume that the state of such a system is described by a set of mutually independent mechanical variables and by only one thermodynamical variable. The models described here are, for simplicity, described in terms of small strain theory and are expressed in terms of Cartesian tensors.

The approach used here is close to that used in the books by [Ziegler, 1983, Germain, 1995, Maugin, 1999] and the review articles by [Collins and Houlsby, 1997, Houlsby and Puzrin, 2000, Puzrin and Houlsby, 2001, Houlsby and Puzrin, 2002].

The strain tensor $\mathbf{E}$ will be the privileged state variable describing the element system. As thermodynamical variable we can choose the entropy $\mathcal{S}$ of the element system or alternatively its temperature T. In many materials the independent state variables $\mathbf{E}$ and $\mathcal{S}$ suffice to determine its state. But the study of dissipative materials usually require the introduction of *internal state variables* that account for the past history of the system. Such variables like the plastic strain tensor $\mathbf{E}^p$ for plastic materials or the damage variable D for damaging materials must be added to the list of the mechanical variables.

For clarity of the report, let us assume that the equilibrium states are entirely determined by the set of mechanical variables $(\mathbf{E}, \mathbf{E^p}, D)$ and by the entropy $\mathcal{S}$. Furthermore, we assume a *quasistatic* evolution of the system in the sense that every evolution is considered as a series of equilibrium states. Let us note that the time derivatives of the state variables do not appear in the definition of the state.

3.2.1 First and second principles of thermodynamics

The *first principle of thermodynamics* in its local form states that there is a convex state function, called the internal energy $U = U(\mathcal{S}, \mathbf{E}, \mathbf{E^p}, D)$, such that

$$\dot{U} = \mathbf{S} : \dot{\mathbf{E}} + P_Q^{ext}(t) \tag{3.24}$$

where $\mathbf{S}$ is the total stress tensor and P_Q^{ext} is the heat supply to the element of volume. U represents the internal energy per unit volume and we assume no chemical exchanges.
As U is a state function, it exists:

$$\begin{array}{rrcl} - & T & \in & \partial_{\mathcal{S}} U \\ - & \mathbf{S}_U^p & \in & -\partial_{\mathbf{E^p}} U \\ - & W_U^D & \in & -\partial_D U \end{array} \tag{3.25}$$

such that

$$\dot{U} = T\,\dot{\mathcal{S}} + \underline{\nabla}_{\mathbf{E}} U : \dot{\mathbf{E}} - \mathbf{S}_U^p : \dot{\mathbf{E}}^{\mathbf{p}} - W_U^D\,\dot{D} \tag{3.26}$$

where $\underline{\nabla}_{\mathbf{E}} U \in \partial_{\mathbf{E}} U$ is a subgradient of U with respect to $\mathbf{E}$. The state function values T, $\mathbf{S}_U^p$ and W_U^D are given by the so-called *state laws* (3.25) and are in this case the temperature, the plastic stress and the damage energy, respectively.

In the case of non-differentiability of the internal energy, the partial derivatives must be calculated with the formalism of convex analysis (e.g. [Rockafellar, 1970, Curnier, 2001]). The set belonging symbols are justified by potentially multi-valued derivative results. If U is differentiable, they are replaced by simple equalities.

The state laws play the role of the generalized forces (dual variables) associated to the state variables (primal variables) in the sense of developed powers. Combining equations (3.24) and (3.26) we have:

$$\dot{U} = T\dot{\mathcal{S}} + \underline{\nabla}_{\mathbf{E}} U : \dot{\mathbf{E}} - \mathbf{S}_U^p : \dot{\mathbf{E}}^p - W_U^D \dot{D} = \mathbf{S} : \dot{\mathbf{E}} + P_Q^{ext}(t) \tag{3.27}$$

The *second principle of thermodynamics* states that in the absence of external heat supply ($P_Q^{ext} \equiv 0$) the entropy rate always is a non-negative function

$$\dot{\mathcal{S}} =: I(t) \geq 0 \tag{3.28}$$

defined as the *internal entropy production*.
Together with equation (3.27), we have

$$I(t) = \frac{1}{T}\left\{(\mathbf{S} - \underline{\nabla}_{\mathbf{E}} U) : \dot{\mathbf{E}} + \mathbf{S}_U^p : \dot{\mathbf{E}}^p + W_U^D \dot{D}\right\} \geq 0 \tag{3.29}$$

Let us define the *elastic stress* deriving from U by:

$$\mathbf{S}_U^e := \underline{\nabla}_{\mathbf{E}} U \tag{3.30}$$

and the *viscous stress* deriving from U by:

$$\mathbf{S}_U^v := \mathbf{S} - \mathbf{S}_U^e \tag{3.31}$$

Therefore, the internal entropy production and the second principle can be written as:

$$I(t) = \frac{1}{T}\left\{\mathbf{S}_U^v : \dot{\mathbf{E}} + \mathbf{S}_U^p : \dot{\mathbf{E}}^p + W_U^D \dot{D}\right\} \geq 0 \tag{3.32}$$

Let us define the *mechanical dissipation* φ as:

$$\varphi(\dot{\mathbf{E}}, \dot{\mathbf{E}}^p, \dot{D}, \mathcal{S}, \mathbf{E}, \mathbf{E}^p, D) := TI(t) = \mathbf{S}_U^v : \dot{\mathbf{E}} + \mathbf{S}_U^p : \dot{\mathbf{E}}^p + W_U^D \dot{D} \tag{3.33}$$

Assuming that the temperature is a positive quantity, the mechanical dissipation satisfies

$$\varphi = \mathbf{S}_U^v : \dot{\mathbf{E}} + \mathbf{S}_U^p : \dot{\mathbf{E}}^p + W_U^D \dot{D} \geq 0 \tag{3.34}$$

Furthermore, the mechanical dissipation vanishes at the origin ($\dot{\mathbf{E}} = \mathbf{0}, \dot{\mathbf{E}}^p = \mathbf{0}$, $\dot{D} = 0$).

Instead of using the internal energy as thermodynamical potential, it is equivalent to use the free energy Ψ of the element system. They are related through a partial Legendre transform:

$$\Psi = U - T\mathcal{S} \tag{3.35}$$

In this formulation, the temperature plays the role of the thermodynamical variable: $\Psi = \Psi(T, \mathbf{E}, \mathbf{E}^p, D)$. The state functions are then obtained by derivation of the free energy potential.
In the case of isothermal processes, the temperature does not appear explicitly in the free energy potential.

In summary, the internal energy U or the free energy potential Ψ allows to define the state laws as functions of the state variables. A non-negative mechanical dissipation guarantees that the second principle of thermodynamics is satisfied. However, the evolution of the internal state variables $\mathbf{E}^p$ and D remains undetermined. To compensate for this lack, we must introduce the generalized dissipative forces associated to the rates of the state variables $\dot{\mathbf{E}}$, $\dot{\mathbf{E}}^p$ and $\dot{D}$.

3.2.2 Dissipation potential

Following [Moreau, 1970], let us admit the existence of a potential, called the *dissipation potential* Φ, depending on the rates of the state variables $\dot{\mathbf{E}}$, $\dot{\mathbf{E}}^p$, $\dot{D}$ and eventually on the state variables as parameters:

$$\Phi = \Phi(\dot{\mathbf{E}}, \dot{\mathbf{E}}^p, \dot{D}\,;\, \mathcal{S}, \mathbf{E}, \mathbf{E}^p, D) \tag{3.36}$$

Furthermore, let us assume that Φ is convex in $\dot{\mathbf{E}}$, $\dot{\mathbf{E}}^p$ and $\dot{D}$, non-negative and zero at the origin in the rate variables space. The variables appearing after the semicolon symbol (;) in the list of arguments of Φ are taken as parameters.
The generalized dissipative forces $\mathbf{S}_\Phi^v, \mathbf{S}_\Phi^p$ and W_Φ^D associated to $\dot{\mathbf{E}}$, $\dot{\mathbf{E}}^p$ and $\dot{D}$ are respectively defined by the *complementary laws*:

$$\mathbf{S}_\Phi^v \in \partial_{\dot{\mathbf{E}}}\Phi \quad \text{and} \quad \mathbf{S}_\Phi^p \in \partial_{\dot{\mathbf{E}}^p}\Phi \quad \text{and} \quad W_\Phi^D \in \partial_{\dot{D}}\Phi \tag{3.37}$$

Although not fully general, complementary laws deriving from a dissipation potential define a fairly broad class of material behaviour, the so-called *generalized standard materials* ([Halphen and Nguyen, 1974, Halphen and Nguyen, 1975]).

The complementary laws can be expressed as flow rules of the internal variables by taking the Legendre-Fenchel transform of the dissipation potential:

$$\begin{aligned}\Phi^*(\mathbf{S}^v_\Phi, \mathbf{S}^p_\Phi, W^D_\Phi\,;\,\mathcal{S}, \mathbf{E}, \mathbf{E}^p, D) := \sup_{\dot{\mathbf{E}},\dot{\mathbf{E}}^p,\dot{D}} \big[&\mathbf{S}^v_\Phi : \dot{\mathbf{E}} + \mathbf{S}^p_\Phi : \dot{\mathbf{E}}^p + W^D_\Phi \dot{D} + \\ &- \Phi(\dot{\mathbf{E}}^p, \dot{D}\,;\,\mathcal{S}, \mathbf{E}, \mathbf{E}^p, D)\big]\end{aligned} \tag{3.38}$$

Expressed in terms of the dual dissipation potential Φ^*, the complementary laws take the form

$$\dot{\mathbf{E}} \in \partial_{\mathbf{S}^v_\Phi}\Phi^* \quad \text{and} \quad \dot{\mathbf{E}}^p \in \partial_{\mathbf{S}^p_\Phi}\Phi^* \quad \text{and} \quad \dot{D} \in \partial_{W^D_\Phi}\Phi^* \tag{3.39}$$

In order to determine uniquely the constitutive behaviour of the element system (in particular of its internal state variables), the formalism of generalized standard materials also called *hypothesis of normal dissipativity* provides a systematic method for deriving simple constitutive behaviours. It links the mechanical dissipation φ to the dissipation potential Φ by finding

$$\mathbf{S}^v \equiv \mathbf{S}^v_U \cap \mathbf{S}^v_\Phi \quad \text{and} \quad \mathbf{S}^p \equiv \mathbf{S}^p_U \cap \mathbf{S}^p_\Phi \quad \text{and} \quad W^D \equiv W^D_U \cap W^D_\Phi \tag{3.40}$$

Remark 3.1 *The conditions of convexity of Φ (or equivalently of Φ^*), of non-negativeness and to be zero at the origin together with the assumption of normal dissipativity guarantee that the second principle of thermodynamics is satisfied a priori.*

To see it, let us assume that Φ is convex in $\dot{\mathbf{E}}^p$ and $\dot{D}$. Then

$$\begin{aligned}\Phi(\dot{\mathbf{E}}_1, \dot{\mathbf{E}}^p_1, \dot{D}_1) \geq \Phi(\dot{\mathbf{E}}_0, \dot{\mathbf{E}}^p_0, \dot{D}_0) &+ \partial_{\dot{\mathbf{E}}}\Phi(\dot{\mathbf{E}}_0, \dot{\mathbf{E}}^p_0, \dot{D}_0) : (\dot{\mathbf{E}}_1 - \dot{\mathbf{E}}_0) + \\ &+ \partial_{\dot{\mathbf{E}}^p}\Phi(\dot{\mathbf{E}}_0, \dot{\mathbf{E}}^p_0, \dot{D}_0) : (\dot{\mathbf{E}}^p_1 - \dot{\mathbf{E}}^p_0) + \\ &+ \partial_{\dot{D}}\Phi(\dot{\mathbf{E}}_0, \dot{\mathbf{E}}^p_0, \dot{D}_0)(\dot{D}_1 - \dot{D}_0) \quad \forall\ \dot{\mathbf{E}}_0, \dot{\mathbf{E}}_1, \dot{\mathbf{E}}^p_0, \dot{\mathbf{E}}^p_1, \dot{D}_0, \dot{D}_1\end{aligned}$$

where the parametric dependence on the state variables has been omitted for clarity. If we choose $\dot{\mathbf{E}}_1 = \mathbf{0}$, $\dot{\mathbf{E}}^p_1 = \mathbf{0}$ and $\dot{D}_1 = 0$, we have:

$$0 \geq \Phi(\dot{\mathbf{E}}_0, \dot{\mathbf{E}}^p_0, \dot{D}_0) - \mathbf{S}^v_\Phi : \dot{\mathbf{E}}_0 - \mathbf{S}^p_\Phi : \dot{\mathbf{E}}^p_0 - W^D_\Phi \dot{D}_0 \quad \forall\ \dot{\mathbf{E}}_0, \dot{\mathbf{E}}^p_0, \dot{D}_0$$

as $\Phi(\mathbf{0}, \mathbf{0}, 0) = 0$ by hypothesis. The assumption of normal dissipativity allows us to write:

$$0 \geq \Phi(\dot{\mathbf{E}}_0, \dot{\mathbf{E}}^p_0, \dot{D}_0) - \varphi(\dot{\mathbf{E}}_0, \dot{\mathbf{E}}^p_0, \dot{D}_0)$$

Finally, the non-negativeness of the dissipation potential leads to:

$$\varphi(\dot{\mathbf{E}}_0, \dot{\mathbf{E}}_0^p, \dot{D}_0) \geq \Phi(\dot{\mathbf{E}}_0, \dot{\mathbf{E}}_0^p, \dot{D}_0) \geq 0 \quad \forall\ \dot{\mathbf{E}}_0, \dot{\mathbf{E}}_0^p, \dot{D}_0$$

Thus, the second principle is satisfied.

Remark 3.2 *Convexity of Φ is sufficient but not necessary for defining its conjugate Φ^*. Indeed, the Legendre-Fenchel transformation remains meaningful provided the function Φ is finite at least at one point and minorised by an affine function (e.g. [Hiriart-Urruty and Lemaréchal, 1996, Curnier, 2001]). [Panagiotopoulos, 1981] examined the case of non-convex potentials.*

Remark 3.3 *The existence of Φ is related to the symmetry of the generalized dissipative forces with respect to the flow variables ([Curnier, 2005]).*

Remark 3.4 *When the dissipation potential depends on the velocities alone ($\Phi = \Phi(\dot{\mathbf{E}}, \dot{\mathbf{E}}^p, \dot{D})$), the dissipation surfaces $\Phi = \Phi_0$ are stationary in velocities space. This is no longer true when Φ depends also on the state variables as parameters ($\Phi = \Phi(\dot{\mathbf{E}}, \dot{\mathbf{E}}^p, \dot{D}\,;\, \mathcal{S}, \mathbf{E}, \mathbf{E}^p, D)$). In that case, the potential or the dissipation surfaces must be considered at a given time t and all conclusions deriving from the generalized standard materials formalism remain unaffected ([Ziegler et al., 1974, Ziegler, 1983]).*

In summary, the state and the quasistatic evolution of the element system is completely determined by two thermodynamical potentials. From the internal energy U (or the free energy Ψ) we get the state laws associated to the state variables of the system. The complementary laws are obtained from the dissipation potential Φ. Equivalently, the flow (or evolution) rules of the internal state variables are dictated by the dual dissipation potential Φ^*. The behaviour of the system is uniquely determined by finding the intersection of the state laws with the complementary laws.

3.2.3 Plastic yield and damage threshold functions

For clarity reasons, we omit the parametric state variable dependence of the dissipation potential in the following. We restrict ourselves to rate-independent processes. In this case, Φ is a positively homogeneous function of degree one in $\dot{\mathbf{E}}^p$ and $\dot{D}$ and the dual dissipation potential is non-differentiable (e.g. [Lemaitre and Chaboche, 2001]).

We decompose the dissipation potential and its dual potential in a plastic and damage part (i.e. we uncouple plasticity and damage):

$$\Phi(\dot{\mathbf{E}}^p, \dot{D}) = \Phi^p(\dot{\mathbf{E}}^p) + \Phi^D(\dot{D})$$

Thank to this decoupling, the total dual dissipation potential is just the sum of the plastic and damage ones:

$$\Phi^*(\mathbf{S}^p, W^D) = \Phi^{p*}(\mathbf{S}^p) + \Phi^{D*}(W^D)$$

An equivalent way to write the flow rules (3.39) consists to define the *plastic yield* and *damage threshold functions* $Y^p(\mathbf{S}^p)$ and $Y^D(W^D)$ whose convex sets $Y^p = 0$ and $Y^D = 0$ have Φ^{p*} and Φ^{D*} as indicator functions, respectively:

$$\left\{ \begin{array}{lllll} \Phi^{p*} = 0 & \text{if} & Y^p \leq 0 & \Longrightarrow & \dot{\mathbf{E}}^p = \mathbf{0} \\ \Phi^{p*} = +\infty & \text{if} & Y^p > 0 & \Longleftarrow & \dot{\mathbf{E}}^p \neq \mathbf{0} \end{array} \right.$$

and

$$\left\{ \begin{array}{lllll} \Phi^{D*} = 0 & \text{if} & Y^D \leq 0 & \Longrightarrow & \dot{D} = 0 \\ \Phi^{D*} = +\infty & \text{if} & Y^D > 0 & \Longleftarrow & \dot{D} \neq 0 \end{array} \right.$$

Therefore, it is equivalent to write

$$\dot{\mathbf{E}}^p \in \partial_{\mathbf{S}^p} \Phi^* \quad \Longleftrightarrow \quad \dot{\mathbf{E}}^p = \Lambda^p \frac{\partial Y^p}{\partial \mathbf{S}^p}\,,\ Y^p \leq 0\ ,\ \Lambda^p \geq 0\ ,\ \Lambda^p Y^p = 0 \quad (3.41)$$

and

$$\dot{D} \in \partial_{W^D} \Phi^* \quad \Longleftrightarrow \quad \dot{D} = \Lambda^D \frac{\partial Y^D}{\partial W^D}\,,\ Y^D \leq 0\ ,\ \Lambda^D \geq 0\ ,\ \Lambda^D Y^D = 0 \quad (3.42)$$

where Λ^p and Λ^D are plastic and damage Lagrangian multipliers, respectively. The second form of (3.41) or (3.42) is referred to as the Kuhn-Tucker form in optimization.

In this particular case, the plastic strain flow direction is normal to the criterion $Y^p = 0$ in stress space, and plasticity is said to be *associated*.

3.3 Rheological models

The objective of theoretical rheology of materials is to provide a limited number of mathematical models describing different classical constitutive behaviours which are independent of the microscopic structure. A class of constitutive behaviour (elastic, unilateral, viscous, plastic, viscoelastic, elastoplastic, ...) is therefore associated to a specific *rheological model* (spring, thrust, dashpot, pad and their principal combinations).

In the following, we present some basic rheological elements. We derive their constitutive laws using the thermostatics and generalized standard materials formalisms presented in the previous Section. Then, we show how these elements can be connected in order to describe a larger variety of constitutive behaviours.

3.3.1 Basic rheological behaviours

Hooke's elasticity

A purely elastic behaviour is modeled by a spring (Figure 3.2). In this case, the strains are fully reversible and the dissipation is identically zero. The state of the system is completely determined by the strain tensor $\mathbf{E}$ (in a regular way). In *linear* elasticity, the free energy potential is quadratic (and convex):

$$\Psi(\mathbf{E}) = \frac{1}{2}\,\mathbf{E} : \mathbb{S}\,\mathbf{E} \tag{3.43}$$

where $\mathbb{S} = \mathbb{S}^{\mathrm{T}}$ and positive definite is the fourth-order elasticity tensor (Young's modulus ϵ in one dimension). As no internal variable is necessary to describe a purely elastic material, the dissipation potential is identically zero:

$$\Phi \equiv 0 \tag{3.44}$$

The unique state law is simply derived from the twice differentiable free energy potential:

$$\mathbf{S} = \nabla_{\mathbf{E}}\Psi = \mathbb{S}\,\mathbf{E} \tag{3.45}$$

Therefore, the constitutive law can be written as $\mathbf{S}(\mathbf{E}) = \mathbb{S}\,\mathbf{E}$, with $\mathbf{S}$ the second-order stress tensor. There is no complementary law in this case.
The inverse law can be found from the dual free energy potential Ψ^*:

$$\Psi^*(\mathbf{S}) = \frac{1}{2}\,\mathbf{S} : \mathbb{C}\,\mathbf{S} \tag{3.46}$$

where $\mathbb{C} = \mathbb{S}^{-1}$ is the compliance tensor. We get the inverse state law $\mathbf{E}(\mathbf{S})$ by derivation of Ψ^*:

$$\mathbf{E} = \nabla_{\mathbf{S}}\Psi^* = \mathbb{C}\,\mathbf{S} \tag{3.47}$$

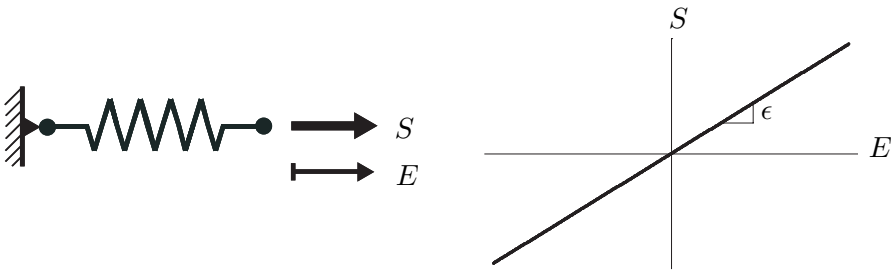

Figure 3.2: 1D rheological element and constitutive law of a linear elastic material.

Isotropic symmetry. An isotropic elastic material is characterized by only two constants. The elasticity tensor can be written as:

$$\mathbb{S} = \lambda(\mathbf{I} \otimes \mathbf{I}) + 2\mu(\mathbf{I} \underline{\overline{\otimes}} \mathbf{I}) \tag{3.48}$$

where λ and μ are the bulk and shear Lamé coefficients, $\mathbf{I}$ the second-order identity tensor and $\otimes$, $\underline{\overline{\otimes}}$ tensorial products defined in Appendix A.
In this case, there is a unique orthogonal decomposition of $\mathbb{S}$ into a hydrostatic and a deviatoric part:

$$\mathbb{S} = \overline{\mathbb{S}} + \mathbb{S}' \tag{3.49}$$

with

$$\overline{\mathbb{S}} = \kappa(\mathbf{I} \otimes \mathbf{I}) \tag{3.50}$$

$$\mathbb{S}' = 2\mu(\mathbf{I} \underline{\overline{\otimes}} \mathbf{I} - \frac{1}{3}\mathbf{I} \otimes \mathbf{I}) \tag{3.51}$$

and κ is the compressibility modulus

$$\kappa = \frac{3\lambda + 2\mu}{3}$$

The compliance tensor is given by:

$$\mathbb{C} = -\frac{\nu}{\epsilon}(\mathbf{I} \otimes \mathbf{I}) + \frac{1+\nu}{\epsilon}(\mathbf{I} \underline{\overline{\otimes}} \mathbf{I}) \tag{3.52}$$

where ϵ is Young's modulus and ν Poisson's ratio. We have the following relations between the elastic constants:

$$\lambda = \frac{\nu\epsilon}{(1+\nu)(1-2\nu)} \quad , \quad \mu = \frac{\epsilon}{2(1+\nu)}$$

$$\epsilon = \frac{\mu(3\lambda + 2\mu)}{\lambda + \mu} \quad , \quad \nu = \frac{\lambda}{2(\lambda + \mu)}$$

and the restrictions: $-\frac{2}{3}\mu < \lambda < \infty$, $0 < \mu < \infty$, $0 < \epsilon < \infty$ and $-1 < \nu < \frac{1}{2}$. The limit case $\nu = \frac{1}{2}$ stands for an incompressible material. The equipotential $\Psi^* = \Psi_0^*$ represents an ellipsoid (or a cylinder for $\nu = \frac{1}{2}$) in the space of principal stresses.
The compliance tensor can also be decomposed into:

$$\mathbb{C} = \overline{\mathbb{C}} + \mathbb{C}' \tag{3.53}$$

Remark 3.5 *When the material does not have isotropic symmetry, the orthogonal decomposition of the elasticity tensor in a purely hydrostatic part, accounting for volume changes, and a deviatoric part, for shape changes, is not unique ([Sutcliffe, 1992]).*

Transverse isotropic symmetry. A transverse isotropic material is characterized by five elastic constants. The elasticity tensor can be written as:

$$\mathbb{S} = \lambda_{ab}\mathbf{A}_a \otimes \mathbf{A}_b + \mu_a[\mathbf{A}_a \underline{\overline{\otimes}}\, \mathbf{I} + \mathbf{I} \underline{\overline{\otimes}}\, \mathbf{A}_a] \tag{3.54}$$

with $a, b = 1, 2$, $\mathbf{A}_1 = \mathbf{I}$ and $\mathbf{A}_2 = \mathbf{m} \otimes \mathbf{m}$ ([Curnier et al., 1995]). The vector $\mathbf{m}$ is the direction normal to the transverse isotropy plane ($||\mathbf{m}|| = 1$). Note that [Zysset, 1994] uses a slightly different expression than (3.54) which provides another definition and physical interpretation of the shear coefficients μ_a.
The relations with the usual elastic constants (e.g. [Ting, 1996]) for transverse isotropy are (with $\mathbf{m} = \mathbf{e}_3$):

$$\begin{array}{ll} \lambda = \lambda_{11} & \mu = \mu_1 \\ \lambda_3 = \lambda_{11} + \lambda_{12} & \mu_3 = \mu_1 + \mu_2 \\ \lambda_{33} = \lambda_{11} + 2\lambda_{12} + \lambda_{22} & \end{array}$$

Orthotropic symmetry. An orthotropic material is characterized by nine independent elastic constants. The elasticity tensor can be expressed as:

$$\mathbb{S} = \lambda_{ab}\mathbf{A}_a \otimes \mathbf{A}_b + \mu_a[\mathbf{A}_a \underline{\overline{\otimes}}\, \mathbf{I} + \mathbf{I} \underline{\overline{\otimes}}\, \mathbf{A}_a] \tag{3.55}$$

with $a, b = 1, 2, 3$, $\mathbf{A}_1 = \mathbf{I} - \mathbf{A}_2 - \mathbf{A}_3 = \mathbf{k} \otimes \mathbf{k}$, $\mathbf{A}_2 = \mathbf{m} \otimes \mathbf{m}$ and $\mathbf{A}_3 = \mathbf{n} \otimes \mathbf{n}$ ([Curnier et al., 1995]). λ_{ab} and μ_a are bulk and shear Lamé-like coefficients. The directions of orthotropy are defined by the orthonormal vectors $\mathbf{k}$, $\mathbf{m}$ and $\mathbf{n}$.
The compliance tensor is defined in terms of the orthotropic engineering constants:

$$\mathbb{C} = -\frac{\nu_{ab}}{\epsilon_a}\,\mathbf{A}_a \otimes \mathbf{A}_b + \frac{1+\nu_{aa}}{2\epsilon_a}\,[\mathbf{A}_a \underline{\overline{\otimes}}\, \mathbf{I} + \mathbf{I} \underline{\overline{\otimes}}\, \mathbf{A}_a] \tag{3.56}$$

where ϵ_a are Young's like elastic moduli and ν_{ab} Poisson's like ratios and the hyperelasticity or major symmetry

$$\frac{\nu_{ab}}{\epsilon_a} = \frac{\nu_{ba}}{\epsilon_b} \tag{3.57}$$

holds. The more usual shear moduli $G_{ab} \equiv \mu_{ab}$ are defined by:

$$2\mu_{ab} := \mu_a + \mu_b \quad , \quad a \neq b \tag{3.58}$$

When represented as symmetric six-dimensional square matrices (Subsection 3.1.4) expressed in the frame of the corresponding material symmetry, the

aforementioned elasticity tensors $\mathbb{S}$ become:

$$\mathbb{S}^{ISOT} = \begin{bmatrix} \lambda+2\mu & \lambda & \lambda & & & & \\ \lambda & \lambda+2\mu & \lambda & & & & \\ \lambda & \lambda & \lambda+2\mu & & & & \\ & & & 2\mu & & & \\ & & & & 2\mu & & \\ & & & & & 2\mu & \end{bmatrix}$$

$$\mathbb{S}^{TRAN} = \begin{bmatrix} \lambda+2\mu & \lambda & \lambda_3 & & & & \\ \lambda & \lambda+2\mu & \lambda_3 & & & & \\ \lambda_3 & \lambda_3 & \lambda_{33}+2\mu_3 & & & & \\ & & & \mu+\mu_3 & & & \\ & & & & \mu+\mu_3 & & \\ & & & & & 2\mu & \end{bmatrix}$$

$$\mathbb{S}^{ORTH} = \begin{bmatrix} \lambda_{11}+2\mu_1 & \lambda_{12} & \lambda_{13} & & & & \\ \lambda_{12} & \lambda_{22}+2\mu_2 & \lambda_{23} & & & & \\ \lambda_{13} & \lambda_{23} & \lambda_{33}+2\mu_3 & & & & \\ & & & \mu_2+\mu_3 & & & \\ & & & & \mu_3+\mu_1 & & \\ & & & & & \mu_1+\mu_2 & \end{bmatrix}$$

The stiffness matrices of materials with different symmetry planes have other structures ([Ting, 1996]).

Halfspacewise linear elasticity. When the elastic behaviour of a material is different in tension and compression, we can use a piecewise formulation of elasticity (Figure 3.3). This is achieved by dividing the strain space into tensile and compressive domains by means of a hyperplane $n(\mathbf{E}) = 0$. A tensile state is then characterized by $n(\mathbf{E}) \geq 0$ and a compressive one by $n(\mathbf{E}) < 0$ ([Curnier et al., 1995]).
Using two distinct elasticity tensors, $\mathbb{S}_+$ and $\mathbb{S}_-$, the free energy potential for halfspacewise linear elasticity is:

$$\Psi(\mathbf{E}) = \begin{cases} \frac{1}{2}\,\mathbf{E} : \mathbb{S}_+\,\mathbf{E} & \text{if } n(\mathbf{E}) \geq 0 \\ \frac{1}{2}\,\mathbf{E} : \mathbb{S}_-\,\mathbf{E} & \text{if } n(\mathbf{E}) < 0 \end{cases} \tag{3.59}$$

To ensure that the resulting state law remains continuous, a compatibility or continuity condition must be imposed on $\mathbb{S}_+$ and $\mathbb{S}_-$:

$$\mathbb{S}_+ - \mathbb{S}_- = s\,\mathbf{N} \otimes \mathbf{N} \tag{3.60}$$

where $\mathbf{N}$ is the unit normal tensor to the interface hyperplane $n(\mathbf{E}) = 0$. (3.60) expresses that the jump in the elasticity tensor across the interface is

normal to the interface. It can be shown ([Curnier et al., 1995]), that:

$$n(\mathbf{E}) = \mathbf{N} : \mathbf{E} \tag{3.61}$$

The state law which derive from Ψ is:

$$\mathbf{S} \in \partial_{\mathbf{E}}\Psi = \begin{cases} \mathbb{S}_+ \mathbf{E} & \text{if } n(\mathbf{E}) \geq 0 \\ \mathbb{S}_- \mathbf{E} & \text{if } n(\mathbf{E}) < 0 \end{cases} \tag{3.62}$$

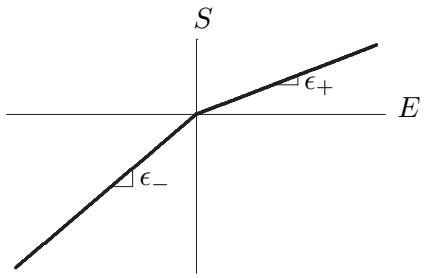

Figure 3.3: 1D constitutive law of a halfspacewise linear elastic material.

The components of the tensor $\mathbf{N}$ depend on the symmetry of the elasticity tensors. For an isotropic material, we have:

$$\mathbf{N} = \frac{1}{\sqrt{3}}\mathbf{I}$$

In that case, the hyperplane can also be written: $n(\mathbf{E}) = \frac{1}{\sqrt{3}} \operatorname{Tr} \mathbf{E}$.
For orthotropic symmetry, we have:

$$\mathbf{N} = \alpha_a \mathbf{A}_a$$

where

$$\alpha_a = \sqrt{(\lambda_{+aa} - \lambda_{-aa})/\sigma}\,, \quad \sigma = \lambda_{+bb} - \lambda_{-bb}$$

and λ_{ab}, $\mathbf{A}_a$ defined in (3.55).
The continuity condition (3.60) leads to:

$$\lambda_{+ab} - \lambda_{-ab} = \sqrt{(\lambda_{+aa} - \lambda_{-aa})(\lambda_{+bb} - \lambda_{-bb})}$$

The shear coefficients μ_a are the same in tension and compression.
In stress space, the interface is given by:

$$m(\mathbf{S}) = \mathbf{M} : \mathbf{S} \quad \text{with} \quad \mathbf{M} = \mathbb{C}_+ \mathbf{N} \quad \text{or} \quad \mathbb{C}_- \mathbf{N} \tag{3.63}$$

where $\mathbb{C}_+$ and $\mathbb{C}_-$ are the tensile and compressive compliance tensors, respectively. They must satisfy the compatibility condition

$$\mathbb{C}_+ - \mathbb{C}_- = e\,\mathbf{M}\otimes\mathbf{M} \quad \text{with} \quad e = -s/(1+s\,\mathbf{M}:\mathbf{N}) \tag{3.64}$$

The inverse law reads:

$$\mathbf{E}(\mathbf{S}) = \begin{cases} \mathbb{C}_+\,\mathbf{S} & \text{if } m(\mathbf{S}) \geq 0 \\ \mathbb{C}_-\,\mathbf{S} & \text{if } m(\mathbf{S}) < 0 \end{cases} \tag{3.65}$$

Orthotropic morphology-based elasticity (Zysset-Curnier model).

For general orthotropic materials, experimental identification of the nine elastic constants is delicate. Theoretical models relating the elastic properties of a porous material and its geometric symmetry have been developed ([Cowin, 1985, Zysset and Curnier, 1995]). The good results obtained by Zysset ([Zysset, 1994]) for the elastic constants of compact bone extrapolated from those of trabecular bone show the relevance of using morphology-based elasticity for cortical bone. A review of morphology-based elasticity relationships for human trabecular bone can be found in [Zysset, 2003].

In order to characterize the solid microstructure of an elastic porous solid, one has to find relevant geometric measures of its local structure. One of the most important quantity describing such a material is the solid *volume fraction* or porosity (noted further as ρ_s).
Structural anisotropy can be described by means of a second-order *fabric tensor*:

$$\hat{\mathbf{M}} := m_i\,\mathbf{m}_i\otimes\mathbf{m}_i \tag{3.66}$$

where $i = 1,2,3$ ([Kanatani, 1984, Cowin, 1985]). The eigenvectors $\mathbf{m}_i$ provide the normal directions of the symmetry plane whereas the eigenvalues m_i reflect the extent of anisotropy. If two eigenvalues are equal, the underlying symmetry is transverse isotropy whereas when all three eigenvalues degenerate, isotropic symmetry is considered. The tensors $\mathbf{M}_i = \mathbf{m}_i\otimes\mathbf{m}_i$ are called the structural tensors. The fabric tensor is normalized by

$$\det(\hat{\mathbf{M}}) = 1 \tag{3.67}$$

which provides $\hat{\mathbf{M}} = \mathbf{I}$ when the three eigenvalues degenerate into unity.
With the help of the fabric tensor and its spectral decomposition, it is possible to approximate a scalar-valued function characterizing the body [Boehler, 1987]. A morphological orientation distribution function, like volume fraction or mean intercept length, can be expanded in a convergent

Fourier series ([He and Curnier, 1995]).
Restricting this expansion to the second-order, assuming that the mechanical anisotropy of the material is identical to that of the single microstructural property ρ_s and assuming a homogeneity property for ρ_s and $\hat{\mathbf{M}}$ with respect to the elastic constitutive law, [Zysset, 1994, Zysset and Curnier, 1995] provide a full derivation of a simplified elastic law. The resulting compliance tensor is:

$$\mathbb{C} = \frac{1}{\epsilon_i}\,\mathbf{M_i}\otimes\mathbf{M_i} - \frac{\nu_{ij}}{\epsilon_i}\,(\mathbf{M}_i\otimes\mathbf{M}_j + \mathbf{M}_j\otimes\mathbf{M}_i) + \frac{1}{\mu_{ij}}\,(\mathbf{M}_i\,\overline{\underline{\otimes}}\,\mathbf{M}_j + \mathbf{M}_j\,\overline{\underline{\otimes}}\,\mathbf{M}_i) \tag{3.68}$$

with $i \neq j$ and where the orthotropic engineering constants are:

$$\epsilon_i = \varepsilon_0\,\rho_s^v\,m_i^{2w} \tag{3.69}$$

$$\nu_{ij} = \nu_0\,\frac{m_i^w}{m_j^w} \tag{3.70}$$

$$\mu_{ij} = \mu_0\,\rho_s^v\,m_i^w\,m_j^w \tag{3.71}$$

The constants ε_0, ν_0 and μ_0 represent the extrapolated elastic constants of the plain isotropic material. Thus, the orthotropic elasticity of the porous material is approximated by the constants ϵ_0, ν_0 and μ_0, the exponents v, w, the volume fraction ρ_s and the fabric tensor $\hat{\mathbf{M}}$.

Hertz's unilateral behaviour

A unilateral constraint is modeled by a thrust (Figure 3.4). In this case, the stress depends only on the applied strain (singular dependence). The dissipation potential is identically zero:

$$\Phi \equiv 0 \tag{3.72}$$

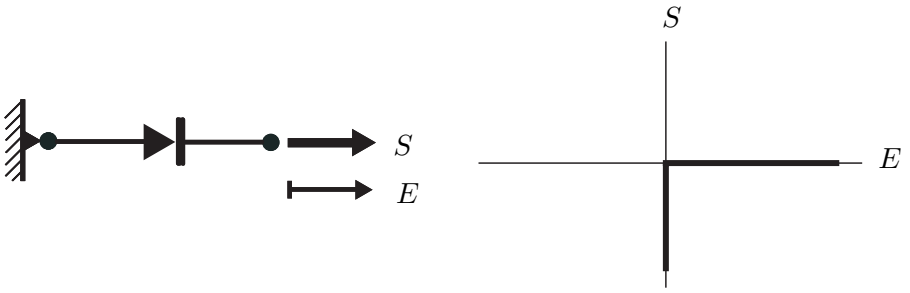

Figure 3.4: 1D rheological element and constitutive law of a unilateral thrust.

If we assume the aforementioned partition of strain space into tensile and compressive domains, (Equation (3.61)), and a unilateral stop in

compression, the free energy is:

$$\Psi(\mathbf{E}) = I_{\mathbb{R}_+}(n(\mathbf{E})) \tag{3.73}$$

with $I_{\mathbb{R}_+}$ the indicator function of $\mathbb{R}_+$.
The state law which derive from the free energy potential is:

$$\mathbf{S} \in \partial_{\mathbf{E}}\Psi = \begin{cases} \emptyset & \text{if } n(\mathbf{E}) < 0 \\ ]-\infty, 0] & \text{if } n(\mathbf{E}) = 0 \\ 0 & \text{if } n(\mathbf{E}) > 0 \end{cases} \tag{3.74}$$

where the singleton 0 is abbreviated by 0.

Newton's viscosity

A purely viscous process is modeled by a dashpot (Figure 3.5). In this case, the constitutive behaviour is dissipative and rate-dependent (regular dependence). The strains are purely irreversible and the free energy is identically zero:

$$\Psi \equiv 0 \tag{3.75}$$

The state of the system is uniquely determined by the strain rate tensor $\dot{\mathbf{E}}$. In *linear* viscosity, the dissipation potential is a quadratic function:

$$\Phi(\dot{\mathbf{E}}) = \frac{1}{2}\,\eta\,\dot{\mathbf{E}} : \dot{\mathbf{E}} \tag{3.76}$$

where $\eta > 0$ is the viscosity coefficient. The dissipative stress associated to $\dot{\mathbf{E}}$ is derived from the dissipation potential:

$$\mathbf{S} = \nabla_{\dot{\mathbf{E}}}\Phi = \eta\,\dot{\mathbf{E}} \tag{3.77}$$

Therefore, the complementary law is $\mathbf{S}(\dot{\mathbf{E}}) = \eta\,\dot{\mathbf{E}}$, with $\mathbf{S}$ the second-order stress tensor.

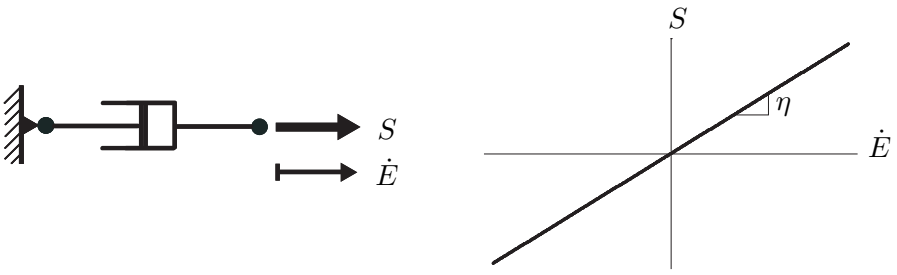

Figure 3.5: 1D rheological element and constitutive law of a linear viscous element.

Tresca's plasticity

A purely plastic dissipative process associated with permanent strains is modeled by a plastic pad (Figure 3.6). In this case, the constitutive law is rate-dependent. If the dependence is singular (dependence on the sign of the plastic strain rate but not on its norm), the plastic processes will be referred to as rate-independent. The strains are purely irreversible and the free energy is identically zero:

$$\Psi \equiv 0 \tag{3.78}$$

The state of the system is uniquely determined by the plastic strain rate tensor $\dot{\mathbf{E}}^p$. An example of dissipation potential for a plastic behaviour without hardening is the positively homogeneous of degree one function:

$$\Phi(\dot{\mathbf{E}}^p) := \sigma^p \sqrt{\dot{\mathbf{E}}^p : \mathbb{G}\, \dot{\mathbf{E}}^p} \tag{3.79}$$

where $\mathbb{G}$ is a fourth-order tensor associated to the shape of the plastic criterion and $\sigma^p > 0$ the radius of the convex elastic domain (e.g. [He and Curnier, 1994]). In one dimension, the dissipation potential reduces to $\Phi(\dot{E}^p) = \sigma^p |\dot{E}^p|$.

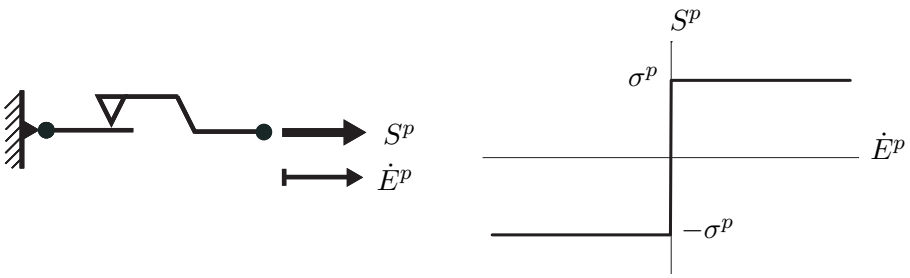

Figure 3.6: 1D rheological element and constitutive law of a plastic element.

The complementary law associated to $\dot{\mathbf{E}}^p$ is obtained by derivation of Φ:

$$\mathbf{S}^p \in \partial_{\dot{\mathbf{E}}^p} \Phi = \begin{cases} \sigma^p \dfrac{\mathbb{G}\dot{\mathbf{E}}^p}{\sqrt{\dot{\mathbf{E}}^p : \mathbb{G}\, \dot{\mathbf{E}}^p}} & \text{if } \dot{\mathbf{E}}^p \neq \mathbf{0} \\ \left\{ \mathbf{S}^p \mid \sqrt{\mathbf{S}^p : \mathbb{G}^{-1}\, \mathbf{S}^p} < \sigma^p \right\} & \text{if } \dot{\mathbf{E}}^p = \mathbf{0} \end{cases} \tag{3.80}$$

The dual dissipation potential Φ^* is obtained via the Legendre-Fenchel transform:

$$\Phi^*(\mathbf{S}^p) = I_{[0,\, \sigma^p]}(\sqrt{\mathbf{S}^p : \mathbb{G}^{-1}\, \mathbf{S}^p}) \tag{3.81}$$

where $I_{[0,\,\sigma^p]}$ is the indicator function of $[0, \sigma^p]$. By derivation of Φ^*, we get the flow rule:

$$\dot{\mathbf{E}}^p \in \partial_{\mathbf{S}^p}\Phi^* = \begin{cases} \mathbf{0} & \text{if } \sqrt{\mathbf{S}^p : \mathbb{G}^{-1}\,\mathbf{S}^p} \in [0, \sigma^p[\\ \Lambda^p \dfrac{\mathbb{G}^{-1}\,\mathbf{S}^p}{\sqrt{\mathbf{S}^p : \mathbb{G}^{-1}\,\mathbf{S}^p}} & \text{if } \sqrt{\mathbf{S}^p : \mathbb{G}^{-1}\,\mathbf{S}^p} = \sigma^p \\ \emptyset & \text{if } \sqrt{\mathbf{S}^p : \mathbb{G}^{-1}\,\mathbf{S}^p} > \sigma^p \end{cases} \tag{3.82}$$

where $\Lambda^p \in [0, +\infty[$.
We note that $\mathbf{N}^p(\mathbf{S}^p) := \dfrac{\mathbb{G}^{-1}\,\mathbf{S}^p}{\sqrt{\mathbf{S}^p : \mathbb{G}^{-1}\mathbf{S}^p}}$ represents the (non-unitary) outward normal of the convex elastic domain. Plastic flow occurs if and only if $\mathbf{S}^p$ reaches the boundary of the elastic domain and the flow direction is governed by $\mathbf{N}^p(\mathbf{S}^p)$. Once again, the scalar quantities appearing in the right-hand side of (3.80) and (3.82) are to be considered as singletons.
The flow rule can also be written in the Kuhn-Tucker form:

$$Y^p(\mathbf{S}^p) := \sqrt{\mathbf{S}^p : \mathbb{G}^{-1}\,\mathbf{S}^p} - \sigma^p \tag{3.83}$$

$$\dot{\mathbf{E}}^p = \Lambda^p \frac{\partial Y^p}{\partial \mathbf{S}^p} \quad , \quad \Lambda^p \geq 0 \quad , \quad Y^p \leq 0 \quad , \quad \Lambda^p Y^p = 0 \tag{3.84}$$

where $Y^p(\mathbf{S}^p)$ is the *plastic yield function* of the plastic pad (Figure 3.7).

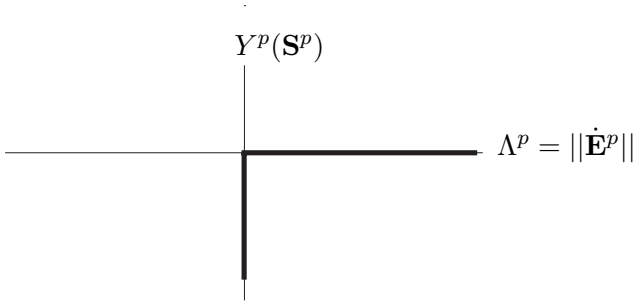

Figure 3.7: Illustration of the plastic flow rule.

The tensor $\mathbb{G}^{-1}$ is related to the shape of the plastic criterion in stress space. When an isotropic material exhibits a plastic yield stress related to the shear elastic energy, we can choose (e.g. [Lemaitre and Chaboche, 1985, Lemaitre and Chaboche, 2001]):

$$\mathbb{G}^{-1} = \mathbb{C}' \tag{3.85}$$

where $\mathbb{C}'$ is the deviatoric part of the isotropic compliance tensor. Such materials obey the well-known *von Mises plastic criterion*. In the space of

principal stresses, the yield function (3.83) delimits a cylinder of radius σ^p centered around the trisectrix of the frame $\{S^p_{11}, S^p_{22}, S^p_{33}\}$ as axis (Figure 3.8).

Another classical model for isotropic plasticity is *Tresca's criterion*. It relates the plastic yield stress to the elastic shear stress. In the space of principal stresses, Tresca's criterion is represented by a straight prism with hexagonal base inscribed in von Mises cylinder (Figure 3.8).
The yield function of Tresca's plastic criterion reads:

$$Y^p(\mathbf{S}^p) := \sigma_1(\mathbf{S}^p) - \sigma_3(\mathbf{S}^p) - \sigma^p \tag{3.86}$$

where

$$\mathbf{S}^p = \sigma_i \, \mathbf{n}_i \otimes \mathbf{n}_i$$

is the spectral decomposition of $\mathbf{S}^p$ with $\sigma_1 \geq \sigma_2 \geq \sigma_3$.

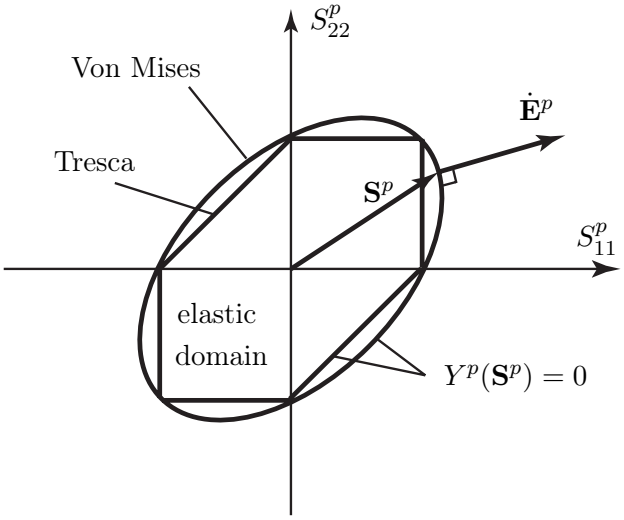

Figure 3.8: Plane stress cross-sections of von Mises and Tresca's plastic criteria and the normal flow rule.

When the material does not have isotropic symmetry, the equivalent of the von Mises or Tresca plastic criterion is delicate to formulate. As the elasticity tensor cannot be uniquely decomposed into a purely hydrostatic and deviatoric part, the physical interpretation of such a criterion is difficult. One simple way to formulate an anisotropic plastic criterion (e.g. [Hill, 1950, Curnier, 1980, Zysset, 1994]) is to choose:

$$\mathbb{G}^{-1} = \mathbb{C} \tag{3.87}$$

In the space of principal stresses, the yield function delimits an ellipsoid associated to the elasticity tensor (Figure 3.9). In this case, a plastic deformation

does not occur at constant volume. For an orthotropic material, the axes of the ellipsoid coincide with the directions of orthotropy in stress space.

A plastic behaviour with *hardening* requires the introduction of an internal state variable describing the plastic strain history of the material and the evolution of the initial plastic criterion. The hardening variable can be the accumulated plastic strain or a damage variable for example.
We will not formulate a model of plasticity with hardening here, but we will include it (Chapter 4) when combining plastic and damage rheological elements together.

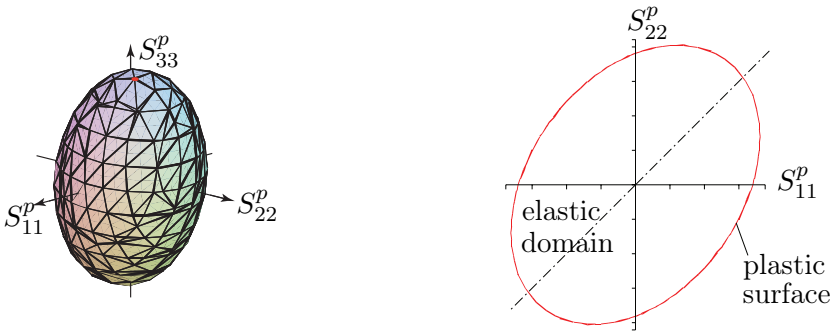

Figure 3.9: Anisotropic plastic criterion $Y(\mathbf{S}^p) = \sqrt{\mathbf{S}^p : \mathbb{C}\,\mathbf{S}^p} - \sigma^p = 0$ and its intersection with the plane $S^p_{33} = 0$.

Rate-independent damage

A damage process is modeled by an elastic spring with a degradable elasticity (Figure 3.10). Damage is a pure dissipative phenomenon affecting the elasticity of the material (or a part of it). There is a large variety of damage models and each requires the introduction of an internal state variable related to the strain history of the material (e.g. [Krajcinovic, 1989, Lemaitre, 1996]).

When the damage process is supposed to be perfectly "isotropic", a scalar damage variable D is sufficient to define the state of the system (in addition of the total strain tensor $\mathbf{E}$) i.e. the Lamé constants are damaged the same way. In the case of an anisotropic damage process, a tensorial damage variable must be used (e.g. [He and Curnier, 1995]).

Let us assume that damage reduces *all* elastic constants of the elasticity tensor by the same amount (perfectly "isotropic" damage) and that the elasticity is linear. The free energy of the simplest damage model can be

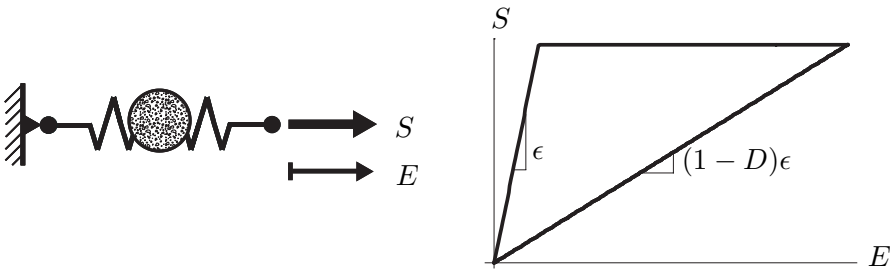

Figure 3.10: 1D rheological element and constitutive law of a rate-independent damage element.

written as:

$$\Psi(\mathbf{E}, D) = \frac{1}{2}(1 - D)\,\mathbf{E} : \mathbb{S}\,\mathbf{E} \tag{3.88}$$

where $\mathbb{S}$ is the undamaged elasticity tensor and $D \in [0, 1[$.
Thus, the state laws are:

$$\mathbf{S} = \nabla_{\mathbf{E}}\Psi = (1 - D)\,\mathbb{S}\,\mathbf{E} \tag{3.89}$$

$$W_{\Psi}^{D} = \partial_D \Psi = \frac{1}{2}\,\mathbf{E} : \mathbb{S}\,\mathbf{E} \tag{3.90}$$

We see that $(1-D)$ represents the decrease of the tangent elastic modulus. If $D = 0$ the material is undamaged whereas if $D \to 1$ the material is completely damaged ([Kachanov, 1958]). As D is a dimensionless scalar variable, we see that its conjugate variable W_{Ψ}^{D} is an energy (hence its notation). Let us note that the damage energy W_{Ψ}^{D} is independent of D in that case.

We can define a damage criterion stating that damage accumulates beyond a certain threshold i.e. whenever the energy W_{Ψ}^{D} reaches a certain value $h(D)$ (h increases from $h(0) = h_0 > 0$ to $h(D \to 1) = +\infty$ typically). Let us assume that no repair process takes place in the evolution of the material, and define the following dissipation potential:

$$\Phi(\dot{D}; D) := \phi(\dot{D}; D) + I_{\mathbb{R}_+}(\dot{D}) \tag{3.91}$$

where $\phi(\dot{D}; D) := h(D)\dot{D}$ and $I_{\mathbb{R}_+}$ the indicator function of $\mathbb{R}_+$. Ψ and Φ are illustrated in Figure 3.11 for the one-dimensional case.
We find the complementary law by deriving Φ:

$$W_{\Phi}^{D} \in \partial_{\dot{D}}\Phi = \begin{cases} \emptyset & \text{if } \dot{D} < 0 \\ ]-\infty, h(D)\,] & \text{if } \dot{D} = 0 \\ h(D) & \text{if } \dot{D} > 0 \end{cases} \tag{3.92}$$

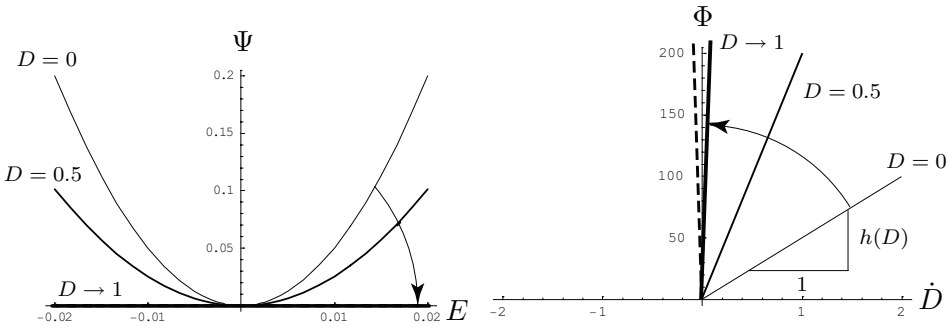

Figure 3.11: Free energy and dissipation potential of the damage element plotted for $\epsilon = 1000$. The dashed line of the right-hand side graph represents the contribution of the indicator function in Φ (see (3.91)).

The dual dissipation potential is obtained via the Legendre-Fenchel transform of Φ:

$$\Phi^*(W_\Phi^D) = I_{[-\infty,h(D)]}(W_\Phi^D) \tag{3.93}$$

The associated evolution rule reads:

$$\dot{D} \in \partial_{W_\Phi^D}\Phi^* = \begin{cases} 0 & \text{if } W_\Phi^D \in]-\infty, h(D)[\\ [0,+\infty[& \text{if } W_\Phi^D = h(D) \\ \emptyset & \text{if } W_\Phi^D > h(D) \end{cases} \tag{3.94}$$

In order to calculate W^D, we use the fact that the damaged reversible elastic energy must be equal to the damaged irreversible dissipative work according to a series mounting of the two damage mechanisms typical of a generalized standard material, i.e. find:

$$W^D = W_\Psi^D \cap W_\Phi^D$$

We can define the *damage threshold function*

$$Y^D(W^D) := W^D - h(D) \tag{3.95}$$

and write the evolution rule in the Kuhn-Tucker form:

$$\dot{D} = \Lambda^D \frac{\partial Y^D}{\partial W^D} = \Lambda^D \tag{3.96}$$

$$\Lambda^D \geq 0 \quad , \quad Y^D \leq 0 \quad , \quad \Lambda^D Y^D = 0 \tag{3.97}$$

A less conventional manner to define the damage threshold criterion is to consider the stress of the damageable spring instead of its energy. Let $\mathbf{S}^D$ be this stress. In our case we have

$$\mathbf{S}^D \equiv \mathbf{S} = (1-D)\,\mathbb{S}\,\mathbf{E} \tag{3.98}$$

The following relation links W^D to $\mathbf{S}^D$:

$$W^D = \frac{\mathbf{S}^D : \mathbb{C}\,\mathbf{S}^D}{2(1-D)^2} \tag{3.99}$$

In analogy with a plastic criterion, let us define a damage threshold function of the form:

$$Y^D(\mathbf{S}^D, D) = \sqrt{\mathbf{S}^D : \mathbb{F}\,\mathbf{S}^D} - r^D(D) \tag{3.100}$$

where $\mathbb{F}$ is a fourth-order tensor associated with the shape of the damage criterion in stress space and $r^D(D) > 0$ its radius.
In strain space we have:

$$Y^D(\mathbf{E}, D) = (1-D)\sqrt{\mathbb{S}\,\mathbf{E} : \mathbb{F}\,\mathbb{S}\,\mathbf{E}} - r^D(D)$$

The dissipation potential now reads:

$$\Phi(\dot{D}; \mathbf{E}, D) = h(\mathbf{E}, D)\dot{D} + I_{\mathbb{R}_+}(\dot{D}) \tag{3.101}$$

with

$$h(\mathbf{E}, D) = \frac{r^{D2}(D)}{2(1-D)^2}\frac{\mathbf{E} : \mathbb{S}\,\mathbf{E}}{\mathbb{S}\,\mathbf{E} : \mathbb{F}\,\mathbb{S}\,\mathbf{E}} \tag{3.102}$$

The complementary laws (3.92) and (3.94) still have the same structure, as well as (3.95), but h depends now on $\mathbf{E}$ and D.
Let us focus on the damage mode ($\dot{D} > 0$). In that case we have:

$$W^D_\Psi = \frac{1}{2}\,\mathbf{E} : \mathbb{S}\,\mathbf{E} = \frac{r^{D2}(D)}{2(1-D)^2}\frac{\mathbf{E} : \mathbb{S}\,\mathbf{E}}{\mathbb{S}\,\mathbf{E} : \mathbb{F}\,\mathbb{S}\,\mathbf{E}} = h(\mathbf{E}, D) = W^D_\Phi$$

thus

$$(1-D)^2\,\mathbb{S}\,\mathbf{E} : \mathbb{F}\,\mathbb{S}\,\mathbf{E} = r^{D2}(D)$$

or equivalently:

$$\sqrt{\mathbf{S}^D : \mathbb{F}\,\mathbf{S}^D} - r^D(D) = 0$$

We see that introducing a parametric dependence of the state variable $\mathbf{E}$ in the dissipation potential, we get a more general damage criterion that is not reduced to a single scalar damage criterion. In particular, it is possible to define a halfspacewise damage criterion that accounts for distinct tensile and compressive threshold stresses in tension and compression without introducing a further internal state variable.

Remark 3.6 *The energy based and the stress based formulations of the damage criterion are equivalent if and only if* $\mathbb{F} = \mathbb{C}$ *and* $r^D(D) = (1-D)\sqrt{2h(D)}$.

Remark 3.7 *A rate-dependent damage process can be modeled by changing the dissipation potential (3.91). This is done by choosing a function* ϕ *which is no longer homogeneous of degree one in* $\dot{D}$*, but of a higher order typically.*

3.3.2 Coupling of basic rheological models

The simplest way to connect the rheological elements described in the foregoing Section is to place them either in *series* or in *parallel*. Then, the rheological equation of a complex model is derived from the equations of the rheological elements by adding the deformations if the coupling is in series, and by adding the stresses if the coupling is in parallel.

Classical rheological models are one-dimensional and scalars. They can be extended into three dimensions by replacing the scalar uniaxial strains and stresses by three-dimensional triaxial tensor ones. A limitative characteristic of rheological models is that they exclusively involve addition of strains and stresses i.e. very simple linear operations. One-dimensional models cannot take into account rheological inhomogeneities with structural configuration of elastic, viscous and plastic phases or the effect of internal cohesion.

In order to give a rational basis for the realistic union of phenomenological and structural points of view, *two-dimensional* or even *three dimensional* rheological models are required. They can represent accurately the body structure of the material like the orientation and proportion of different elements. The main idea is to divide a unit representative area (or volume) into rheological regions, to introduce the necessary state variables and to define the cohesion between the different regions (Figure 3.12). The state law of the resulting model can then be derived from the state laws of the basic elements.

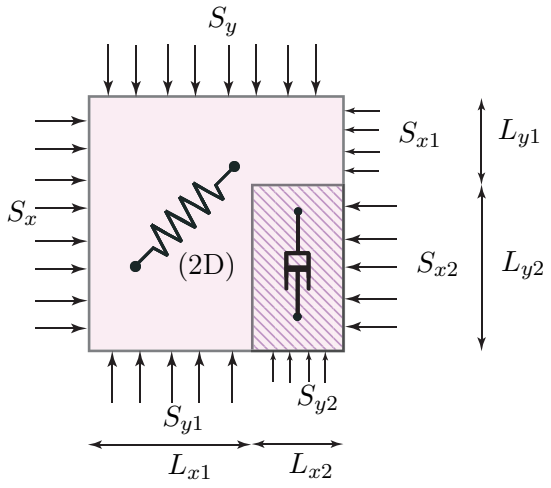

Figure 3.12: 2D rheological model for fibre-reinforced viscoelastic material.

We studied only one-dimensional rheological elements in this thesis, but the reader is referred to [Sobotka, 1984] for a complete treatment of two- and three-dimensional models. We now examine two simple cases of elasto-plastic bodies using the serial and parallel arrangements of basic rheological elements. The framework of generalized standard materials is used.

Serial coupling

A rheological model of an elasto-plastic body without hardening consists of the Hookean elastic spring coupled in series with Tresca's plastic pad (Figure 3.13).
As the elements are connected in series, we assume the usual additive strain decomposition ([Prandtl, 1924, Reuss, 1930, Green and Naghdi, 1965], e.g. [Lemaitre and Chaboche, 1985, Lemaitre and Chaboche, 2001]):

$$\mathbf{E} = \mathbf{E}^e + \mathbf{E}^p \tag{3.103}$$

where $\mathbf{E}$ is the total, $\mathbf{E}^e$ the elastic and $\mathbf{E}^p$ the plastic strain. We choose the independent variables $\mathbf{E}$ and $\mathbf{E}^p$ as the state variables of the system.

The elastic energy of the spring is the only component of the free energy potential:

$$\Psi(\mathbf{E}, \mathbf{E}^p) = \frac{1}{2} (\mathbf{E} - \mathbf{E}^p) : \mathbb{S} (\mathbf{E} - \mathbf{E}^p) \tag{3.104}$$

The state laws which derive from the free energy are:

$$\mathbf{S} = \nabla_{\mathbf{E}} \Psi = \mathbb{S} (\mathbf{E} - \mathbf{E}^p) \tag{3.105}$$

$$\mathbf{S}^p_\Psi = -\nabla_{\mathbf{E}^p} \Psi = \mathbb{S} (\mathbf{E} - \mathbf{E}^p) \tag{3.106}$$

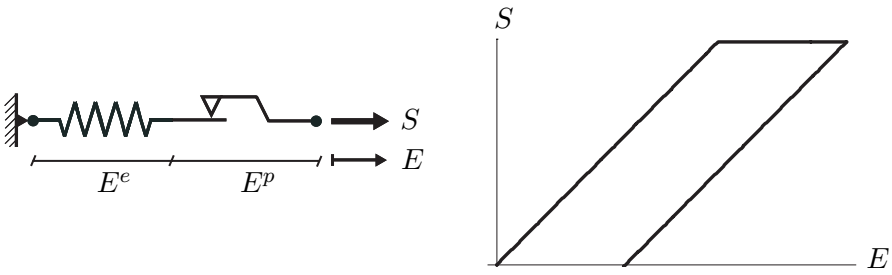

Figure 3.13: 1D serial mounting for an elasto-plastic body and its constitutive law.

We choose the following dissipation potential associated to the plastic element:

$$\Phi(\dot{\mathbf{E}}^p) = \sigma^p \sqrt{\dot{\mathbf{E}}^p : \mathbb{S}\,\dot{\mathbf{E}}^p} \tag{3.107}$$

The complementary law associated to $\dot{\mathbf{E}}^p$ reads:

$$\mathbf{S}^p_\Phi \in \partial_{\dot{\mathbf{E}}^p}\Phi = \begin{cases} \sigma^p \dfrac{\mathbb{S}\,\dot{\mathbf{E}}^p}{\sqrt{\dot{\mathbf{E}}^p : \mathbb{S}\,\dot{\mathbf{E}}^p}} & \text{if } \dot{\mathbf{E}}^p \neq \mathbf{0} \\ \{\, \mathbf{S}^p_\Phi \mid \sqrt{\mathbf{S}^p_\Phi : \mathbb{C}\,\mathbf{S}^p_\Phi} < \sigma^p \} & \text{if } \dot{\mathbf{E}}^p = \mathbf{0} \end{cases} \tag{3.108}$$

The flow rule is found with the dual dissipation potential

$$\Phi^*(\mathbf{S}^p_\Phi) = I_{[0,\,\sigma^p]}(\sqrt{\mathbf{S}^p_\Phi : \mathbb{C}\,\mathbf{S}^p_\Phi}) \tag{3.109}$$

and reads:

$$\dot{\mathbf{E}}^p \in \partial_{\mathbf{S}^p_\Phi}\Phi^* = \begin{cases} \mathbf{0} & \text{if } \sqrt{\mathbf{S}^p_\Phi : \mathbb{C}\,\mathbf{S}^p_\Phi} < \sigma^p \\ \Lambda^p \dfrac{\mathbb{C}\,\mathbf{S}^p_\Phi}{\sqrt{\mathbf{S}^p_\Phi : \mathbb{C}\,\mathbf{S}^p_\Phi}} & \text{if } \sqrt{\mathbf{S}^p_\Phi : \mathbb{C}\,\mathbf{S}^p_\Phi} = \sigma^p \\ \emptyset & \text{if } \sqrt{\mathbf{S}^p_\Phi : \mathbb{C}\,\mathbf{S}^p_\Phi} > \sigma^p \end{cases} \tag{3.110}$$

with $\Lambda^p \in [0, +\infty[$ a rate-like plastic multiplier.
As $\mathbf{S}^p_\Psi = \mathbf{S}$, we can simplify (3.110) in the case of plastic flow:

$$\dot{\mathbf{E}}^p = \frac{\Lambda^p}{\sigma^p}\,(\mathbf{E} - \mathbf{E}^p) \tag{3.111}$$

In order to find the expression of the plastic multiplier Λ^p, we must rewrite the flow rule (3.111) in its incremental form. To this end, let us start with a given *trial strain state* $\mathbf{E}$,$\mathbf{E}^p_0$ such that the trial plastic stress $\mathbf{S}^p_{\mathrm{T}} := \mathbb{S}\,(\mathbf{E} - \mathbf{E}^p_0)$ lies outside the convex elastic domain. That means that:

$$Y^p(\mathbf{S}^p_{\mathrm{T}}) := \sqrt{\mathbf{S}^p_{\mathrm{T}} : \mathbb{C}\,\mathbf{S}^p_{\mathrm{T}}} - \sigma^p > 0$$

We must find the *final* plastic strain $\mathbf{E}^p$ such that $\mathbf{S}^p = \mathbb{S}\,(\mathbf{E} - \mathbf{E}^p)$ satisfies $Y^p(\mathbf{S}^p) = 0$ and obeys the incremental flow rule:

$$\mathbf{E}^p - \mathbf{E}^p_0 = \frac{\lambda^p}{\sigma^p}\,(\mathbf{E} - \mathbf{E}^p) \tag{3.112}$$

with λ^p a stress-like plastic multiplier. Thus

$$\mathbf{E}^p = \frac{\sigma^p}{\lambda^p + \sigma^p}\,\mathbf{E}^p_0 + \frac{\lambda^p}{\lambda^p + \sigma^p}\,\mathbf{E}$$

or

$$\mathbb{S}\left(\mathbf{E}-\mathbf{E}^p\right)=\frac{\sigma^p}{\lambda^p+\sigma^p}\,\mathbb{S}\left(\mathbf{E}-\mathbf{E}_0^p\right)$$

Equivalently, we have:

$$\mathbf{S}^p=\frac{\sigma^p}{\lambda^p+\sigma^p}\,\mathbf{S}_{\mathrm{T}}^p \tag{3.113}$$

The final plastic stress $\mathbf{S}^p$ is therefore collinear to the trial plastic stress $\mathbf{S}_{\mathrm{T}}^p$. Thus, its projection on the convex elastic domain is *radial* ([Wilkins, 1964, Moreau, 1979]).
With (3.113), we finally get:

$$\sigma^p=\sqrt{\mathbf{S}^p:\mathbb{C}\,\mathbf{S}^p}=\frac{\sigma^p}{\lambda^p+\sigma^p}\,\sqrt{\mathbf{S}_{\mathrm{T}}^p:\mathbb{C}\,\mathbf{S}_{\mathrm{T}}^p}$$

or

$$\lambda^p=\sqrt{\mathbf{S}_{\mathrm{T}}^p:\mathbb{C}\,\mathbf{S}_{\mathrm{T}}^p}-\sigma^p \tag{3.114}$$

If $\mathbf{E}_0^p=\mathbf{0}$, we have:

$$\mathbf{E}^p=\left(1-\frac{\sigma^p}{\sqrt{\mathbf{E}:\mathbb{S}\mathbf{E}}}\right)\mathbf{E} \tag{3.115}$$

In fact, one can show that this solution remains valid for all further plastic strain increments.

Parallel and serial coupling

Another rheological model of an elasto-plastic body without "isotropic" hardening consists of an elastic spring coupled in series with an elasto-plastic complex formed by an elastic spring placed in parallel with a plastic pad (Figure 3.14).

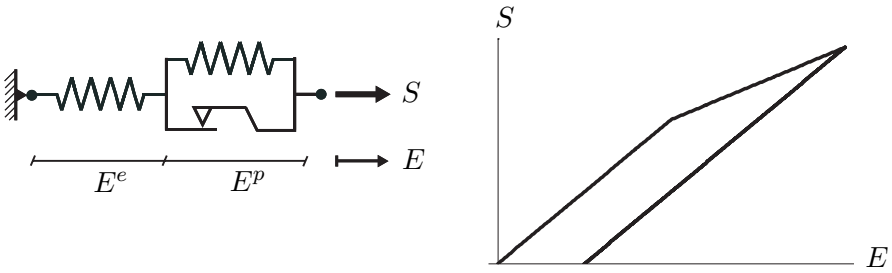

Figure 3.14: 1D serial and parallel mounting for an elasto-plastic body and its constitutive law.

For the elements connected in series, we assume the same additive decomposition as (3.103):

$$\mathbf{E}=\mathbf{E}^e+\mathbf{E}^p \tag{3.116}$$

The total strain $\mathbf{E}$ and the internal variable $\mathbf{E}^p$ (plastic strain) determine uniquely the state of the system.

The elastic energies of the two springs compose the free energy potential:

$$\Psi(\mathbf{E}, \mathbf{E}^p) = \frac{1}{2}(\mathbf{E} - \mathbf{E}^p) : \mathbb{S}(\mathbf{E} - \mathbf{E}^p) + \frac{1}{2}\mathbf{E}^p : \mathbb{S}\,\mathbf{E}^p \tag{3.117}$$

where the same elasticity tensor $\mathbb{S}$ is assumed for both springs for simplicity.

The state laws which derive from the free energy are:

$$\mathbf{S} = \nabla_{\mathbf{E}}\Psi = \mathbb{S}(\mathbf{E} - \mathbf{E}^p) \tag{3.118}$$

$$\mathbf{S}^p_\Psi = -\nabla_{\mathbf{E}^p}\Psi = \mathbb{S}(\mathbf{E} - 2\mathbf{E}^p) \tag{3.119}$$

We choose the same dissipation potential as (3.107) associated to the plastic element:

$$\Phi(\dot{\mathbf{E}}^p) = \sigma^p\sqrt{\dot{\mathbf{E}}^p : \mathbb{S}\,\dot{\mathbf{E}}^p} \tag{3.120}$$

Thus, the complementary laws (3.108) and (3.110) remain unchanged.
In that case, the incremental flow rule reads:

$$\mathbf{E}^p - \mathbf{E}^p_0 = \frac{\lambda^p}{\sigma^p}(\mathbf{E} - 2\mathbf{E}^p)$$

with λ^p a stress-like plastic multiplier. The radial return projection algorithm leads to:

$$\lambda^p = \frac{1}{2}(\sqrt{\mathbf{S}^p_{\mathrm{T}} : \mathbb{C}\,\mathbf{S}^p_{\mathrm{T}}} - \sigma^p)$$

and we find that, in the plastic mode, the plastic strain satisfies

$$\mathbf{E}^p = \frac{1}{2}\Big(1 - \frac{\sigma^p}{\sqrt{\mathbf{S}^p_{\mathrm{T}} : \mathbb{C}\,\mathbf{S}^p_{\mathrm{T}}}}\Big)\mathbf{E}$$

Chapter 4

Formulation of one-dimensional laws

In this Chapter, original one-dimensional constitutive laws for cortical bone are formulated. Firstly, two rate-independent models are presented. Secondly, viscosity is added to damage accumulation in order to account for rate-dependent processes. Finally, the predictions and differences of each model are discussed.

The formalism of generalized standard materials presented in the previous Chapter is applied to a specific one-dimensional rheological setup in which all variables are scalar. All models look like the second elasto-plastic body discussed in Subsection 3.3.2. However, the elastic spring mounted in parallel is replaced by an elastic damageable spring of appropriate stiffness (Figure 4.1). It is characterized by distinct tensile and compressive damage threshold stresses. The only difference between the rate-independent and rate-dependent models lies in their dissipation potential which govern a different evolution of damage accumulation.

4.1 Rate-independent models

In this Section, we present in detail two rate-independent one-dimensional elastic plastic damage constitutive laws for cortical bone. The first rate-independent damage model, abbreviated by RI, is characterized by only one internal damage variable. Being the simplest, this model will serve as a basis for the three-dimensional generalization of the damage law for cortical bone. The second, the RI± damage model, requires two distinct damage variables (one for tensile and one for compressive damage) and leads to finer predictions of the experimental stress-strain curves.

Remark 4.1 *By rate-independent, we mean rate-independency of the norm of a velocity (strain or stress rate) but not of its sign.*

4.1.1 RI theoretical formulation

Rheological setup

As mentioned before, the rheological setup of the one-dimensional (rate-independent *and* rate-dependent) constitutive laws is that of an elastic plastic damage body. It includes a primary elastic spring in series with a damage element that is composed of a secondary elastic spring undergoing rate-independent (*or* rate-dependent) damage in parallel with a rate-independent plastic pad (Figure 4.1). The damageable spring is endowed with distinct tensile and compressive damage threshold stresses.

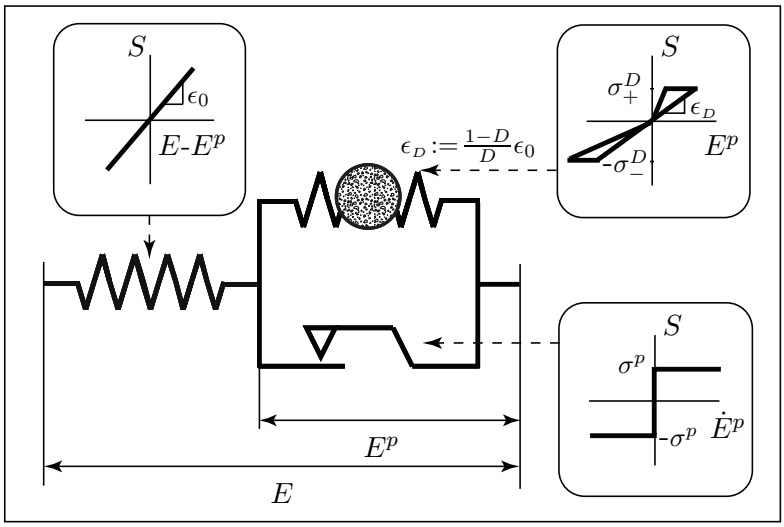

Figure 4.1: One-dimensional rheological setup for both rate-independent *and* rate-dependent damage models.

Variables and material constants definitions

As cortical bone tissue is known to have an elastic plastic damage behaviour at low strain rates (e.g. [Cowin, 2001]), the introduction of two internal state variables is necessary in order to take into account its past history and dissipative processes. On the one hand, plasticity requires the definition of a plastic strain. On the other hand, damage can be expressed by an internal damage state variable (e.g. [Lemaitre, 1996]).

We adopt the usual strain partition for an elasto-plastic material body:

$$E = E^e + E^p \tag{4.1}$$

where E denotes the total strain, E^e the elastic and E^p the plastic strain ([Prandtl, 1924, Reuss, 1930, Green and Naghdi, 1965], e.g. [Lemaitre and Chaboche, 2001]).
The amount of damage experienced by the body is quantified by the single damage variable D and represents its intact stiffness reduction. $D = 0$ is for an intact material (undamaged), whereas $D \to 1$ is for a totally damaged material.
Hence, the RI damage model can be characterized by three *independent variables* (among which two are internal state variables):

- $E \in \mathbb{R}$ the total strain,
- $E^p \in \mathbb{R}$ the plastic strain and
- $D \in [0, 1[$ the damage variable.

Their dual variables are respectively the total stress S, the plastic stress S^p and the damage energy W^D (dual in the sense that their scalar or duality product $S\dot{E}$, $S^p\dot{E}^p$ and $W^D\dot{D}$ represents their power).

Moreover, the *material constants* have to be defined. The intact (or initial) elastic stiffness of cortical bone is denoted by $\epsilon_0 > 0$ and modeled by the primary linear elastic spring.
In addition, three damage-dependent functions express the plastic and damage dissipative processes. They will appear in the formulation of the dissipation potential.
Firstly, a plastic hardening function $\sigma^p(D) \geq 0$ is defined in order to express the plastic yield stress evolution with increasing damage.
Secondly, two damage hardening functions $\sigma^D_+(D) > 0$ and $\sigma^D_-(D) > 0$ account for the tensile and compressive damage behaviours, respectively.

Motivated by experimental identification (Chapter 5), we assume the following exponential hardening functions for the plastic yield and damage threshold stresses, respectively:

$$\sigma^p(D) = \chi^p\big(1 - \exp\left(-lD\right)\big) \tag{4.2}$$

$$\sigma^D_\pm(D) = \sigma^D_{0\pm}\Big(1 + \chi^D\big(1 - \exp\left(-kD\right)\big)\Big) \tag{4.3}$$

$\chi^p \geq 0$ and $l > 0$ are plastic hardening coefficients. $\sigma^D_{0\pm} > 0$ are the initial tensile and compressive damage threshold stresses, respectively. $\chi^D \in \mathbb{R}$ and $k > 0$ are damage hardening parameters. Therefore, six constants fully characterize the RI nonlinear behaviour of cortical bone.

Free energy potential and conjugate stresses

The nonsmooth convex free energy potential of the rheological model is:

$$\Psi(E, E^p, D) = \begin{cases} \frac{1}{2}\epsilon_0(E - E^p)^2 + \frac{1}{2}\epsilon_0\frac{1-D}{D}E^{p2} + I_{[0,1[}(D) & \text{if } D > 0 \\ \frac{1}{2}\epsilon_0 E^2 + I_{\{0\}}(E^p) & \text{if } D = 0 \end{cases} \tag{4.4}$$

with $\epsilon_0 > 0$, $I_{[0,1[}$ the indicator function of $[0, 1[$, and $I_{\{0\}}$ the indicator function of $\{0\}$. The potential is shown in Figure 4.2.

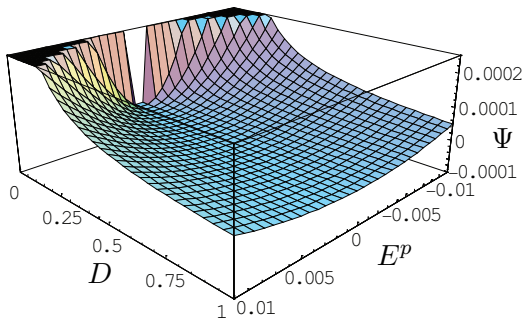

Figure 4.2: RI free energy potential $\Psi(E, E^p, D)$, plotted for $E = 0$ and $\epsilon_0 = 1$.

The state laws which derive from the free energy potential are:

$$S_\Psi \in \quad \partial_E\Psi = \begin{cases} \epsilon_0(E - E^p) & \text{if } D \in]0, 1[\\ \epsilon_0 E & \text{if } D = 0 \end{cases} \tag{4.5}$$

$$S^p_\Psi \in -\partial_{E^p}\Psi = \begin{cases} \epsilon_0 E - \epsilon_0\frac{E^p}{D} & \text{if } D \in]0, 1[\\ \mathbb{R} & \text{if } D = 0 \end{cases} \tag{4.6}$$

$$W^D_\Psi \in -\partial_D\Psi = \begin{cases} \frac{1}{2}\epsilon_0\frac{E^{p2}}{D^2} & \text{if } D \in]0, 1[\\ [0, \infty[& \text{if } D = 0 \end{cases} \tag{4.7}$$

For convenience, let us define the stress in the damageable spring:

$$S^D := S_\Psi - S^p_\Psi \in \begin{cases} \epsilon_0\frac{1-D}{D}E^p & \text{if } D \in]0, 1[\\ \mathbb{R} & \text{if } D = 0 \end{cases} \tag{4.8}$$

We recall that the scalar quantities appearing in the right-hand sides of (4.5) to (4.8) are to be considered as singletons. This will not be repeated for similar encountered expressions.

Remark 4.2 *We see that the elastic stiffness of the damageable spring is* $\epsilon_D := \epsilon_0 \frac{1-D}{D}$ *creating a singularity for* $D = 0$*. This means that it becomes infinitely rigid when* $D = 0$ *and that the plastic pad cannot slide as long as the total damage yield threshold is not reached. This specific choice guarantees also the plastic unloading slope being equal to* $\epsilon_0(1-D)$*, which allows a simple interpretation of* D*: it measures the reduction of the intact stiffness.*

The complementary free energy is obtained via the Legendre-Fenchel transform:

$$\Psi^*(S, S^p, W^D) := \sup_{E,E^p,D} [SE - S^p E^p - W^D D - \Psi(E, E^p, D)]$$

We find:

$$\Psi^*(S, S^p, W^D) = \frac{1}{2}\frac{S^2}{\epsilon_0} - \frac{\left(|S - S^p| - \sqrt{2\epsilon_0 W^D}\right)^2}{2\epsilon_0} \tag{4.9}$$

It can be checked that $\partial_S \Psi^* = E$, $-\partial_{S^p} \Psi^* = E^p$ and $-\partial_{W^D} \Psi^* = D$.
When $D = 0$, the dual potential reduces to:

$$\Psi^*(S, S^p, W^D) = \frac{S^2}{2\epsilon_0} \tag{4.10}$$

Therefore, we obtain $\partial_S \Psi^* = E$, $-\partial_{S^p} \Psi^* = 0$ and $-\partial_{W^D} \Psi^* = 0$, which is consistent with the implication $D = 0 \Rightarrow E^p = 0$ associated with $I_{\{0\}}(E^p)$ of the potential $\Psi(E, E^p, D)$ when $D = 0$.
The complementary free energy is shown in Figure 4.3.

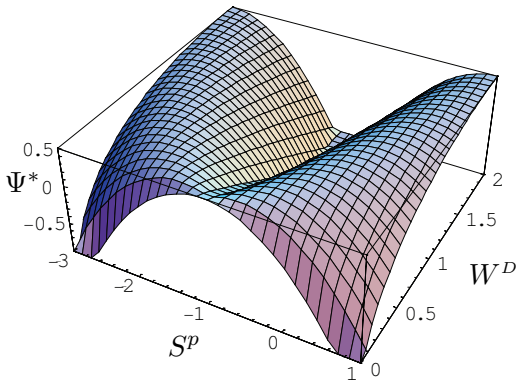

Figure 4.3: RI complementary free energy potential $\Psi^*(S, S^p, W^D)$, plotted for $S = -1$ and $\epsilon_0 = 1$.

Dissipation potential and flow rules

The nonsmooth convex dissipation potential is defined by:

$$\Phi(\dot{E}^p, \dot{D}; E, E^p, D) := \Phi^p(\dot{E}^p; D) + \Phi^D(\dot{D}; E, E^p, D) \tag{4.11}$$

with

$$\Phi^p(\dot{E}^p; D) := \sigma^p(D)|\dot{E}^p| \tag{4.12}$$

and

$$\Phi^D(\dot{D}; E, E^p, D) := \phi(\dot{D}; E, E^p, D) + I_{\mathbb{R}_+}(\dot{D}) \tag{4.13}$$

where

$$\phi(\dot{D}; E, E^p, D) := \begin{cases} h_+(D)\dot{D} & \text{if } E^p > 0 \quad \text{or} \quad E^p = 0 \text{ and } E \geq 0 \\ h_-(D)\dot{D} & \text{if } E^p < 0 \quad \text{or} \quad E^p = 0 \text{ and } E < 0 \end{cases} \tag{4.14}$$

and $h_\pm(D) := \dfrac{\sigma_\pm^{D2}(D)}{2\epsilon_0(1-D)^2}$ is a damage-dependent energy and $I_{\mathbb{R}_+}$ is the indicator function of $\mathbb{R}_+$.
We recall that in contrast with the *variables* $\dot{E}^p$ and $\dot{D}$, the arguments appearing after the semicolon symbol (;) are only *parameters* (Subsection 3.2.2, Remark 3.4).
The dissipation potential illustrated in Figure 4.4 for $E^p > 0$ and $E^p < 0$.

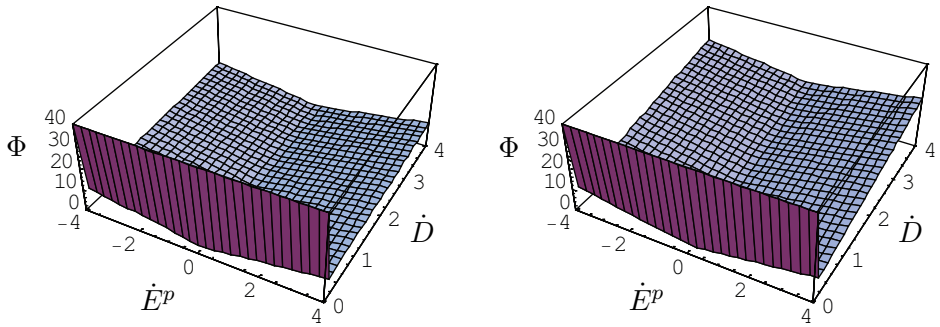

(a) $E^p > 0$ (b) $E^p < 0$

Figure 4.4: RI dissipation potential $\Phi(\dot{E}^p, \dot{D}; E, E^p, D)$, plotted for $\sigma^p(D) = 2$, $h_+(D) = 1$ and $h_-(D) = 4$. (a) $E^p > 0$ and (b) $E^p < 0$.

Remark 4.3 *From (4.13), we see that the function ϕ, and thus Φ, is not continuous along $E^p = 0$. However, this discontinuity has no incidence on the consequences of the generalized standard material formalism because E^p is only a parameter.*

The aforementioned hardening function $\sigma^p(D)$ represents the symmetric yield stress of the plastic pad and the functions $\sigma^D_\pm(D)$ are the tensile/compressive threshold stresses of the damageable spring, respectively. Their dependency on D express the increase of stress during plastic flow and damage evolution.

Remark 4.4 *In (4.2), we note that $\sigma^p(0) = 0$. This choice was made for convenience and in order to transfer all initial stresses on the initially rigid damageable spring. Thus, as $S = S^p + S^D$, the initial total damage stress is equal to the initial partial damage stress i.e. $\pm\sigma^p(0) \pm \sigma^D_\pm(0) = \pm\sigma^D_{0\pm}$, $+$ for tensile and $-$ for compressive damage, respectively.*

The constitutive equations which derive from the dissipation potential are:

$$S^p_\Phi \in \partial_{\dot{E}^p}\Phi = \begin{cases} -\sigma^p(D) & \text{if } \dot{E}^p < 0 \\ [-\sigma^p(D), \sigma^p(D)] & \text{if } \dot{E}^p = 0 \\ \sigma^p(D) & \text{if } \dot{E}^p > 0 \end{cases} \tag{4.15}$$

and

$$W^D_\Phi \in \partial_{\dot{D}}\Phi = \begin{cases} \phi'(E, E^p, D) & \text{if } \dot{D} > 0 \\ ]-\infty, \phi'(E, E^p, D)] & \text{if } \dot{D} = 0 \\ \emptyset & \text{if } \dot{D} < 0 \end{cases} \tag{4.16}$$

where ϕ' is the derivative of ϕ with respect to $\dot{D}$:

$$\phi'(E, E^p, D) = \begin{cases} h_+(D) & \text{if } E^p > 0 \quad \text{or} \quad E^p = 0 \text{ and } E \geq 0 \\ h_-(D) & \text{if } E^p < 0 \quad \text{or} \quad E^p = 0 \text{ and } E < 0 \end{cases} \tag{4.17}$$

We see that $h_\pm$ (defined in (4.14)) represent the tensile/compressive quasistatic damage energy thresholds, respectively.

The dual dissipation potential is obtained via the same Legendre-Fenchel transform:

$$\Phi^*(S^p, W^D; E, E^p, D) := \sup_{\dot{E}^p, \dot{D}} \left[S^p\dot{E}^p + W^D\dot{D} - \Phi(\dot{E}^p, \dot{D}; E, E^p, D) \right]$$

As the dissipation potential is separate in $\dot{E}^p$ and $\dot{D}$ and as these variables are independent (uncoupled, mounted in parallel), the conjugate of the sum is simply the sum of the conjugates. Thus, we find:

$$\Phi^*(S^p, W^D; E, E^p, D) = I_{[-\sigma^p(D), \sigma^p(D)]}(S^p) + I_{[-\infty, \phi'(E,E^p,D)]}(W^D) \tag{4.18}$$

The dual dissipation potential is shown in Figure 4.5 for $E^p > 0$ and $E^p < 0$.

The flow rules of the internal variables E^p and D are found from the dual dissipation potential (inverse complementary laws):

$$\dot{E}^p \in \partial_{S^p}\Phi^* = \begin{cases} \emptyset & \text{if } S^p < -\sigma^p(D) \\ ]-\infty, 0] & \text{if } S^p = -\sigma^p(D) \\ 0 & \text{if } -\sigma^p(D) < S^p < \sigma^p(D) \\ [0, +\infty[& \text{if } S^p = \sigma^p(D) \\ \emptyset & \text{if } S^p > \sigma^p(D) \end{cases} \tag{4.19}$$

and

$$\dot{D} \in \partial_{W^D}\Phi^* = \begin{cases} 0 & \text{if } W^D \in]-\infty, \phi'(E, E^p, D)[\\ [0, +\infty[& \text{if } W^D = \phi'(E, E^p, D) \\ \emptyset & \text{if } W^D > \phi'(E, E^p, D) \end{cases} \tag{4.20}$$

The partial Legendre-Fenchel transform is illustrated in Figure 4.6 for a positive value of the parameter E^p.

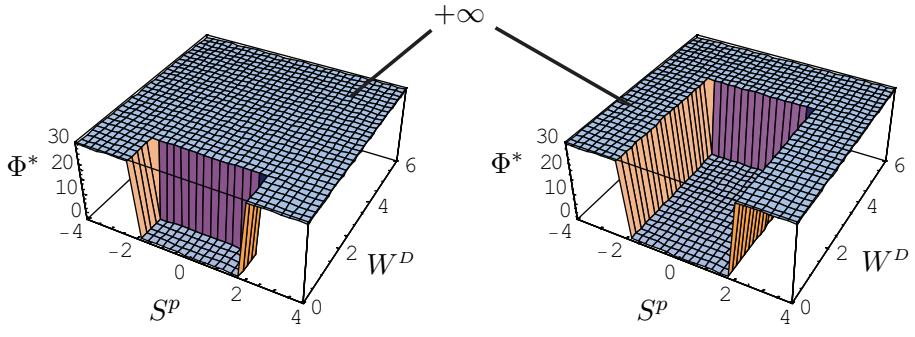

(a) $E^p > 0$ (b) $E^p < 0$

Figure 4.5: RI dual dissipation potential $\Phi^*(S^p, W^D; E, E^p, D)$, plotted for $\sigma^p(D) = 2$, $h_+(D) = 1$ and $h_-(D) = 4$. (a) $E^p > 0$ and (b) $E^p < 0$.

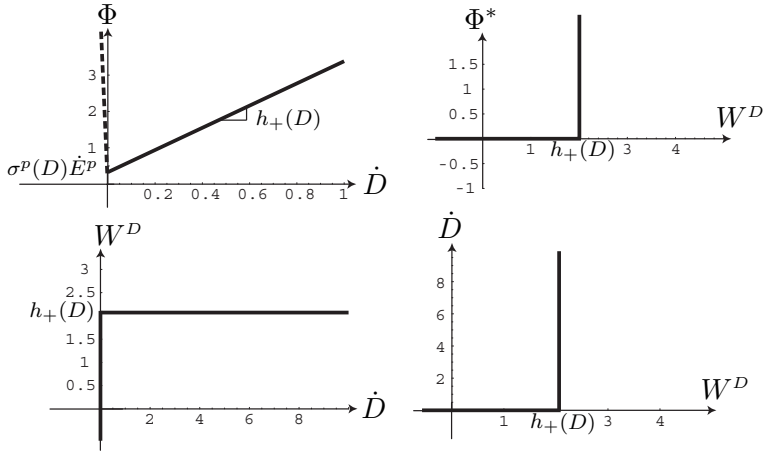

Figure 4.6: Illustration of the partial Legendre-Fenchel transform of Φ with respect to $\dot{D}$, plotted for $E^p > 0$ and $h_+(D) = 2$.

Plastic yield and damage threshold functions

A more classical but equivalent way to express the plastic and damage criteria resulting from (4.15) and (4.16) is to define their corresponding *yield and threshold functions* in stress or strain space.
On the one hand, the plastic yield function can be defined as:

$$Y^p(S^p; D) := |S^p| - \sigma^p(D) \tag{4.21}$$

and the plastic criterion defining the elastic domain as:

$$Y^p(S^p; D) \leq 0 \tag{4.22}$$

On the other hand, we write the damage threshold function as:

$$Y^D(W^D; E, E^p, D) := \left|(1-D)\sqrt{2\epsilon_0 W^D}\,\mathrm{sign}(E^p) - \frac{\sigma_+^D(D) - \sigma_-^D(D)}{2}\right| + \\ - \frac{\sigma_+^D(D) + \sigma_-^D(D)}{2} \tag{4.23}$$

where $\mathrm{sign}(E^p) = \mathrm{sign}(E)$ for $E^p = 0$, and define the damage criterion delimiting the undamaged domain by:

$$Y^D(W^D; E, E^p, D) \leq 0 \tag{4.24}$$

In terms of the damage stress S^D defined in (4.8), this criterion can be expressed as $-\sigma_-^D(D) \leq S^D \leq \sigma_+^D(D)$ or:

$$S^{D2} - \left(\sigma_+^D(D) - \sigma_-^D(D)\right) S^D - \sigma_+^D(D)\sigma_-^D(D) \leq 0 \tag{4.25}$$

Equation (4.24) or (4.25) can be interpreted as a one-dimensional Tsai-Wu criterion ([Tsai and Wu, 1971]). The damage criterion is also equivalent to:

$$Y^D(S^D; E, E^p, D) =$$

$$= \begin{cases} \frac{1}{\sigma^D_{0+}}|S^D| - r^D(D) \leq 0 & \text{if} \quad E^p > 0 \quad \text{or} \quad E^p = 0 \text{ and } E \geq 0 \\ \frac{1}{\sigma^D_{0-}}|S^D| - r^D(D) \leq 0 & \text{if} \quad E^p < 0 \quad \text{or} \quad E^p = 0 \text{ and } E < 0 \end{cases} \tag{4.26}$$

with $r^D(D) := 1 + \chi^D\big(1 - \exp(-kD)\big)$ for exponential hardening. The formulation (4.26) can be interpreted as a bimodular or halfplanewise damage criterion and will be generalized to three dimensions (Chapter 6). The initial plastic and damage criteria and their corresponding evolution with increasing damage are illustrated in Figure 4.7 for $E^p > 0$ and $E^p < 0$.

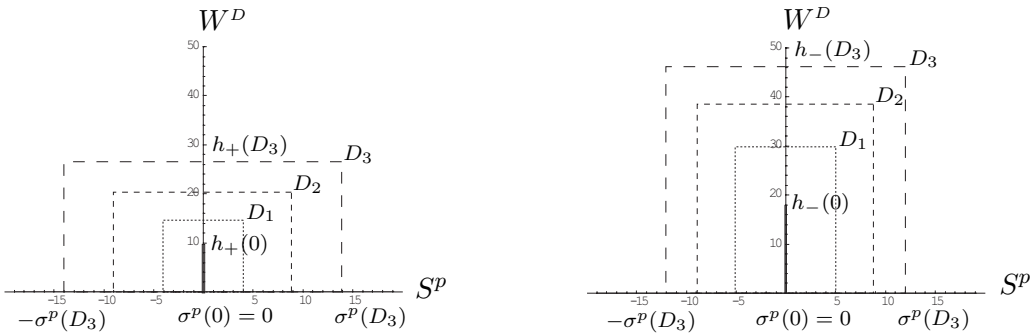

(a) $E^p > 0$ (b) $E^p < 0$

Figure 4.7: Evolution of the initial shape ($D = 0$) of the plastic and damage criteria with increasing damage ($D_1 < D_2 < D_3$).

4.1.2 Numerical algorithm

In this Subsection, we formulate the algorithm used for the numerical implementation of the one-dimensional RI damage model. In particular, the integration of the flow rules (4.19) and (4.20) is explained.

Time integration algorithm with projection

In order to implement it in a finite element mechanical analysis program, the elastic plastic damage evolution law needs to be discretized in time. To this end, let us divide the overall time interval $[0, \texttt{TFINAL}]$ into NSTEPS intervals of equal length $\tau := \frac{\texttt{TFINAL}}{\texttt{NSTEPS}}$.

Furthermore, let us start with an *initial strain state* E_0, E_0^p, D_0 for any given time instant $t = n\tau$, $n = 0, \ldots,$ `NSTEPS`. To this state corresponds the unique *initial stress state* S_0, S_0^p, W_0^D defined by the state laws (4.5), (4.6) and (4.7), respectively (unique when $D_0 \neq 0$). This state is supposed to be plastically and damageably *admissible* in the sense that it satisfies both plastic and damage criteria:

$$Y^p(S_0^p, D_0) \leq 0 \quad \text{and} \quad Y^D(W_0^D; E_0, E_0^p, D_0) \leq 0 \tag{4.27}$$

Given a new total strain E, consider the *trial strain state* E, E_0^p, D_0 (to which corresponds the *trial stress state* $S_{\mathrm{T}} = S(E, E_0^p)$, $S_{\mathrm{T}}^p = S^p(E_0^p, D_0)$, $W_{\mathrm{T}}^D = W^D(E_0^p, D_0)$), which may violate the yield and threshold conditions (4.27). If $D_0 = 0$, then S_{T}^p and W_{T}^D are undefined. Thus, the yield and damage criteria cannot be tested. The undetermination can be lifted by defining a *global* equivalent criterion which depends on the trial total stress (Remarks 4.2 and 4.4):

$$Y(S_{\mathrm{T}}) := \begin{cases} S_{\mathrm{T}} - \sigma_{0+}^D & \text{if } S_{\mathrm{T}} \geq 0 \\ S_{\mathrm{T}} + \sigma_{0-}^D & \text{if } S_{\mathrm{T}} < 0 \end{cases}$$

The purpose of the algorithm is to find the *final strain state* E, E^p, D (and corresponding *final stress state* S, S^p, W^D) which is admissible. At the projection point, the conjugate variables S^p and W^D are well defined in the case $D_0 = 0$ and normality of the flow rule is guaranteed through the incremental process.

Before presenting the final algorithm, we explain the final values taken by the internal state variables in the case $D_0 \neq 0$ for the three distinct evolution modes of the model (elastic, plastic and damage). To this end, we use the formalism of generalized standard materials (i.e. find $S_\Psi^p \cap S_\Phi^p$ and $W_\Psi^D \cap W_\Phi^D$). Then, for each mode, we present the tangent operators required in a load driven simulation.

Internal variables evolution

a) Elastic mode: $Y^p(S_{\mathrm{T}}^p, D_0) \leq 0$ **and** $Y^D(W_{\mathrm{T}}^D; E, E_0^p, D_0) \leq 0$

In that case, $\dot{E}^p$=0 and $\dot{D} = 0$. Thus, we just have $E^p = E_0^p$ and $D = D_0$.

b) Plastic mode: $Y^p(S_{\mathrm{T}}^p, D_0) > 0$ **and** $Y^D(W_{\mathrm{T}}^D; E, E_0^p, D_0) \leq 0$

In that case, we have $\dot{E}^p \neq 0$ and $\dot{D} = 0$. Thus $D = D_0$.
Let us focus on the tensile case ($\dot{E}^p > 0$). The radial return algorithm

([Wilkins, 1964, Moreau, 1979]), or projection of the final plastic stress on the convex elastic set leads to $S^p = \sigma^p(D)$ (e.g. [Simo and Hughes, 1999, Curnier, 1993]). Thus

$$E^p = D\left(E - \frac{\sigma^p(D)}{\epsilon_0}\right) \tag{4.28}$$

In the compressive case ($\dot{E}^p < 0$), $\sigma^p(D)$ has to be replaced by $-\sigma^p(D)$.

c) Damage mode: $Y^p(S^p_{\mathrm{T}}, D_0) > 0$ and $Y^D(W^D_{\mathrm{T}}; E, E^p_0, D_0) > 0$

In that case, $\dot{E}^p \neq 0$ and $\dot{D} \neq 0$. Once more, let us focus on the tensile case ($\dot{E}^p > 0$). Equation (4.28) still holds as $S^p = \sigma^p(D)$.
Furthermore, the evolution rule (4.16) imposes that $W^D = h_+(D)$. Thus

$$\frac{1}{2}\epsilon_0 \frac{E^{p\,2}}{D^2} = \frac{\sigma_+^{D2}(D)}{2\epsilon_0(1-D)^2}$$

or equivalently

$$\epsilon_0 \frac{1-D}{D} E^p = \sigma_+^D(D) \tag{4.29}$$

In order to find the values of E^p and D, we have to solve simultaneously (4.28) and (4.29) where E is assumed to be known (predicted). By substituting (4.28) into (4.29), we get:

$$f(D) := \epsilon_0(1-D)\left(E - \frac{\sigma^p(D)}{\epsilon_0}\right) - \sigma_+^D(D) = 0 \tag{4.30}$$

where $f : [0,1[\to \mathbb{R}$.
In order to find the value of D, we have to solve $f(D) = 0$. In the compressive case ($\dot{E}^p < 0$), $\sigma^p(D)$ has to be replaced by $-\sigma^p(D)$ and $\sigma_+^D(D)$ by $-\sigma_-^D(D)$, respectively.
In the tensile case, the derivative of f reads:

$$f'(D) = -\epsilon_0 E + \sigma^p(D) - (1-D)\sigma^{p\prime}(D) - \sigma_+^{D\prime}(D) \tag{4.31}$$

We can use the generalized Newton method ([Alart and Curnier, 1991]) to solve this C^0 nonlinear equation:

$$D^{j+1} = D^j - \frac{f(D^j)}{f'(D^j)} \quad \text{with} \quad j = 0, 1, 2, \ldots \tag{4.32}$$

Incremental linearization algorithm

For a uniform deformation test with homogeneous stress state, a situation occurring in a single finite element (Section 6.3), the problem is equivalent to the following *local* problem: find E such that the equation of force equilibrium is satisfied i.e.:

$$S(E, E^p, D) - \bar{S} = 0$$

where $\bar{S}$ denotes the imposed stress. We also use the generalized Newton method to solve this problem:

$$E^{i+1} = E^i + \mathrm{d}E^i \quad \text{with} \quad i = 0, 1, 2, \ldots \tag{4.33}$$

where

$$\mathrm{d}E^i = -\frac{S(E^i, E^p, D) - \bar{S}}{\frac{\mathrm{d}S}{\mathrm{d}E}(E^i, E^p, D)} \tag{4.34}$$

where $\frac{\mathrm{d}S}{\mathrm{d}E}$ is the total stress derivative with respect to the strain. That means that the determination of E requires the computation of the tangent operator $\frac{\mathrm{d}S}{\mathrm{d}E}$. Its analytical expression is derived in the following.

Remark 4.5 *Unfortunately the graph of the stress-strain response function is convex in compression and concave in tension which is a situation where the Newton method may diverge (cycle) without some kind of additional control (Figure 4.8). Cycling is easily detected by checking the sign of two successive iterates $S^i \cdot S^{i+1} < 0$ a situation called* ***stress reversal****. One way to prevent cycling, is to set the subderivative $S'_\lambda(E^i)$ (or derivative $S'(E^i)$ if differentiable) to the elastic slope ϵ_0 as soon as a stress reversal is detected.*

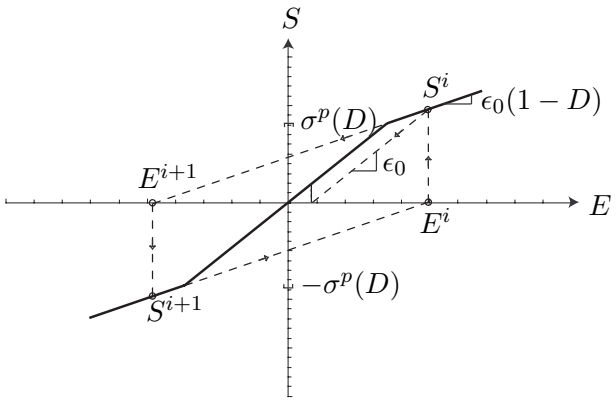

Figure 4.8: Illustration of a reversal situation of the generalized Newton method.

Tangent operator computation

We now compute the tangent operator required by the generalized Newton method (4.33) for the three evolution modes of the model.

a) Elastic mode: $Y^p(S^p_{\mathrm{T}}, D_0) \leq 0$ **and** $Y^D(W^D_{\mathrm{T}}; E, E^p_0, D_0) \leq 0$

As $\dot{E}^p = 0$ and $S = \epsilon_0(E - E^p)$, we have:

$$\frac{\mathrm{d}S}{\mathrm{d}E} = \epsilon_0 \tag{4.35}$$

b) Plastic mode: $Y^p(S^p_{\mathrm{T}}, D_0) > 0$ **and** $Y^D(W^D_{\mathrm{T}}; E, E^p_0, D_0) \leq 0$

If $\dot{E}^p > 0$ (tensile case), then $S^p = \sigma^p(D)$. From (4.6), we have:

$$E^p = D\left(E - \frac{\sigma^p(D)}{\epsilon_0}\right)$$

Thus, the total stress can be rewritten as $S(E, D) = \epsilon_0(1 - D)E + D\sigma^p(D)$. In the compressive case, $\sigma^p(D)$ has to be replaced by $-\sigma^p(D)$.
As $\dot{D} = 0$, we have:

$$\frac{\mathrm{d}S}{\mathrm{d}E} = (1 - D)\epsilon_0 \tag{4.36}$$

c) Damage mode: $Y^p(S^p_{\mathrm{T}}, D_0) > 0$ **and** $Y^D(W^D_{\mathrm{T}}; E, E^p_0, D_0) > 0$

Once more, let us focus on the tensile case ($\dot{E}^p > 0$). As in the plastic mode, we have:

$$S = S(E, D) = \epsilon_0(1 - D)E + D\sigma^p(D) \tag{4.37}$$

From

$$\frac{\mathrm{d}S}{\mathrm{d}E} = \frac{\partial S}{\partial E}\underbrace{\frac{\mathrm{d}E}{\mathrm{d}E}}_{=1} + \frac{\partial S}{\partial D}\frac{\mathrm{d}D}{\mathrm{d}E} \tag{4.38}$$

we get:

$$\frac{\mathrm{d}S}{\mathrm{d}E} = \epsilon_0(1 - D) + \left(-\epsilon_0 E + \sigma^p(D) + D\sigma^{p\prime}(D)\right)\frac{\mathrm{d}D}{\mathrm{d}E} \tag{4.39}$$

We still have to determine $\frac{\mathrm{d}D}{\mathrm{d}E}$.
Let us rewrite the function f defined in (4.30) as a function of the two variables E and D. Then, we have:

$$\dot{f}(E, D) = \frac{\partial f}{\partial D}\dot{D} + \frac{\partial f}{\partial E}\dot{E} \tag{4.40}$$

As $\dot{f} = 0$, (4.40) leads to

$$\frac{\mathrm{d}D}{\mathrm{d}E} = -\frac{\partial f/\partial E}{\partial f/\partial D} \tag{4.41}$$

On the one hand, $\frac{\partial f}{\partial D}$ has been calculated in (4.31) and was denoted by $f'(D)$.
On the other hand,

$$\frac{\partial f}{\partial E} = \epsilon_0(1 - D) \tag{4.42}$$

The tangent operator of the damage mode is finally obtained by combining (4.39), (4.41), (4.42) and (4.31).
In the compressive case ($\dot{E}^p < 0$), $\sigma^p(D)$ has to be replaced by $-\sigma^p(D)$ and $\sigma_+^D(D)$ by $-\sigma_-^D(D)$, respectively.

Remark 4.6 *From (4.39) and (4.42), we see that* $\frac{\mathrm{d}S}{\mathrm{d}E}$ *vanishes if* $D \to 1$ *leading to a divergence of Newton's algorithm. In a tensile load driven simulation with* $S = \bar{S}$ *and in the case of damage growth implying that* $\max(\bar{S}) > \sigma_{0+}^D$, *we have:*

$$\bar{S} = S^p + S^D = \sigma^p(D) + \sigma_+^D(D)$$

For the exponential hardenings defined in (4.2) and (4.3), we get:

$$\bar{S} = \sigma_{0+}^D + \chi^p\big(1 - \exp(-lD)\big) + \chi^D\sigma_{0+}^D\big(1 - \exp(-kD)\big)$$

For $k = l$ *and* $\chi^p + \chi^D\sigma_{0+}^D = 0$, $\bar{S} = \sigma_{0+}^D$. *Thus in that case* $\frac{\mathrm{d}S}{\mathrm{d}E} = 0$ *and the simulation cannot be executed.*
Suppose that $k = l$ *and* $\chi^p + \chi^D\sigma_{0+}^D \neq 0$. *Then*

$$\bar{S} = \sigma_{0+}^D + (\chi^p + \chi^D\sigma_{0+}^D)\big(1 - \exp(-kD)\big)$$

As $0 < D < 1$, *we derive the following consistency conditions:*

$$\begin{cases} \max(\bar{S}) < \sigma_{0+}^D + (\chi^p + \chi^D\sigma_{0+}^D)\big(1 - \exp(-k)\big) \\ \chi^p + \chi^D\sigma_{0+}^D > 0 \end{cases} \tag{4.43}$$

The last condition expresses that we cannot simulate a softening of the total stress in a load driven experiment which is obvious for stability reasons. Analog conditions can be derived for the compressive case.

Remark 4.7 *Due to the choice of the nonlinear hardening functions (4.2) and (4.3), there is no analytical solution* $S(E)$ *available even in a simple ramp test. If linear functions were chosen, an analytical solution would be available.*

Algorithm formulation

The elastic plastic damage algorithm of the RI model is described in Boxes 1, 2, 3a, 3 and 4 (Table 4.1). The order in which the two different trial stresses are calculated is important. As damage can occur only if the plastic pad is sliding, the first stress to be tested is the one in the plastic pad. This stress depends on the total strain whereas the stress in the damageable spring does not.

The features and simulation results of the RI model will be discussed in detail together with the other models in Section 4.3.

The major drawback of the RI model is that the damaged reloading curve is not collinear with the origin as it seems to be the case for cyclic mechanical tests carried out on both bovine and human cortical bone (Subsection 2.2.1, [Kotha and Guzelsu, 2003, Zioupos, 2002, Fondrk et al., 1999b, Fondrk et al., 1988]), and on trabecular bone as well ([Keaveny et al., 1999]). This motivates the following alternative (Subsection 4.1.3).

BOX 1 − State variables initialization, time and strain Newton loop

1. Set $n = 0$, $E_0^p = 0$, $D_0 = 0$
   $E_0 = 0$ if `stress driven`
2. FOR $n = 1$ TO N, DO:
3. Set $i = 0$, $E_n^0 = E_{n-1}$ if `stress driven`
   $E_n^0 = E_n$ if `strain driven`
4. WHILE $|\mathrm{d}E^i| > \mathrm{TOL}$, DO:
   Goto BOX **2**

Table 4.1: One-dimensional RI elastic plastic damage algorithm

BOX 2 – Elastic-plastic predictor

1. Find elastic predictor

   Set $E^p = E^p_{n-1}, \qquad D = D_{n-1}$

   Compute $S = \partial_E \Psi(E^i_n, E^p, D)$, $\frac{\mathrm{d}S}{\mathrm{d}E}$

2. IF $D \neq 0$, THEN compute trial plastic stress:

   $S^p_{\mathrm{T},n} = -\partial_{E^p} \Psi(E^i_n, E^p_{n-1}, D_{n-1})$

   ELSE:

   Goto BOX **3a**

   END IF.

3. Check for plastic process

   IF $Y^p(S^p_{\mathrm{T},n}, D_{n-1}) \leq 0$, THEN:

   Goto BOX **4**

   ELSE:

   Set $D = D_{n-1}$

   Project $S^p_{\mathrm{T},n}$ on $Y^p(S^p, D) = 0$

   Compute $S = \partial_E \Psi(E^i_n, E^p, D)$, $\frac{\mathrm{d}S}{\mathrm{d}E}$

   Goto BOX **3**

   END IF.

BOX 3a – Initial damage predictor

1. Check for damage process

   IF $Y(S) \leq 0$, THEN:

   Goto BOX **4**

   ELSE:

   Project S by solving simultaneously

   $Y^p(S^p, D) = 0$ and

   $Y^D(W^D, E^i_n, E^p, D) = 0$

   Compute $S = \partial_E \Psi(E^i_n, E^p, D)$, $\frac{\mathrm{d}S}{\mathrm{d}E}$

   Goto BOX **4**

   END IF.

Table 4.1: (continued)

BOX 3 – Damage predictor

1. Compute trial damage energy

   $W^D_{\mathrm{T},n} = -\partial_D \Psi(E^i_n, E^p_{n-1}, D_{n-1})$

2. Check for damage process

   IF $Y^D(W^D_{\mathrm{T},n}, E^i_n, E^p_{n-1}, D_{n-1}) \leq 0$, THEN:

   Goto BOX **4**

   ELSE:

   Project simultaneously

   $S^p_{\mathrm{T},n}$ on $Y^p(S^p, D) = 0$ and

   $W^D_{\mathrm{T},n}$ on $Y^D(W^D_n, E^i_n, E^p, D) = 0$

   Compute $S = \partial_E \Psi(E^i_n, E^p, D)$, $\frac{\mathrm{d}S}{\mathrm{d}E}$

   Goto BOX **4**

   END IF.

BOX 4 – Total strain correction, state variables update

1. Total strain correction

   IF `stress-driven`, THEN:

   Compute $\mathrm{d}E^i = -\frac{\mathrm{d}S}{\mathrm{d}E}^{-1} (S - \overline{S}_n)$

   Set $E^{i+1}_n = E^i_n + \mathrm{d}E^i$

   ELSE:

   Set $\mathrm{d}E^i = 0$

   END IF.
   Set $i \leftarrow i + 1$ END DO. (i-loop)

2. Update state variables

   Set $E_n = E^i_n, \qquad S_n = S$

   Set $E^p_n = E^p, \qquad D_n = D$

   Set $n \leftarrow n + 1$ END DO. (n-loop)

Table 4.1: (continued).

4.1.3 RI± theoretical formulation

The rate-independent model with two internal damage variables, abbreviated by RI±, allows for finer simulations, but its complexity is slightly increased. In this model, the damage state is described by a tensile (D_+) and a compressive (D_-) damage variable.

The main motivation for the formulation of this model is that it guarantees a damaged reloading collinear with the origin (Subsection 2.2.1).

Nevertheless, the differences with the RI model are not drastic. Thus, we only present the major and necessary differences in order to understand this new model.

Rheological setup

The rheological setup of the RI± damage model is the same than the RI one (Figure 4.1).

Variables and material constants definitions

The total strain $E \in \mathbb{R}$ and the plastic strain $E^p \in \mathbb{R}$ still describe the deformation state of the system.
New tensile and compressive damage variables, denoted by $D_+ \in [0, 1[$ and $D_- \in [0, 1[$ respectively, replace D. Actually, the total damage state of the system can be interpreted by the amount $D_+ + D_-$.
Isotropic plastic hardening is no longer considered in this model. Two new exponential plastic hardening functions are defined:

$$\sigma_+^p(D_-) = \chi^p\big(1 - \exp\left(-lD_-\right)\big) \geq 0 \tag{4.44}$$

and

$$\sigma_-^p(D_+) = \chi^p\big(1 - \exp\left(-lD_+\right)\big) \geq 0 \tag{4.45}$$

The exponential damage hardening functions are analogously defined by:

$$\sigma_\pm^D(D_+, D_-) = \sigma_{0\pm}^D\left(1 + \chi^D\Big(1 - \exp\big(-k(D_+ + D_-)\big)\Big)\right) \tag{4.46}$$

Remark 4.8 *We see that the tensile (resp. compressive) plastic yield stress depends only on the compressive (resp. tensile) damage variable. This argument added to the condition that D_+ (resp. D_-) evolves only during the tensile (resp. compressive) damage mode guarantee a damaged reloading collinear with the origin. This is included in the new dissipation potential.*

Remark 4.9 *The damage threshold stresses are chosen to depend on the sum of both damage variables which describe the total damage state of the system.*

Free energy potential and conjugate stresses

The new nonsmooth convex free energy potential of the RI± model is:

$$\Psi(E, E^p, D_+, D_-) = \\ = \begin{cases} \frac{1}{2}\epsilon_0(E-E^p)^2 + \frac{1}{2}\epsilon_0\frac{1-(D_++D_-)}{D_++D_-}E^{p2} + I_\Delta(D_+, D_-) & \text{if } D_+ + D_- > 0 \\ \frac{1}{2}\epsilon_0(E-E^p)^2 + I_{\{0\}}(E^p) & \text{if } D_+ + D_- = 0 \end{cases} \tag{4.47}$$

with $\Delta = [0,1[\times[0,1[$, I_Δ the indicator function of Δ and $I_{\{0\}}$ that of $\{0\}$.

Remark 4.10 *We note that Ψ is invariant with respect to a permutation of D_+ and D_-. The distinct tensile and compressive behaviours of cortical bone tissue will be included in the definition of an asymmetric dissipation potential.*

The state laws which derive from the free energy potential are:

$$S_\Psi \in \quad \partial_E\Psi \ = \begin{cases} \epsilon_0(E-E^p) & \text{if } D_+ + D_- > 0 \\ \epsilon_0 E & \text{if } D_+ + D_- = 0 \end{cases} \tag{4.48}$$

$$S^p_\Psi \in -\partial_{E^p}\Psi \ = \begin{cases} \epsilon_0 E - \epsilon_0\frac{E^p}{D_++D_-} & \text{if } D_+ + D_- > 0 \\ \mathbb{R} & \text{if } D_+ + D_- = 0 \end{cases} \tag{4.49}$$

$$W^{D_+}_\Psi \in -\partial_{D_+}\Psi = \begin{cases} \frac{1}{2}\epsilon_0\frac{E^{p2}}{(D_++D_-)^2} & \text{if } D_+ + D_- > 0 \\ [0,\infty[& \text{if } D_+ + D_- = 0 \end{cases} \tag{4.50}$$

$$W^{D_-}_\Psi \in -\partial_{D_-}\Psi = \begin{cases} \frac{1}{2}\epsilon_0\frac{E^{p2}}{(D_++D_-)^2} & \text{if } D_+ + D_- > 0 \\ [0,\infty[& \text{if } D_+ + D_- = 0 \end{cases} \tag{4.51}$$

We see that the stress in the damageable spring is:

$$S^D := S - S^p \in \begin{cases} \epsilon_0\frac{1-(D_++D_-)}{D_++D_-}E^p & \text{if } D_+ + D_- > 0 \\ \mathbb{R} & \text{if } D_+ + D_- = 0 \end{cases} \tag{4.52}$$

Thus, the stiffness of the damageable elastic spring is $\epsilon_0\frac{1-(D_++D_-)}{D_++D_-}$.

Dissipation potential and flow rules

The new nonsmooth convex dissipation potential is defined by:

$$\Phi(\dot{E}^p, \dot{D}_+, \dot{D}_-; E, E^p, D_+, D_-) := \Phi^p(\dot{E}^p; D_+, D_-) + \\ + \Phi^D(\dot{D}_+, \dot{D}_-; E, E^p, D_+, D_-) \tag{4.53}$$

with

$$\Phi^p(\dot{E}^p) := \sigma^p_-(D_+)\mathcal{D}_{\mathbb{R}_+}(\dot{E}^p) + \sigma^p_+(D_-)\mathcal{D}_{\mathbb{R}_-}(\dot{E}^p) \tag{4.54}$$

and

$$\Phi^D(\dot{D}_+, \dot{D}_-; E, E^p, D_+, D_-) := \phi(\dot{D}_+, \dot{D}_-; E, E^p, D_+, D_-) + I_{\mathbb{R}_+\times\mathbb{R}_+}(\dot{D}_+, \dot{D}_-) \tag{4.55}$$

where

$$\phi(\dot{D}_+, \dot{D}_-; E, E^p, D_+, D_-) :=$$

$$:= \begin{cases} h_+(D_+, D_-)\dot{D}_+ & \text{if } E^p > 0 \quad \text{or} \quad E^p = 0 \text{ and } E \geq 0 \\ h_-(D_+, D_-)\dot{D}_- & \text{if } E^p < 0 \quad \text{or} \quad E^p = 0 \text{ and } E < 0 \end{cases}$$

and $h_\pm(D_+, D_-) := \dfrac{\sigma^{D2}_\pm(D_+, D_-)}{2\epsilon_0(1-(D_+ + D_-))^2}$.

$\mathcal{D}_{\mathbb{R}_\pm}$ are the distance functions to $\mathbb{R}_\pm$ representing the positive or negative parts respectively, and $I_{\mathbb{R}_+\times\mathbb{R}_+}$ is the indicator function of $\mathbb{R}_+ \times \mathbb{R}_+$. The plastic and damage dissipations (Φ^p and Φ^D) are different in forward and backward plastic strain rate.

By a Legendre-Fenchel transformation of Φ, we find the dual dissipation potential:

$$\begin{aligned} \Phi^*(S^p, W^{D_+}, W^{D_-}; E, E^p, D_+, D_-) = \\ = \Phi^{p*}(S^p; D) + \Phi^{D*}(W^{D_+}, W^{D_-}; E, E^p, D_+, D_-) \end{aligned} \tag{4.56}$$

with

$$\Phi^{p*}(S^p; D) := I_{[-\sigma^p_-(D_+), \sigma^p_+(D_-)]}(S^p)$$

and

$$\Phi^{D*}(W^{D_+}, W^{D_-}; E, E^p, D_+, D_-) :=$$

$$:= \begin{cases} I_{[-\infty, h_+(D_+, D_-)]} & \text{if } E^p > 0 \quad \text{or} \quad E^p = 0 \text{ and } E \geq 0 \\ I_{[-\infty, h_-(D_+, D_-)]} & \text{if } E^p < 0 \quad \text{or} \quad E^p = 0 \text{ and } E < 0 \end{cases}$$

The associated flow rules (inverse complementary laws) are:

$$\dot{E}^p \in \partial_{S^p}\Phi^* = \begin{cases} \emptyset & \text{if } S^p < -\sigma^p(D_+) \\ ]-\infty, 0] & \text{if } S^p = -\sigma^p(D_+) \\ 0 & \text{if } -\sigma^p(D_+) < S^p < \sigma^p(D_-) \\ [0, +\infty[& \text{if } S^p = \sigma^p(D_-) \\ \emptyset & \text{if } S^p > \sigma^p(D_-) \end{cases} \tag{4.57}$$

and, if $E^p > 0$ or $E^p = 0$ and $E \geq 0$, then $\dot{D}_- = 0$ and

$$\dot{D}_+ \in \partial_{W^{D_+}} \Phi^* = \begin{cases} 0 & \text{if } W^{D_+} \in]-\infty, h_+(E, E^p, D_+, D_-)[\\ [0, +\infty[& \text{if } W^{D_+} = h_+(E, E^p, D_+, D_-) \\ \emptyset & \text{if } W^{D_+} > h_+(E, E^p, D_+, D_-) \end{cases} \tag{4.58}$$

whereas if $E^p < 0$ or $E^p = 0$ and $E < 0$, then $\dot{D}_+ = 0$ and

$$\dot{D}_- \in \partial_{W^{D_-}} \Phi^* = \begin{cases} 0 & \text{if } W^{D_-} \in]-\infty, h_-(E, E^p, D_+, D_-)[\\ [0, +\infty[& \text{if } W^{D_-} = h_-(E, E^p, D_+, D_-) \\ \emptyset & \text{if } W^{D_-} > h_-(E, E^p, D_+, D_-) \end{cases} \tag{4.59}$$

Remark 4.11 *The kinematic complementarity relation $\dot{D}_+ \dot{D}_- = 0$ ($\dot{D}_+ \geq 0$, $\dot{D}_- \geq 0$) follows from the definition of the dissipation potential and its parametric dependence on E^p (distinguishing tensile and compressive states).*

Numerical implementation

The numerical algorithm of the RI± damage model can easily be generalized from the RI model. The resulting algorithm has the same structure as the one presented in Table 4.1 upon replacing the hardening functions (4.2) and (4.3) by their RI± counterparts (4.44), (4.45) and (4.46).

4.2 Rate-dependent models

In this Section, two rate-dependent models based on the RI and RI± models are presented. They account for rate-dependent damage processes. Since our experiments and other investigators show that viscoelastic effects are relatively small at physiological strain rates, we choose to include rate-dependent effects only during damage accumulation mechanisms (e.g. [McElhaney, 1966, Fondrk et al., 1988]).

As the rate-dependent models are similar to the rate-independent ones, we present only their major new characteristics.

4.2.1 RD damage model formulation

Rheological setup

The rheological model is identical to the rate-independent setup. The only difference lies in the damage evolution rule deriving from a power complementary dissipation potential.

Variables and material constants definitions

The rate-dependent model with one damage variable (abbreviated by RD) shares the same three independent variables as the RI model: E, E^p and D. Furthermore, the plastic and damage hardening functions are identical. However, rate-dependent damage accumulation requires the introduction of two new material constants: an exponent N and a viscosity parameter ζ.
Therefore, nine constants fully characterize the RD damage model (ϵ_0, χ^p, l, σ^D_{0+}, σ^D_{0-}, χ^D, k, N and ζ).

Free energy potential and conjugate stresses

The free energy potential and the conjugate stresses are the *same* as in the RI model.

Dissipation potential and flow rules

The new nonsmooth convex dissipation potential is defined by:

$$\Phi(\dot{E}^p, \dot{D}; E, E^p, D) = \Phi^p(\dot{E}^p; D) + \Phi^D(\dot{D}; E, E^p, D) \tag{4.60}$$

with

$$\Phi^p(\dot{E}^p; D) := \sigma^p(D)|\dot{E}^p| \tag{4.61}$$

and

$$\Phi^D(\dot{D}; E, E^p, D) := \phi(\dot{D}; E, E^p, D) + I_{\mathbb{R}_+}(\dot{D}) \tag{4.62}$$

where

$$\phi(\dot{D}; E, E^p, D) := \frac{1}{2\epsilon_0(1-D)^2}\left[\frac{N\zeta^2}{N+2}\left(\frac{|E^p|}{(1-D)D}\right)^{2/N}\dot{D}^{(N+2)/N} + \right.$$

$$\left. + \begin{cases} \frac{2N\zeta\sigma^D_+(D)}{N+1}\left(\frac{|E^p|}{(1-D)D}\right)^{1/N}\dot{D}^{(N+1)/N} + \sigma^{D2}_+(D)\dot{D} & \text{if } E^p > 0 \text{ or } E^p = 0 \text{ and } E \geq 0 \\ \frac{2N\zeta\sigma^D_-(D)}{N+1}\left(\frac{|E^p|}{(1-D)D}\right)^{1/N}\dot{D}^{(N+1)/N} + \sigma^{D2}_-(D)\dot{D} & \text{if } E^p < 0 \text{ or } E^p = 0 \text{ and } E < 0 \end{cases}\right]$$

and $I_{\mathbb{R}_+}$ is the indicator function of $\mathbb{R}_+$.
The complementary laws are derived without difficulty from the dissipation potential:

$$S^p_\Phi \in \partial_{\dot{E}^p}\Phi = \begin{cases} -\sigma^p(D) & \text{if } \dot{E}^p < 0 \\ [-\sigma^p(D), \sigma^p(D)] & \text{if } \dot{E}^p = 0 \\ \sigma^p(D) & \text{if } \dot{E}^p > 0 \end{cases} \tag{4.63}$$

and

$$W_\Phi^D \in \partial_{\dot D}\Phi = \begin{cases} \phi'(\dot D; E, E^p, D) & \text{if } \dot D > 0 \\ ]-\infty, \phi'(0; E, E^p, D)] & \text{if } \dot D = 0 \\ \emptyset & \text{if } \dot D < 0 \end{cases} \tag{4.64}$$

where ϕ' is the derivative of ϕ with respect to $\dot D$:

$$\phi'(\dot D; E, E^p, D) = \begin{cases} \frac{1}{2\epsilon_0}\left(\frac{\zeta\left(\frac{|E^p|}{(1-D)D}\right)^{1/N}\dot D^{1/N} + \sigma_+^D(D)}{1-D}\right)^2 \\ \qquad \text{if} \quad E^p > 0 \text{ or } E^p = 0 \text{ and } E \geq 0 \\ \frac{1}{2\epsilon_0}\left(\frac{\zeta\left(\frac{|E^p|}{(1-D)D}\right)^{1/N}\dot D^{1/N} + \sigma_-^D(D)}{1-D}\right)^2 \\ \qquad \text{if} \quad E^p < 0 \text{ or } E^p = 0 \text{ and } E < 0 \end{cases}$$

Remark 4.12 *We note that $\phi'(0; E, E^p, D) = \phi'(E, E^p, D)$, previously defined as the quasistatic damage energy threshold of the RI model in (4.17). As the function ϕ' depends on $\dot D$, damage accumulation is rate-dependent in this model. The damage energy W^D no longer needs to be projected on the quasistatic damage energy but obeys the evolution rule (4.64).*

Remark 4.13 *For $D = 0$ and thus $E^p = 0$, the ratio $\frac{|E^p|}{D}$ tends to the finite value $|E|$, which is consistent with the choice $\sigma^p(0) = 0$ (see (4.28)).*

The dual dissipation potential is obtained via the Legendre-Fenchel transform:

$$\Phi^*(S^p, W^D; E, E^p, D) = \Phi^{p*}(S^p; D) + \Phi^{D*}(W^D; E, E^p, D) \tag{4.65}$$

with

$$\Phi^{p*}(S^p; D) := I_{[-\sigma^p(D), \sigma^p(D)]}(S^p)$$

the indicator function of $[-\sigma^p(D), \sigma^p(D)]$ and

$$\Phi^{D*}(W^D; E; E^p, D) := \begin{cases} \phi_+^*(W^D; E^p, D) & \text{if } E^p > 0 \quad \text{or} \quad E^p = 0 \text{ and } E \geq 0 \\ \phi_-^*(W^D; E^p, D) & \text{if } E^p < 0 \quad \text{or} \quad E^p = 0 \text{ and } E < 0 \end{cases}$$

where

$$\phi_\pm^*(W^D; E^p, D) := -\frac{2}{(N+1)(N+2)}\frac{(1-D)D}{|E^p|}\left[h_\pm(D) - (N+1)W^D + \right.$$
$$\left. + N\sqrt{h_\pm(D)W^D}\right]\mathcal{D}_{\mathbb{R}_-}^N\left(\frac{(1-D)\sqrt{2\epsilon_0 W^D} - \sigma_\pm^D(D)}{\zeta}\right)$$

and $h_{\pm}(D)$ defined in (4.14).
The flow rules of the internal variables E^p and D are found from Φ^* (inverse complementary laws):

$$\dot{E^p} \in \partial_{S^p_\Phi} \Phi^* = \begin{cases} \emptyset & \text{if } S^p < -\sigma^p(D) \\ ]-\infty, 0] & \text{if } S^p = -\sigma^p(D) \\ 0 & \text{if } -\sigma^p(D) < S^p < \sigma^p(D) \\ [0, +\infty[& \text{if } S^p = \sigma^p(D) \\ \emptyset & \text{if } S^p > \sigma^p(D) \end{cases} \tag{4.66}$$

and

$$\dot{D} \in \partial_{W^D_\Phi} \Phi^* = \begin{cases} \frac{(1-D)D}{|E^p|} \mathcal{D}^N_{\mathbb{R}_-}\left(\frac{|S^D| - \sigma^D_+(D)}{\zeta}\right) & \text{if } E^p > 0 \text{ or } E^p = 0 \text{ and } E \geq 0 \\ \frac{(1-D)D}{|E^p|} \mathcal{D}^N_{\mathbb{R}_-}\left(\frac{|S^D| - \sigma^D_-(D)}{\zeta}\right) & \text{if } E^p < 0 \text{ or } E^p = 0 \text{ and } E < 0 \end{cases} \tag{4.67}$$

where $\mathcal{D}_{\mathbb{R}_-}$ is the distance function to $\mathbb{R}_-$ and Remark 4.13 is enforced.

Remark 4.14 *In (4.67), we used the equivalence:*

$$(1 - D)\sqrt{2\epsilon_0 W^D} = |S^D|$$

Remark 4.15 *In contrast with the RI model, we see from (4.67) that the damage evolution rule allows for a stress overshoot in the damageable spring. The damage variable evolves according to a power law governed by the exponent N and the viscosity factor ζ as in the cumulative damage model for bone fracture proposed by [Carter and Caler, 1985].*

The partial Legendre-Fenchel transform is illustrated in Figure 4.9 for $E^p > 0$, $N = 18$ and $\zeta = 35$. We note that a high exponent N approximates a plastic behaviour; this is referred to as a *pseudo-plastic* behaviour.

4.2.2 Numerical algorithm

The numerical implementation of the RD model differs from the RI version only in the damage mode. The formulation of the elastic and plastic modes remains unchanged. Once again, the formalism of generalized standard materials is applied.

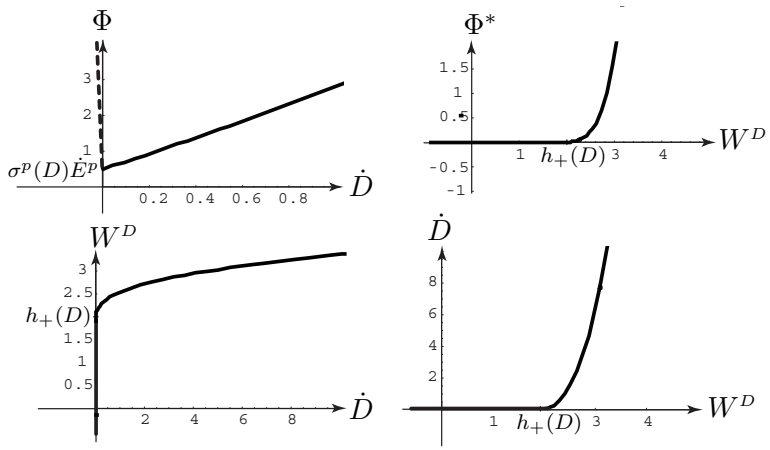

Figure 4.9: Illustration of the partial Legendre-Fenchel transform of Φ, plotted for $E^p > 0$, $h_+(D) = 1.9$, $N = 3$ and $\zeta = 35$.

Internal variables evolution

Damage mode: $Y^p(S^p_{\mathrm{T}}, D_0) > 0$ **and** $Y^D(W^D_{\mathrm{T}}; E, E^p_0, D_0) > 0$

In this case, $\dot{E}^p \neq 0$ and $\dot{D} \neq 0$. (4.28) still holds as $S^p = \pm\sigma^p(D)$ but the evolution rule of D is dictated by (4.67). The time derivative can be approximated to the first order by the backward Euler rule ([Hughes and Taylor, 1978]):

$$\dot{D} \simeq \frac{D - D_0}{\tau} \tag{4.68}$$

Combining (4.28) with (4.67), we get:

$$\frac{D - D_0}{\tau} - \frac{1 - D}{\left|E \mp \frac{\sigma^p(D)}{\epsilon_0}\right|}\left(\frac{\epsilon_0(1-D)\left|E \mp \frac{\sigma^p(D)}{\epsilon_0}\right| - \sigma^D_{\pm}(D)}{\zeta}\right)^N = 0 \tag{4.69}$$

This nonlinear equation has to be solved for D as E is assumed to be known (predicted).
Let us define the function $f_{\pm} : [0, 1[\to \mathbb{R}$ by

$$\begin{aligned} f_{\pm}(D) :=& \left|E \mp \frac{\sigma^p(D)}{\epsilon_0}\right|(D - D_0) + \\ & - \tau(1 - D)\left(\frac{\epsilon_0(1-D)\left|E \mp \frac{\sigma^p(D)}{\epsilon_0}\right| - \sigma^D_{\pm}(D)}{\zeta}\right)^N \end{aligned} \tag{4.70}$$

with f_+ and the upper sign symbols for $E^p > 0$ or $E^p = 0$ and $E \geq 0$ and f_- and the lower sign symbols for $E^p < 0$ or $E^p = 0$ and $E < 0$, respectively. The derivative of $f_\pm$ reads:

$$\begin{aligned} f'_\pm(D) = &\left|E \mp \frac{\sigma^p(D)}{\epsilon_0}\right| + \frac{E \mp \frac{\sigma^p(D)}{\epsilon_0}}{\left|E \mp \frac{\sigma^p(D)}{\epsilon_0}\right|}\left(\mp\frac{\sigma^{p\prime}(D)}{\epsilon_0}\right)(D - D_0) + \\ &+ \tau \left(\frac{\epsilon_0(1-D)\left|E \mp \frac{\sigma^p(D)}{\epsilon_0}\right| - \sigma^D_\pm(D)}{\zeta}\right)^N + \\ &- \tau\epsilon_0(1-D)\frac{N}{\zeta}\left(\frac{\epsilon_0(1-D)\left|E \mp \frac{\sigma^p(D)}{\epsilon_0}\right| - \sigma^D_\pm(D)}{\zeta}\right)^{N-1} \cdot \\ &\cdot \left[-\left|E \mp \frac{\sigma^p(D)}{\epsilon_0}\right| + (1-D)\frac{E \mp \frac{\sigma^p(D)}{\epsilon_0}}{\left|E \mp \frac{\sigma^p(D)}{\epsilon_0}\right|}\left(\mp\frac{\sigma^{p\prime}(D)}{\epsilon_0}\right) - \frac{\sigma^{D\prime}_\pm(D)}{\epsilon_0}\right] \end{aligned} \tag{4.71}$$

In order to find the value of D, we have to solve $f_\pm(D) = 0$.
We use the generalized Newton method ([Alart and Curnier, 1991]) to solve this nonsmooth C^0 nonlinear equation

$$D^{j+1} = D^j - \frac{f_\pm(D^j)}{f_\pm{}'(D^j)} \quad \text{with} \quad j = 0, 1, 2, \ldots \tag{4.72}$$

Tangent operator computation

The tangent operators are unchanged in the elastic and plastic modes.

Damage mode: $Y^p(S^p_{\mathrm{T}}, D_0) > 0$ **and** $Y^D(W^D_{\mathrm{T}}; E, E^p_0, D_0) > 0$

In this mode, $\frac{\mathrm{d}S}{\mathrm{d}E}$ is still given by (4.39) but $\frac{\mathrm{d}D}{\mathrm{d}E}$ reads:

$$\frac{\mathrm{d}D}{\mathrm{d}E} = -\frac{\partial f_\pm/\partial E}{\partial f_\pm/\partial D} \tag{4.73}$$

where $\frac{\partial f_\pm}{\partial D}$ is given by (4.71) and

$$\begin{aligned} \frac{\partial f_\pm}{\partial E} = &\frac{E \mp \frac{\sigma^p(D)}{\epsilon_0}}{\left|E \mp \frac{\sigma^p(D)}{\epsilon_0}\right|}(D - D_0) - \tau\epsilon_0(1-D)^2\frac{N}{\zeta}\frac{E \mp \frac{\sigma^p(D)}{\epsilon_0}}{\left|E \mp \frac{\sigma^p(D)}{\epsilon_0}\right|} \cdot \\ &\cdot \left(\frac{\epsilon_0(1-D)|E \mp \frac{\sigma^p(D)}{\epsilon_0}| - \sigma^D_\pm(D)}{\zeta}\right)^{N-1} \end{aligned} \tag{4.74}$$

Algorithm formulation

The algorithm has exactly the same structure as the one presented in Table 4.1. The only difference is the use of the generalized Newton method (4.72) instead of (4.32) in order to find the adequate value of D in the damage mode.

4.2.3 RD± damage model formulation

The extension of the RD model to a rate-dependent model with two internal damage variables (abbreviated by RD±) is done exactly in the same way as the rate-independent case. Thus, we will not formulate it in this Subsection.

We recall that the few changes to be done are to introduce tensile and compressive damage variables, to make use of the *same* free energy potential as (4.47) and the *same* dissipation potential as (4.60) where the plastic and hardening functions must be replaced by (4.44), (4.45) and (4.46).

The state laws are then obtained by the usual method of generalized standard materials. As for the RI± model, the RD± leads to a damaged reloading collinear with the origin, a lack of the RD model.

4.3 Discussion and comparison of the models

Firstly, in order to visualize and understand the different evolution modes of the models, we carry out a cyclic loading-unloading numerical experiment. Secondly, we show that the rate-independent models can be viewed as the quasistatic limit of the rate-dependent ones.

4.3.1 Loading-unloading cycles

In a typical loading-unloading simulation, the algorithm of our constitutive laws for cortical bone can go through three main evolution modes. For clarity of the discussion, we assume a strain driven pure tensile saw tooth like cyclic test (Figure 4.10). Two successive cycles of same magnitude carried out on the RI and RI± damage models are illustrated in Figure 4.11 (a) and (b), respectively.

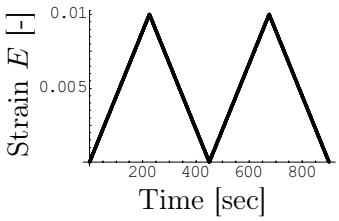

Figure 4.10: Pure tensile strain driven saw tooth like test.

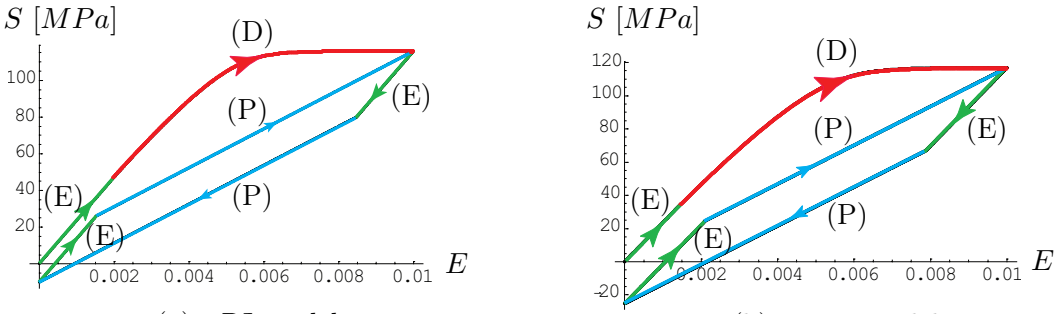

(a) RI model (b) RI± model

Figure 4.11: Stress-strain diagrams of the three evolution modes of cortical bone: (E) Initial and subsequent elastic mode, (P) plastic mode and (D) damage mode. Both graphs are plotted for $\epsilon_0 = 24.4\,GPa$ and $k = l = 14$. Further left-hand side material constants are: $\sigma^D_{0+} = 48\,MPa$, $\chi^p = 18\,MPa$ and $\chi^D = 50$; right-hand side: $\sigma^D_{0+} = 32\,MPa$, $\chi^p = 50\,MPa$ and $\chi^D = 85.6$.

Initial linear elastic mode (E)

For an intact tissue, the plastic strain and the damage variable are supposed to be initially equal to zero. Thus, the plastic yield stress is also zero and immediately reached as stress increases. However, as long as the damage threshold stress has not been reached, the damageable spring mounted in parallel with the plastic pad behaves like a rigid bar. Thus, it prevents the sliding of the plastic pad.
In this initial elastic mode, only the primary spring of stiffness ϵ_0 governs the evolution of the system.

Damage mode (D)

Once the initial damage threshold stress is reached, both plastic strain and damage increase. The damageable spring is no longer rigid and the plastic pad begins to slide in the tensile direction.
In the rate-independent case, the trial elastic stress of the damageable spring

is projected on the updated damage threshold surface to give the final damaged stress. In the rate-dependent case, the value of the damage variable is regulated by the rate-dependent evolution rule. In the case of the two damage variables models, only the tensile damage variable increases.
In both cases, the plastic stress is simultaneously projected on the positive plastic surface to give the final plastic stress: a non-zero stress in the case of the one damage variable models and a zero stress for the ± models.
This plastic and damage mode of cortical bone tissue is assigned to the generation and growth of microcracks.

Subsequent linear elastic mode (E)

As soon as the total stress decreases, like during the unloading phase, the stress in the damageable spring drops below its damage threshold. Furthermore, the stress in the plastic pad also decreases below its positive plastic yield point. Thus, the plastic pad remains fixed until its stress reaches its negative plastic yield point and begins to slide in the opposite direction.
In this subsequent elastic regime, only the primary spring of stiffness ϵ_0 accounts for the evolution of the system.
The length of the elastic unloading phase is directly proportional to the value of the positive and negative plastic yield stresses. In the ± models, the positive plastic yield stress remains equal to zero as it depends only on the compressive damage variable. Thus, the length of the subsequent elastic mode is half of the length of the models with one damage variable which undergo an isotropic plastic hardening. This particular feature ensures a damaged reloading in a second loading cycle to be collinear with the origin (Figure 4.11 (b)).

Plastic mode (P)

Once the negative plastic yield stress is reached, the plastic pad begins to slide in the compressive direction. This mode has a slope of $(1-D)\epsilon_0$ on the stress-strain curve, giving an intuitive interpretation of the damage variable. It represents the reduction of the intact elastic stiffness.
This plastic mode is attributed to a microcrack sliding mode.

Second loading cycle

During the second loading cycle, the material will first undergo the linear elastic regime, then the plastic mode (with the plastic pad sliding in the tensile direction). For the rate-independent models, if the reloading cycle is of same magnitude as the first, the plastic mode will reach the adaptation stress

level reached before, and thus not accumulate further damage. However, for the rate-dependent models, little damage is accumulated because the quasistatic damage threshold stress is smaller than the viscous threshold stress level reached during the previous cycle.
The final unloading phase is composed of a subsequent elastic mode followed by a plastic mode.

4.3.2 Quasistatic limit

To see that the rate-independent models are the quasistatic limit of the rate-dependent ones, let us focus on the tensile damage mode of the RD model. The same conclusions can be drawn for the RD± model and for the compressive damage mode without additional difficulty.
In such a case, $W^D > h_+(D)$ (or equivalently $S^D > \sigma_+^D(D)$) and the internal variable D evolves according to the function:

$$\dot{D} = \frac{(1-D)D}{|E^p|}\left(\frac{|S^D| - \sigma_+^D(D)}{\zeta}\right)^N \tag{4.75}$$

where $|S^D| = (1-D)\sqrt{2\epsilon_0 W^D}$. The plot of $\dot{D}$ against W^D is shown in Figure 4.12 for various exponents N. We see that all curves pass through the points of coordinates $W^D = \frac{1}{2\epsilon_0}\left(\frac{\zeta+\sigma_+^D(D)}{1-D}\right)^2 := g_+(D)$ and $\dot{D} = \frac{(1-D)D}{|E^p|}$.

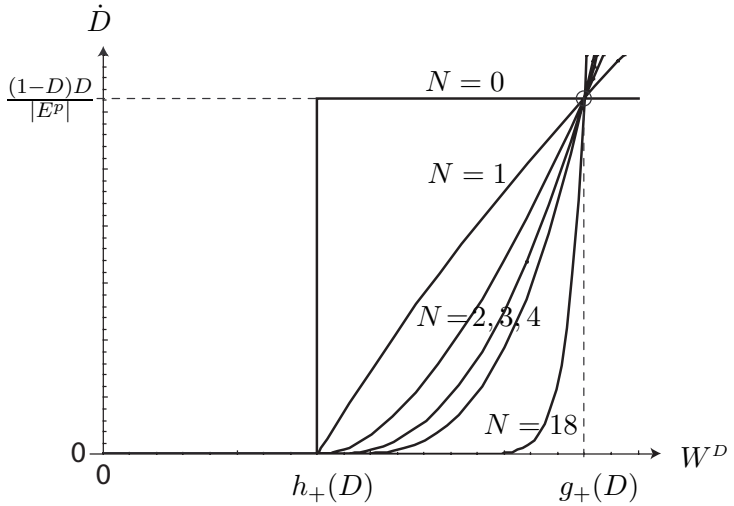

Figure 4.12: Tensile rate-dependent flow rule of D plotted for various exponents N.

We have the following result:

$$\lim_{\zeta \to 0} g_+(D) = h_+(D) = \frac{\sigma_+^{D2}(D)}{2\epsilon_0(1-D)^2} \tag{4.76}$$

The limit (4.76) means that the rate-dependent damage model tends to the rate-independent damage model for $\zeta \to 0$, allowing thus no rate-dependent damage stress overshoot. This statement remains true for all N.

4.3.3 Final considerations

For all four models, a range of mechanical tests were successfully simulated covering both strain and stress driven constant step (relaxation and creep), monotonic ramp, saw tooth like cycles, cyclic sine both in tension and/or compression.

The Newton integration scheme used to overcome the nonlinearity of the stress-strain law under stress control shows asymptotically quadratic convergence (in the absence of a damage state change).

The algorithm used to calculate the rate-dependent accumulation of damage (implicit time integration scheme of the RD and RD± models) is robust.

Chapter 5

Identification of one-dimensional laws

We carried out a series of *in vitro* uniaxial mechanical tests on bovine cortical bone specimens in order to identify the different constants characterizing our one-dimensional constitutive laws. The tests included tensile or compressive ramps, tensile or/and compressive saw tooth cycles and finally creep, all tests being conducted along the principal direction of the bone fibers. In order to examine the behaviour of cortical bone subject to strain rates ranging from the quasistatic domain to the physiological one, strain rates varying from $4.6 \cdot 10^{-5}$ to $10^{-2} s^{-1}$ were selected.

Artefacts associated to inhomogeneous boundary conditions were avoided using dumbbell (or "dogbone") specimens. Thus, we expect a good quantitative evaluation of the plastic and damage processes.

Cortical bone, like most biological tissues, show a high variability in its properties from one individual to another and within the same individual. This is essentially due to different densities, porosities and degrees of mineralization. The purpose of our mechanical tests was not to develop a rigorous identification procedure involving large statistics, but rather to prove the relevance of the proposed models.

5.1 Uniaxial tests

5.1.1 Materials and methods

Specimen preparation

Fresh bovine femurs were obtained from a local slaughterhouse and stored at $-20^o C$ within one hour. Then, the diaphyses were isolated with a Metabo band-saw (Metabowerke GmbH) and cut into cylindrical cylinders of $50\, mm$

length. After cleaning the marrow, 7-8 mm thick slices were extracted from the cylinders with an EXAKT 300 CL band-saw (EXAKT Vertriebs GmbH) along the longitudinal direction of the fibers. The parallelepiped-like specimens were then dried in an oven at 40^oC for 24 hours. Finally, the blocks were milled down into cylindrical specimens with dimensions $44 \times 5\, mm$ (Figure 5.1 Left).

Prior to testing, each specimen was weighed and then thawned in a physiological saline solution for two hours at room temperature ($\sim 22^oC$). Finally, the weight of the wet specimen was determined just before the test. The effects of drying and re-wetting the specimens on the mechanical properties of cortical bone are small and can probably be ignored ([Currey, 1988a]).

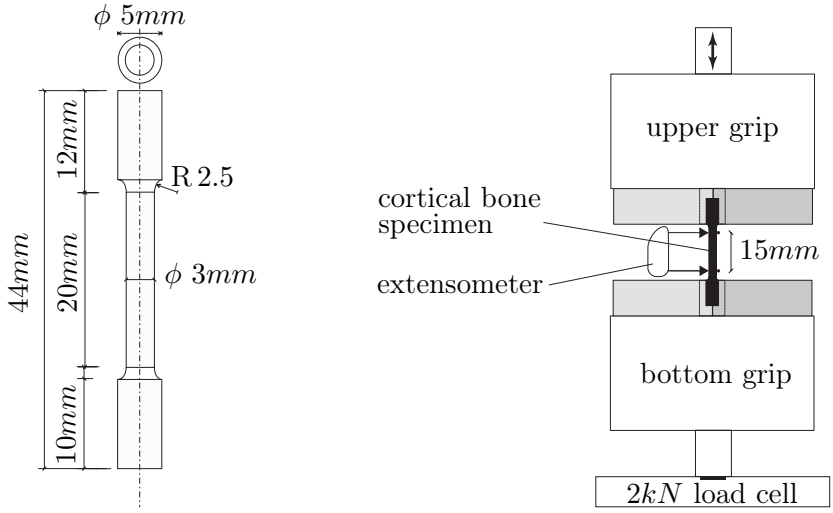

Figure 5.1: Cortical bone specimen geometry and schematic experimental setup.

Mechanical testing

Uniaxial tests were carried out on a 5848 Instron electromechanical microtester (Instron Corp.). The specimens were fixed on customised grips specially adapted to the size of our specimens (Figure 5.1 Right). Force was measured using a $2\, kN$ Instron load cell. Displacement was measured using a calibrated SANDNER EXA15-2o extensometer (SANDNER-Messtechnik GmbH) of $L = 15\, mm$ gauge length directly attached to the central part of the specimen. Drying of the specimen during all the testing procedure was prevented using a moist gauze placed around the specimen. The gauze was regularly kept wet during the testing using a physiological solution spray. All tests were carried out at room temperature ($\sim 22^oC$) under displacement control (except for creep tests). Data were recorded on an appropriate computer acquisition system.

Imposed schedules

Different schedules were imposed including tensile or compressive ramps, tensile or/and compressive cycles and finally creep tests. Strain-driven tests were carried out at different strain rates ranging from $4.6 \cdot 10^{-5}$ to $10^{-2}s^{-1}$. Each test was repeated five times using five different specimens. We tested a total of 90 specimens.

Single ramp tests. A series of tensile or compressive ramps were carried out up to rupture of the specimens at three different strain rates (Figure 5.2 a)). The imposed rates were $\dot{E}_0 = 4.6 \cdot 10^{-5}s^{-1}$, $\dot{E}_1 = 3.4 \cdot 10^{-4}s^{-1}$ and $\dot{E}_3 = 3.4 \cdot 10^{-3}s^{-1}$. A total of 30 specimens were tested this way.

Cyclic tests. Four kinds of cyclic tests were carried out. The first two schedules were exclusive tensile or compressive saw tooth like displacements of increasing amplitude (Figure 5.2 b)). A single ramp was finally applied in the opposite direction up to rupture of the specimen. The strain rate for this series was $\dot{E}_0 = 4.6 \cdot 10^{-5}s^{-1}$. The other two schedules consisted of saw tooth like cyclic tests combining tension and compression (Figure 5.2 c)). In the first series (at $\dot{E}_0 = 4.6 \cdot 10^{-5}s^{-1}$, $\dot{E}_1 = 3.4 \cdot 10^{-4}s^{-1}$ and $\dot{E}_4 = 10^{-2}s^{-1}$), we began with a tensile part (Figure 5.2 c)), whereas in the second (at $\dot{E}_0 = 4.6 \cdot 10^{-5}s^{-1}$, $\dot{E}_2 = 10^{-3}s^{-1}$ and $\dot{E}_4 = 10^{-2}s^{-1}$) with a compressive one. In order to verify the absence of damage accumulation for an already reached strain (or stress) level, all cycles were repeated twice. A total of 40 specimens were tested this way.

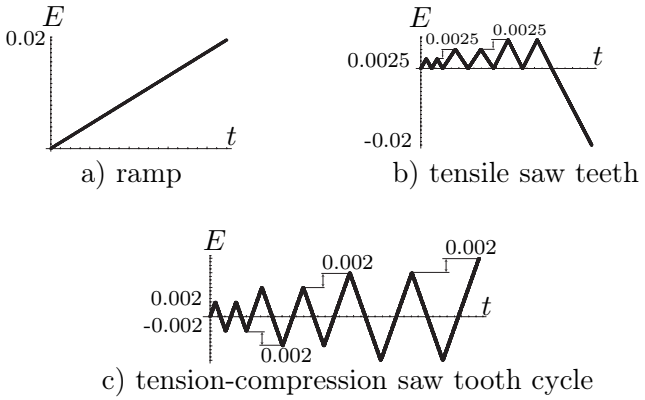

Figure 5.2: Uniaxial tensile strain schedules. The compressive counterparts are obtained by a symmetry with respect to the time axis.

Creep tests. Tensile creep tests were carried out at two stress levels: $106\,MPa$ and $113\,MPa$. The stress levels of the compressive creep tests were a slightly higher in modulus: $-113\,MPa$ and $-120\,MPa$. The mentioned creep stresses were reached in $10\,s$ with a linear ramp, then held constant during $90\,s$. At the end, stress was decreased to zero in $10\,s$ and then maintained at this level during $90\,s$ (Figure 5.3). A total of 20 specimens were tested this way.

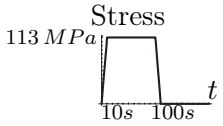

Figure 5.3: Tensile creep schedule.

Elasticity. Prior to each test, we carried out twelve saw tooth preconditioning cycles in the elastic range in order to measure the longitudinal initial elastic modulus. Only the last two cycles were used for its evaluation. To this end, we imposed a displacement corresponding to a force of approximately $100\,N$ (or a stress of $14\,MPa$).

All strain-driven uniaxial tests are summarized in Table 5.1 and the stress-driven ones in Table 5.2.

Loading schedule	Strain rate	Number of specimens
Single tensile ramp	$\dot{E}_0$, $\dot{E}_1$, $\dot{E}_3$	$N = 15$
Single compressive ramp	$\dot{E}_0$, $\dot{E}_1$, $\dot{E}_3$	$N = 15$
Tensile cycles (final compr. ramp)	$\dot{E}_0$	$N = 5$
Compr. cycles (final tensile ramp)	$\dot{E}_0$	$N = 5$
Tensile-compressive cycles	$\dot{E}_0$, $\dot{E}_1$, $\dot{E}_4$	$N = 15$
Compressive-tensile cycles	$\dot{E}_0$, $\dot{E}_2$, $\dot{E}_4$	$N = 15$

Table 5.1: Overview of the 70 strain-driven uniaxial tests.

Loading schedule	Creep stress	Number of specimens
Tensile creep	$106\,MPa$, $113\,MPa$	$N = 10$
Compressive creep	$-113\,MPa$, $-120\,MPa$	$N = 10$

Table 5.2: Overview of the 20 uniaxial creep experiments.

5.1.2 Preliminary discussion

For all mechanical tests, we observed a large quantitative scatter of the measurements. This is common to all biological tissues and can be explained by two main arguments.

Firstly, it is obvious that due to very different loading conditions, intrinsic shapes and functions, the mechanical, microstructural and chemical properties of a given tissue will vary from one location to another within the same body. In addition, living tissues have the remarkable property to adapt their structure to their function, leading thus to heterogeneous mechanical properties.

Secondly, all aforementioned properties vary greatly from one individual to another. They are altered by age, sex, genetic material, physical activity, illness, and external living conditions.

Identification of constitutive laws describing the behaviour of biological tissues is therefore a difficult task. A major goal for the biomechanicists of this century is to build a huge database founded on a minimum set of physiological variables like age, sex, weight, ... which allows to predict the value of the parameters of certified constitutive laws. Due to the lack of information about the origin of our specimens and their limited number, this was not attempted in this study.

5.2 Results

All experiments carried out on cortical bone specimens delivered the expected constitutive behaviour qualitatively described in Subsection 2.2.1 except in compression. Although the dumbbell geometry of the traction specimens ensures reliable measurements avoiding inhomogeneous boundary effects, the small section of the specimens added to heterogeneities facilitated its buckling and rupture in compression.

Most tensile fractures occurred in horizontal fracture patterns (Figures 5.4a) and b)), whereas most compressive ones in 45^o oblique fracture patterns (Figures 5.4 c) and d)). In some few cases, the specimen broke at the knives of the extensometer but most fractures occurred away from the knives, either near the knives or in the middle of the specimen. However, the recorded pre-fracture stress-strain curves were qualitatively very similar in all cases.

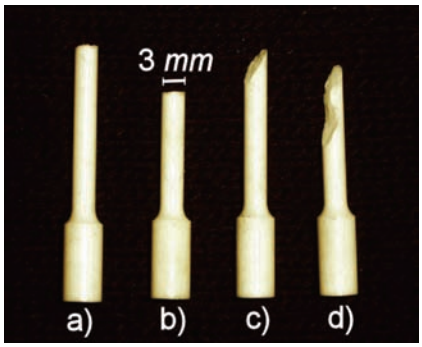

Figure 5.4: Fracture patterns: a) and b) macroscopically flat, transverse plane, c) and d) oblique plane.

Selected experimental results for the quasistatic behaviour of cortical bone at $\dot{E} = 4.6 \cdot 10^{-5} s^{-1}$ are presented in Figure 5.5 a) to f). The results are expressed in terms of stretch $H := (L_t - L)/L$ and nominal stress $P := \bar{p}/A$, where L and L_t are the initial and actual gauge lengths, $\bar{p}$ the load and A the initial specimen area. Tests at higher strain rates are shown in Figure 5.6 a) to f). At this point, we wish to thank R. Balet ([Balet, 2005]) for carrying out and providing us the tests at higher strain rates. We now briefly discuss qualitatively the main characteristics of the recorded stress-strain curves.

5.2.1 Elasticity

All elastic preconditioning cycles (for example Figure 5.5 f)) suggest that the same longitudinal elastic modulus holds in tension and compression. Symmetric elastic properties have also been found for trabecular bone ([Keaveny et al., 1994, Zysset, 1994]).
Although the apparent tangent traction modulus of cortical bone is known to have a strong dependence on strain rate ([McElhaney, 1966]), we find no significant correlation for our range of velocities (Figure 5.6 a) and b)).

5.2.2 Damage threshold stress or elastic limit

All tests reveal a disymmetry between the compressive and the tensile damage threshold stresses (Figures 5.5 a) to f) and 5.6 a) to f)). We find that in magnitude, the longitudinal compressive threshold stress is approximately 1.4 times higher than the tensile one (Figures 5.5 c-d) vs 5.5 e-f)). This result agrees well with previous investigations on bovine cortical bone (e.g. [Reilly and Burstein, 1975, Cowin, 1989]).

In contrast with the longitudinal elastic modulus, damage threshold stresses show a stronger rate-dependence. A higher strain rate results in a higher damage threshold stress (Figure 5.6 a) and b)). However, a strict comparison between these curves must be done carefully because of the large scatter of the results.

5.2.3 Hardening or damage behaviour

The damage behaviour of cortical bone is very similar to a hardening plastic state leading to permanent strains (Figures 5.5 a) to f)). Reduction of the initial elastic modulus visible during the unloading phase (Figures 5.5 c), e-f), and 5.6 c) to f)) reveals a plastic damaging mode (later on called damaging mode).

Our results suggest that the material response is dominated by time-dependent effects above the damage threshold stress, whereas below it, the behaviour is primarily linear viscoelastic, with time effects playing only a secondary role. This corroborates the study of [Fondrk et al., 1988] and justifies the need for rate-dependent damage accumulation mechanisms as the ones taken into account in our rate-dependent models. For small velocities, the slope of the damaging mode is of small magnitude (Figure 5.5 a) to f)), whereas for increasing strain rates, the slope of the damaged curve increases (Figure 5.6 a) to f)).

Due to experimental instabilities, our compressive threshold stresses coincides almost with the compressive ultimate stresses. Rupture of the specimen, mainly by buckling, occurs shortly after this point (Figures 5.5 b-c), e-f) and 5.6 b), e)). Thus, we do not observe the compressive damaging mode which is clearly visible in the tensile counterpart. Nevertheless, successful compressive experiments carried out on cortical bone show a similar damage behaviour in tension and compression (Figure 5.6 f), [Reilly and Burstein, 1975]). These instabilities lead to near values for the tensile and compressive ultimate strains which is not usual for cortical bone ([Cowin, 1989]).

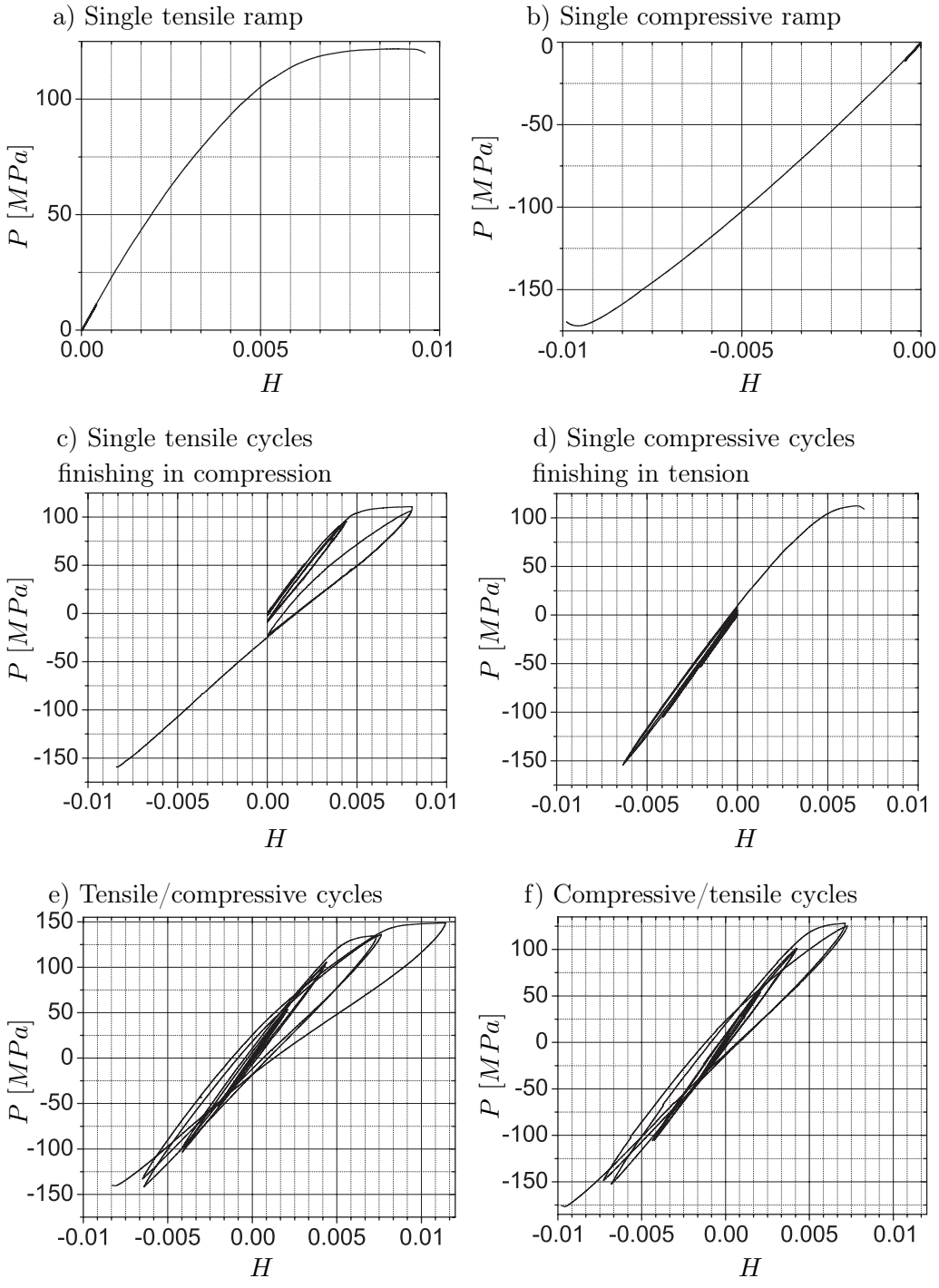

Figure 5.5: Stress-strain curves of the uniaxial tests at $\dot{E} = 4.6 \cdot 10^{-5} s^{-1}$: a) and b) single ramps, c) and d) tensile/compressive cycles and e) and f) cycles mixing tension and compression.

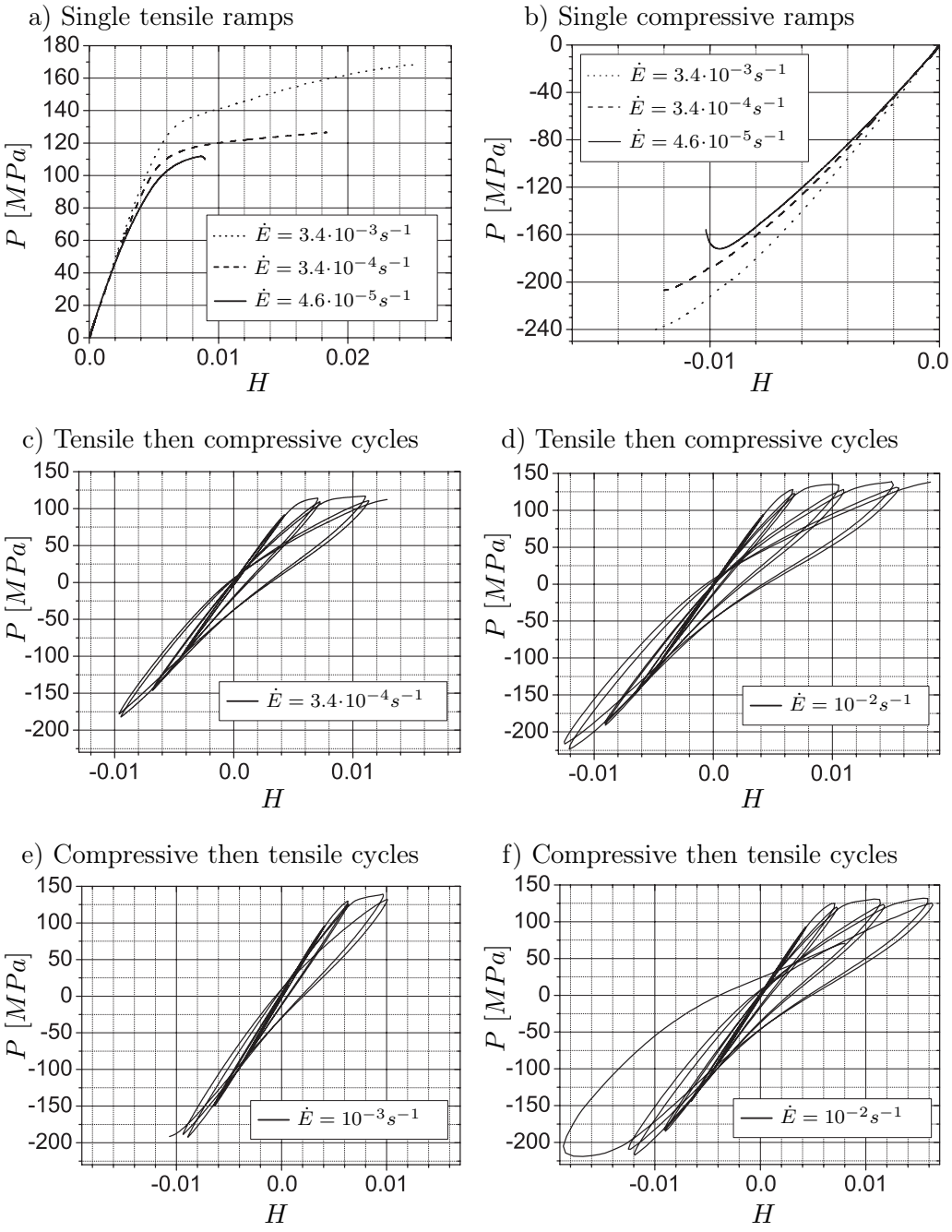

Figure 5.6: Stress-strain curves of the uniaxial tests at various strain rates: a) and b) single ramps, c) to f) cycles mixing tension and compression.

5.3 Identification

In order to properly identify the constants of our one-dimensional constitutive laws for bovine cortical bone, we carried out the average of all responses for a given test. Then, we chose the nearest and most representative test to be identified.

We recall that the elastic mode of our one-dimensional models is described by the initial Young's modulus ϵ_0. Damage-dependent hardening functions account for the plastic and damage evolution modes.

If exponential hardening is assumed for both plastic and damage criteria, the hardening functions are characterized by six parameters: $\sigma^D_{0\pm}$, χ^p, χ^D, k and l.

This Section is divided into two parts. Firstly, we identify the seven parameters of the two uniaxial rate-independent constitutive laws for cortical bone. Secondly, the two additional constants ζ and N defining rate-dependent damage are identified for both rate-dependent models.

In view of the large quantitative scatter between each test, probably due to specimen density, porosity and mineralization scatter, we insist on the fact that identification is done in the sense of a good *qualitative* agreement retaining the main features of the material behaviour. Paying too much attention to exact curve fitting is irrelevant.

5.3.1 Identification of the rate-independent laws

We proceed now to the identification of the seven aforementioned material constants and discuss the ability of the models to fit the experimental curves. We base the identification of the rate-independent constitutive laws upon the lowest strain rate ($\dot{E} = 4.6{\cdot}10^{-5}\, s^{-1}$).

Elasticity. The overall mean longitudinal intact elastic modulus is $\epsilon_0 = 24.4 \pm 1.4\ GPa$ which lies in the range of other authors findings (e.g. [Reilly and Burstein, 1975, Cowin, 1989]).

Damage threshold stresses. Plastic and damage thresholds are difficult to define because plastic and damage modes appear progressively. Therefore, there are several ways to define the elastic limit of a stress-strain curve.

It can be defined as the point of maximal curvature in a monotonic tension (or compression) test. Another arbitrary way but which gives realistic estimations is the conventional 0.2% strain offset criterion. In that case, the threshold point is defined as the point from which we get 0.2% permanent strain if we unload a perfectly plastic material (starting from zero strain).

However, our initial damage threshold stresses $\sigma^D_{0\pm} = \sigma^D_{\pm}(D = 0)$ have a slightly different meaning. The experiments suggest that it is more realistic to choose a low damage threshold stress and to assume a high exponential hardening law (accumulating little damage for low stress levels) instead of the usual high damage threshold stress and low hardening. Making this choice, the identified tensile and compressive damage threshold stresses are: $\sigma^D_{0+} = 48\ MPa$, $\sigma^D_{0-} = 80\ MPa$ for the RI model and $\sigma^D_{0+} = 32\ MPa$, $\sigma^D_{0-} = 53\ MPa$ for the RI$\pm$ model, respectively.

Hardening constants. The identified hardening constants of the RI model are $\chi^p = 18.0\ MPa$, $\chi^D = 50.0$ and $k = l = 14$. We find $\chi^p = 50.0\ MPa$, $\chi^D = 85.6$ and $k = l = 14$ for the RI$\pm$ model.

Predicted stress-strain curves. The numerical stress-strain curves predicted by the RI and RI$\pm$ models are compared to the experimental results in Figure 5.7 a) to f). We recall that $H = (L_t - L)/L$ is the stretch whereas $P = \bar{p}/A$ is the nominal stress. A summary of the identified material constants for the rate-independent models is given in Table 5.3.

Remark 5.1 *Due to inherent scatter of biological tissues, Figure 5.7 e) is obtained with a slightly higher value of* χ^D *(*$\chi^D = 85$*) and Figure 5.7 f) with* $\chi^p = 40\ MPa$ *and* $\chi^D = 115$*. The values of the other parameters remain unchanged.*

5.3.2 Identification of the rate-dependent laws

Adding rate-dependency to damage accumulation induces a new rheological behaviour in the models. Therefore, the identified damage parameters of the rate-independent models must be adapted in order to take into account this new effect.

Elasticity. As only damage behaviour is supposed to be rate-dependent, the value of the initial longitudinal elastic modulus ϵ_0 remains unchanged ($\epsilon_0 = 24.4 \pm 1.4\ GPa$).

Damage threshold stresses. For RD, identification provides the values $\sigma^D_{0+} = 1.0\ MPa$ and $\sigma^D_{0-} = 4.3\ MPa$, whereas for the RD$\pm$ model, we find $\sigma^D_{0+} = 1.0\ MPa$ and $\sigma^D_{0-} = 1.9\ MPa$.

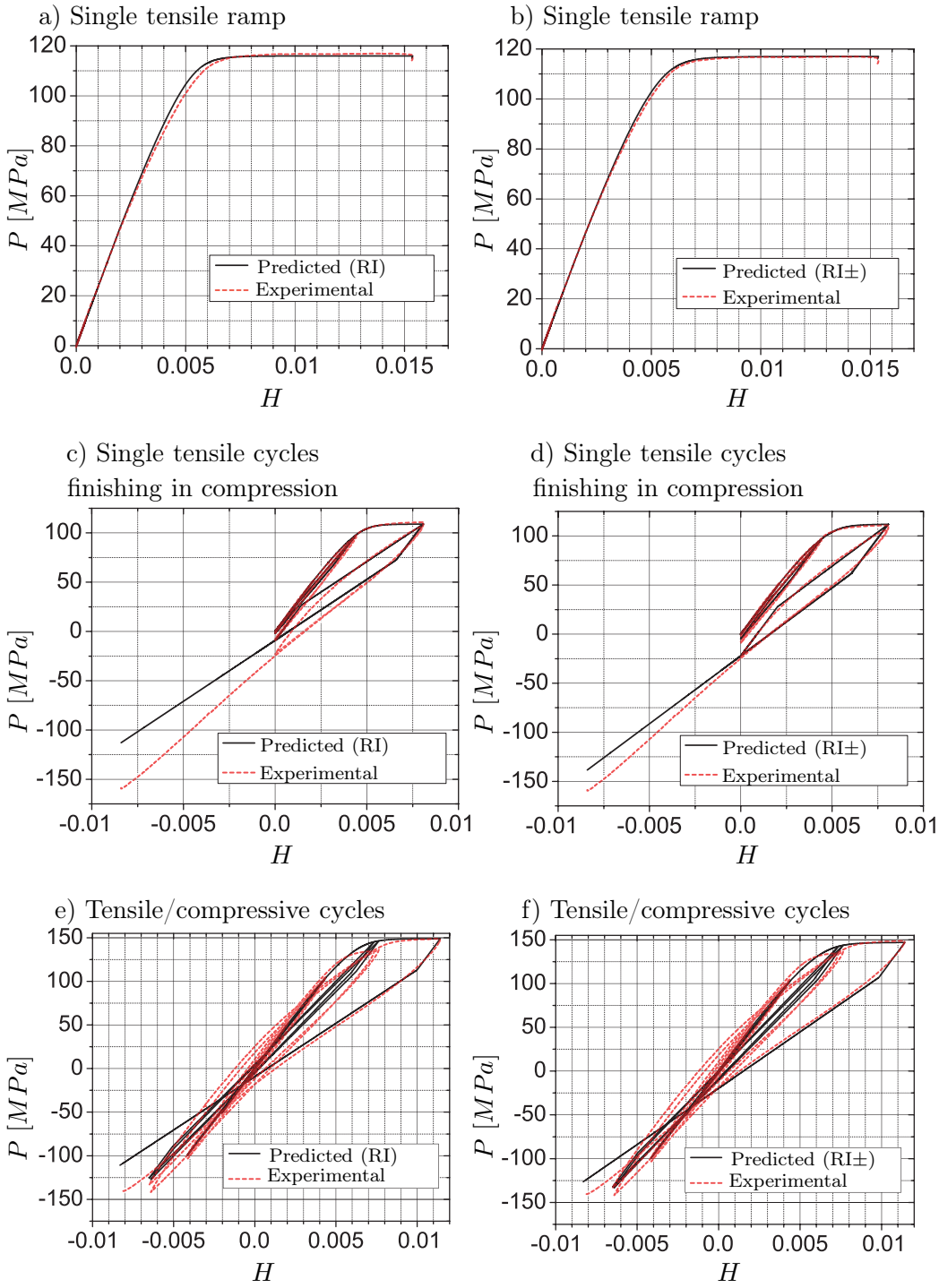

Figure 5.7: Experimental against predicted stress-strain curves of the one-dimensional RI and RI± models (strain rate $\dot{E} = 4.6 \cdot 10^{-5}\, s^{-1}$). Models parameters: RI: $\epsilon_0 = 24.4\, GPa$, $\sigma^D_{0+} = 48\, MPa$, $\sigma^D_{0-} = 80\, MPa$, $\chi^p = 18\, MPa$, $\chi^D = 50$, $k = l = 14$; RI±: $\epsilon_0 = 24.4\, GPa$, $\sigma^D_{0+} = 32\, MPa$, $\sigma^D_{0-} = 53\, MPa$, $\chi^p = 50\, MPa$, $\chi^D = 85.6$, $k = l = 14$. (Curve 5.7 e) obtained with $\chi^D = 85$ and 5.7 f) with $\chi^p = 40\, MPa$ and $\chi^D = 115$ respectively).

Hardening constants. We find $\chi^p = 18.0\ MPa$, $\chi^D = 21.6$ for RD and $\chi^p = 40.0\ MPa$, $\chi^D = 90.6$ for the RD± model, respectively. For both models, we find $k = l = 14$.

Damage viscosity coefficients. The exponent N describing the damage accumulation power law reads $N = 18$ for RD and $N = 5$ for the RD± model, respectively. Identification of the viscosity coefficients ζ provides $\zeta = 18\,MPa \cdot s^{1/18}$ for RD and $\zeta = 160\,MPa \cdot s^{1/5}$ for the RD± model, respectively.

The high exponents are characteristic of a "pseudo-plastic" type of damage evolution i.e. almost rate-independent. This corroborates Remark 5.2 and the cumulative damage model for bone fracture proposed by [Carter and Caler, 1985].

Predicted stress-strain curves. The simulation results of the rate-dependent models do not differ qualitatively from the rate-independent ones. Some are shown in Figure 5.9 and discussed later. A summary of the identified material constants for the rate-dependent models is given in Table 5.3.

Remark 5.2 *Let us note that identification of the uniaxial test mixing tension then compression (the equivalent of Figure 5.7 e)) required higher values of* χ^D *(*$\chi^D = 50$ *for RD and* $\chi^D = 125$ *for the RD± model, respectively).*

	units	RI	RI±	RD	RD±
ϵ_0	$[GPa]$	24.4	24.4	24.4	24.4
σ^D_{0+}	$[MPa]$	46	32	1.0	1.0
σ^D_{0-}	$[MPa]$	80	53	4.3	1.9
χ^p	$[MPa]$	18	50	18	40
χ^D	[-]	50.0	85.6	21.6	90.6
k	[-]	14	14	14	14
l	[-]	14	14	14	14
N	[-]	-	-	18	5
ζ	$[MPa \cdot s^{1/N}]$	-	-	135	160

Table 5.3: Overview of the identified material constants of the two rate-independent and the two rate-dependent one-dimensional damage models.

5.3.3 Creep tests

As other materials, the tensile and compressive creep behaviour of cortical bone exhibits three successive stages. However, our creep tests were not creep-fracture tests. Therefore, the third stage is absent from our creep curves (Figure 5.8 a) to d)). The primary stage where strain rate decreases progressively is associated to the transient response of the specimen to the applied load. The secondary stage where strain rate remains approximately constant is the proper creep behaviour of the material. The third stage where strain rate increases rapidly (no present in our tests) leads to fracture of the specimen. Thus, time to failure has not been investigated in this series of tests.

The experimental results of the tensile and compressive creep tests (at $113\,MPa$ and $-120\,MPa$, respectively) are compared to the simulations of the RD and RD± models in Figures 5.8 a) to d).

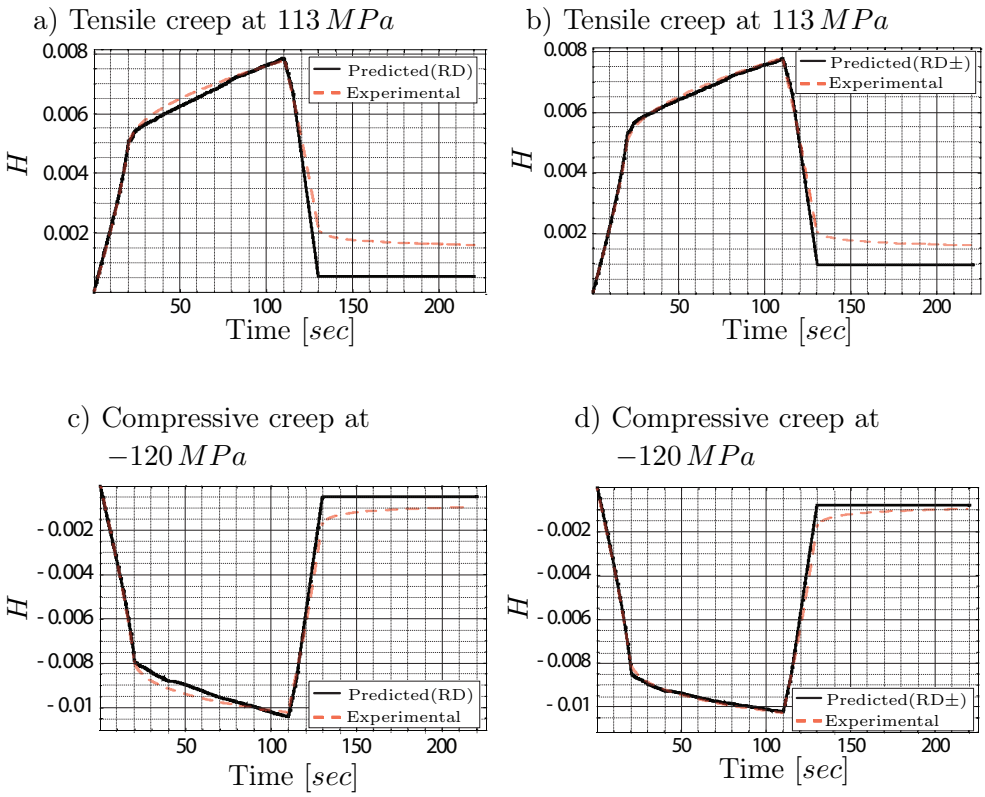

Figure 5.8: Experimental creep tests compared to the predictions of the RD and RD± models (stretch versus time diagrams).

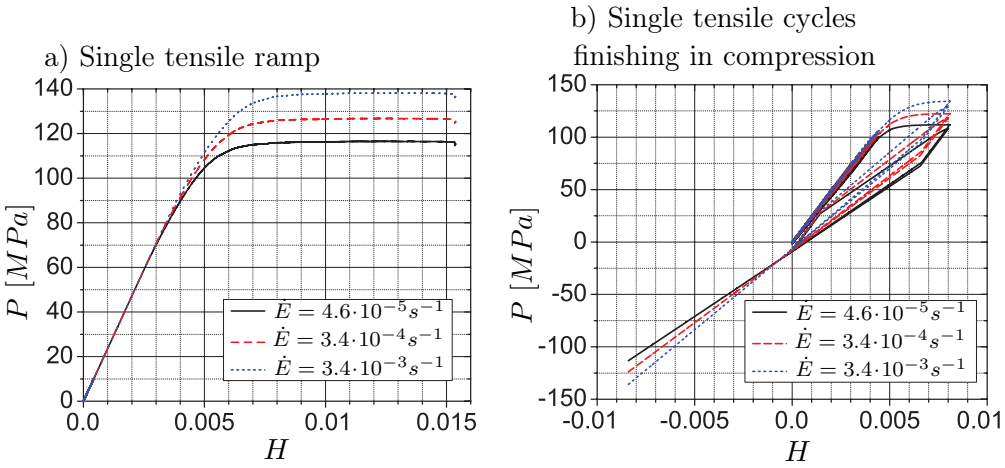

Figure 5.9: Strain-rate dependence of the numerical RD model.

5.4 Discussion

Our own uniaxial cyclic mechanical tests confirm the presence of the three main modes of deformation of cortical bone described in Subsection 2.2.1: the elastic, plastic and damage deformation regimes are clearly identified. The agreement between the numerical and experimental results show that plastic and damage mechanisms are closely related. The microstructural interpretation of the three modes is reinforced: an instantaneous linear elastic regime due to bone cohesion, a rate-dependent damage accumulation mode where microcracks are generated and a mode of sliding with friction at the microcracks. Plasticity and damage in bone may be associated with slipping between mineralized collagen fibrils or even between collagen fibers and hydroxyapatite platelets and caused by shear failure of the organic matrix ([Keaveny et al., 2001]).

All four proposed constitutive laws successfully reproduce the main features of cortical bone's behaviour: the intact elastic reloading phase, a stiffness reduction and an increasing energy dissipation. Let us discuss now some specific points.

Damage thresholds and damage mode

The very low values found for the initial tensile and compressive threshold stresses, associated to an exponential hardening and a power law damage evo-

lution rule shows that the true elastic domain of cortical bone is extremely small. However, all models slightly underestimate the observed damage hysteresis of the early cycles mixing tension and compression (Figures 5.7 e) and f)).

The models with one damage variable generally overestimate damage accumulation as can be seen in Figures 5.7 c) and e) (they overestimate the stiffness reduction). This is accentuated for the creep tests as can be seen in Figures 5.8 a) and c) i.e. the permanent strains resulting from tensile and compressive overloadings are underestimated. However, the $\pm$ models lead to better results (Figures 5.8 b) and d)). Generally, we see that positive permanent strains observed after compressive unloadings are globally underestimated by our models. This may be due to a viscosity of the plastic deformation.

During successive overloading cycles of same magnitude carried out on trabecular bone, [Keaveny et al., 1999] observed that all reloading curves approached the extrapolated envelope of the previous cycles. Furthermore, they found that the damaged reloadings were collinear with the origin. All our models predict the first feature, but only the models with a distinct tensile and compressive damage variable guarantee a damaged reloading which is collinear with the origin (Figures 5.7 d) and f)).

Plastic mode

The uniaxial piecewise linear behaviour of damaged bone observed by [Kotha and Guzelsu, 2003, Zioupos, 2002] (Subsection 2.2.1) was present in all our tensile cyclic overloading experiments. This mode is clearly different than the response of undamaged bone (e.g. Figure 5.5 c)).

Our models do not predict the observed stiffening of the plastic mode occurring when crossing from the tensile to the compressive part of the stress-strain diagram (and the softening going from the compressive to the tensile part, respectively). It is emphasized that it is not an experimental artefact. This behaviour may be explained by the closing of cracks and has also been observed in concrete ([Ortiz, 1985]). A model with different elastic damage in tension and compression would be required to take into account this observed behaviour.

Viscous effects

The creep tests give evidence of the viscous nature of damage accumulation mechanisms in cortical bone. The rate-dependent models predict

strain rate in the secondary stage with good accuracy. They also predict a stress limit under which creep deformation stops and does not lead to failure.

Rate-dependent effects of the RD model can be seen in Figures 5.9 a) and b) where the strain rate has been increased by a factor 10 between two successive tests. The qualitative shape of the predicted stress-strain curves does not change by adding rate-dependency to damage accumulation. This is in agreement with previous experimental investigations ([Carter and Caler, 1985, Fondrk et al., 1988]) and our own ones. Thus, in this study, we confirm that the viscoelastic effects are relatively small at physiological strain rates. However, the experimental creep tests shown Figure 5.8 demonstrate the presence of moderate viscoplastic effects which are not included in our rate-dependent models.

The increase of the (usual) damage threshold stress and ultimate stress with increasing strain rate agrees well with our experimental measures and with the findings of [McElhaney, 1966]. The same result holds for the RD$\pm$ model.

Failure

We repeat that inhomogeneous boundary effects were avoided using dumbbell specimens. This ensured reliable measurements of uniaxial displacements of the specimens. Use of waisted specimens is of primary importance for accurate identification of the material constants.

Of course, successful damage compression tests would probably affect the identified material constants $\sigma_{0-}^{D}, \chi^{p}$ and χ^{D} (and N and ζ for the rate-dependent models). Perhaps a modification of the model involving distinct material properties in tension and compression $(\chi_{\pm}^{p}, \chi_{\pm}^{D}, N_{\pm}, \zeta_{\pm})$ instead of a single ones $(\chi^{p}, \chi^{D}, N, \zeta)$ would improve the fitting.

The lateral force exerted by the knives and the weight of the very small extensometer was close to $1\,N$. Even if this force was small, it may have induced local damage leading to failure of the specimens which broke at the knives.

Macroscopic failure of the material always corresponds to a localization of the damage process. The fracture zone varied in our uniaxial tests because of the inhomogeneities of cortical bone and inhomogeneous stress distribution in the section of the specimens. Nevertheless, even if waisting of the specimen was not sufficient to force the failure process in the middle, the recorded stress-strain curves before failure seem to be independent of the fracture zone.

The specimens which broke in tension exhibited a macroscopically flat,

transverse fracture plane. Scanning electron micrographs actually reveal an extremely rough, irregular fracture surface ([Caler and Carter, 1989]). This fracture process can be attributed to osteon pullout, fiber elongation, and separation of lamellae from each other failing at cement lines. The compressive fracture patterns are markedly different than that of the tensile ones. The fracture plane is oblique to the specimen axis. Scanning electron micrographs show that the fracture crosses through the osteons themselves at an oblique angle exposing the concentric layers in steps ([Caler and Carter, 1989]). The ends of the lamellae are drawn out and folded over. We see that the extremely complex damage accumulation mechanisms and fracture processes in bone involve all hierarchical levels of its structure. The remarkable ability of our models to predict the macroscopic uniaxial damaged behaviour of bone justifies the continuum approach used in this study.

In summary, novel mechanical tests carried out on bovine cortical bone mixing tension and compression were made and confirm the three main deformation regimes of cortical bone in tension. Its mechanical behaviour is very different from traditional engineering materials such as metals, wood and concrete. The tests allowed successful identification of the material constants characterizing the one-dimensional laws. Even though all constitutive ingredients are not included in the models, they faithfully reproduce accumulation of plastic strains, reduction in elastic modulus and time-dependent effects for arbitrary one-dimensional loading histories. As bone tissue exhibits an anisotropic behaviour, multiaxial tests are needed to formulate robust constitutive equations. Nevertheless, we emphasize that the constitutive laws developed in this work describe the behaviour of cortical bone under conditions of interest, i.e. cyclic overloading at physiological strain rates.

Chapter 6

Three-dimensional law: formulation and implementation

In this Chapter, we generalize the rate-independent (RI) damage model to three dimensions. It is based on only two internal state variables. The scalar plastic strain E^p is replaced by a symmetric second-order tensor $\mathbf{E}^p$, and for simplicity, the damage variable D remains a scalar quantity. Thus, in this model, damage affects equally all constants of the fourth-order elastic stiffness tensor of cortical bone (isotropic damage).

This last assumption is not realistic even for a linear elastic damageable material (e.g. [Ladevèze, 1993, He and Curnier, 1995]) but is reasonable for proportional loading. Damage induced material anisotropy may be characterized by a symmetric second-order or even fourth-order tensor (e.g. [Lubarda and Krajcinovic, 1993, Zhu and Cescotto, 1995, Carol et al., 2001a]).

This Chapter is divided into four parts. In the first part, the three-dimensional elastic plastic damage constitutive law for cortical bone is formulated. The corresponding algorithm is described in the second part. In the third part, the finite element method used for spatial discretization, the linear iteration method for solving nonlinearities and the finite difference method for time discretization are briefly described. Finally, the numerical implementation is validated through some elementary simulations in the fourth part.

6.1 Theoretical formulation

6.1.1 Rheological setup and variables definition

Rheological setup

The coupling of the three-dimensional basic rheological elements composing the model is one-dimensional (in series and parallel). The rheological setup is similar to the one-dimensional mounting (Figure 6.1).
In this model, the elastic stiffness of the primary linear spring is a symmetric fourth-order tensor $\mathbb{S}$. In analogy with the one-dimensional RI model, the stiffness of the damageable spring is chosen to be equal to $\mathbb{S}_D := \frac{1-D}{D}\,\mathbb{S}$.
The damage threshold criterion includes distinct tensile and compressive threshold stresses whereas the plastic yield criterion is based on the symmetric intact elastic compliance tensor for simplicity.

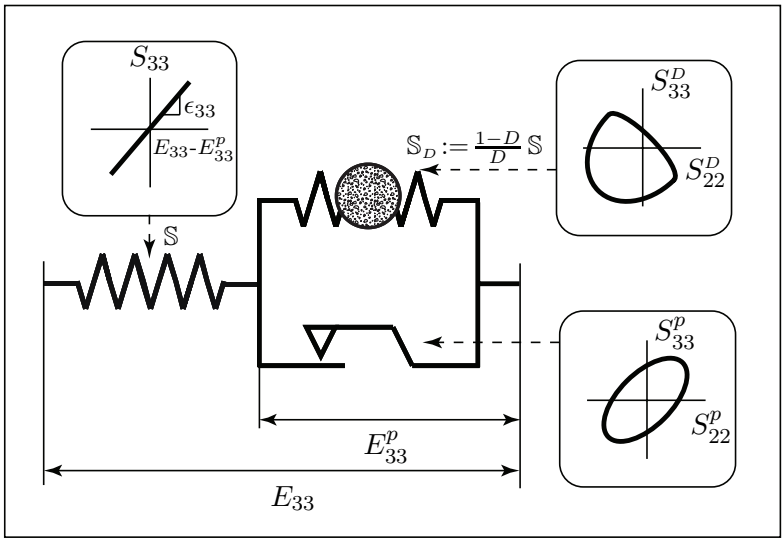

Figure 6.1: Rheological setup of the three-dimensional constitutive law for cortical bone.

Variables and material constants definition

Three independent variables describe the rheological model:

- the total strain $\mathbf{E} \in \mathbf{S}\mathrm{ym}$,
- the plastic strain $\mathbf{E}^p \in \mathbf{S}\mathrm{ym}$ and
- the damage variable $D \in [0, 1[$

where **S**ym denotes the space of symmetric second-order tensors.
As in the one-dimensional case, we use the usual strain partition $\mathbf{E} = \mathbf{E}^e + \mathbf{E}^p$ with $\mathbf{E}^e$ the elastic strain ([Prandtl, 1924, Reuss, 1930, Green and Naghdi, 1965], e.g. [Lemaitre and Chaboche, 2001]).

If we assume orthotropic linear elasticity, nine material constants characterize the stiffness tensor $\mathbb{S}$ of the primary spring (without counting the three constants of the principal directions of symmetry). Five constants are sufficient if we consider transverse isotropic symmetry (plus two for the directions). We recall that $\mathbb{S}$ is symmetric and positive definite.

The plastic yield criterion is also characterized by a fourth-order tensor. It delimits a convex elastic domain in plastic stress space. Furthermore, a plastic hardening function is needed in order to describe its evolution with increasing damage.

The same holds for the three-dimensional damage threshold criterion. The non-damaging states are enclosed in a convex non-damaging set, which evolves with increasing damage according to its corresponding damage hardening function.

In summary, the two yield and threshold functions and their domains must be defined (as in Section 3.3):

$$Y^p(\mathbf{S}^p, D) \leq 0$$
$$Y^D(\mathbf{S}^D, D) \leq 0$$

with $\mathbf{S}^p$ the stress in the plastic pad and $\mathbf{S}^D$ that in the damageable spring, respectively.

Remark 6.1 *For conciseness of the report, we will not define the yield and threshold functions here. Nevertheless, we can say that:*

- *if we choose the orthotropic Zysset-Curnier model for elasticity based on volume fraction and fabric, i.e. extrapolating the elastic properties of trabecular bone to compact bone (Section 3.3),*
- *and, to simplify, the intact orthotropic elastic compliance tensor $\mathbb{C} = \mathbb{S}^{-1}$ as a special fourth-order tensor describing the plastic yield criterion,*
- *a generalized Hill criterion for damage based on volume fraction and fabric,*
- *and finally exponential plastic and damage isotropic hardenings,*

then the number of necessary material constants is 18. This number reduces to 17 for transverse isotropic symmetry.

6.1.2 Free energy and dissipation potentials

Free energy potential

The nonsmooth convex free energy potential of the rheological model is:

$$\Psi(\mathbf{E},\mathbf{E}^p,D) =$$

$$= \begin{cases} \frac{1}{2}\,(\mathbf{E}-\mathbf{E}^p) : \mathbb{S}\,(\mathbf{E}-\mathbf{E}^p) + \frac{1}{2}\frac{1-D}{D}\,\mathbf{E}^p : \mathbb{S}\,\mathbf{E}^p + I_{[0,1[}(D) & \text{if } D>0 \\ \frac{1}{2}\,\mathbf{E} : \mathbb{S}\,\mathbf{E} + I_{\{\mathbf{0}\}}(\mathbf{E}^p) & \text{if } D=0 \end{cases} \tag{6.1}$$

with $I_{[0,1[}$ the indicator function of $[0,1[$, $I_{\{\mathbf{0}\}}$ the indicator function of $\{\mathbf{0}\}$ and $\mathbb{S}$ the symmetric positive definite fourth-order elastic stiffness tensor.

The state laws which derive from the free energy potential are:

$$\mathbf{S}_\Psi \in \quad \partial_{\mathbf{E}}\Psi = \begin{cases} \mathbb{S}\,(\mathbf{E}-\mathbf{E}^p) & \text{if } D\in\,]0,1[\\ \mathbb{S}\,\mathbf{E} & \text{if } D=0 \end{cases} \tag{6.2}$$

$$\mathbf{S}^p_\Psi \in -\partial_{\mathbf{E}^p}\Psi = \begin{cases} \mathbb{S}\,\mathbf{E} - \frac{1}{D}\,\mathbb{S}\,\mathbf{E}^p & \text{if } D\in\,]0,1[\\ \mathbf{S}\text{ym} & \text{if } D=0 \end{cases} \tag{6.3}$$

$$W^D_\Psi \in -\partial_D\Psi \;= \begin{cases} \frac{1}{2D^2}\,\mathbf{E}^p :\, \mathbb{S}\,\mathbf{E}^p & \text{if } D\in\,]0,1[\\ [0,\infty[& \text{if } D=0 \end{cases} \tag{6.4}$$

For convenience, let us define the stress in the damageable spring:

$$\mathbf{S}^D := \mathbf{S}_\Psi - \mathbf{S}^p_\Psi \in \begin{cases} \frac{1-D}{D}\,\mathbb{S}\,\mathbf{E}^p & \text{if } D\in\,]0,1[\\ \mathbf{S}\text{ym} & \text{if } D=0 \end{cases} \tag{6.5}$$

The complementary free energy is obtained via the Legendre-Fenchel transform:

$$\Psi^*(\mathbf{S},\mathbf{S}^p,W^D) := \sup_{\mathbf{E},\mathbf{E}^p,D} \left[\mathbf{S} : \mathbf{E} - \mathbf{S}^p : \mathbf{E}^p - W^D D - \Psi(\mathbf{E},\mathbf{E}^p,D)\right]$$

With $\mathbb{C} = \mathbb{S}^{-1}$, we find:

$$\Psi^*(\mathbf{S},\mathbf{S}^p,W^D) = \frac{1}{2}\,\mathbf{S} : \mathbb{C}\,\mathbf{S} - \frac{1}{2}\left(\sqrt{(\mathbf{S}-\mathbf{S}^p) : \mathbb{C}\,(\mathbf{S}-\mathbf{S}^p)} - \sqrt{2W^D}\right)^2 \tag{6.6}$$

It can be checked that $\partial_{\mathbf{S}}\Psi^* = \mathbf{E}$, $-\partial_{\mathbf{S}^p}\Psi^* = \mathbf{E}^p$ and $-\partial_{W^D}\Psi^* = D$.
When $D=0$, the dual potential reduces to:

$$\Psi^*(\mathbf{S},\mathbf{S}^p,W^D) = \frac{1}{2}\,\mathbf{S} : \mathbb{C}\,\mathbf{S}\,. \tag{6.7}$$

Therefore, we obtain $\partial_{\mathbf{S}}\Psi^* = \mathbf{E}$, $-\partial_{\mathbf{S}^p}\Psi^* = \mathbf{0}$ and $-\partial_{W^D}\Psi^* = 0$, which is consistent with the implication $D = 0 \Rightarrow \mathbf{E}^p = \mathbf{0}$ associated with $I_{\{\mathbf{0}\}}(\mathbf{E}^p)$ of the potential $\Psi(\mathbf{E}, \mathbf{E}^p, D)$ when $D = 0$.

Dissipation potential

The nonsmooth convex dissipation potential is defined by:

$$\Phi(\dot{\mathbf{E}}^p, \dot{D}; \mathbf{E}, \mathbf{E}^p, D) := \Phi^p(\dot{\mathbf{E}}^p; D) + \Phi^D(\dot{D}; \mathbf{E}, \mathbf{E}^p, D) \tag{6.8}$$

with

$$\Phi^p(\dot{\mathbf{E}}^p; D) := \sigma^p(D)\sqrt{\dot{\mathbf{E}}^p : \mathbb{S}\,\dot{\mathbf{E}}^p} \tag{6.9}$$

and

$$\Phi^D(\dot{D}; \mathbf{E}, \mathbf{E}^p, D) := \phi(\dot{D}; \mathbf{E}, \mathbf{E}^p, D) + I_{\mathbb{R}_+}(\dot{D}) \tag{6.10}$$

where

$$\phi(\dot{D}; \mathbf{E}, \mathbf{E}^p, D) := \begin{cases} h_+(\mathbf{E}, \mathbf{E}^p, D)\dot{D} & \text{if } n(\mathbf{E}, \mathbf{E}^p) > 0 \\ h_-(\mathbf{E}, \mathbf{E}^p, D)\dot{D} & \text{if } n(\mathbf{E}, \mathbf{E}^p) < 0 \end{cases}$$

$h_\pm$ are the tensile/compressive quasistatic damage energy thresholds, respectively, defined by

$$h_\pm(\mathbf{E}, \mathbf{E}^p, D) := \begin{cases} \dfrac{r^{D2}(D)}{2(1-D)^2}\dfrac{\mathbf{E}^p : \mathbb{S}\,\mathbf{E}^p}{\mathbb{S}\,\mathbf{E}^p : \mathbb{F}_\pm\mathbb{S}\,\mathbf{E}^p} & \text{if } ||\mathbf{E}^p|| > 0 \\ \dfrac{r^{D2}(D)}{2(1-D)^2}\dfrac{\mathbf{E} : \mathbb{S}\,\mathbf{E}}{\mathbb{S}\,\mathbf{E} : \mathbb{F}_\pm\mathbb{S}\,\mathbf{E}} & \text{if } ||\mathbf{E}^p|| = 0 \end{cases}$$

n is the tension/compression criterion defined below and $I_{\mathbb{R}_+}$ is the indicator function of $\mathbb{R}_+$. We repeat that the variables appearing after the semicolon symbol (;) in the dissipation potential are only parameters (Subsection 3.2.2, Remark 3.4).

Distinct tensile and compressive threshold damage stresses are obtained with a halfspacewise generalization of the Hill criterion. They appear in ϕ through the functions $h_\pm$ and the hyperplane $n(\mathbf{E}, \mathbf{E}^p) = 0$ dividing the strain space into tensile and compressive domains (previously defined for halfspacewise linear elasticity in (3.61), [Curnier et al., 1995]). The fourth-order tensors $\mathbb{F}_\pm$ play the role of the tensile/compressive elastic stiffnesses defined in Section 3.3 and define a non-symmetric non-damaging states set in damage stress space. $\sigma^p(D)$ and $r^D(D)$ are the radii of the plastic and damage criteria, respectively. Their dependency with D expresses the increase of stress during plastic flow and damage evolution. By analogy with the one-dimensional RI model (Subsection 4.1.1), we define *exponential hardening functions*:

$$\sigma^p(D) := \chi^p\big(1 - \exp\left(-lD\right)\big) \tag{6.11}$$

$$r^D(D) := R\Big(1 + \chi^D\big(1 - \exp\left(-kD\right)\big)\Big) \tag{6.12}$$

χ^p, l are plastic and χ^D and k damage hardening parameters, respectively. The constant R is an additional (redundant) parameter which could be incorporated in the definition of $\mathbb{F}_\pm$. It defines the initial radius of the damage criterion. We note that the same choice $\sigma^p(0) = 0$ done in the RI model is made.

The constitutive equations which derive from the dissipation potential are:

$$\mathbf{S}^p_\Phi \in \partial_{\dot{\mathbf{E}}^p}\Phi = \begin{cases} \sigma^p(D)\dfrac{\mathbb{S}\,\dot{\mathbf{E}}^p}{\sqrt{\dot{\mathbf{E}}^p\,:\,\mathbb{S}\,\dot{\mathbf{E}}^p}} & \text{if } ||\dot{\mathbf{E}}^p|| > 0 \\ \mathbf{S}^p \,|\, \sqrt{\mathbf{S}^p\,:\,\mathbb{C}\,\mathbf{S}^p} - \sigma^p(D) < 0 & \text{if } ||\dot{\mathbf{E}}^p|| = 0 \end{cases} \tag{6.13}$$

and

$$W^D_\Phi \in \partial_{\dot{D}}\Phi = \begin{cases} \phi'(\mathbf{E}, \mathbf{E}^p, D) & \text{if } \dot{D} > 0 \\ ]-\infty, \phi'(\mathbf{E}, \mathbf{E}^p, D)] & \text{if } \dot{D} = 0 \\ \emptyset & \text{if } \dot{D} < 0 \end{cases} \tag{6.14}$$

where ϕ' is the derivative of ϕ with respect to $\dot{D}$, representing thus the quasistatic damage energy thresholds $h_\pm$.
The dual dissipation potential is obtained via the same Legendre-Fenchel transform:

$$\Phi^*(\mathbf{S}^p, W^D; \mathbf{E}, \mathbf{E}^p, D) := \sup_{\dot{\mathbf{E}}^p, \dot{D}} \Big[\mathbf{S}^p : \dot{\mathbf{E}}^p + W^D\dot{D} - \Phi(\dot{\mathbf{E}}^p, \dot{D}; \mathbf{E}, \mathbf{E}^p, D)\Big]$$

We find:

$$\Phi^*(\mathbf{S}^p, W^D; \mathbf{E}, \mathbf{E}^p, D) = I_{[0,\sigma^p(D)]}(\sqrt{\mathbf{S}^p : \mathbb{C}\,\mathbf{S}^p}) + I_{[-\infty,\phi'(\mathbf{E},\mathbf{E}^p,D)]}(W^D) \tag{6.15}$$

The flow and evolution rules of the internal variables $\mathbf{E}^p$ and D are found from the dual dissipation potential (inverse complementary laws):

$$\dot{\mathbf{E}}^p \in \partial_{\mathbf{S}^p}\Phi^* = \begin{cases} \emptyset & \text{if } \sqrt{\mathbf{S}^p : \mathbb{C}\,\mathbf{S}^p} - \sigma^p(D) > 0 \\ \Lambda^p\,\dfrac{\mathbb{C}\,\mathbf{S}^p}{\sqrt{\mathbf{S}^p\,:\,\mathbb{C}\mathbf{S}^p}} & \text{if } \sqrt{\mathbf{S}^p : \mathbb{C}\,\mathbf{S}^p} - \sigma^p(D) = 0 \\ \mathbf{0} & \text{if } \sqrt{\mathbf{S}^p : \mathbb{C}\,\mathbf{S}^p} - \sigma^p(D) < 0 \end{cases} \tag{6.16}$$

with $\Lambda^p \in [0, +\infty[$ and

$$\dot{D} \in \partial_{W^D}\Phi^* = \begin{cases} 0 & \text{if } W^D \in]-\infty, \phi'(\mathbf{E}, \mathbf{E}^p, D)[\\ [0, +\infty[& \text{if } W^D = \phi'(\mathbf{E}, \mathbf{E}^p, D) \\ \emptyset & \text{if } W^D > \phi'(\mathbf{E}, \mathbf{E}^p, D) \end{cases} \tag{6.17}$$

6.1.3 Plastic and damage criteria

A more classical but equivalent way to express the flow and evolution rules of the internal variables is to define their corresponding criteria in stress or strain space and to associate them to adequate flow and evolution rules.

Plastic criterion

The relation (6.13) defines a convex elastic domain which can be characterized by the *plastic yield function* $Y^p(\mathbf{S}^p, D)$ defined by:

$$Y^p(\mathbf{S}^p; D) := \sqrt{\mathbf{S}^p : \mathbb{C}\,\mathbf{S}^p} - \sigma^p(D) \tag{6.18}$$

with $\sigma^p(D)$ given in (6.11).

The flow rule and the convex elastic domain can be expressed as:

$$\begin{aligned} &\dot{\mathbf{E}}^p = \Lambda^p\,\mathbf{N}^p(\mathbf{S}^p), \quad \mathbf{N}^p(\mathbf{S}^p) := \frac{\partial Y^p}{\partial \mathbf{S}^p}(\mathbf{S}^p) \\ &Y^p(\mathbf{S}^p, D) \le 0, \qquad \Lambda^p \ge 0, \quad \Lambda^p\,Y^p(\mathbf{S}^p, D) = 0 \end{aligned} \tag{6.19}$$

The first line of equations is the *associated flow rule* which defines the plastic strain rate direction as an outward normal (not unitary) to the convex elastic domain in stress space. The second line of inequalities expresses the plastic *yield* and *consistency* conditions (Kuhn-Tucker in optimization).

We restricted ourselves to the simplest anisotropic model for plasticity by choosing the elastic compliance tensor $\mathbb{C}$ to define the convex elastic domain (e.g. [Curnier, 1980, Zysset, 1994]).

Damage criterion

The relation (6.14) can be interpreted as a threshold function defining a non-damaging convex domain. For $||\mathbf{E}^p|| > 0$, we find:

$$Y^D(W^D; \mathbf{E}, \mathbf{E}^p, D) :=$$

$$:= \begin{cases} \sqrt{2(1-D)^2 W^D \frac{\mathbb{S}\,\mathbf{E}^p : \mathbb{F}_+ \mathbb{S}\,\mathbf{E}^p}{\mathbf{E}^p : \mathbb{S}\,\mathbf{E}^p}} - r^D(D) \le 0 \quad \text{if} \quad n(\mathbf{E}, \mathbf{E}^p) \ge 0 \\ \sqrt{2(1-D)^2 W^D \frac{\mathbb{S}\,\mathbf{E}^p : \mathbb{F}_- \mathbb{S}\,\mathbf{E}^p}{\mathbf{E}^p : \mathbb{S}\,\mathbf{E}^p}} - r^D(D) \le 0 \quad \text{if} \quad n(\mathbf{E}, \mathbf{E}^p) < 0 \end{cases} \tag{6.20}$$

and for $||\mathbf{E}^p|| = 0$, we have:

$$Y^D(W^D; \mathbf{E}, \mathbf{0}, D) :=$$
$$:= \begin{cases} \sqrt{2(1-D)^2 W^D \frac{\mathbb{S}\mathbf{E}:\mathbb{F}_+\mathbb{S}\mathbf{E}}{\mathbf{E}:\mathbb{S}\mathbf{E}}} - r^D(D) \leq 0 & \text{if} \quad n(\mathbf{E}, \mathbf{0}) \geq 0 \\ \sqrt{2(1-D)^2 W^D \frac{\mathbb{S}\mathbf{E}:\mathbb{F}_-\mathbb{S}\mathbf{E}}{\mathbf{E}:\mathbb{S}\mathbf{E}}} - r^D(D) \leq 0 & \text{if} \quad n(\mathbf{E}, \mathbf{0}) < 0 \end{cases} \tag{6.21}$$

which is strictly equivalent to:

$$Y^D(\mathbf{S}^D; D) := \begin{cases} \sqrt{\mathbf{S}^D : \mathbb{F}_+ \mathbf{S}^D} - r^D(D) \leq 0 & \text{if} \quad m(\mathbf{S}^D) \geq 0 \\ \sqrt{\mathbf{S}^D : \mathbb{F}_- \mathbf{S}^D} - r^D(D) \leq 0 & \text{if} \quad m(\mathbf{S}^D) < 0 \end{cases} \tag{6.22}$$

with $r^D(D)$ defined in (6.12) and $n(\mathbf{E}, \mathbf{E}^p)$ (resp. $m(\mathbf{S}^D)$) the function dividing the strain (resp. damage stress) space into tensile and compressive domains, (given by (3.61), resp. (3.63)). We recognize the form of the quadratic free energy potential presented in (3.59) for halfspacewise linear elasticity. The formulation (6.22) can be interpreted as a halfspacewise generalized Hill criterion ([Hill, 1950]).

Let $\hat{\mathbf{M}} := m_i \, \mathbf{M}_i$ be the second-order fabric tensor of cortical bone describing its structural anisotropy, previously defined for orthotropic morphologic based elasticity (Section 3.3, Equation (3.66)). $\mathbf{M}_i := \mathbf{m}_i \otimes \mathbf{m}_i$ are the structural tensors. Combining the orthotropic formulations of halfspacewise linear and morphology based elasticity, one gets the general forms of the fourth-order tensors $\mathbb{F}_\pm$ derived by [Zysset and Rincón, 2005]:

$$\mathbb{F}_+ = \sum_{i=1}^{3} \frac{1}{(\sigma_{ii}^+)^2} \mathbf{M}_i \otimes \mathbf{M}_i - \sum_{i,j=1}^{3}{}' \frac{\chi_{ij}^+}{(\sigma_{ii}^+)^2} \mathbf{M}_i \otimes \mathbf{M}_j + \sum_{i,j=1}^{3}{}' \frac{1}{2\tau_{ij}^2} \mathbf{M}_i \underline{\overline{\otimes}} \mathbf{M}_j \tag{6.23}$$

$$\mathbb{F}_- = \sum_{i=1}^{3} \frac{1}{(\sigma_{ii}^-)^2} \mathbf{M}_i \otimes \mathbf{M}_i - \sum_{i,j=1}^{3}{}' \frac{\chi_{ij}^-}{(\sigma_{ii}^-)^2} \mathbf{M}_i \otimes \mathbf{M}_j + \sum_{i,j=1}^{3}{}' \frac{1}{2\tau_{ij}^2} \mathbf{M}_i \underline{\overline{\otimes}} \mathbf{M}_j \tag{6.24}$$

where $\sum'$ denotes a sum on $i \neq j$. $\sigma_{ii}^+(\rho_s, m_1, m_2, m_3)$ and $\sigma_{ii}^-(\rho_s, m_1, m_2, m_3)$ are the uniaxial tensile and compressive strengths along the axis of index $i = 1, 2, 3$, $\tau_{ij}(\rho_s, m_1, m_2, m_3)$ are the shear strengths in the plane of index $i, j = 1, 2, 3$; $i \neq j$, $\chi_{ij}^+(\rho_s, m_1, m_2, m_3)$ and $\chi_{ij}^-(\rho_s, m_1, m_2, m_3)$ are stress interaction coefficients. Following the approach used in fabric elasticity ([Zysset and Curnier, 1995]), power functions are selected for the dependence of the material properties with volume fraction and fabric eigenvalues:

$$\begin{array}{lll} \sigma_{ii}^+ = \sigma_0^+ \rho_s^p m_i^{2q} & \sigma_{ii}^- = \sigma_0^- \rho_s^p m_i^{2q} & \tau_{ij} = \tau_0 \rho_s^p m_i^q m_j^q \\ \chi_{ij}^+ = \chi_0^+ \frac{m_i^{2q}}{m_j^{2q}} & \chi_{ij}^- = \chi_0^- \frac{m_i^{2q}}{m_j^{2q}} & \end{array} \tag{6.25}$$

where σ_0^+ and σ_0^- are the uniaxial tensile and compressive strengths, τ_0 is the shear strength, χ_0^+ and χ_0^- are interaction coefficients for a poreless ($\rho_s = 1$) bone material with at least cubic symmetry ($m_1 = m_2 = m_3 = 1$).
The continuity relation (3.60) (or (3.64)) between $\mathbb{F}_+$ and $\mathbb{F}_-$ leads to:

$$\frac{\chi_0^- + 1}{(\sigma_0^-)^2} = \frac{\chi_0^+ + 1}{(\sigma_0^+)^2} \tag{6.26}$$

For arbitrary volume fraction and fabric, positive definiteness conditions of the fourth-order tensors lead to the constraints:

$$\begin{array}{lll} \sigma_0^+ \geq 0 & \sigma_0^- \geq 0 & \tau_0 \geq 0 \\ \frac{1}{2} \geq \chi_0^+ \geq -1 & & \frac{1}{2} \geq \chi_0^- \geq -1 \end{array} \tag{6.27}$$

Given volume fraction and fabric values, the set of six material constants defining the halfspacewise damage criterion has been identified for trabecular bone by [Rincón, 2003, Zysset and Rincón, 2005]. In view of the similar composition and damage accumulation mechanisms of the extracellular matrix of trabecular and cortical bone, we use the same values of the identified parameters for cortical bone and change only the initial global radius $r^D(0)$ of the criterion. This assumption should be verified on experimental grounds.
The shape of the halfspacewise damage criterion is illustrated in Figure 6.2.

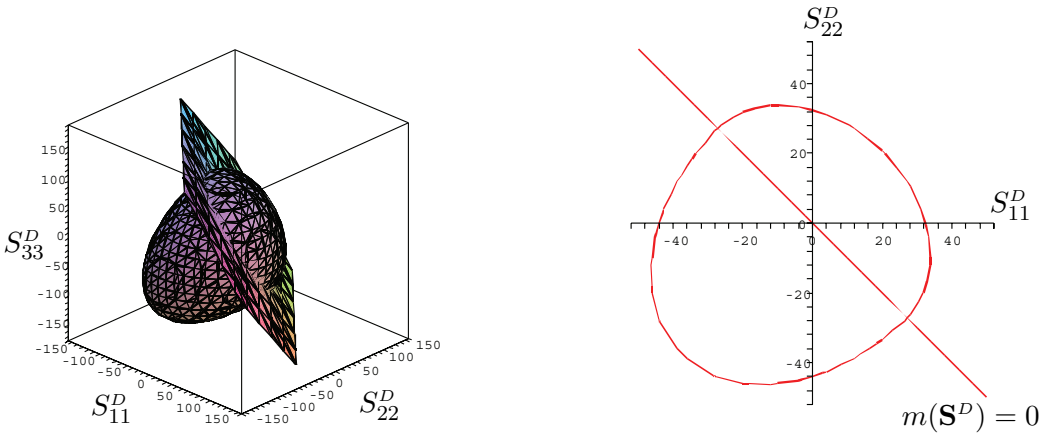

Figure 6.2: Left: Shape of damage threshold criterion in the space of principal damage stresses with respect to the orthotropic planes of symmetry of cortical bone Right: its intersection with the plane $S_{33}^D = 0$. The hyperplane $m(\mathbf{S}^D) = 0$ divides the damage stress space into tensile and compressive domains.

6.2 Numerical algorithm

In order to implement it in a finite element mechanical analysis program, the elastic plastic damage evolution law needs to be discretized in time (e.g. [Doghri, 1993, Mahnken et al., 2000]).

6.2.1 Time integration algorithm with projection

Assume that we have an *initial strain state* to start with

$$\mathbf{E}_0, \mathbf{E}_0^p, D_0 \quad \text{(to which corresponds the } \textit{initial stress state } \mathbf{S}_0, \mathbf{S}_0^p, W_0^D)$$

and that this state is *plastically and damageably admissible* in the sense that it satisfies both plastic and damage criteria:

$$Y^p(\mathbf{S}_0^p, D_0) \leq 0 \quad \text{and} \quad Y^D(W_0^D; \mathbf{E}_0, \mathbf{E}_0^p, D_0) \leq 0$$

Given a new total strain $\mathbf{E}$, integrating the flow rule consists of finding a new plastic strain $\mathbf{E}^p$ and a new damage state variable D such that the *final state* defined by:

$$\mathbf{E}, \mathbf{E}^p, D \quad \text{(and corresponding } \textit{final stress state } \mathbf{S}, \mathbf{S}^p, W^D)$$

will also be plastically and damageably admissible i.e.

$$Y^p(\mathbf{S}^p, D) \leq 0 \quad \text{and} \quad Y^D(W^D; \mathbf{E}, \mathbf{E}^p, D) \leq 0$$

To this end, a *trial state* is first considered in the form:

$$\mathbf{E}, \mathbf{E}_0^p, D_0 \quad \text{(and corresponding } \textit{trial stress state } \mathbf{S}_{\text{T}}, \mathbf{S}_{\text{T}}^p, W_{\text{T}}^D)$$

which can be non-admissible. The final state is then reached by projecting the trial state on the convex plastic and damage sets enclosed by the corresponding yield and threshold surfaces.

As in the one-dimensional case, $\mathbf{S}_{\text{T}}^p$ and W_{T}^D are undefined for $D_0 = 0$. Thus, the following *global* damage criterion must be used to detect the onset of damage:

$$Y(\mathbf{S}_{\text{T}}) := \begin{cases} \sqrt{\mathbf{S}_{\text{T}} : \mathbb{F}_+ \, \mathbf{S}_{\text{T}}} - r^D(0) & \text{if } m(\mathbf{S}_{\text{T}}) \geq 0 \\ \sqrt{\mathbf{S}_{\text{T}} : \mathbb{F}_- \, \mathbf{S}_{\text{T}}} - r^D(0) & \text{if } m(\mathbf{S}_{\text{T}}) < 0 \end{cases}$$

As for the one-dimensional models, we divide the analysis into three steps.

a) Elastic mode: $Y^p(\mathbf{S}^p_{\mathrm{T}}, D_0) \leq 0$ **and** $Y^D(W^D_{\mathrm{T}}; \mathbf{E}, \mathbf{E}^p_0, D_0) \leq 0$

In this case, we simply have $\mathbf{E}^p = \mathbf{E}^p_0$ and $D = D_0$.

b) Plastic mode: $Y^p(\mathbf{S}^p_{\mathrm{T}}, D_0) > 0$ **and** $Y^D(W^D_{\mathrm{T}}; \mathbf{E}, \mathbf{E}^p_0, D_0) \leq 0$

In this case, we only must satisfy $Y^p(\mathbf{S}^p, D) = 0$. The relation between the initial and new plastic strains is given by the incremental flow rule for $\mathrm{d}\mathbf{E}^p$:

$$\mathrm{d}\mathbf{E}^p = \lambda^p \, \mathbf{N}^p(\mathbf{S}^p) \tag{6.28}$$

where $\mathbf{N}^p(\mathbf{S}^p)$ is the normal of the plastic criterion evaluated at the final unknown stress state $\mathbf{S}^p$. Therefore it is an *implicit projection algorithm* (e.g. [Curnier, 1993, Matzenmiller and Taylor, 1994, Simo and Hughes, 1999]). As

$$\mathbf{E}^p = \mathbf{E}^p_0 + \mathrm{d}\mathbf{E}^p \tag{6.29}$$

and

$$D = D_0 \tag{6.30}$$

we have:

$$\mathbf{S}^p = \mathbf{S}^p_{\mathrm{T}} - \frac{1}{D_0} \, \mathbb{S} \, \mathrm{d}\mathbf{E}^p$$

Furthermore,

$$\mathbf{N}^p(\mathbf{S}^p) = \frac{\mathbb{C} \, \mathbf{S}^p}{\sqrt{\mathbf{S}^p : \mathbb{C} \, \mathbf{S}^p}} = \frac{\mathbb{C} \, \mathbf{S}^p}{\sigma^p(D_0)} \tag{6.31}$$

thus

$$\mathbf{S}^p_{\mathrm{T}} = \left(1 + \frac{\lambda^p}{D_0 \, \sigma^p(D_0)} \right) \mathbf{S}^p \tag{6.32}$$

and

$$\sqrt{\mathbf{S}^p_{\mathrm{T}} : \mathbb{C} \, \mathbf{S}^p_{\mathrm{T}}} = \left(1 + \frac{\lambda^p}{D_0 \, \sigma^p(D_0)} \right) \underbrace{\sqrt{\mathbf{S}^p : \mathbb{C} \, \mathbf{S}^p}}_{\sigma^p(D_0)}$$

We finally get the analytical expression for the plastic multiplier:

$$\lambda^p = D_0 \, Y^p(\mathbf{S}^p_{\mathrm{T}}, D_0) \tag{6.33}$$

As the final plastic stress is collinear to the trial stress, the projection is *radial* ([Wilkins, 1964, Moreau, 1979]).

c) Damage mode: $Y^p(\mathbf{S}^p_{\mathrm{T}}, D_0) > 0$ and $Y^D(W^D_{\mathrm{T}}; \mathbf{E}, \mathbf{E}^p_0, D_0) > 0$

In this case, we must satisfy simultaneously:

$$\begin{cases} Y^p(\mathbf{S}^p, D) = 0 \quad \text{and} \\ Y^D(W^D; \mathbf{E}, \mathbf{E}^p, D) = 0 \end{cases}$$

Once more, we compute the final plastic strain with the incremental flow rule for $\mathrm{d}\mathbf{E}^p$:

$$\mathrm{d}\mathbf{E}^p = \lambda^p \, \mathbf{N}^p(\mathbf{S}^p) \tag{6.34}$$

We have

$$\mathbf{E}^p = \mathbf{E}^p_0 + \mathrm{d}\mathbf{E}^p \tag{6.35}$$

and

$$D = D_0 + \mathrm{d}D \tag{6.36}$$

As

$$\mathbf{N}^p(\mathbf{S}^p) = \frac{\mathbb{C}\,\mathbf{S}^p}{\sqrt{\mathbf{S}^p : \mathbb{C}\,\mathbf{S}^p}} = \frac{\mathbb{C}\,\mathbf{S}^p}{\sigma^p(D)} = \frac{\mathbf{E} - \frac{1}{D}\mathbf{E}^p}{\sigma^p(D)}$$

we get

$$\mathbf{E}^p = \frac{D\,\sigma^p(D)}{\lambda^p + D\,\sigma^p(D)}\,\mathbf{E}^p_0 + \frac{\lambda^p D}{\lambda^p + D\,\sigma^p(D)}\,\mathbf{E} \tag{6.37}$$

and

$$\mathbf{S}^p = \frac{\sigma^p(D)}{\lambda^p + D\,\sigma^p(D)}\,\mathbb{S}\,(D\mathbf{E} - \mathbf{E}^p_0) \tag{6.38}$$

Injecting the final plastic stress (6.38) in the plastic criterion, we get the following expression for the plastic multiplier:

$$\lambda^p = \sqrt{(D\mathbf{E} - \mathbf{E}^p_0) : \mathbb{S}\,(D\mathbf{E} - \mathbf{E}^p_0)} - D\,\sigma^p(D) \tag{6.39}$$

The final damage state variable D remains to be found. To this end, we use the projection of W^D_{T} (or equivalently of $\mathbf{S}^D_{\mathrm{T}}$) on the damage criterion.
With (6.37), we have:

$$\mathbf{S}^D = \frac{1 - D}{\lambda^p + D\,\sigma^p(D)}\left(\lambda^p\,\mathbb{S}\,\mathbf{E} + \sigma^p(D)\,\mathbb{S}\,\mathbf{E}^p_0\right)$$

Let us define the function $f_\pm : [0, 1[\to \mathbb{R}$ by:

$$\begin{aligned} f_\pm(D) &:= \mathbf{S}^D : \mathbb{F}_\pm\,\mathbf{S}^D - r^{D2}(D) = \\ &= \left(\frac{1 - D}{\lambda^p + D\,\sigma^p(D)}\right)^2 \left(\lambda^{p2}\,\mathbb{S}\,\mathbf{E} : \mathbb{F}_\pm\mathbb{S}\,\mathbf{E} + 2\lambda^p\sigma^p(D)\,\mathbb{S}\,\mathbf{E} : \mathbb{F}_\pm\mathbb{S}\,\mathbf{E}^p_0 + \right. \\ &\quad \left. + \sigma^{p2}(D)\,\mathbb{S}\,\mathbf{E}^p_0 : \mathbb{F}_\pm\mathbb{S}\,\mathbf{E}^p_0\right) - r^{D2}(D) \end{aligned} \tag{6.40}$$

with $\mathbb{F}_+$ for $m(\mathbf{S}_{\mathrm{T}}^D) > 0$ and $\mathbb{F}_-$ for $m(\mathbf{S}_{\mathrm{T}}^D) < 0$, respectively, and $\lambda^p = \lambda^p(D)$ given by (6.39). In order to find the value of D, we have to solve $f_\pm(D) = 0$ where $\mathbf{E}$ is assumed to be known (predicted).
The derivative of $f_\pm$ reads:

$$f'_\pm(D) = 2\left(\frac{1-D}{\lambda^p + D\,\sigma^p(D)}\right)\left(\frac{-\lambda^p - (1-D)\lambda^{p\prime} - \sigma^p(D) - (1-D)D\,\sigma^{p\,\prime}(D)}{(\lambda^p + D\,\sigma^p(D))^2}\right)\cdot$$
$$\cdot\left(\lambda^{p2}\,A + 2\lambda^p\sigma^p(D)\,B + \sigma^{p2}(D)\,C\right) + 2\left(\frac{1-D}{\lambda^p + D\,\sigma^p(D)}\right)^2\Big(\lambda^p\lambda^{p\prime}\,A +$$
$$+\left(\lambda^{p\prime}\sigma^p(D) + \lambda^p\sigma^{p\,\prime}(D)\right)B + \sigma^p(D)\sigma^{p\,\prime}(D)\,C\Big) - 2r^D(D)r^{D\prime}(D) \tag{6.41}$$

where $\lambda^{p\prime} = \dfrac{\mathrm{d}\lambda^p}{\mathrm{d}D} = \dfrac{\mathbf{E}:\mathbb{S}(D\mathbf{E}-\mathbf{E}_0^p)}{\sqrt{(D\mathbf{E}-\mathbf{E}_0^p):\mathbb{S}(D\mathbf{E}-\mathbf{E}_0^p)}} - \sigma^p(D) - D\,\sigma^{p\,\prime}(D)$, $A = \mathbb{S}\,\mathbf{E} : \mathbb{F}_\pm\mathbb{S}\,\mathbf{E}$, $B = \mathbb{S}\,\mathbf{E} : \mathbb{F}_\pm\mathbb{S}\,\mathbf{E}_0^p$ and $C = \mathbb{S}\,\mathbf{E}_0^p : \mathbb{F}_\pm\mathbb{S}\,\mathbf{E}_0^p$.

We can use the generalized Newton method ([Alart and Curnier, 1991]) to solve this nonsmooth C^0 nonlinear equation:

$$D^{j+1} = D^j - \frac{f_\pm(D^j)}{f_\pm{}'(D^j)} \quad \text{with} \quad j = 0, 1, 2, \ldots \quad \text{and} \quad D^0 = D_0 \tag{6.42}$$

6.2.2 Incremental linearization algorithm

For a uniform deformation test with a homogeneous stress state, a situation occurring in a single finite element (Section 6.3), the problem is equivalent to the following *local* problem: find $\mathbf{E}$ such that the equation of force equilibrium is satisfied i.e.:

$$\mathbf{S}(\mathbf{E}, \mathbf{E}^p, D) - \bar{\mathbf{S}} = 0$$

where $\bar{\mathbf{S}}$ denotes the imposed stress. We also use the generalized Newton method to solve this problem:

$$\mathbf{E}^{i+1} = \mathbf{E}^i + \mathrm{d}\mathbf{E}^i \quad \text{with} \quad i = 0, 1, 2, \ldots \tag{6.43}$$

where

$$\mathrm{d}\mathbf{E}^i = -\mathbb{P}^{-1}(\mathbf{E}^i, \mathbf{E}^p, D)\left(\mathbf{S}(\mathbf{E}^i, \mathbf{E}^p, D) - \bar{\mathbf{S}}\right) \tag{6.44}$$

and $\mathbb{P} := \frac{\mathrm{d}\mathbf{S}}{\mathrm{d}\mathbf{E}}$ is the total stress derivative with respect to the strain. That means that the determination of $\mathbf{E}$ requires the computation of the tangent operator $\mathbb{P}$. Two different tangent operators can be defined depending on the

type of flow and evolution rules which are linearized. The linearization of the *continuum* rules leads to the *continuous tangent operator* whereas the linearization of the *incremental* rules leads to the *algorithmic tangent operator*. Their analytic expressions are derived in the following two Subsections.

6.2.3 Continuous tangent operator

In this Subsection, we compute the *continuous tangent operator* $\mathbb{P} := \frac{\mathrm{d}\mathbf{S}}{\mathrm{d}\mathbf{E}}$ required by the Newton method (6.43) for the three evolution modes of the model ($\mathbb{P}^e$ for the elastic, $\mathbb{P}^p$ for the plastic and $\mathbb{P}^D$ for the damage mode, respectively). The word continuous refers to a velocity-based definition of the tangent operator ($\mathrm{d}\mathbf{E} \to \mathbf{0}$), opposed to an incremental definition. The continuum tangent operator corresponds to the linearization of the continuum flow and evolution rules.

a) Elastic mode: case $\dot{\mathbf{E}}^p = \mathbf{0}$ and $\dot{D} = 0$

As $\mathrm{d}\mathbf{E}^p = \mathbf{0}$ in this mode and $\mathbf{S} = \mathbb{S}\,(\mathbf{E} - \mathbf{E}^p)$, we have $\mathrm{d}\mathbf{S} = \mathbb{S}\,\mathrm{d}\mathbf{E}$. Thus

$$\mathbb{P}^e = \mathbb{S} \tag{6.45}$$

b) Plastic mode: case $\dot{\mathbf{E}}^p \neq \mathbf{0}$ and $\dot{D} = 0$

For this mode, we must find the relation $\mathrm{d}\mathbf{S} = \mathbb{P}^p\,\mathrm{d}\mathbf{E}$ for $\mathrm{d}\mathbf{E}^p \neq \mathbf{0}$ and $\mathrm{d}D = 0$. To this end, let us determine $\mathrm{d}\mathbf{E}^p(\mathrm{d}\mathbf{E})$.
From $\mathbf{S}^p = \mathbb{S}\,\mathbf{E} - \frac{1}{D}\,\mathbb{S}\,\mathbf{E}^p$, we have:

$$\mathrm{d}\mathbf{S}^p = \mathbb{S}\,\mathrm{d}\mathbf{E} - \frac{1}{D}\,\mathbb{S}\,\mathrm{d}\mathbf{E}^p \tag{6.46}$$

Furthermore, $Y^p(\mathbf{S}^p, D) = 0$. Thus

$$\mathrm{d}Y^p = \mathbf{N}^p(\mathbf{S}^p) : \mathrm{d}\mathbf{S}^p = 0 \tag{6.47}$$

where $\mathbf{N}^p(\mathbf{S}^p) := \frac{\partial Y^p}{\partial \mathbf{S}^p}$. Combining (6.46) and (6.47), we get:

$$\mathbf{N}^p(\mathbf{S}^p) : \mathbb{S}\,\mathrm{d}\mathbf{E} = \frac{1}{D}\,\mathbf{N}^p(\mathbf{S}^p) : \mathbb{S}\,\mathrm{d}\mathbf{E}^p$$

The incremental flow rule imposes that $\mathrm{d}\mathbf{E}^p = \lambda^p\,\mathbf{N}^p(\mathbf{S}^p)$. Therefore, we have:

$$\lambda^p = D\,\frac{\mathbf{N}^p(\mathbf{S}^p) : \mathbb{S}\,\mathrm{d}\mathbf{E}}{\mathbf{N}^p(\mathbf{S}^p) : \mathbb{S}\,\mathbf{N}^p(\mathbf{S}^p)}$$

or equivalently:

$$\mathrm{d}\mathbf{E}^p = D\,\frac{\mathbf{N}^p(\mathbf{S}^p)\otimes\mathbb{S}\,\mathbf{N}^p(\mathbf{S}^p)}{\mathbf{N}^p(\mathbf{S}^p):\mathbb{S}\,\mathbf{N}^p(\mathbf{S}^p)}\,\mathrm{d}\mathbf{E} \tag{6.48}$$

As $\mathrm{d}\mathbf{S} = \mathbb{S}\,\mathrm{d}\mathbf{E} - \mathbb{S}\,\mathrm{d}\mathbf{E}^p$, we finally get:

$$\mathbb{P}^p = \mathbb{S} - D\,\frac{\mathbb{S}\,\mathbf{N}^p(\mathbf{S}^p)\otimes\mathbb{S}\,\mathbf{N}^p(\mathbf{S}^p)}{\mathbf{N}^p(\mathbf{S}^p):\mathbb{S}\,\mathbf{N}^p(\mathbf{S}^p)} \tag{6.49}$$

Remark 6.2 *The plastic stiffness tensor is a rank-1 modification of the elasticity tensor as usual, but this modification is scaled by the damage intensity D.*

c) Damage mode: case $\dot{\mathbf{E}}^p \neq \mathbf{0}$ and $\dot{D} > 0$

For this mode, we must find the relation $\mathrm{d}\mathbf{S} = \mathbb{P}^D\,\mathrm{d}\mathbf{E}$ for $\mathrm{d}\mathbf{E}^p \neq \mathbf{0}$ and $\mathrm{d}D \neq 0$. To this end, let us determine $\mathrm{d}\mathbf{E}^p(\mathrm{d}\mathbf{E})$.
From $\mathbf{S}^p = \mathbb{S}\,\mathbf{E} - \frac{1}{D}\,\mathbb{S}\,\mathbf{E}^p$, we have:

$$\mathrm{d}\mathbf{S}^p = \mathbb{S}\,\mathrm{d}\mathbf{E} - \frac{1}{D}\,\mathbb{S}\,\mathrm{d}\mathbf{E}^p + \frac{\mathrm{d}D}{D^2}\,\mathbb{S}\,\mathbf{E}^p \tag{6.50}$$

Furthermore, $Y^p(\mathbf{S}^p, D) = 0$. Thus

$$\mathrm{d}Y^p = \mathbf{N}^p(\mathbf{S}^p):\mathrm{d}\mathbf{S}^p + \frac{\partial Y^p}{\partial D}\,\mathrm{d}D = 0 \tag{6.51}$$

Combining (6.50) and (6.51), we get:

$$\mathbf{N}^p(\mathbf{S}^p):\mathbb{S}\,\mathrm{d}\mathbf{E} = \frac{1}{D}\,\mathbf{N}^p(\mathbf{S}^p):\mathbb{S}\,\mathrm{d}\mathbf{E}^p - \left[\frac{\partial Y^p}{\partial D} + \frac{\mathbf{N}^p(\mathbf{S}^p):\mathbb{S}\,\mathbf{E}^p}{D^2}\right]\mathrm{d}D$$

The incremental flow rule imposes that $\mathrm{d}\mathbf{E}^p = \lambda^p\,\mathbf{N}^p(\mathbf{S}^p)$. Therefore, we have:

$$\mathbf{N}^p(\mathbf{S}^p):\mathbb{S}\,\mathrm{d}\mathbf{E} = \frac{\lambda^p}{D}\,\mathbf{N}^p(\mathbf{S}^p):\mathbb{S}\,\mathbf{N}^p(\mathbf{S}^p) - \left[\frac{\partial Y^p}{\partial D} + \frac{\mathbf{N}^p(\mathbf{S}^p):\mathbb{S}\,\mathbf{E}^p}{D^2}\right]\mathrm{d}D \tag{6.52}$$

$\mathrm{d}D$ is found by projection of $\mathbf{S}^D$ on the damage criterion. As $Y^D(\mathbf{S}^D, D) = 0$, we have:

$$\mathrm{d}Y^D = \mathbf{N}^D(\mathbf{S}^D):\mathrm{d}\mathbf{S}^D + \frac{\partial Y^D}{\partial D}\,\mathrm{d}D = 0 \tag{6.53}$$

where $\mathbf{N}^D(\mathbf{S}^D) := \dfrac{\partial Y^D}{\partial \mathbf{S}^D}$. Furthermore, $\mathbf{S}^D = \dfrac{1-D}{D}\,\mathbb{S}\,\mathbf{E}^p$. Thus

$$\mathrm{d}\mathbf{S}^D = \frac{1-D}{D}\,\mathbb{S}\,\mathrm{d}\mathbf{E}^p - \frac{\mathrm{d}D}{D^2}\,\mathbb{S}\,\mathbf{E}^p \tag{6.54}$$

Combining (6.53) and (6.54), we get:

$$\mathrm{d}D = \frac{\frac{1-D}{D}\,\mathbf{N}^D(\mathbf{S}^D) : \mathbb{S}\,\mathrm{d}\mathbf{E}^p}{\frac{\mathbf{N}^D(\mathbf{S}^D):\mathbb{S}\,\mathbf{E}^p}{D^2} - \frac{\partial Y^D}{\partial D}} \tag{6.55}$$

Using the incremental flow rule for $\mathrm{d}\mathbf{E}^p$ and injecting (6.55) into (6.52), we get:

$$\begin{aligned}\lambda^p = (D\,\mathbf{N}^p(\mathbf{S}^p) : \mathbb{S}\,\mathrm{d}\mathbf{E})\,\big[\mathbf{N}^p(\mathbf{S}^p) : \mathbb{S}\,\mathbf{N}^p(\mathbf{S}^p) + \\ + (1-D)\frac{D^2\frac{\partial Y^p}{\partial D} + \mathbf{N}^p(\mathbf{S}^p) :: \mathbb{S}\,\mathbf{E}^p}{D^2\frac{\partial Y^D}{\partial D} - \mathbf{N}^D(\mathbf{S}^D) :: \mathbb{S}\,\mathbf{E}^p}\,\mathbf{N}^D(\mathbf{S}^D) :: \mathbb{S}\,\mathbf{N}^p(\mathbf{S}^p)\big]^{-1}\end{aligned}$$

or equivalently:

$$\begin{aligned}\mathrm{d}\mathbf{E}^p = D\,\mathbf{N}^p(\mathbf{S}^p) \otimes \mathbb{S}\,\mathbf{N}^p(\mathbf{S}^p)\big[\mathbf{N}^p(\mathbf{S}^p) : \mathbb{S}\,\mathbf{N}^p(\mathbf{S}^p) + \\ + (1-D)\frac{D^2\frac{\partial Y^p}{\partial D} + \mathbf{N}^p(\mathbf{S}^p) :: \mathbb{S}\,\mathbf{E}^p}{D^2\frac{\partial Y^D}{\partial D} - \mathbf{N}^D(\mathbf{S}^D) :: \mathbb{S}\,\mathbf{E}^p}\,\mathbf{N}^D(\mathbf{S}^D) :: \mathbb{S}\,\mathbf{N}^p(\mathbf{S}^p)\big]^{-1}\,\mathrm{d}\mathbf{E}\end{aligned} \tag{6.56}$$

As $\mathrm{d}\mathbf{S} = \mathbb{S}\,\mathrm{d}\mathbf{E} - \mathbb{S}\,\mathrm{d}\mathbf{E}^p$, we finally get:

$$\begin{aligned}\mathbb{P}^D = \mathbb{S} - D\,\big[\mathbf{N}^p(\mathbf{S}^p) : \mathbb{S}\,\mathbf{N}^p(\mathbf{S}^p) + (1-D)\frac{D^2\frac{\partial Y^p}{\partial D} + \mathbf{N}^p(\mathbf{S}^p) :: \mathbb{S}\,\mathbf{E}^p}{D^2\frac{\partial Y^D}{\partial D} - \mathbf{N}^D(\mathbf{S}^D) :: \mathbb{S}\,\mathbf{E}^p}\cdot \\ \cdot\mathbf{N}^D(\mathbf{S}^D) :: \mathbb{S}\,\mathbf{N}^p(\mathbf{S}^p)\big]^{-1}\,\mathbb{S}\,\mathbf{N}^p(\mathbf{S}^p) \otimes \mathbb{S}\,\mathbf{N}^p(\mathbf{S}^p)\end{aligned} \tag{6.57}$$

Remark 6.3 *The damage stiffness tensor is again a scaled rank-1 modification of the elasticity tensor, but the scaling factor is more complicated. The damage continuum tangent operator is symmetric.*

6.2.4 Incremental tangent operator

The *incremental* or *algorithmic* form $\mathbb{P}_a$ of the continuous tangent operator $\mathbb{P}$ has to be determined for any discretized computer implementation of the constitutive law ([Simo and Taylor, 1985]). In that case, the total strain increment $\mathrm{d}\mathbf{E}$ does not tend to zero but must be computed as:

$$\mathrm{d}\mathbf{E} = \mathrm{d}(\mathbf{E} - \mathbf{E}_0^p)$$

The old plastic strain is taken as a kind of origin. The incremental tangent operator corresponds to the linearization of the incremental flow rule (or of the incremental implicit projection algorithm) (e.g. [Hartmann and Haupt, 1993]). Once again, we proceed in three steps.

a) Elastic mode: case $\mathrm{d}\mathbf{E}^p = \mathbf{0}$ and $\mathrm{d}D = 0$

In this case, $\mathrm{d}(\mathbf{E}^p - \mathbf{E}_0^p) = \mathbf{0}$ thus $\mathrm{d}\mathbf{S} = \mathbb{S}\,\mathrm{d}(\mathbf{E} - \mathbf{E}_0^p)$.
As in the continuous case, we have:

$$\mathbb{P}_a^e = \mathbb{P}^e = \mathbb{S} \tag{6.58}$$

b) Plastic mode: case $\mathrm{d}\mathbf{E}^p \neq 0$ and $\mathrm{d}D = 0$

As $\mathbf{S} = \mathbb{S}(\mathbf{E} - \mathbf{E}^p)$, we have:

$$\mathrm{d}\mathbf{S} = \mathbb{S}\,\mathrm{d}(\mathbf{E} - \mathbf{E}_0^p) - \mathbb{S}\,\mathrm{d}(\mathbf{E}^p - \mathbf{E}_0^p) \tag{6.59}$$

Furthermore, $\mathbf{S}^p = \mathbb{S}\,\mathbf{E} - \dfrac{1}{D}\,\mathbb{S}\,\mathbf{E}^p$. Thus

$$\mathrm{d}\mathbf{S}^p = \mathbb{S}\,\mathrm{d}(\mathbf{E} - \mathbf{E}_0^p) - \frac{1}{D}\,\mathbb{S}\,\mathrm{d}(\mathbf{E}^p - \mathbf{E}_0^p) \tag{6.60}$$

The incremental flow rule for $\mathrm{d}\mathbf{E}^p$ can be written as:

$$\mathrm{d}(\mathbf{E}^p - \mathbf{E}_0^p) = \mathrm{d}(\lambda^p\,\mathbf{N}^p(\mathbf{S}^p)) = \mathrm{d}\lambda^p\,\mathbf{N}^p(\mathbf{S}^p) + \lambda^p\,\mathbb{H}^p(\mathbf{S}^p)\mathrm{d}\mathbf{S}^p \tag{6.61}$$

where $\mathbb{H}^p(\mathbf{S}^p) := \dfrac{\partial^2 Y^p}{\partial \mathbf{S}^{p2}}$. Combining equations (6.60) and (6.61), we get:

$$\mathrm{d}\mathbf{S}^p = \mathbb{S}_a\,\mathrm{d}(\mathbf{E} - \mathbf{E}_0^p) - \frac{\mathrm{d}\lambda^p}{D}\,\mathbb{S}_a\,\mathbf{N}^p(\mathbf{S}^p) \tag{6.62}$$

where $\mathbb{S}_a := \left[\mathbb{C} + \dfrac{\lambda^p}{D}\,\mathbb{H}^p(\mathbf{S}^p)\right]^{-1}$.
As $Y^p(\mathbf{S}^p, D) = 0$, we have:

$$\mathrm{d}Y^p = \mathbf{N}^p(\mathbf{S}^p) : \mathrm{d}\mathbf{S}^p = 0$$

Together with (6.62), we get:

$$\mathrm{d}\lambda^p = D\,\frac{\mathbf{N}^p(\mathbf{S}^p) :\, \mathbb{S}_a\,\mathrm{d}(\mathbf{E} - \mathbf{E}_0^p)}{\mathbf{N}^p(\mathbf{S}^p) :\, \mathbb{S}_a\,\mathbf{N}^p(\mathbf{S}^p)}$$

or

$$\mathrm{d}\mathbf{S}^p = \mathbb{S}_a\,\mathrm{d}(\mathbf{E} - \mathbf{E}_0^p) - \frac{\mathbb{S}_a\,\mathbf{N}^p(\mathbf{S}^p) \otimes \mathbb{S}_a\,\mathbf{N}^p(\mathbf{S}^p)}{\mathbf{N}^p(\mathbf{S}^p) : \mathbb{S}_a\,\mathbf{N}^p(\mathbf{S}^p)}\,\mathrm{d}(\mathbf{E} - \mathbf{E}_0^p)$$

Furthermore, $\mathbf{S} = \mathbf{S}^p + \mathbf{S}^D$, where $\mathbf{S}^D = \dfrac{1-D}{D}\,\mathbb{S}\,\mathbf{E}^p$. Thus $\mathrm{d}\mathbf{S} = \mathrm{d}\mathbf{S}^p + \mathrm{d}\mathbf{S}^D$.
Equation (6.59) allows us to write:

$$\mathrm{d}\mathbf{S}^D = \frac{1-D}{D}\,\mathbb{S}\,\mathrm{d}(\mathbf{E}^p - \mathbf{E}_0^p) = \frac{1-D}{D}\,\mathbb{S}\,[\mathrm{d}(\mathbf{E} - \mathbf{E}_0^p) - \mathbb{C}\,\mathrm{d}\mathbf{S}]$$

Thus, we finally get $\mathrm{d}\mathbf{S} = (1-D)\,\mathbb{S}\,\mathrm{d}(\mathbf{E}-\mathbf{E}_0^p) + D\,\mathrm{d}\mathbf{S}^p$ or:

$$\mathbb{P}_a^p = (1-D)\,\mathbb{S} + D\,\left[\mathbb{S}_a - \frac{\mathbb{S}_a\,\mathbf{N}^p(\mathbf{S}^p)\otimes\mathbb{S}_a\,\mathbf{N}^p(\mathbf{S}^p)}{\mathbf{N}^p(\mathbf{S}^p):\mathbb{S}_a\,\mathbf{N}^p(\mathbf{S}^p)}\right] \tag{6.63}$$

Remark 6.4 *If $\lambda^p = 0$, then $\mathbb{S}_a = \mathbb{S}$ and $\mathbb{P}_a^p = \mathbb{P}^p$, which is consistent with the continuous description.*

Remark 6.5 *In the absence of the damageable spring, $\mathrm{d}\mathbf{S} = \mathrm{d}\mathbf{S}^p$. Thus*

$$\mathbb{P}_a = \mathbb{S}_a - \frac{\mathbb{S}_a\,\mathbf{N}^p(\mathbf{S}^p)\otimes\mathbb{S}_a\,\mathbf{N}^p(\mathbf{S}^p)}{\mathbf{N}^p(\mathbf{S}^p):\mathbb{S}_a\,\mathbf{N}^p(\mathbf{S}^p)}$$

which is the algorithmic tangent operator for perfect elasto-plasticity found by [Rakotomanana et al., 1991] .

c) Damage mode: case $\mathrm{d}\mathbf{E}^p \neq \mathbf{0}$ and $\mathrm{d}D > 0$

Once again, we have $\mathbf{S} = \mathbb{S}\,(\mathbf{E}-\mathbf{E}^p)$, and:

$$\mathrm{d}\mathbf{S} = \mathbb{S}\,\mathrm{d}(\mathbf{E}-\mathbf{E}_0^p) - \mathbb{S}\,\mathrm{d}(\mathbf{E}^p-\mathbf{E}_0^p) \tag{6.64}$$

thus

$$\mathrm{d}(\mathbf{E}^p-\mathbf{E}_0^p) = \mathrm{d}(\mathbf{E}-\mathbf{E}_0^p) - \mathbb{C}\,\mathrm{d}\mathbf{S} \tag{6.65}$$

On the one hand, $\mathbf{S}^p = \mathbb{S}\,\mathbf{E} - \frac{1}{D}\,\mathbb{S}\,\mathbf{E}^p$. Thus

$$\mathrm{d}\mathbf{S}^p = \mathbb{S}\,\mathrm{d}(\mathbf{E}-\mathbf{E}_0^p) - \frac{1}{D}\,\mathbb{S}\,\mathrm{d}(\mathbf{E}^p-\mathbf{E}_0^p) + \frac{\mathrm{d}(D-D_0)}{D^2}\,\mathbb{S}\,\mathbf{E}^p \tag{6.66}$$

On the other hand, $\mathbf{S}^D = \frac{1-D}{D}\,\mathbb{S}\,\mathbf{E}^p$. Thus

$$\mathrm{d}\mathbf{S}^D = \frac{1-D}{D}\,\mathbb{S}\,\mathrm{d}(\mathbf{E}^p-\mathbf{E}_0^p) - \frac{\mathrm{d}(D-D_0)}{D^2}\,\mathbb{S}\,\mathbf{E}^p \tag{6.67}$$

As $Y^D(\mathbf{S}^D, D) = 0$ holds, we have:

$$\mathrm{d}Y^D = \mathbf{N}^D(\mathbf{S}^D):\mathrm{d}\mathbf{S}^D + \frac{\partial Y^D}{\partial D}\,\mathrm{d}(D-D_0) = 0 \tag{6.68}$$

Combining (6.67) and (6.68), we get:

$$\mathrm{d}(D-D_0) = \frac{D(1-D)\,\mathbf{N}^D(\mathbf{S}^D):\mathbb{S}\,\mathrm{d}(\mathbf{E}^p-\mathbf{E}_0^p)}{\mathbf{N}^D(\mathbf{S}^D):\mathbb{S}\,\mathbf{E}^p - \frac{\partial Y^D}{\partial D}D^2} \tag{6.69}$$

The normality flow rule for $\mathrm{d}\mathbf{E}^p$ can be written as:

$$\mathrm{d}(\mathbf{E}^p - \mathbf{E}_0^p) = \mathrm{d}(\lambda^p\,\mathbf{N}^p(\mathbf{S}^p)) = \mathrm{d}\lambda^p\,\mathbf{N}^p(\mathbf{S}^p) + \lambda^p\,\mathbb{H}^p(\mathbf{S}^p)\,\mathrm{d}\mathbf{S}^p \tag{6.70}$$

After some rearrangements, (6.66), (6.69) and (6.70) give:

$$\mathrm{d}\mathbf{S}^p = \mathbb{S}_{ad}\,\mathrm{d}(\mathbf{E} - \mathbf{E}_0^p) - \frac{\mathrm{d}\lambda^p}{D}\,\mathbb{S}_{ad}\,(\mathbb{I} - \mathbb{A})\,\mathbf{N}^p(\mathbf{S}^p) \tag{6.71}$$

where $\mathbb{I}$ is the symmetric fourth-order identity tensor, $\mathbb{S}_{ad} = \left[\mathbb{C} + \dfrac{\lambda^p}{D}\,(\mathbb{I} - \mathbb{A})\,\mathbb{H}^p(\mathbf{S}^p)\right]^{-1}$ and $\mathbb{A} = \dfrac{(1-D)\,\mathbf{E}^p \otimes \mathbb{S}\,\mathbf{N}^D(\mathbf{S}^D)}{\mathbf{N}^D(\mathbf{S}^D) :: \mathbb{S}\,\mathbf{E}^p - \frac{\partial Y^D}{\partial D}\,D^2}$.
Furthermore, as $Y^p(\mathbf{S}^p, D) = 0$, we have:

$$\mathrm{d}Y^p = \mathbf{N}^p(\mathbf{S}^p) : \mathrm{d}\mathbf{S}^p + \frac{\partial Y^p}{\partial D}\,\mathrm{d}(D - D_0) = 0 \tag{6.72}$$

Together with (6.69) and (6.71) we get:

$$\begin{aligned}\mathrm{d}\lambda^p = \frac{D}{\alpha}\Big[&\mathbf{N}^p(\mathbf{S}^p) : \mathbb{S}_{ad}\,\mathrm{d}(\mathbf{E} - \mathbf{E}_0^p) + \\ &+ \frac{\partial Y^p}{\partial D} D(1-D)\lambda^p\,\frac{\mathbf{N}^D(\mathbf{S}^D) :: \mathbb{S}\,\mathbb{H}^p(\mathbf{S}^p)\,\mathbb{S}_{ad}\,\mathrm{d}(\mathbf{E} - \mathbf{E}_0^p)}{\mathbf{N}^D(\mathbf{S}^D) :: \mathbb{S}\,\mathbf{E}^p - \frac{\partial Y^D}{\partial D}\,D^2}\Big]\end{aligned} \tag{6.73}$$

where

$$\begin{aligned}\alpha = \mathbf{N}^p(\mathbf{S}^p) : \mathbb{S}_{ad}\,(\mathbb{I} - \mathbb{A})\mathbf{N}^p(\mathbf{S}^p) - \frac{\partial Y^p}{\partial D}\,D(1-D)\cdot \\ \cdot\,\frac{D\,\mathbf{N}^D(\mathbf{S}^D) :: \mathbb{S}\,\mathbf{N}^p(\mathbf{S}^p) - \lambda^p\,\mathbf{N}^D(\mathbf{S}^D) :: \mathbb{S}\,\mathbb{H}^p(\mathbf{S}^p)\,\mathbb{S}_{ad}\,(\mathbb{I} - \mathbb{A})\,\mathbf{N}^p(\mathbf{S}^p)}{\mathbf{N}^D(\mathbf{S}^D) :: \mathbb{S}\,\mathbf{E}^p - \frac{\partial Y^D}{\partial D}\,D^2}\end{aligned}$$

As $\mathbf{S} = \mathbf{S}^p + \mathbf{S}^D$, we have $\mathrm{d}\mathbf{S} = \mathrm{d}\mathbf{S}^p + \mathrm{d}\mathbf{S}^D$.
Injecting (6.65) and (6.69) into (6.67) and injecting (6.73) into (6.71), we finally get the desired result:

$$\mathbb{P}_a^D = \mathbb{S}\,[\mathbb{I} - \mathbb{A}]^{-1}[\,(\mathbb{I} - \mathbb{A}) - D\,(\mathbb{I} - \mathbb{C}\,\mathbb{S}_{ad}) - \frac{D}{\alpha}\,\mathbb{C}\,\mathbb{S}_{ad}\,(\mathbb{I} - \mathbb{A})\,\mathbb{B}\,] \tag{6.74}$$

where

$$\begin{aligned}\mathbb{B} = \Big[&\mathbf{N}^p(\mathbf{S}^p) \otimes \mathbb{S}_{ad}\,\mathbf{N}^p(\mathbf{S}^p) + \\ &+ \frac{\partial Y^p}{\partial D}\,D(1-D)\lambda^p\,\frac{\mathbf{N}^p(\mathbf{S}^p) \otimes \mathbf{N}^D(\mathbf{S}^D)}{\mathbf{N}^D(\mathbf{S}^D) :: \mathbb{S}\,\mathbf{E}^p - \frac{\partial Y^D}{\partial D}\,D^2}\,\mathbb{S}\,\mathbb{H}^p(\mathbf{S}^p)\,\mathbb{S}_{ad}\Big]\end{aligned}$$

Remark 6.6 *If* $\lambda^p = 0$, *then* $\mathbb{S}_{ad} = \mathbb{S}$, $\mathbb{B} = \mathbf{N}^p(\mathbf{S}^p) \otimes \mathbb{S}\,\mathbf{N}^p(\mathbf{S}^p)$ *and* $\alpha = \mathbf{N}^p(\mathbf{S}^p) : \mathbb{S}\,\mathbf{N}^p(\mathbf{S}^p) - (1-D)\,\frac{\mathbf{N}^p(\mathbf{S}^p):\mathbb{S}\,\mathbf{E}^p + \frac{\partial Y^p}{\partial D}\,D^2}{\mathbf{N}^D(\mathbf{S}^D):\mathbb{S}\,\mathbf{E}^p - \frac{\partial Y^D}{\partial D}\,D^2}\,\mathbf{N}^D(\mathbf{S}^D) : \mathbb{S}\,\mathbf{N}^p(\mathbf{S}^p)$, *which is consistent with the continuous description.*

Remark 6.7 *In the absence of the damageable spring* $\mathbf{N}^D(\mathbf{S}^D) = \mathbf{0}$, *thus* $\mathbb{A}$ *vanishes and* $\mathbb{S}_{ad} = \mathbb{S}_a$. *Thus* $\mathbb{P}_a^D = \mathbb{P}_a^p$ *which is the algorithmic tangent operator for perfect elasto-plasticity.*

Remark 6.8 *The final algorithm has exactly the same structure than the one-dimensional one presented in Table 4.1. Thus, it will not be repeated here. Scalar strain and stress quantities must be replaced by the corresponding second-order tensors and the scalar tangent operators by the algorithmic fourth-order tangent operators. The plastic and damage yield and threshold functions must be tested as mentioned in Subsection 6.2.1.*

6.3 Finite element and linearization methods

In this Section, we briefly describe the finite element and linearization methods used for the resolution of a boundary value problem. The notations are largely inspired from [Curnier, 1993]. The finite element method (FEM) is appropriate to solve a boundary value problem whenever the geometry is complex and the linearization method (LIM) whenever the behaviour of the material is nonlinear. Indeed, the strongly nonlinear problem presented in Subsection 3.1.5 (the principle of virtual power) has to be solved numerically.

6.3.1 Finite element method

The FEM is based on a subdivision of the solid $\boldsymbol{\Omega}$ into a finite number `NELE` of elements connected at a finite number `NODE` of nodes (Figure 6.3). The exact, continuous problem in space is then replaced by an approximate, discrete problem which is more tractable and provides an approximate solution in space.

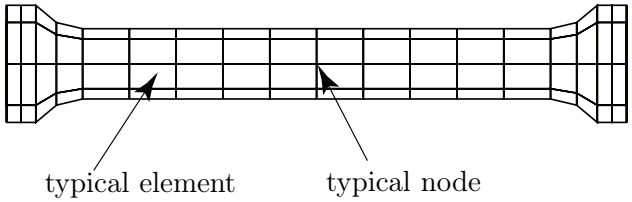

Figure 6.3: FEM mesh.

Approximating the solution in each element by a polynomial, the method is based on finding a *piecewise polynomial solution* on the entire domain. Substituting this approximate solution in the principle of virtual power, we get a system of equations (generally, a system of nonlinear ordinary differential equations in time) which is the discrete counterpart of the continuous differential equation and whose solution is the *nodal discrete solution*.

Instead of the principle of virtual power (3.23), finite element softwares refer to the equivalent *principle of virtual work*. It is obtained by replacing the virtual velocity $\mathring{\mathbf{y}}$ by a *virtual displacement* $\mathbf{w}$, which is kinematically admissible but not necessarily dynamically admissible.
Approximating the virtual and real displacement functions by a series of nodal basis functions, we get:

$$\begin{aligned}\mathbf{w}(\boldsymbol{x},t) &\simeq b^n(\boldsymbol{x})\mathbf{w}^n(t)\\ \mathbf{u}(\boldsymbol{x},t) &\simeq b^n(\boldsymbol{x})\mathbf{u}^n(t), \quad n=1,\texttt{NODE}\end{aligned}$$

where the summation convention is applied on the repeated indices, $\mathbf{w}^n$ and $\mathbf{u}^n$ are discrete values of the virtual and real displacements at node n, and b^n are piecewise polynomial basis functions equal to unity at node n and to zero at all other nodes (Figure 6.4).

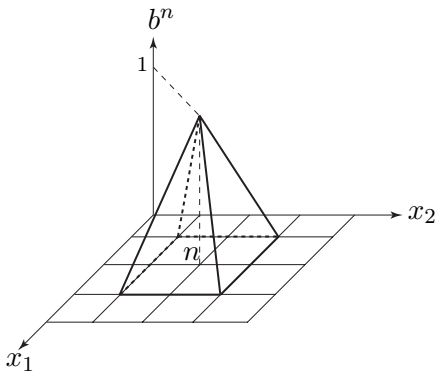

Figure 6.4: Linear nodal basis function.

Substitution of these series expansions into the principle of virtual work leads to the discrete weak form:

$$\begin{aligned}\int_{\boldsymbol{\Omega}} \mathbf{w}^n(t)\cdot\left(b^n(\boldsymbol{x})\rho(\boldsymbol{x},t)b^m(\boldsymbol{x})\ddot{\mathbf{u}}^m(t)-b^n(\boldsymbol{x})\mathbf{g}^t(\boldsymbol{x},t)\right)\,\mathrm{d}V+\\ +\int_{\boldsymbol{\Omega}}\mathbf{w}^n(t)\cdot\mathbf{P}(\boldsymbol{x},t)\nabla b^n(\boldsymbol{x})\,\mathrm{d}V-\int_{\boldsymbol{\Gamma}_{\mathbf{p}}}\mathbf{w}^n(t)\cdot b^n(\boldsymbol{x})\bar{\mathbf{p}}\,\mathrm{d}A=0,\ \forall\,\mathbf{w}^n\end{aligned} \tag{6.75}$$

or equivalently to the discrete strong form:

$$\begin{aligned}\int_{\mathbf{\Omega}} \left(b^n(\boldsymbol{x})\rho(\boldsymbol{x},t)b^m(\boldsymbol{x})\ddot{\mathbf{u}}^m(t) - b^n(\boldsymbol{x})\mathbf{g}^t(\boldsymbol{x},t)\right)\,\mathrm{d}V + \\ + \int_{\mathbf{\Omega}} \mathbf{P}(\boldsymbol{x},t)\nabla b^n(\boldsymbol{x})\,\mathrm{d}V - \int_{\mathbf{\Gamma_p}} b^n(\boldsymbol{x})\bar{\mathbf{p}}\,\mathrm{d}A = \mathbf{0},\ n = 1,\mathtt{NODE}\end{aligned} \tag{6.76}$$

Equation (6.76) represents the force equilibrium at node n. The discrete nodal inertia, body, internal, and contact forces are easily recognized. Of course, the displacement boundary conditions $\mathbf{u}^n = \bar{\mathbf{u}}^n$ are also discretized for the relevant boundary nodes n.

Instead of building the equilibrium node by node, it is preferable to adopt an element by element approach. The spatial subdivision of $\mathbf{\Omega}$ allows a computation of the virtual work (6.76) element by element according to the rule:

$$\int_{\mathbf{\Omega}} = \sum_{e=1}^{\mathtt{NELE}} \int_{{}^e\mathbf{\Omega}}$$

This approach assumes a *localization* of the nodes and variables. Let $\mathbb{x}$ and ${}^e\mathbb{x}$ be the discrete global and local nodal position vectors, respectively, defined by:

$$\begin{aligned}\mathbb{x} &= (\boldsymbol{x}^1, \boldsymbol{x}^2, \ldots, \boldsymbol{x}^{\mathtt{NODE}})^{\mathrm{T}} \\ {}^e\mathbb{x} &= ({}^e\boldsymbol{x}^1, {}^e\boldsymbol{x}^2, \ldots, {}^e\boldsymbol{x}^{\mathtt{NOEL}})^{\mathrm{T}}\end{aligned}$$

where NODE is the total number of nodes and NOEL the number of nodes composing the specific element e.
Arbitrary discrete global and local nodal vectors, like the aforementioned position vectors, are related by a ($3\mathtt{NOEL} \times 3\mathtt{NODE}$) *localization matrix* ${}^e\mathbf{L}$:

$${}^e\mathbb{x} = {}^e\mathbf{L}\mathbb{x}$$

Within each element e, the virtual and real displacements are interpolated between the NOEL nodes delimiting the element by means of polynomial shape functions equal to unity at one node and to zero at the others:

$$\begin{aligned}{}^e\mathbf{w}(\boldsymbol{x},t) &= {}^eb^a(\boldsymbol{x}){}^e\mathbf{w}^a(t) \\ {}^e\mathbf{u}(\boldsymbol{x},t) &= {}^eb^a(\boldsymbol{x}){}^e\mathbf{u}^a(t), \quad a = 1,\mathtt{NOEL}\end{aligned}$$

where ${}^e\mathbf{w}$ and ${}^e\mathbf{u}$ are the localized virtual and real displacements and the polynomial local basis functions ${}^eb^a$ are the restriction to the element e of the global basis functions b^n relative to the same node, relatively identified by the global node number n or by the couple (e,a).

With this new notation, (6.76) becomes an *assembly* of elementary contributions:

$$\sum_{e=1}^{\texttt{NELE}} [{}^e\mathbf{L}]_{cn}^{\mathrm{T}} \int_{{}^e\boldsymbol{\Omega}} \left({}^eb^c(\boldsymbol{x})\rho(\boldsymbol{x},t)\,{}^eb^a(\boldsymbol{x})\,{}^e\ddot{\mathbf{u}}^a(t) - {}^eb^c(\boldsymbol{x})\mathbf{g}^t(\boldsymbol{x},t) \right) \mathrm{d}V + \\ + \sum_{e=1}^{\texttt{NELE}} [{}^e\mathbf{L}]_{cn}^{\mathrm{T}} \left\{ \int_{{}^e\boldsymbol{\Omega}} \mathbf{P}(\boldsymbol{x},t) \nabla {}^eb^c(\boldsymbol{x})\,\mathrm{d}V - \int_{{}^e\boldsymbol{\Gamma}^{\mathbf{P}}} {}^eb^c(\boldsymbol{x})\bar{\mathbf{p}}\,\mathrm{d}A \right\} = \mathbf{0} \tag{6.77}$$

for $n = 1, \texttt{NODE}$. The *scatter matrices* ${}^e\mathbf{L}^{\mathrm{T}}$ transform the elementary contributions of the local force vectors into global force vectors.

The integration over the elementary domain ${}^e\boldsymbol{\Omega}$ is usually done by transforming the element into an *isoparametric element* of fixed size and shape. For example, an arbitrary hexahedral element is transformed into a unitary cube (Figure 6.5).

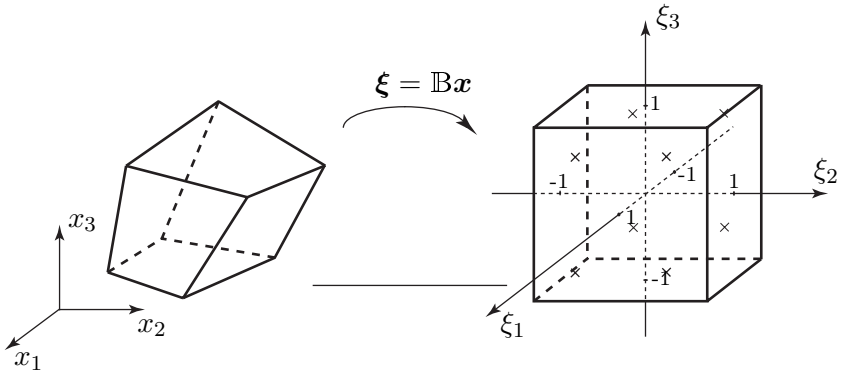

Figure 6.5: Eight integration points three-dimensional isoparametric element.

In this process, the coordinates $\boldsymbol{x}$ are transformed into *natural coordinates* $\boldsymbol{\xi}$ by:

$$\boldsymbol{x}(\boldsymbol{\xi}) = b^a(\boldsymbol{\xi})\boldsymbol{x}^a$$

where b^a are the natural basis function of the isoparametric element. Thus, the local displacement vector can be written as:

$${}^e\mathbf{u}(\boldsymbol{x},t) = {}^e\hat{\mathbf{u}}(\boldsymbol{\xi},t) = {}^eb^a(\boldsymbol{\xi})\,{}^e\boldsymbol{u}^a(t)$$

Numerical integration of the elementary forces is then carried out in the

natural coordinates using an L-integration point Gauss formula:

$$\int_{\Omega_e} f(\boldsymbol{x})\,\mathrm{d}V = \int_{-1}^{+1}\int_{-1}^{+1}\int_{-1}^{+1} \hat{f}(\boldsymbol{\xi})j(\boldsymbol{\xi})\,\mathrm{d}\hat{V} = \\ = \sum_{l=1}^{L} \hat{f}(\boldsymbol{\xi}^l)j(\boldsymbol{\xi}^l)\Omega^l$$

where j is the determinant of the jacobian matrix of the isoparametric transformation and Ω^l are the weights associated to the integration points $\boldsymbol{\xi}^l$.

Remark 6.9 *If* NDIM *is the spatial dimension of the integration domain, we remind that an L-integration point Gauss formula, with $L = I^{\mathtt{NDIM}}$, integrates exactly a polynomial of degree $2I - 1$.*

6.3.2 Linearization and finite difference methods

Linear iteration method

After discretizing the problem with the FEM, the resulting system of 3NODE equations with 3NODE unknowns remains nonlinear and must be linearized in order to be solved numerically. If the global nodal displacements are collected in a vector $\mathbb{u} := (\mathbf{u}^1, \mathbf{u}^2, \ldots, \mathbf{u}^{\mathtt{NODE}})^{\mathrm{T}}$, the system (6.77) can be rewritten as:

$$\mathbb{r}(\mathbb{u}) = \mathbb{0}$$

where $\mathbb{r}$ is the global nodal residual force vector.

The generalized Newton method [Alart and Curnier, 1991] can be used to solve this set of nonlinear equations. The resulting linearization leads to the iterative scheme:

$$\mathbb{u}^{i+1} = \mathbb{u}^i - \mathbb{T}^{-1}(\mathbb{u}^i)\mathbb{r}(\mathbb{u}^i)$$

where $\mathbb{T}$ is the tangent stiffness matrix $\dfrac{\mathrm{d}\mathbb{r}}{\mathrm{d}\mathbb{u}}$.

The computation and inversion of the tangent matrix at each iteration is rather costly. However, when the initial state of the algorithm lies near the solution, the quadratic rate of convergence of the method guarantees a low number of iterations. In some applications, the modified Newton method, i.e. keeping the same tangent matrix over several iterations, is preferable. A convergence criterion mixing a force residual and a displacement increment norm is used in our simulations. The one-dimensional full Newton linear iteration method is illustrated in Figure 6.6.

Combining the FEM with the above described linear iteration method allows to compute the tangent matrix $\mathbb{T}(\mathbb{u}_i)$ by assembling the contributions of all the elements.

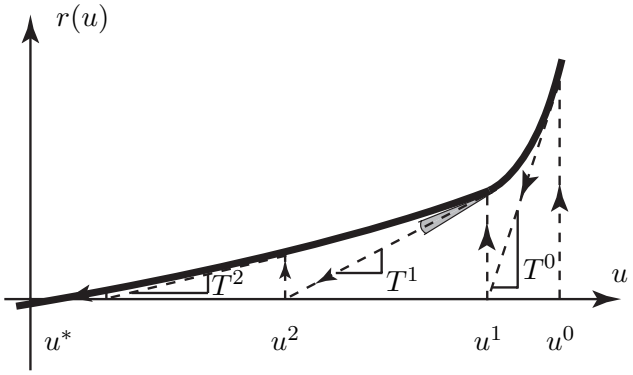

Figure 6.6: One-dimensional illustration of the full Newton iteration method. In the case of non-differentiability (e.g. in $u = u^1$), a subgradient of r is chosen.

Finite difference method

In dynamics, the system of equations resulting from the space discretization and linearization is a set of linear ordinary differential equations in time. A further numerical approximation must be used in order to transform it into a system of linear equations which can be solved exactly by standard methods of linear algebra. Various schemes can be used for approximating time derivatives and thus integrating differential equations in time. They are referred to as *finite difference methods*. We will not describe them in detail here, but the reader is referred to standard textbooks on numerical analysis or numerical solid mechanics [Press et al., 1992, Curnier, 1993].

We just illustrate the main idea of the method by approximating a first time derivative by the finite differences ratio:

$$\dot{\mathbf{u}}_{n+1} \simeq \frac{\mathbf{u}_{n+1} - \mathbf{u}_n}{t_{n+1} - t_n}$$

Solving an ordinary differential equation of the type:

$$\dot{\mathbf{u}}(t) = f(\mathbf{u}(t), t)$$
$$\mathbf{u}(0) = \mathbf{u}_0$$

suggests the two following *explicit* and *implicit* schemes:

$$\frac{\mathbf{u}_{n+1} - \mathbf{u}_n}{t_{n+1} - t_n} = f(\mathbf{u}_n, t_n)$$

$$\frac{\mathbf{u}_{n+1} - \mathbf{u}_n}{t_{n+1} - t_n} = f(\mathbf{u}_{n+1}, t_{n+1})$$

known as the forward and backward Euler finite difference methods, respectively. Both methods are of order 1, but only the latter is unconditionally

stable. Methods of higher-order, like the Runge-Kutta family, can also be used to solve first-order ordinary differential equations, but are computationally more expensive.
For second-order ordinary differential equations, the Newmark methods are particularly well adapted. However, in our applications, inertia effects will be neglected.

In summary, the FEM allows a spatial discretization of the solid. Combined with the linear iteration method, it overcomes the geometric and material nonlinearities. Finally, the finite difference method carries out the time discretization of the problem. Thus, the initial nonlinear continuous boundary value problem deriving from the principle of virtual work is straightforwardly approximated by a time and an iterative sequence of linear algebraic problems.

6.3.3 ABAQUS stress and strain measures

All throughout this work, the material (total Lagrangian) description was used. Thus, the undeformed configuration occupied by the body at the time origin was used to define the strain, the stress and their rates.
The objective material stress measure $\mathbf{S}$ (material Piola-Kirchhoff-2 stress tensor) and its conjugate (or dual) variable $\mathbf{E}$ (Green-St Venant or Lagrangian material strain tensor) were used to formulate the constitutive law. This formulation is adequate for moderate strains and finite rotations.

In ABAQUS (Hibbitt, Karlsson & Sorensen, Inc.) and at large strains, the stress measure is the Kirchhoff stress $J\mathbf{T}$ conjugate to the strain measure whose rate is the rate of deformation:

$$\mathbf{D} := \frac{1}{2}\left(\mathbf{L} + \mathbf{L}^{\mathrm{T}}\right) \quad \text{with} \quad \mathbf{L} = \dot{\mathbf{F}}\mathbf{F}^{-1}$$

namely $\int \mathbf{D}\,\mathrm{d}t$.
When considering large strains, one has to take care to use the proper stress and strain measures together with the exact consistent (algorithmic) tangent operator. Of course, for small strains applications, all measures coincide. The following congruence relations between the different measures hold:

Cauchy stress (force per current area):

$$\mathbf{T} = \frac{1}{J}\,\mathbf{F}\mathbf{S}\mathbf{F}^{\mathrm{T}}$$

Kirchhoff stress:

$$J\mathbf{T} = \mathbf{F}\mathbf{S}\mathbf{F}^{\mathrm{T}}$$

Power per unit reference volume (defined in Subsection 3.1.3):

$$\mathbf{S} : \dot{\mathbf{E}} = J\mathbf{T} : \mathbf{D} \tag{6.78}$$

Spatial strain rate:

$$\mathbf{D} = \mathbf{F}^{-\mathrm{T}}\dot{\mathbf{E}}\mathbf{F}^{-1}$$

The ABAQUS exact consistent tangent operator $\mathbb{P}_{\mathrm{AB}}$ is defined through the variation in Kirchhoff stress ([HKS, 2001]):

$$\delta(J\mathbf{T}) =: J\,\mathbb{P}_{\mathrm{AB}}\,\delta\mathbf{D} \quad \text{with} \quad \delta\mathbf{D} = \mathbf{F}^{-\mathrm{T}}\delta\dot{\mathbf{E}}\mathbf{F}^{-1}$$

From (6.78), we get:

$$\mathbb{P}_{\mathrm{AB}} = \frac{1}{J}\,[\mathbf{F}\,\underline{\otimes}\,\mathbf{F}]\;\mathbb{P}\;\left[\mathbf{F}^{\mathrm{T}}\,\underline{\otimes}\,\mathbf{F}^{\mathrm{T}}\right]$$

where $\mathbb{P} = \frac{\mathrm{d}\mathbf{S}}{\mathrm{d}\mathbf{E}}$ is the material tangent operator ($\delta\mathbf{S} =: \mathbb{P}\,\delta\mathbf{E}$).

In conclusion, if large volume changes and geometric nonlinearities are considered, adequate strain and stress measures must be used in order to ensure an objective formulation, and the consistent (algorithmic) tangent operator in order to ensure rapid convergence.

6.4 Validation

In this Section, we present the validation of the three-dimensional rate-independent constitutive law for cortical bone through some elementary simulations. In particular, we give the values of the material constants defining the halfspacewise damage criterion, which agree with our uniaxial mechanical tests.

The validation of the implementation of the three-dimensional constitutive law was done in two steps.
Firstly, the three-dimensional algorithm has been implemented in the commercial software Mathematica® (Wolfram Research, Inc) and submitted to extensive testing.
Secondly, the model has been coded in a FORTRAN user subroutine UMATDAMA3D and integrated in the commercial finite element software ABAQUS (version 6.4, HKS, Inc., [Kari, 1993]). The material constants of the model were then identified by direct comparison with our uniaxial experiments.
The validation was achieved by testing a single finite element with appropriate one-dimensional schedules and then boundary value problems were chosen in order to check the convergence of the projection algorithms.

6.4.1 Material constants and one-dimensional tests

Transverse isotropic elasticity

We use the porous transverse isotropic elasticity described by volume fraction and a second-order fabric tensor (Zysset-Curnier model, Section 3.3, Equation (3.68)). Table 6.1 summarizes the values of the constants of the plain isotropic bone together with the exponents v and w characterizing its volume fraction and anisotropy, respectively.

$\varepsilon_0\,[GPa]$	$\mu_0\,[GPa]$	ν_0	v	w
15.75	5.28	0.32	2.0	1.0

Table 6.1: Volume fraction and fabric-based Zysset-Curnier elasticity model parameters (from [Zysset, 1994]).

They were identified by [Zysset, 1994] for bovine cortical bone. The resulting elastic constants (defined in Section 3.3) are close to the ones measured by ultrasound by [van Buskirk et al., 1981] and are compared in Table 6.2.

	ϵ_1	ϵ_2	ϵ_3	G_{12}	G_{13}	G_{23}
A	$10.2\,GPa$	$10.2\,GPa$	$20.0\,GPa$	$4.7\,GPa$	$4.7\,GPa$	$3.4\,GPa$
B	$11.6\,GPa$	$14.6\,GPa$	$21.9\,GPa$	$5.29\,GPa$	$6.29\,GPa$	$6.99\,GPa$
	ν_{12}	ν_{13}	ν_{23}	ν_{21}	ν_{31}	ν_{32}
A	0.320	0.228	0.228	0.320	0.448	0.448
B	0.302	0.109	0.205	0.380	0.206	0.307

Table 6.2: Technical elastic constants for bovine cortical bone: A values resulting from the Zysset-Curnier model and B values measured by ultrasound by [van Buskirk et al., 1981]. The third direction coincide with the long axis of the bone.

The constants of the Zysset-Curnier model define the transverse isotropic elastic compliance tensor $\mathbb{C}$ (and thus $\mathbb{S} = \mathbb{C}^{-1}$). The positiveness of $\mathbb{C}$ was checked. The elastic stiffness tensor $\mathbb{S}$ plays the key role of the intact elastic stiffness (primary spring of the model). Furthermore, its inverse defines the convex elastic ellipsoid in plastic strain space associated to the plastic yield criterion (Section 6.1).

Halfspacewise damage criterion

As mentioned before, we use the same shape of the damage criterion as the one identified for trabecular bone by [Rincón, 2003, Zysset and Rincón, 2005]. Its material constants are given in Table 6.3. In order to adapt it for cortical bone, we change only its initial global radius by identifying the constant R (Table 6.5) appearing in the associated damage hardening function (6.12).

σ_0^-	σ_0^+	τ_0	χ_0^-	χ_0^+	p	q
$58.4\,MPa$	$43.3\,MPa$	$23.1\,MPa$	0.31	-0.28	1.32	0.56

Table 6.3: Material constants defining the halfspacewise damage criterion for trabecular bone (from [Rincón, 2003, Zysset and Rincón, 2005]).

Volume fraction and fabric

We use the classical mean value of 0.9 for cortical bone volume fraction that accounts for residual porosity associated with the vascular Havers and Volkmann canals as well as the lacunae (e.g. [Cowin, 2001]) and the mean values found by [Zysset, 1994] for fabric, with the normalization $\det(\hat{\mathbf{M}}) = 1$:

ρ_s	m_1	m_2	m_3
0.9	0.894	0.894	1.252

Table 6.4: Volume fraction and fabric values (from [Cowin, 2001, Zysset, 1994]).

Plastic and damage hardening parameters

The identification with our own uniaxial data of bovine cortical bone experiments provides:

χ^p	l	χ^D	k	R
$0.12\sqrt{MPa}$	14	5.12	14	0.33

Table 6.5: Identified plastic and damage hardening parameters, based on our own uniaxial tests.

where χ^p, l, χ^D, k and R are the plastic and damage hardening parameters of the corresponding exponential functions defined in (6.11) and (6.12), respectively.

One-dimensional tests

All uniaxial mechanical tests carried out on the one-dimensional RI model were successfully simulated with the three-dimensional model making confined traction experiments along the principal direction of the material ($E_{11} = E_{22} = 0, E_{33} = \bar{E}_{33}$). In addition, confined traction tests along the other two orthogonal directions were made. Finally, a pure shear experiment was simulated. Similar experiments were carried out under load control in order to check the correctness of the algorithmic tangent operators. The schedules were applied to a single linear 8-node brick finite element (Figure 6.7).

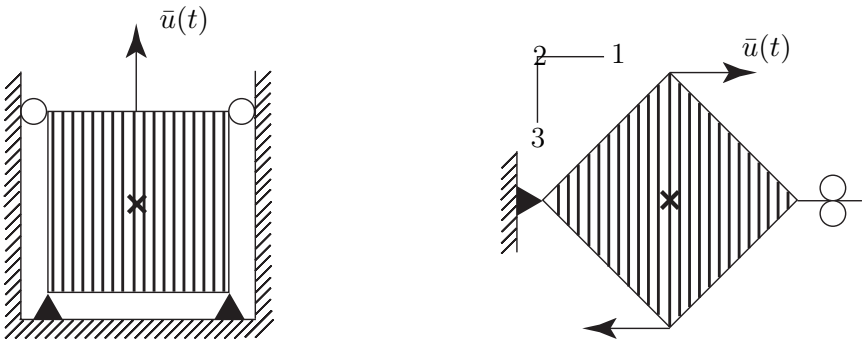

Figure 6.7: One-dimensional confined traction experiment carried out along the principal material direction and pure shear experiment of a single linear eight-node brick element with one integration point.

Figures 6.8 (a) and (b) show the agreement between the one-dimensional programming of the three-dimensional law and its three-dimensional finite element implementation. The lateral stresses S_{11} and S_{22} are not shown in Figure 6.8 (a) but are obviously non-zero in this confined traction experiment. For the pure shear experiment, we get a pure shear state $S_{31} \neq 0$, $S_{12} = S_{23} = 0$ and $S_{11} = S_{22} = S_{33} = 0$ at the central integration point. We note that the shear damage threshold stresses are symmetric (Figure 6.8 (b)).

6.4.2 Boundary values problems

Two classes of experiments were simulated. In the first class, we studied the traction and compression of a bar starting with one single finite element (Figure 6.9 (a)) and ending with a cylindrical bar made of 800 elements. In the second class, we discretized the geometry of the traction specimens investigated experimentally in Chapter 5 into 184 8-node brick linear elements (Figure 6.9 (b)).

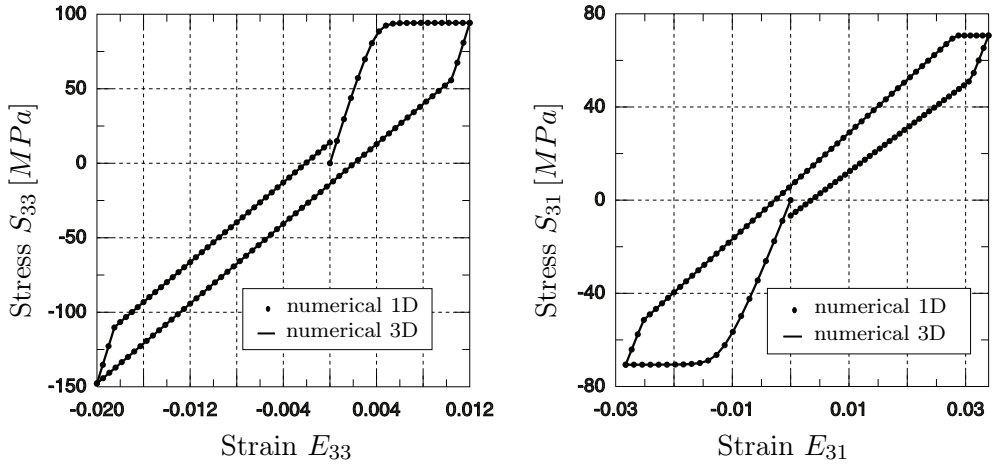

(a) Confined traction test (b) Pure shear test

Figure 6.8: Numerical results for both one-dimensional and three-dimensional implementation of the three-dimensional constitutive law for cortical bone. The material constants used in these simulations are given in Tables 6.2, 6.3, 6.4 and 6.5.

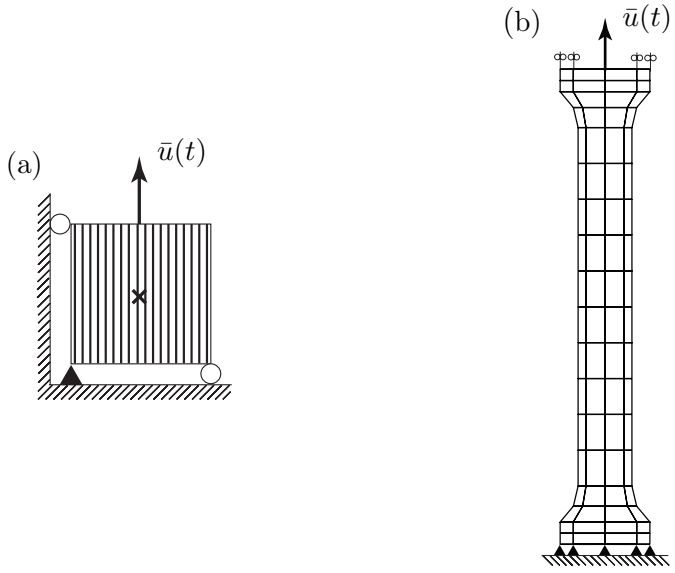

Figure 6.9: Boundary values experiments: (a) pure traction and (b) cortical bone specimen traction test.

For the first experiment, Figure 6.10 shows the differences between the confined and the pure traction test (with shrinking of the element). In the latter case, we see that the additional degrees of freedom (related to zero lateral stresses) result in a lower longitudinal elastic modulus and thus a higher damage threshold stress along the principal direction of the material.

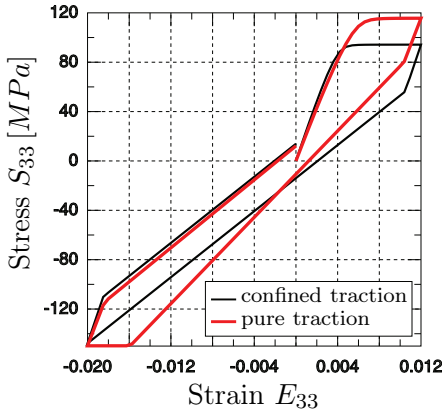

Figure 6.10: Confined and pure traction tests carried out on a single finite element whose principal material direction is aligned along the direction of traction (for the same material constants as those of Figure 6.8).

For the second experiment, the von Mises equivalent stress distribution in the specimen, defined as $v := ||\frac{3}{2}\mathbf{S}'||$ where $\mathbf{S}'$ is the deviatoric stress tensor ($\mathbf{S}' := \mathbf{S} - \frac{1}{3}\,\mathrm{Tr}\,\mathbf{S}\,\mathbf{I}$), is displayed in Figure 6.11. Although inappropriate for an orthotropic material, von Mises isotropic criterion still gives an adequate image of the stress state intensity in such a material. In this traction test, the material fibers are aligned along the direction of traction, inducing a homogeneous stress state in the central part of the specimen.
Figure 6.12 shows the von Mises equivalent stress distribution in a specimen whose material fibers form an angle of 30° with the direction of traction. In both Figures, the deformed (or actual) configuration of the body is scaled up by a factor 50. The inhomogeneous stress state induced by material anisotropy leads to a well-known shape of the deformed configuration, namely that of a buckling bar ([Timoshenko, 1968]).

In all simulations, the Newton integration scheme used to overcome the nonlinearity of the stress-strain law under stress control showed quadratic convergence in the neighborhood of the solution as it should. The same statement holds for the damage implicit projection algorithm. For statically admissible boundary conditions (for example total load not exceeding maximal reachable load), the three-dimensional algorithm has proven to behave properly and can be used in large finite element applications.

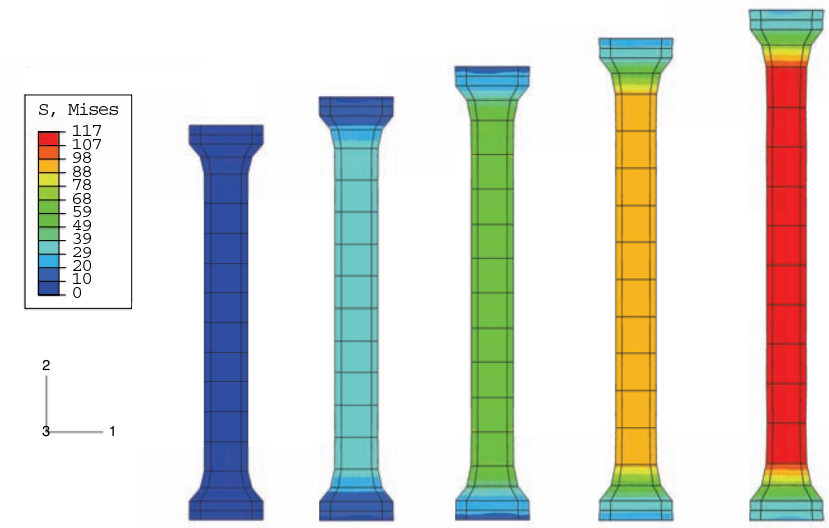

Figure 6.11: Traction test carried out on cortical bone specimen with material fibers aligned along the direction of traction (deformation scale: 50).

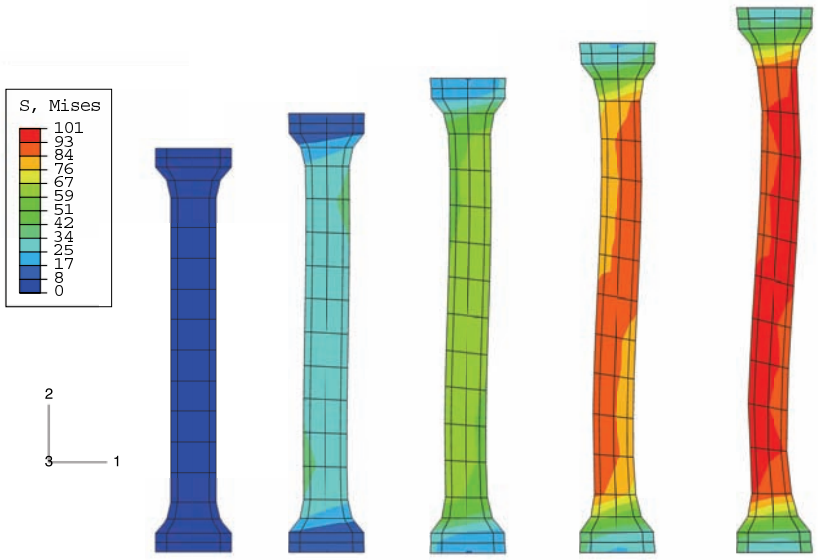

Figure 6.12: Traction test carried out on cortical bone specimen with material fibers forming an angle of 30° with the direction of traction (deformation scale: 50). The specimen twist is characteristic of orthotropy.

Chapter 7

Biomechanical application: damage of a lumbar vertebra

In this Chapter, the developed three-dimensional rate-independent constitutive law for cortical bone is used in a finite element mechanical analysis software in order to assess the mechanical state of a lumbar vertebra under uniaxial load by means of two plano-parallel polymethyl methacrylate (PMMA) plates. The vertebra is constituted of an external cortical bone shell and an internal trabecular bone core. The same damage model is used for both bone tissues but with different material constants. Thus, we warn about the moderate clinical relevance of the simulation. The predictions concerning the internal state of the lumbar vertebra are only *illustrative* and are intended to show the potential of the novel three-dimensional law. Experimental investigations should be made in order to compare them to the results of the simulations on solid grounds.

To begin, we describe the model of the lumbar vertebra. Then, we present and discuss the results of the simulations. Damage accumulation is visualized in terms of stress distribution in the body.

7.1 Model description

In this Section, we describe the finite element model investigated in this biomechanical application of the three-dimensional constitutive law for cortical bone tissue. As mentioned before, the bone under study is a lumbar vertebra or rather vertebral body. Supporting the entire body, the vertebrae are mechanically solicited at high loads in daily activities.

From an anatomical point of view, there are five lumbar vertebrae. Each of them is separated from its neighbour by a cartilagenous disc (Figure

7.1 Left). The anterior portion of the vertebra is called the vertebral body (Figure 7.1 Right). The body provides the surface against which the discs rest. The discs provide flexibility and are essential in absorbing shocks. They also experience damage from fatigue and overloading conditions.

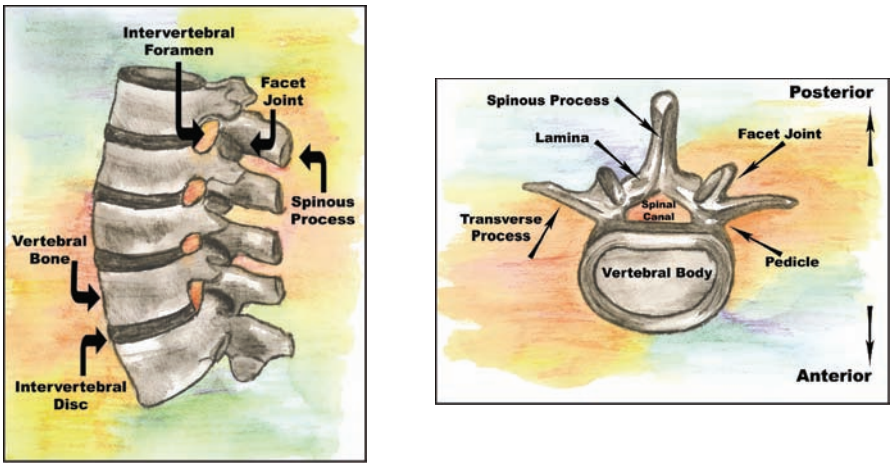

Figure 7.1: Human lumbar vertebrae and isolated vertebra (from the Northern California Neurosurgery Medical Group, Inc.).

7.1.1 Origin and properties of the mesh

The mesh is based on quantitative computed tomography (QCT) scans (μCT80, SCANCO Medical AG, Switzerland) carried out on the lumbar vertebral body of an elderly woman (born in 1923). Structural density is derived from color contrasts of the scan images. An automatic mesh generator (HyperMesh, Altair Engineering, Inc.) was used to discretize spatially the vertebral body and the two surrounding PMMA plates. At this point, we wish to thank Thomas Kitzler (TU-WIEN) for providing us the finite element mesh. The resulting mesh (Figure 7.2) is formed of three parts including 87'676 elements and 156'122 nodes. The number and type of elements of each part composing the mesh is summarized in Table 7.1.

Both cortical and trabecular bone elements are 10-node quadratic tetrahedron elements (C3D10 in the ABAQUS, Figure 7.3 Left). The elements composing the PMMA plates are 15-node quadratic triangular prism elements (C3D15, Figure 7.3 Right). Unstructured meshes formed of tetrahedral elements have a drawback over structured meshes formed of ordered hexahedral elements. Indeed, geometric orientations of a structured mesh related to true material orientations are lost in unstructured meshes.

	Cortical bone shell	Trabecular bone heart	Cranial PMMA plate	Caudal PMMA plate
Number of el.	29'362	35'769	11'320	11'225
Element type	C3D10	C3D10	C3D15	C3D15

Table 7.1: Number and type of elements composing each part of the finite element mesh of the lumbar vertebral body.

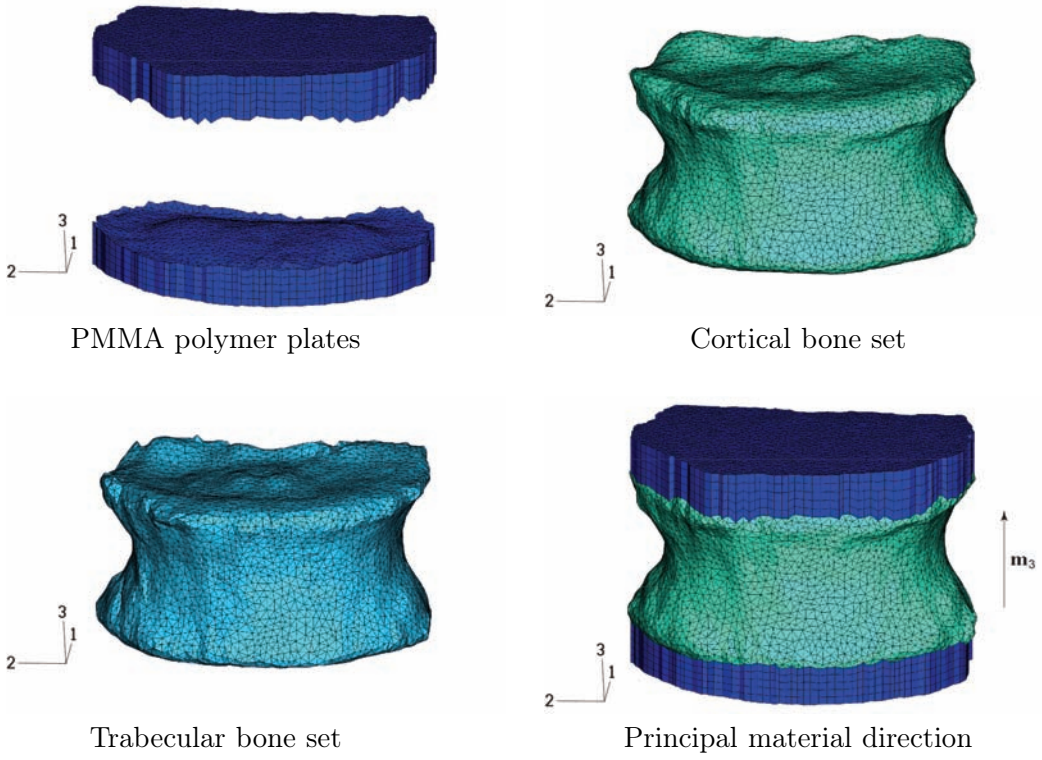

Figure 7.2: PMMA plates, cortical and trabecular bone finite element sets.

Material orientations

For simplicity, the material directions of the elements were chosen to be uniform. The privileged direction of anisotropy of both cortical and trabecular bone elements is the direction of the mechanical solicitation $\mathbf{e}_3$ (Figure 7.2).

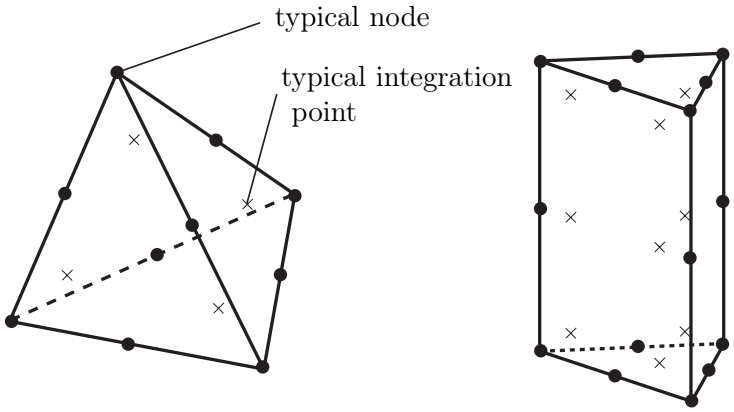

Figure 7.3: 10-node quadratic tetrahedron element and 15-node triangular prism element.

7.1.2 Material properties

Cortical and trabecular bone

Human cortical and trabecular bone is assumed to be porous transverse isotropic and characterized by the constitutive law presented in Chapter 6.

Its porous transverse isotropic elasticity is described by volume fraction and a second-order fabric tensor (Zysset-Curnier model, Section 3.3). The extrapolated constants of the plain isotropic material are given in Table 7.2 together with the exponents v and w characterizing the porosity and anisotropy, respectively. The values are taken from [Zysset, 1994].

The seven material constants describing the fabric-based damage criterion presented in Section 6.1 and identified for human trabecular bone by [Zysset and Rincón, 2005] are summarized in Table 7.3. The plastic and hardening parameters identified for bovine cortical bone in Subsection 6.4.1 are given in Table 7.4. We expect human bone to exhibit a very similar behaviour due to a similar composition of their extracellular bone matrix. Nevertheless, the values of these constants could be somewhat different and should be more precisely identified in subsequent studies.

As mentioned before, bone is assumed to be homogeneous, for simplicity. The extent of anisotropy given by the fabric eigenvalues is assumed to be uniform for all bone elements. They are given in Table 7.5.

As we consider trabecular bone as porous cortical bone, mechanically speaking (Subsection 6.4.1, [Carter and Hayes, 1977b, Zysset, 1994]), we assume that the elastic, plastic and damage constants are scaled in consequence by volume fraction, according to the scaling laws presented in Section 3.3 for the Zysset-Curnier model, and in Section 6.1 for the damage criterion. Due to

the lack of information concerning local volume fraction, it is also assumed to be uniform for all bone elements of the mesh. Cortical and trabecular bone volume fractions are given in Table 7.5. The 1 to 10 ratio is somewhat arbitrary, for simplicity again.

$\varepsilon_0\,[GPa]$	$\mu_0\,[GPa]$	ν_0	v	w
15.75	5.28	0.32	2.0	1.0

Table 7.2: Volume fraction and fabric-based Zysset-Curnier elasticity model parameters (from [Zysset, 1994]).

$\sigma_0^+\,[MPa]$	$\sigma_0^-\,[MPa]$	χ_0^+	χ_0^-	$\tau_0\,[MPa]$	p	q
43.3	58.4	-0.28	0.31	23.1	1.32	0.56

Table 7.3: Volume fraction and fabric-based Zysset halfspacewise orthotropic damage model parameters (from [Zysset and Rincón, 2005]).

$\chi^p\,[\sqrt{MPa}]$	l	χ^D	k	R
0.12	14	5.12	14	0.33

Table 7.4: Plastic and damage hardening parameters.

m_1	m_2	m_3	ρ_s^{cort}	ρ_s^{trab}
0.894	0.894	1.252	0.9	0.09

Table 7.5: Eigenvalues of the fabric tensor reflecting transverse isotropy, and cortical and trabecular bone volume fraction.

PMMA polymer plates

The cranial and caudal PMMA plates are assumed to be isotropic and linearly elastic. Their elastic properties are given in Table 7.6.

$\epsilon\,[GPa]$	ν
3.0	0.3

Table 7.6: Young's modulus and Poisson's ratio of the two PMMA plates.

Model under infinitesimal formulation

The infinitesimal formulation was used in this biomechanical application (small transformations).

7.1.3 Boundary conditions

The vertebral body is vertically loaded through the intermediate of the cranial PMMA plate (Figure 7.4). The caudal plate remains fixed whereas the cranial plate is subject to a uniform distributed stress of $10\,MPa$, corresponding to a load of approximately $9\,kN$. This is several orders of magnitude higher than the weight of the body. It is emphasized that this purely compressive load does not correspond to *in vivo* conditions which involve intervertebral discs and perhaps a bending load. *In vitro* experiments carried out on vertebral bodies have shown that they can support forces higher than $600\,kg$ ([Zysset, 2005]). This non-physiological high load should damage the vertebral body and serve as a basis for showing the potential of our constitutive law.

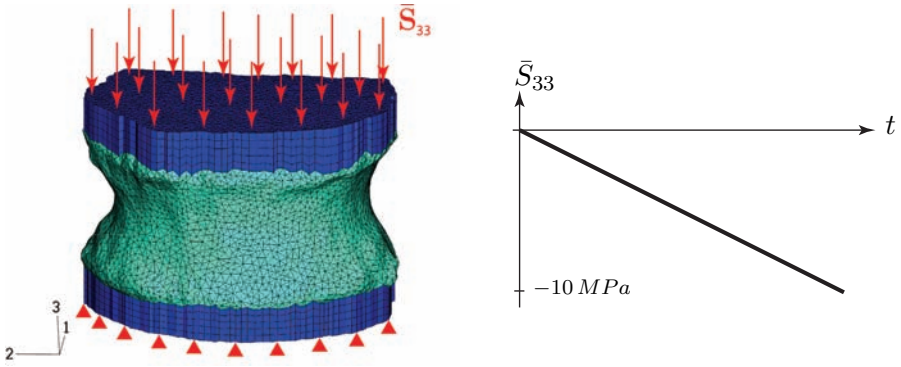

Figure 7.4: Boundary conditions imposed to the finite element model.

7.2 Results

The mechanical state of the lumbar vertebral body (of the trabecular and cortical bone elements) are expressed in terms of:

- the von Mises equivalent stress, defined as $v := ||\frac{3}{2}\mathbf{S}'||$ where $\mathbf{S}'$ is the deviatoric stress tensor ($\mathbf{S}' := \mathbf{S} - \frac{1}{3}\,\mathrm{Tr}\,\mathbf{S}\,\mathbf{I}$)

- the equivalent pressure stress, defined as $\pi := -\frac{1}{3}\operatorname{Tr}\mathbf{S}$
- the damage variable D, ranging from 0 to 1 (0 for an intact and 1 for a completely damaged element)
- the normal anisotropic stress invariant, defined as $n := \operatorname{Tr}(\mathbf{M}_3\mathbf{S})$ and representing the normal stress along the principal direction $\mathbf{m}_3$.

Approximately eight hours were necessary to a 8 processors (RISC $450\,MHz$, $8\,Mbytes$ RAM pro processor) SGI Origin 2000 workstation to achieve the simulation. The computation required ten time increments. Within each increment, convergence of the projection algorithm was reached in one single iteration for the elastic mode and typically three iterations for the damaging mode.

In order to discuss more precisely the mechanical state of the lumbar vertebral body, let us divide the cortical bone elements enclosing the trabecular core into the *cortical shell* and the *endplates*. We define the cortical shell as the cylindrical (vertical) part of cortical bone and the two endplates as the horizontal plates of cortical bone in contact with the two PMMA plates.

The largest vertical displacement was of $-1.2 \cdot 10^{-1}\,mm$ and occurred at an anterior cranial endplate node. The extrema of the equivalent von Mises stress υ, pressure π, damage variable D and normal anisotropic stress invariant n are given in Table 7.7.

	$\upsilon\,[MPa]$	$\pi\,[MPa]$	D	$n\,[MPa]$
min	0.9	−33.4	0.0	−29.0
max	142.7	60.9	0.82	31.5

Table 7.7: Extrema of the equivalent von Mises stress υ, pressure π, damage variable D and normal anisotropic stress invariant n of the trabecular and compact bone finite element model.

The distributions of these quantities within the vertebral body are shown in Figures 7.5 to 7.8, respectively.

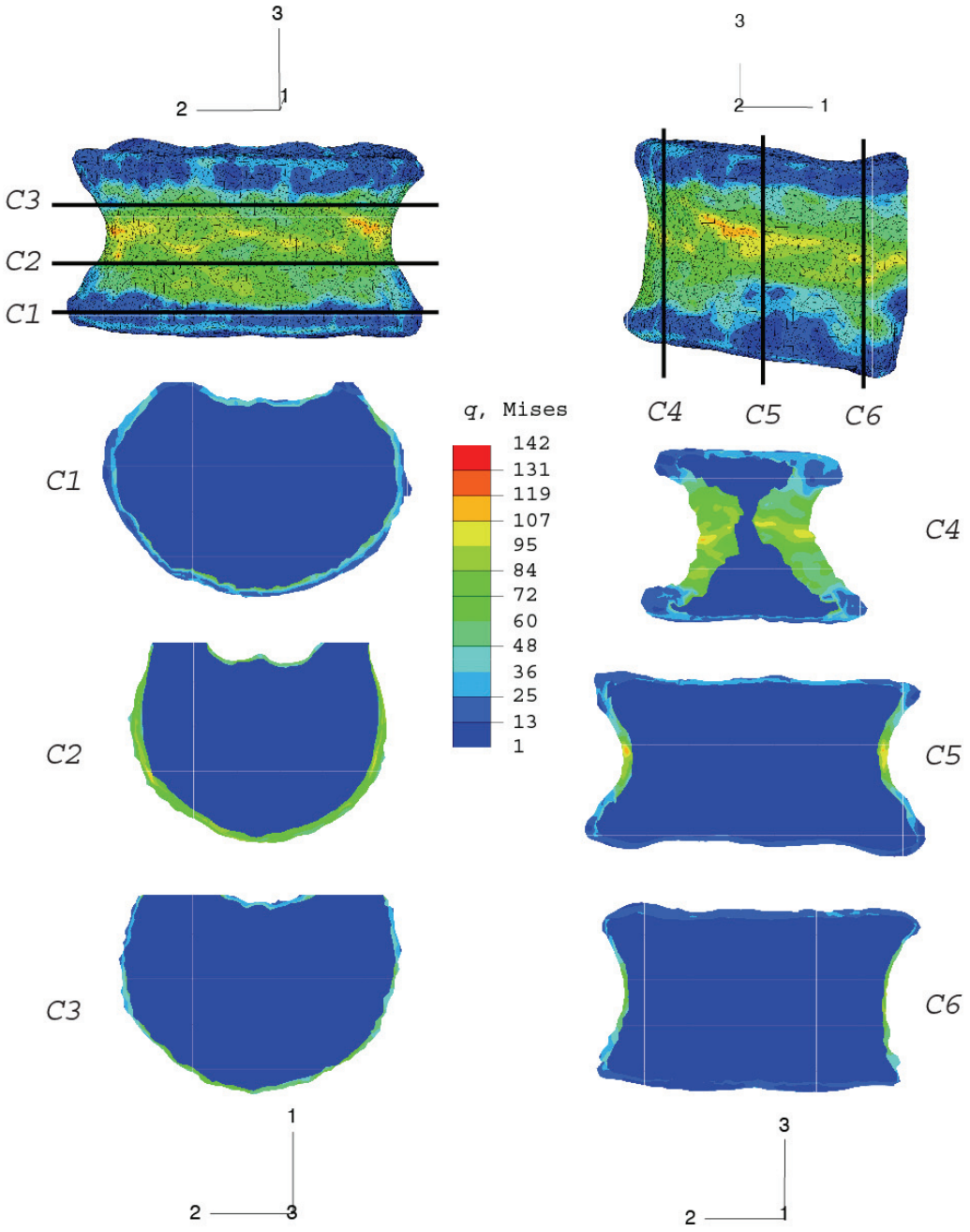

Figure 7.5: Von Mises equivalent stress $\upsilon\,[MPa]$ (q in the Figure).

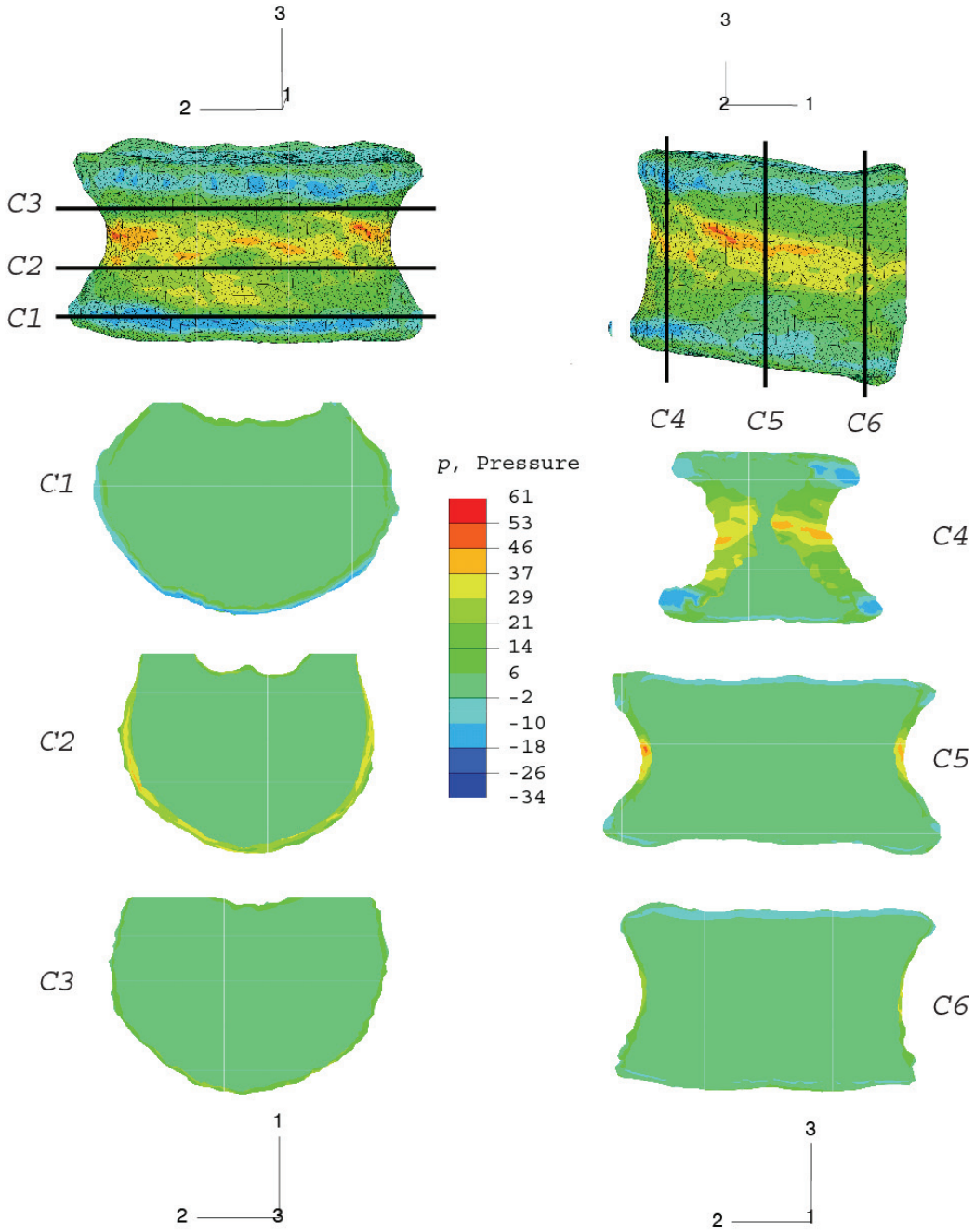

Figure 7.6: Pressure equivalent stress $\pi\,[MPa]$ (p in the Figure).

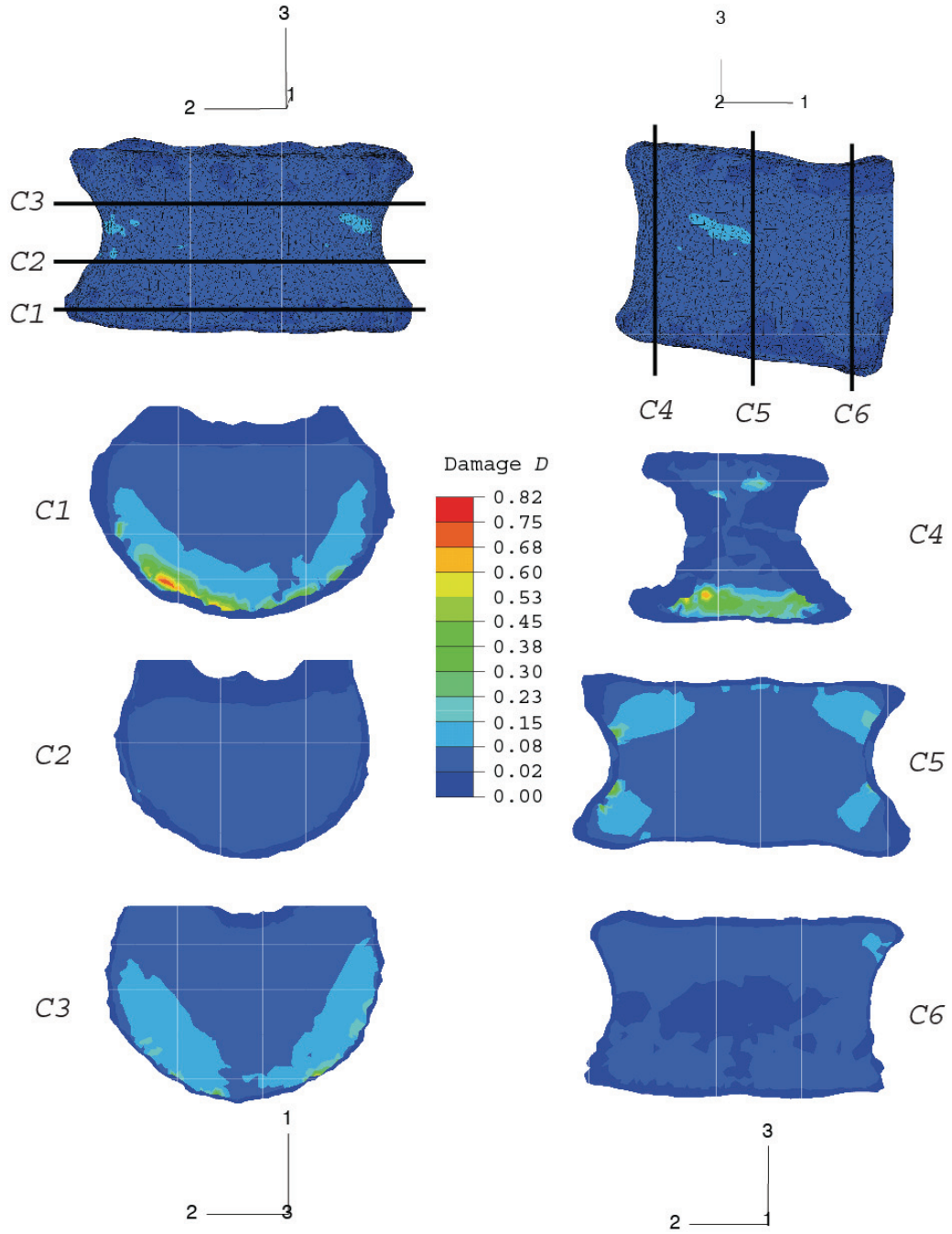

Figure 7.7: Damage variable D.

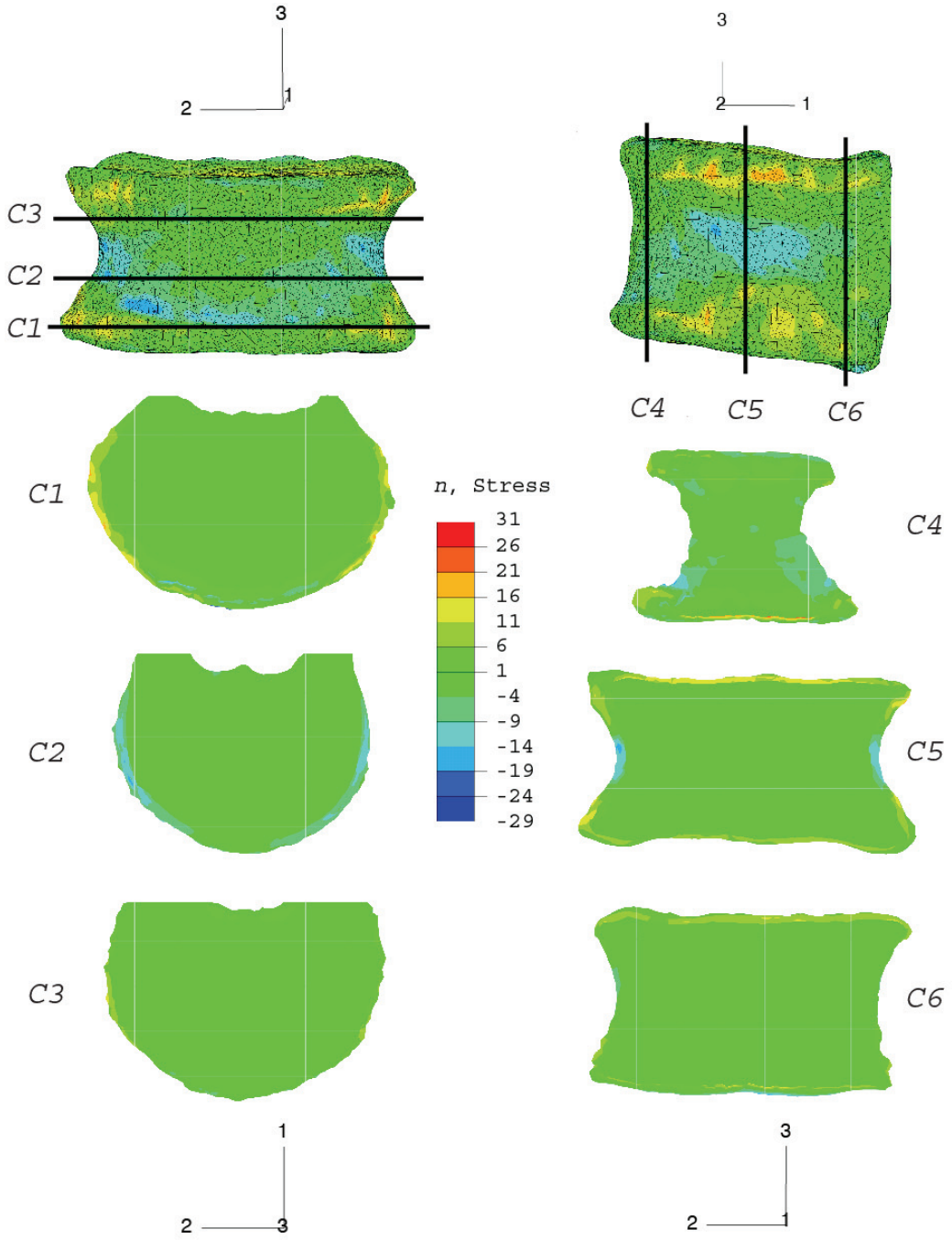

Figure 7.8: Normal anisotropic stress invariant $n\,[MPa]$.

7.3 Discussion

The finite element mechanical analysis can help to understand injury mechanisms and stress distribution patterns within vertebral bodies in clinical evaluation of spinal injuries (e.g. [Mizrahi et al., 1993, Silva et al., 1998]). We insist on the fact that the clinical relevance of this study is moderate for several reasons. Firstly, there is a crucial lack of information concerning local structural density and material orientations in the studied body. Secondly, the assumption that the same damage model can be applied for both trabecular and compact bone does not take into account the collapse of trabecular bone observed in compression overloads. The objective of this study was rather to demonstrate the applicability of the elastic plastic damage constitutive law for bone tissue presented in the previous Chapter. Intensive experimental investigations should be carried out in order to properly identify the material constants of the model, the fracture patterns and to validate the simulation results. However, an exact vertebral body geometry associated to realistic experimental conditions and plausible material constants may allow us to draw some useful conclusions.

Due to the high resolution of the μCT scanner ($82\,\mu m$), the shell thickness should not be overestimated in our finite element model ([Liebschner et al., 2003]). The mean value of the cortical shell thickness lies in the range of 0.18-0.6 mm ([Silva et al., 1994]). The reader should not be mislead by the apparent high values of cortical shell thickness visible in the cross-sections of Figures 7.5 to 7.8. Indeed, the cross-sections are actually not geometrical planes but $1\,mm$ thick layers of elements.

The largest von Mises stresses are experienced by the middle anterior cortical shell elements (Figure 7.5). This may lead to the most common type of vertebral compression fractures, namely the anterior wedge fracture ([Old and Calvert, 2004]). The distribution is approximately symmetric with respect to the sagittal and transverse planes. The von Mises stresses are weaker in the caudal and cranial endplates and their distribution is approximately uniform and of small magnitude in the trabecular bone elements.

The equivalent pressure follows a similar distribution than the von Mises stress distribution (Figure 7.6). High (positive or compressive) pressures occur for the middle transverse shell elements, whereas low (negative or tensile) pressures are found in the caudal and cranial endplate elements. Due to the concave deformation of the endplates, large tension stresses are generated in the anterior regions of the cortical shell. The load is distributed to the peripheral cortical shell through the bending effect. Similar results were found by [Chen et al., 1999]. The pressure distribution is also uniform and

of small magnitude within the vertebrae (in the trabecular bone elements).

Interestingly, important damage values are strongly localized and affect mainly the anterior trabecular bone elements which are near the endplates (Figure 7.7). This suggests that the contribution of the trabecular bone to the total load depends strongly on the location within the vertebra. Near the endplates, the trabecular bone carries most of the load, whereas toward the middle of the vertebra the load is more evenly distributed between the cortical shell and the trabecular bone. This result is confirmed in the study of [Liebschner et al., 2001]. [Homminga et al., 2004] found that for a healthy vertebra, the contribution of the trabecular core is larger than in an osteoporotic case. This strong and localized accumulation of damage may thus cause the anterior part of the vertebral body to crush, forming an anterior wedge fracture.

The highest values of the normal anisotropic stress invariant are found in the endplate elements (Figure 7.8). They confirm the tensile and compressive stress patterns related to bending of the vertebral body.

Generally, ten times physiological loading happens only during extraordinary severe trauma such as an automobile crash or a hard fall. However, we expect similar damage accumulation mechanisms and compression fracture patterns at lower loads in cases of moderate or severe osteoporosis. A uniform distribution of the load within the vertebra is usually the case in healthy bones. Osteoporotic vertebrae exhibit an altered micro-architecture which could result in an uneven distribution of the load, facilitating localized damage. Furthermore, cyclic loading at lower amplitudes leading to fatigue damage may also have similar damaging consequences. Indeed, most vertebral fractures have a gradual onset and remain clinically undetected. They are thought to be the result of normal daily activities rather than traumatic events ([Melton et al., 1992]). In that case, fatigue damage enters in competition with bone remodelling processes and may lead to fractures if the balance is not respected in the long term.

In conclusion, the proposed constitutive law for cortical bone has been successfully applied to a real bone geometry and contains its main behavioural characteristics, namely anisotropy and inhomogeneity, elasticity, plasticity and damage which are closely related. Thus, it may be an efficient and complementary tool for the prevention and treatment of osteoporotic fractures (e.g. [Bono, 2003]).

It gives an useful insight into the damaging behaviour of a vertebra and shows several features which would be occulted if a linear elastic behaviour were used (e.g. [Crawford et al., 2003]). The strong localization of damage within the trabecular structure and permanent strains undergone

after unloading the vertebra are two of them.

Another advantage of our model is that it may reasonably be applied to both compact and trabecular bone tissues (using different material constants). This is mainly due to the similar chemical composition of both tissues and to a formulation of the constitutive law based on volume fraction and fabric. Nevertheless, the constitutive law for trabecular bone adopted in this study did not include pore collapse for high overloading situations.

Chapter 8

Conclusion

The objective of this research was to develop new constitutive laws for cortical bone with emphasis on cyclic overloads at physiological strain rates. In order to reach this objective, we proceeded in five steps:

(i) Two original rate-independent one-dimensional theoretical models combining elasticity, plasticity and damage are formulated in the framework of generalized standard materials. They involve different tensile and compressive damage threshold stresses.

(ii) These models are then extended into rate-dependent alternatives aiming at a more realistic description of the damage behaviour of cortical bone.

(iii) A number of pilot *in vitro* uniaxial experiments have been carried out on bovine cortical bone to check the relevance of the proposed models and identify the material constants.

(iv) Motivated by the explanatory power of finite element analysis of whole bones, a new three-dimensional elastic plastic damage law inspired by the one-dimensional models is formulated. Its orthotropic elasticity and damage is based on porosity and fabric whereas its rate-independent hardening plasticity is based on the fourth-order orthotropic compliance tensor. It takes into account distinct tensile and compressive damage threshold stresses.

(v) This law is then implemented in a mechanical analysis software mainly with the help of implicit projection algorithms and calculus of consistent tangent operators. The potential of the law is demonstrated by means of a finite element analysis of the compression of a vertebra.

8.1 Summary of results

We now discuss in more details the main features and results of the aforementioned contributions.

(i) The free energy potential of the first one-dimensional model is based on two internal state variables: a scalar damage variable that represents the microcrack density and a plastic strain variable representing the deformation associated with these microcracks. The damage variable has another simple interpretation: it represents the stiffness reduction of bone. The dissipation potential expresses rate-independent plasticity and damage with distinct damage thresholds in tension and compression. The originality of this model does not lie in the mounting of the rheological elements (which is a straightforward variation of the classical standard model), but in the choice of the stiffness of the damageable spring, of the plastic and damage criteria and their respective evolution with damage.

An elastic spring with constant stiffness mounted in series accounts for the unaltered response of the extracellular bone matrix. A plastic pad accounts for plastic damage due to microcracks. Initially equal to zero, its thresholds increase with the accumulated damage. A damageable spring accounts for bone elastic damage due to microcracks. In short, damage results into a decrease of elastic stiffness but an increase of plastic resistance.

This model approximates well the loading, unloading and reloading sequence observed experimentally on cortical bone. Nevertheless, most experiments exhibit a damaged reloading which is collinear with the origin. To include this important feature in our law, the model is extended by replacing the single damage variable by two independent damage variables (one in tension and the other in compression). The originality of this new model lies in a special form of kinematic plastic hardening which guarantees a damaged reloading collinear with the origin. This constitutive law captures, for the first time, the main features of the quasistatic mechanical behaviour of cortical bone.

(ii) Rate-dependent effects were then taken into account in order to formulate a more realistic constitutive law. As our experiments and others have shown that viscoelastic effects are relatively small at physiological strain rates, but that rate-dependent effects are more pronounced in the overloading regime, we chose to include them only during damage accumulation. Thus, the proposed models may not be appropriate for impact studies. Following the ideas of [Carter and Caler, 1985] in their cumulative damage model for bone fracture, the rate of damage accumulation of our rate-dependent models is related to some high power of the damage threshold stresses.

In summary, depending on the conditions of interest, we propose four new one-dimensional constitutive laws for cortical bone which describe satisfactorily its mechanical behaviour in tension or compression:

1. in monotonic quasistatic overloads;
2. in cyclic quasistatic overloads;
3. in monotonic overloads at physiological strain rates; and
4. in cyclic overloads at physiological strain rates, respectively.

(iii) A series of *in vitro* uniaxial mechanical tests were carried out on bovine cortical bone to check the applicability of the proposed models and to identify their material constants. Artefacts associated to inhomogeneous boundary conditions were avoided using dumbbell specimens and thus allowing for a good quantification of the overloading plastic and damage processes in tension.

Purely tensile tests provided excellent results which could be related to the predictions of the proposed models in a very satisfactory manner. Nevertheless, due to experimental instabilities, many of our compressive overloads did not show the expected behaviour. Indeed, the small section of the specimens ($3\,mm$ in diameter) added to inhomogeneities of cortical bone and inhomogeneous stress distribution in the specimens facilitated their rupture in compression. However, a few successful experiments of our own and several ones carried out by others show a similar damaged behaviour in tension and compression, a feature which is included in all our models.

The cyclic tests mixing tension and compression exhibited a feature which is not included in our models. Indeed, the closing of cracks occurring when crossing from the tensile to the compressive domain leads to a stiffening of the observed material response. This has also been observed in concrete and it is emphasized that it is not an experimental artefact. Thus, an improvement of the models with different elastic damage in tension and compression would be required to take this behaviour into account.

Identification of the material constants interestingly showed that the true elastic domain of cortical bone is extremely small. Thus, it is more realistic to choose low damage threshold stresses and to define exponential hardening functions and power law damage evolution rules.

(iv) The three-dimensional law for cortical bone proposed in this thesis is based on a straightforward generalization of the one-dimensional rate-independent model with a single damage variable. The rheological setup is similar to the one-dimensional mounting and includes an original combination of existing three-dimensional elastic and damage models for bone.

The elasticity of bone is described by the orthotropic porous model based on a second-order fabric tensor and referred to as the Zysset-Curnier model in the literature ([Zysset, 1994, Zysset and Curnier, 1995]). The reasons why we chose this model lie in the reduced number of material constants and its applicability to both cortical and trabecular bone. Furthermore, its material constants have been carefully identified ([Zysset, 2003]).

The orthotropic stress-based damage criterion with different tensile and compressive thresholds formulated by [Zysset and Rincón, 2005] is used. This model was retained because it is also based on porosity and fabric involving thus a minimal number of material constants. Furthermore, its material constants have been successfully identified for trabecular bone in multiaxial testing by [Rincón, 2003, Zysset and Rincón, 2005].

A strong limitation of the proposed three-dimensional model lies in the choice of the damage variable. Indeed, a scalar damage variable altering isotropically all constants of the elastic tensor is a rather naive description of the anisotropic damage processes occurring in bone. Even if it may be appropriate for proportional loadings, high order tensorial damage variables should be used for complex deformation paths.

(v) The numerical implementation of the three-dimensional law into a mechanical analysis software was done in a straightforward manner. Implicit (radial return) projection algorithms are used for plastic flow calculation and the generalized Newton method is used to overcome the nonlinearities associated with damage evolution and hardening. Consistent (algorithmic) tangent operators are derived in order to ensure rapid convergence of the global Newton algorithm. A large number of validation tests have proven the accuracy and convergence of the final algorithm.

The biomechanical evaluation of a compression of a vertebra showed the potential of the implemented model. The *same* constitutive laws were used for cortical and trabecular bone, but with different porosities. The simulation results show a strong localization of damage within the trabecular structure which may cause the anterior part of the vertebral body to crush. Furthermore, if unloaded, the damaged vertebra undergoes permanent strains which would be occulted if a linear elastic behaviour were used. Thus, taking nonlinear material behaviour such as plasticity and damage into account can help to understand injury mechanisms and stress distribution patterns within vertebrae in clinical evaluation of spinal injuries. In conclusion, our numerical model represents a good compromise between complexity and realism for the simulation of the mechanical behaviour of bone at the continuum level and shows a promising potential.

8.2 Perspectives

The perspectives of this research are multiple. Firstly, the one-dimensional models can be improved further in order to describe realistically the stiffening behaviour of cortical bone observed experimentally in tests mixing tension and compression. Secondly, the formulation of the plasticity of the three-dimensional model should be enhanced by changing its yield criterion which does not describe plastic deformations at constant volume. Thirdly, the hardening functions of the three-dimensional law must be adapted by means of an appropriate kinematic hardening in order to guarantee a damaged reloading collinear with the origin. Fourthly, viscous damage should be included in its formulation to account for rate-dependent effects. Fifthly, a viscoelastic component should be added to the models for impact studies involving high strain-rate dependences. Finally, data must be collected about the mechanical behaviour of bone under complex, time-dependent, multiaxial loading conditions in order to further validate and identify the proposed models.

8.3 Summary of original contributions

To conclude, we recall the *significant contribution* of this thesis:

- Original one- and three-dimensional constitutive laws for cortical bone are formulated in the framework of generalized standard materials. They combine elasticity, plasticity and damage and reproduce faithfully the experimental mechanical behaviour of cortical bone in cyclic uniaxial overloads.
- The material constants of the one-dimensional models are identified on experimental grounds with a method avoiding boundary effects.
- Implicit projection algorithms are formulated and consistent tangent operators are computed in the cases of plasticity and damage.
- The biomechanical relevance of the three-dimensional model is evaluated by simulating the compression of a vertebra.

The developed constitutive laws will hopefully contribute to evaluate fracture risk *in vivo* and help to design orthopaedic implants. Note that one of our one-dimensional model have been adapted and showed a very promising potential for car crash simulations ([Jundt et al., 2005]).

List of symbols

Greek

α	damage term
α_a	interface hyperplane coefficients
$\mathbf{\Gamma_y}$	boundary of $\mathbf{\Omega}$ with prescribed displacement BC
$\mathbf{\Gamma_p}$	boundary of $\mathbf{\Omega}$ with prescribed load BC
ϵ	Young's modulus
ϵ_0	intact Young's modulus
ϵ_a	Young-like elastic moduli
ϵ_D	damaged Young's modulus
ε_0	Young's modulus for a poreless material
ζ	viscosity factor of the power law damage evolution rule
η	viscosity coefficient
κ	compressibility modulus
λ	bulk Lamé coefficient
λ^p	plastic Lagrangian multiplier
Λ^p	rate-like plastic Lagrangian multiplier
λ^D	damage Lagrangian multiplier
Λ^D	rate-like damage Lagrangian multiplier
λ_{ab}	bulk Lamé-like coefficients
λ_{+ab}	tensile orthotropic elastic constants
λ_{-ab}	compressive orthotropic elastic constants
μ_0	shear modulus for a poreless material
μ	shear Lamé coefficient
μ_a	shear Lamé-like coefficients
μ_{ab}	shear moduli
ν	Poisson's ratio
ν_0	Poisson's ratio for a poreless material
ν_{ab}	Poisson-like ratios
$\boldsymbol{\xi}$	natural coordinates

$\boldsymbol{\xi}^l$	integration point natural coordinates
π	pressure equivalent stress
$\rho(\boldsymbol{x})$	density
ρ_a	apparent density
ρ_s	volume fraction or structural density
σ_i	eigenvalues of $\mathbf{S}^p$
σ_0^+	uniaxial tensile strength for a poreless material
σ_0^-	uniaxial compressive strength for a poreless material
σ_{ii}^+	uniaxial tensile strength along axis i
σ_{ii}^-	uniaxial compressive strength along axis i
$\sigma_+^D(D)$	tensile threshold damage stress
$\sigma_-^D(D)$	compressive threshold damage stress
σ_{0+}^D	initial tensile threshold damage stress
σ_{0-}^D	initial compressive threshold damage stress
σ^p	radius or plastic yield stress
τ	time increment
τ_0	shear strength for a poreless material
τ_{ij}	shear strength in the plane ij
υ	von Mises equivalent stress
φ	mechanical dissipation per unit volume
ϕ	part of the damage dissipation potential
ϕ_+^*	tensile part of Φ^{D*}
ϕ_-^*	compressive part of Φ^{D*}
Φ	dissipation potential
Φ^p	plastic dissipation potential
Φ^D	damage dissipation potential
Φ^*	dual dissipation potential
Φ^{p*}	plastic dual dissipation potential
Φ^{D*}	damage dual dissipation potential
χ^p	plastic hardening coefficient
χ^D	damage hardening coefficient
χ_0^+	stress interaction coefficient for a poreless material
χ_0^-	stress interaction coefficient for a poreless material
χ_{ij}^+	stress interaction coefficients
χ_{ij}^-	stress interaction coefficients
Ψ	free energy potential
Ψ^*	dual free energy potential
$\boldsymbol{\omega}$	subset of $\boldsymbol{\Omega}$
$\partial\boldsymbol{\omega}$	boundary of $\boldsymbol{\omega}$
Ω^l	weight associated to $\boldsymbol{\xi}^l$
$\boldsymbol{\Omega}$	reference configuration (at time $t = 0$)

$\boldsymbol{\Omega}_t$	present configuration (at time t)
${}^e\boldsymbol{\Omega}$	subset of $\boldsymbol{\Omega}$ occupied by element e
$\partial\boldsymbol{\Omega}$	boundary of $\boldsymbol{\Omega}$
$\partial\boldsymbol{\Omega}_t$	boundary of $\boldsymbol{\Omega}_t$

Latin

A	initial specimen area
$\mathbf{A}_a$	second-order anisotropic basis tensors
$\mathbb{A}$	fourth-order damage tensor term
$b^n(\boldsymbol{x})$	global basis function
${}^eb^a(\boldsymbol{x})$	local basis function
$\mathbb{B}$	solid body
$\mathbb{B}$	fourth-order damage tensor term
$\mathbf{C}(\boldsymbol{x},t)$	right Cauchy-Green material metric tensor
$\mathbb{C}$	fourth-order compliance tensor
$\overline{\mathbb{C}}$	fourth-order hydrostatic compliance tensor
$\mathbb{C}'$	fourth-order deviatoric compliance tensor
(D)	damage mode
D	scalar damage variable
D_0	initial damage
$\mathbf{D}(\boldsymbol{x},t)$	second-order spatial deformation velocity tensor
D_+	scalar tensile damage variable
D_-	scalar compressive damage variable
$\mathcal{D}_{\{.\}}$	distance function to $\{.\}$
$\mathrm{d}A$	elementary surface element
$\mathrm{d}V$	elementary volume element
$\mathrm{d}\boldsymbol{x}$	original material fiber
$\mathrm{d}\mathbf{y}$	actual material fiber
e	compliance jump at the interface
$\mathbf{e}_i$	canonical basis of $\mathbb{R}^3$
(E)	initial and subsequent linear elastic mode
E	scalar Green-St Venant Lagrangian material strain
E_{ij}	cartesian components of $\mathbf{E}$
$\mathbf{E}(\boldsymbol{x},t)$	Green-St Venant Lagrangian material strain tensor
E_0	initial scalar strain
$\mathbf{E}_0$	initial second-order strain tensor
E^e	scalar elastic strain
$\mathbf{E}^e$	second-order elastic strain tensor
E^p	scalar plastic strain
$\mathbf{E}^p$	second-order plastic strain tensor

E_0^p	initial scalar plastic strain
$\mathbf{E}_0^p$	initial second-order plastic strain tensor
$f(D)$	damage solution function
$f_+(D)$	tensile damage solution function
$f_-(D)$	compressive damage solution function
$\mathbf{F}(\boldsymbol{x}, t)$	deformation gradient
$\mathbb{F}$	fourth-order damage criterion tensor
$\mathbb{F}_+$	fourth-order tensile damage criterion tensor
$\mathbb{F}_-$	fourth-order compressive damage criterion tensor
$g_+(D)$	tensile damage energy function
$\overline{\mathbf{g}}^t(\boldsymbol{\Omega}, t)$	resultant body force vector
$\mathbf{g}^t(\boldsymbol{x}, t)$	nominal body force vector
G_{ab}	shear moduli
$\mathbb{G}$	fourth-order plasticity criterion tensor
$h(D)$	quasistatic damage energy threshold
$h_+(.)$	tensile quasistatic damage energy threshold
$h_-(.)$	compressive quasistatic damage energy threshold
H	stretch
$\mathbf{H}(\boldsymbol{x}, t)$	displacement gradient
$\mathbb{H}^p(\mathbf{S}^p)$	fourth-order plastic hessian operator
$I(t)$	internal entropy production
$I_{\{.\}}$	indicator function of $\{.\}$
$\mathbf{I}$	symmetric second-order identity tensor
$j(\boldsymbol{\xi})$	jacobian of the isoparametric transformation
$J(\boldsymbol{x}, t)$	jacobian of the transformation
k	damage hardening coefficient
$\mathbf{k}$	principal direction of orthotropy
l	plastic hardening coefficient
L	initial gauge length
L_t	actual gauge length
$\mathbf{L}$	spatial velocity of the transformation
${}^e\mathbf{L}$	localization matrix
${}^e\mathbf{L}^{\mathrm{T}}$	scatter matrix
$m(\mathbf{S})$	stress interface hyperplane
m_i	orthotropic eigenvalues
$\mathbf{m}$	principal direction of transverse isotropy or orthotropy
$\mathbf{m}_i$	principal directions of orthotropy
$\overline{\ddot{\mathbf{m}}}^t(\boldsymbol{\Omega}, t)$	resultant inertial force vector
$\mathbf{M}$	unit normal tensor to the interface hyperplane $m(\mathbf{S})$
$\hat{\mathbf{M}}$	fabric tensor

$\mathbf{M}_i$	structural tensors
n	normal anisotropic stress invariant
$n(\mathbf{E})$	strain interface hyperplane
$\mathbf{n}$	principal direction of orthotropy
$\mathbf{n}(\boldsymbol{x})$	outward normal vector
N	exponent of the power law damage evolution rule
$\mathbf{N}$	unit normal tensor to the interface hyperplane $n(\mathbf{E})$
$\mathbf{N}^p(\mathbf{S}^p)$	outward normal of the plastic criterion in stress space
$\mathbf{N}^D(\mathbf{S}^D)$	outward normal of the damage criterion in stress space
`NDIM`	spatial dimension of the integration domain
`NELE`	total number of elements
`NODE`	total number of nodes
`NSTEPS`	total number of time steps
p	porosity exponent for fabric-based damage criterion
$\bar{p}$	applied load
$\overline{\mathbf{p}}(\partial\boldsymbol{\Omega}, t)$	resultant contact force vector
$\mathbf{p}(\boldsymbol{x}, t, \mathbf{n}(\boldsymbol{x}))$	nominal stress vector
$\bar{\mathbf{p}}$	applied load
(P)	plastic mode
$\overline{P}^{\,ext}(t)$	external power of deformation
$\overline{P}^{\,inertia}(t)$	inertial power of deformation
$\overline{P}^{\,int}(t)$	internal power of deformation
$\overset{\circ}{\overline{P}}{}^{\,ext}(t)$	external virtual power of deformation
$\overset{\circ}{\overline{P}}{}^{\,inertia}(t)$	inertial virtual power of deformation
$\overset{\circ}{\overline{P}}{}^{\,int}(t)$	internal virtual power of deformation
P_Q^{ext}	heat supply to a volume element
$\mathbf{P}(\boldsymbol{x}, t)$	first nominal Piola-Kirchhoff stress tensor
$\mathbb{P}$	fourth-order continuous tangent operator
$\mathbb{P}^e$	fourth-order elastic continuous tangent operator
$\mathbb{P}^p$	fourth-order plastic continuous tangent operator
$\mathbb{P}^D$	fourth-order damage continuous tangent operator
$\mathbb{P}_a^e$	fourth-order elastic algorithmic tangent operator
$\mathbb{P}_a^p$	fourth-order plastic algorithmic tangent operator
$\mathbb{P}_a^D$	fourth-order damage algorithmic tangent operator
$\mathbb{P}_{\mathrm{AB}}$	exact consistent ABAQUS tangent operator
q	anisotropy exponent for fabric-based damage criterion
$r^D(D)$	radius of damage criterion
$\mathtt{r}(\mathtt{u})$	global nodal residual force vector
$\mathbb{R}$	real numbers
$\mathbb{R}_+$	positive real numbers

$\mathbb{R}_-$	negative real numbers
RD	rate-dependent elastic plastic damage model
RD±	RD model with two distinct damage variables
RI	rate-independent elastic plastic damage model
RI±	RI model with two distinct damage variables
s	elasticity jump at the interface
$\mathcal{S}$	entropy
S	scalar material Piola-Kirchhoff-2 stress
S_0	initial stress
S_{T}	trial stress
S_Ψ	scalar material stress deriving from Ψ
$\bar{S}$	applied scalar stress
S'_λ	subderivative of S
S_{ij}	cartesian components of $\mathbf{S}$
$\mathbf{S}(\boldsymbol{x}, t)$	second material Piola-Kirchhoff stress tensor
$\mathbf{S}_\Psi$	second-order material stress tensor deriving from Ψ
$\mathbf{S}'$	second-order deviatoric material stress tensor
S^D	scalar stress in the damageable spring
S_0^D	scalar initial stress in the damageable spring
S_{T}^D	scalar trial stress in the damageable spring
$\mathbf{S}^D$	second-order damageable spring stress tensor
$\mathbf{S}_0^D$	second-order damageable spring initial stress tensor
$\mathbf{S}_{\mathrm{T}}^D$	second-order damageable spring trial stress tensor
$\mathbf{S}_U^e$	second-order elastic stress tensor deriving from U
S^p	scalar plastic stress
S_0^p	scalar initial plastic stress
S_{T}^p	scalar trial plastic stress
S_Ψ^p	scalar plastic stress deriving from Ψ
S_Φ^p	scalar plastic stress deriving from Φ
$\mathbf{S}^p$	second-order plastic stress tensor
$\mathbf{S}_0^p$	second-order initial plastic stress tensor
$\mathbf{S}_{\mathrm{T}}^p$	second-order trial plastic stress tensor
$\mathbf{S}_U^p$	second-order plastic stress tensor deriving from U
$\mathbf{S}_\Phi^p$	second-order plastic stress tensor deriving from Φ
$\mathbf{S}_\Psi^p$	second-order plastic stress tensor deriving from Ψ
$\mathbf{S}_U^v$	second-order viscous stress tensor deriving from U
$\mathbf{S}_\Phi^v$	second-order viscous stress tensor deriving from ϕ
$\mathbf{S}\mathrm{ym}$	space of symmetric second-order tensors
$\mathbb{S}$	fourth-order elasticity (stiffness) tensor
$\overline{\mathbb{S}}$	fourth-order hydrostatic stiffness tensor
$\mathbb{S}'$	fourth-order deviatoric stiffness tensor

$\mathbb{S}^{ISOT}$	fourth-order isotropic stiffness tensor
$\mathbb{S}^{TRAN}$	fourth-order transverse isotropic stiffness tensor
$\mathbb{S}^{ORTHO}$	fourth-order orthotropic stiffness tensor
$\mathbb{S}_{+}$	fourth-order tensile stiffness tensor
$\mathbb{S}_{-}$	fourth-order compressive stiffness tensor
$\mathbb{S}_{a}$	fourth-order plastic tensor term
$\mathbb{S}_{ad}$	fourth-order damage tensor term
$\mathbb{S}_{D}$	fourth-order damaged stiffness tensor
t	time
T	temperature
$\mathbf{T}(\mathbf{y}, t)$	spatial Cauchy stress tensor
`TFINAL`	total time of the simulation
$\mathbb{T}$	tangent matrix
$\mathbf{u}(\boldsymbol{x}, t)$	displacement vector
$\mathbf{u}^n(t)$	displacement of node n
${}^e\mathbf{u}(\mathbf{x}, t)$	local displacement
${}^e\mathbf{u}^a(t)$	local displacement of node a
${}^e\hat{\mathbf{u}}(\boldsymbol{\xi}, t)$	local natural displacement
$\bar{\mathbf{u}}(\boldsymbol{x}, t)$	prescribed displacement
$\mathbf{u}^*$	displacement solution of the Newton iteration method
$\mathbb{u}$	discrete global displacement vector
U	internal energy per unit volume
v	porosity exponent for fabric-based elasticity
$\mathbf{v}_0$	initial prescribed velocity
w	anisotropy exponent for fabric-based elasticity
$\mathbf{w}(\boldsymbol{x}, t)$	virtual displacement vector
$\mathbf{w}^n(t)$	virtual displacement of node n
${}^e\mathbf{w}(\mathbf{x}, t)$	local virtual displacement
${}^e\mathbf{w}^a(t)$	local virtual displacement of node a
W^D	damage energy
W_0^D	initial damage energy
W_{T}^D	trial damage energy
W_U^D	damage energy deriving from U
W_Ψ^D	damage energy deriving from Ψ
W_Φ^D	damage energy deriving from Φ
W_Ψ^{D+}	tensile damage energy deriving from Ψ
W_Ψ^{D-}	compressive damage energy deriving from Ψ
W_Φ^{D+}	tensile damage energy deriving from Φ
W_Φ^{D-}	compressive damage energy deriving from Φ
x_i	reference position vector components
$\boldsymbol{x}$	reference position vector

$\mathbb{x}$	discrete global reference position vector
${}^{e}\mathbb{x}$	local reference position vector
$y_i(\boldsymbol{x}, t)$	present deformed position vector components
$\mathbf{y}(\boldsymbol{x}, t)$	present deformed position vector
$\bar{\mathbf{y}}$	prescribed position
$\mathring{\mathbf{y}}$	virtual velocity
Y	initial damage threshold function
Y^p	plastic yield function
Y^D	damage threshold function

Appendix A

3D calculus

In this Appendix we give some useful three-dimensional calculus formulas. $\alpha, \beta, \ldots$ are for scalars, $\mathbf{a}, \mathbf{b}, \ldots$ for vectors, $\mathbf{A}, \mathbf{B}, \ldots$ for second-order tensors and $\mathbb{A}, \mathbb{B}, \ldots$ for fourth-order tensors.

Dyadic product

$$(\mathbf{a} \otimes \mathbf{b})\,\mathbf{x} = (\mathbf{x} \cdot \mathbf{b})\,\mathbf{a}\,, \quad \forall\,\mathbf{x} \tag{A.1}$$

$$(\mathbf{a} \otimes \mathbf{b})(\mathbf{c} \otimes \mathbf{d}) = (\mathbf{b} \cdot \mathbf{c})(\mathbf{a} \otimes \mathbf{d}) \tag{A.2}$$

$$(\mathbf{m} \otimes \mathbf{m})(\mathbf{m} \otimes \mathbf{m}) = \mathbf{m} \otimes \mathbf{m} \quad \text{if} \quad ||\mathbf{m}|| = 1 \tag{A.3}$$

$$(\mathbf{A} \otimes \mathbf{B})\,\mathbf{X} = (\mathbf{X} : \mathbf{B})\,\mathbf{A}\,, \quad \forall\,\mathbf{X} \tag{A.4}$$

Transpose

$$\mathbf{a} \cdot \mathbf{B}\mathbf{c} = \mathbf{B}^{\mathrm{T}}\mathbf{a} \cdot \mathbf{c} \tag{A.5}$$

$$[\mathbf{A} \otimes \mathbf{B}]^{\mathrm{T}} = \mathbf{B} \otimes \mathbf{A} \tag{A.6}$$

Scalar product

$$\mathbf{A} : \mathbf{B} = \mathrm{Tr}\,(\mathbf{A}^{\mathrm{T}}\,\mathbf{B}) \tag{A.7}$$

$$(\mathbf{A} : \mathbf{B}\mathbf{C}\,)\,\mathbf{D}\mathbf{E} = (\,\mathbf{D}\mathbf{E} \otimes \mathbf{B}^{\mathrm{T}}\mathbf{A})\,\mathbf{C} \tag{A.8}$$

Norm

$$||\mathbf{a}|| = \sqrt{\mathbf{a} \cdot \mathbf{a}} \tag{A.9}$$

$$||\mathbf{A}|| = \sqrt{\mathbf{A} : \mathbf{A}} \tag{A.10}$$

Trace

$$\mathrm{Tr}\,(\mathbf{A}+\mathbf{B}) = \mathrm{Tr}\,(\mathbf{A}) + \mathrm{Tr}\,(\mathbf{B}) \tag{A.11}$$

$$\mathrm{Tr}\,(\alpha\,\mathbf{A}) = \alpha\,\mathrm{Tr}\,(\mathbf{A}) \tag{A.12}$$

$$\mathrm{Tr}\,(\mathbf{m}\otimes\mathbf{m}) = ||\mathbf{m}||^2 \tag{A.13}$$

Inverse (Richardson's formula, [Noble and Daniel, 1988])

$$\begin{aligned}[\mathbf{A}+\mathbf{a}\otimes\mathbf{b}]^{-1} &= \mathbf{A}^{-1} - \frac{(\mathbf{A}^{-1}\mathbf{a})\otimes(\mathbf{A}^{-\mathrm{T}}\mathbf{b})}{1+(\mathbf{A}^{-1}\,\mathbf{a})\cdot\mathbf{b}} = \\ &= \mathbf{A}^{-1} - \frac{\mathbf{A}^{-1}[\mathbf{a}\otimes\mathbf{b}]\mathbf{A}^{-1}}{1+(\mathbf{A}^{-1}\,\mathbf{a})\cdot\mathbf{b}}\end{aligned} \tag{A.14}$$

Special tensorial products

$$(\mathbf{A}\,\underline{\otimes}\,\mathbf{B})\,\mathbf{X} = \mathbf{A}\mathbf{X}\mathbf{B}^{\mathrm{T}}, \quad \forall\,\mathbf{X} \tag{A.15}$$

$$(\mathbf{A}\,\overline{\otimes}\,\mathbf{B})\,\mathbf{X} = \mathbf{A}\mathbf{X}^{\mathrm{T}}\mathbf{B}^{\mathrm{T}}, \quad \forall\,\mathbf{X} \tag{A.16}$$

$$(\mathbf{A}\,\underline{\overline{\otimes}}\,\mathbf{B})\,\mathbf{X} = \frac{1}{2}\,(\mathbf{A}\mathbf{X}\mathbf{B}^{\mathrm{T}} + \mathbf{A}\mathbf{X}^{\mathrm{T}}\mathbf{B}^{\mathrm{T}}), \quad \forall\,\mathbf{X} \tag{A.17}$$

$$\mathbf{A}\,\underline{\overline{\otimes}}\,\mathbf{B} = \frac{1}{2}\,(\mathbf{A}\,\underline{\otimes}\,\mathbf{B} + \mathbf{A}\,\overline{\otimes}\,\mathbf{B}) \tag{A.18}$$

$$\mathbf{A}\,\underline{\overline{\otimes}}\,\mathbf{A} = \mathbf{A}\otimes\mathbf{A} \quad \text{if} \quad \mathbf{A} = \mathbf{a}\otimes\mathbf{a} \tag{A.19}$$

$$(\mathbf{a}\otimes\mathbf{b})\,\underline{\otimes}\,(\mathbf{c}\otimes\mathbf{d}) = \mathbf{a}\otimes\mathbf{c}\otimes\mathbf{b}\otimes\mathbf{d} \tag{A.20}$$

$$(\mathbf{a}\otimes\mathbf{b})\,\overline{\otimes}\,(\mathbf{c}\otimes\mathbf{d}) = \mathbf{a}\otimes\mathbf{c}\otimes\mathbf{d}\otimes\mathbf{b} \tag{A.21}$$

Transpose

$$[\mathbf{A}\,\underline{\otimes}\,\mathbf{B}]^{\mathrm{T}} = \mathbf{A}^{\mathrm{T}}\,\underline{\otimes}\,\mathbf{B}^{\mathrm{T}} \tag{A.22}$$

$$[\mathbf{A}\,\overline{\otimes}\,\mathbf{B}]^{\mathrm{T}} = \mathbf{B}^{\mathrm{T}}\,\overline{\otimes}\,\mathbf{A}^{\mathrm{T}} \tag{A.23}$$

Bibliography

[Alart and Curnier, 1991] Alart, P. and Curnier, A. (1991). A mixed formulation for frictional contact problems prone to Newton like solution methods. *Computer Methods in Applied Mechanics and Engineering*, 92:353–375.

[Allix et al., 1987] Allix, O., Ladevèze, P., Dantec, E. L., and Vittecoq, E. (1987). *Damage mechanics for composite laminates under complex loading.* Yielding, Damage, and Failure of Anisotropic Solids (Boheler, ed.), Mechanical Engineering Publication London, pp. 551-569.

[Ascenzi and Bonucci, 1967] Ascenzi, A. and Bonucci, E. (1967). The tensile properties of single osteons. *The Anatomical Record*, 158:375–386.

[Ashby, 1992] Ashby, M. F. (1992). *Materials selection in mechanical design.* Oxford [etc.]: Pergamon Press.

[Ashby et al., 1995] Ashby, M. F., Gibson, L. J., Wegst, U., and Olive, R. (1995). The mechanical properties of natural materials: I. Material property charts. *Proceedings of the Royal Society of London, Series A*, 450:123–140.

[Balet, 2005] Balet, R. (2005). Viscoélasticité avec endommagement de l'os compact. Master's thesis, Ecole Polytechnique Fédérale de Lausanne (EPFL).

[Bayraktar et al., 2004] Bayraktar, H. H., Morgan, E. F., Niebur, G. L., Morris, G. E., Wong, E. K., and Keaveny, T. M. (2004). Comparison of the elastic and yield properties of human femoral trabecular and cortical bone tissue. *Journal of Biomechanics*, 37(1):27–35.

[Boehler, 1987] Boehler, J. P. (1987). *Applications of tensor functions in solid mechanics.* Springer Verlag, Wien.

[Bono, 2003] Bono, C. M. (2003). Vertebral compression fractures: what time destroys, methylmethacrylate may mend. *Cleveland Clinic Journal of Medicine*, 70(2):88–90.

[Bowman et al., 1994] Bowman, S. M., Keaveny, T. M., Gibson, L. J., Hayes, W. C., and McMahon, T. A. (1994). Compressive creep behavior of bovine trabecular bone. *Journal of Biomechanics*, 27:301.

[Budiansky and O'Connell, 1976] Budiansky, B. and O'Connell, R. J. (1976). Elastic moduli of a cracked solid. *International Journal of Solids and Structures*, 12(2):81–97.

[Burckhardt, 2004] Burckhardt, P. (2004). Séminaire sur l'ostéoporose. In *Prix de Lausanne 2004, Lausanne, Switzerland*.

[Burr et al., 1998] Burr, D. B., Martin, R. B., and Sharkey, N. A. (1998). *Skeletal tissue mechanics*. New York: Springer-Verlag.

[Burstein et al., 1976] Burstein, A. H., Reilly, D. T., and Martens, M. J. (1976). Aging of bone tissue: mechanical properties. *Journal of Bone and Joint Surgery*, 59A:82–86.

[Caler and Carter, 1989] Caler, W. E. and Carter, D. R. (1989). Bone creep-fatigue damage accumulation. *Journal of Biomechanics*, 22(6-7):625–635.

[Carol and Bazant, 1997] Carol, I. and Bazant, Z. P. (1997). Damage and plasticity in microplane theory. *International Journal of Solids and Structures*, 34(29):3807–3835.

[Carol et al., 2001a] Carol, I., Jirásek, M., and Bazant, Z. (2001a). A thermodynamically consistent approach to microplane theory. Part I. Free energy and consistent microplane stresses. *International Journal of Solids and Structures*, 38(17):2921–2931.

[Carol et al., 2001b] Carol, I., Rizzi, E., and Willam, K. (2001b). On the formulation of anisotropic elastic degradation. I. Theory based on a pseudo-logarithmic damage tensor rate. *International Journal of Solids and Structures*, 38(4):491–518.

[Carter and Caler, 1983] Carter, D. R. and Caler, W. E. (1983). Cycle-dependent and time-dependent bone fracture with repeated loading. *Journal of Biomechanical Engineering*, 105:166–170.

[Carter and Caler, 1985] Carter, D. R. and Caler, W. E. (1985). A cumulative damage model for bone fracture. *Journal of Orthopaedic Research*, 3:84–90.

[Carter and Hayes, 1977a] Carter, D. R. and Hayes, W. C. (1977a). Compact bone fatigue damage-I. Residual strength and stiffness. *Journal of Biomechanics*, 10(5-6):325–337.

[Carter and Hayes, 1977b] Carter, D. R. and Hayes, W. C. (1977b). The compressive behaviour or bone as a two phase porous structure. *Journal of Bone and Joint Surgery*, 59:954–962.

[Carter et al., 1976] Carter, D. R., Hayes, W. C., and Schurman, D. J. (1976). Fatigue life of compact bone–II. Effects of microstructure and density. *Journal of Biomechanics*, 9(4):211–214.

[Chaboche et al., 2001] Chaboche, J. L., Kruch, S., Maire, J. F., and Pottier, T. (2001). Towards a micromechanics based inelastic and damage modeling of composites. *International Journal of Plasticity*, 17(4):411–439.

[Chen et al., 1999] Chen, S.-I., Chang, C.-H., Lin, R. M., and Lin, T. S. (1999). The osteoporotic lumbar spine finite element analysis. *Chinese Journal of Medical and Biological Engineering*, 19(3):219–227.

[Choi and Goldstein, 1992] Choi, K. and Goldstein, S. A. (1992). A comparison of the fatigue behavior of human trabecular and cortical bone tissue. *Journal of Biomechanics*, 25(12):1371–1381.

[Choi et al., 1990] Choi, K., Kuhn, J. L., Ciarelli, M. J., and Goldstein, S. A. (1990). The elastic moduli of human subchondral trabecular, and cortical bone tissue and the size-dependency of cortical bone modulus. *Journal of Biomechanics*, 23:1103–1113.

[Collins and Houlsby, 1997] Collins, I. F. and Houlsby, G. T. (1997). Application of thermodynamical principles to the modelling of geotechnical materials. *Proceedings of the Royal Society of London A: Mathematical, Physical and Engineering Sciences*, 453(1964):1975–2001.

[Cowin, 1999] Cowin, S. (1999). Bone poroelasticity. *Journal of Biomechanics*, 32(3):217–238.

[Cowin, 1985] Cowin, S. C. (1985). The relationship between the elasticity tensor and the fabric tensor. *Mechanics of Materials*, 4(2):137–147.

[Cowin, 1986] Cowin, S. C. (1986). Fabric dependence of an anisotropic strength criterion. *Mechanics of Materials*, 5(3):251–260.

[Cowin, 1989] Cowin, S. C. (1989). *Bone mechanics*. Boca Raton, CRC Press.

[Cowin, 2001] Cowin, S. C. (2001). *Bone mechanics handbook*. Boca Raton, CRC Press, 2nd edition.

[Crawford et al., 2003] Crawford, R. P., Rosenberg, W. S., and Keaveny, T. M. (2003). Quantitative computed tomography-based finite element models of the human lumbar vertebral body: effect of element size on stiffness, damage, and fracture strength predictions. *Journal of Biomechanical Engineering*, 125:434–438.

[Curnier, 1980] Curnier, A. (1980). Anisotropic plasticity (unpublished).

[Curnier, 1993] Curnier, A. (1993). *Méthodes numériques en mécanique des solides*. Presses Polytechniques et Universitaires Romandes (PPUR).

[Curnier, 2001] Curnier, A. (2001). Discrete contact mechanics. Lecture Notes, Ecole Polytechnique Fédérale de Lausanne (EPFL).

[Curnier, 2005] Curnier, A. (2005). *Mécanique des solides déformables*, volume 1. Presses polytechniques et universitaires romandes (PPUR).

[Curnier et al., 1995] Curnier, A., He, Q.-C., and Zysset, P. K. (1995). Conewise linear elastic materials. *Journal of Elasticity*, 37:1–38.

[Currey, 2004] Currey, J. (2004). Incompatible mechanical properties in compact bone. *Journal of Theoretical Biology*, 231(4):569–580.

[Currey, 1965] Currey, J. D. (1965). Anelasticity in bone and echinoderm skeletons. *Journal of Experimental Biology*, 43:279.

[Currey, 1988a] Currey, J. D. (1988a). The effect of drying and re-wetting on some mechanical properties of cortical bone. *Journal of Biomechanics*, 21:439–441.

[Currey, 1988b] Currey, J. D. (1988b). The effect of porosity and mineral content on the Young's modulus of elasticity of compact bone. *Journal of Biomechanics*, 21:131–139.

[Currey, 1990] Currey, J. D. (1990). Physical characteristics affecting the tensile failure properties of compact bone. *Journal of Biomechanics*, 23(8):837–844.

[Currey, 2002] Currey, J. D. (2002). *Bones: Structure and Mechanics*. Princeton University Press, Princeton, NJ.

[Doblaré et al., 2004] Doblaré, M., García, J. M., and Gómez, M. J. (2004). Modelling bone tissue fracture and healing: a review. *Engineering Fracture Mechanics*, 71(13-14):1809–1840.

[Doghri, 1993] Doghri, I. (1993). Fully implicit integration and consistent tangent modulus in elasto-plasticity. *International Journal for Numerical Methods in Engineering*, 36:3915–3932.

[Fan et al., 2001] Fan, Z., Swadener, J., Rho, J., Roy, M., and Pharr, G. (2001). Anisotropy nanoindentation properties of human cortical bone. In *47th annual meeting of the Orthopaedic Research Society, San Fransisco, California*.

[Ferrari and Granik, 1995] Ferrari, M. and Granik, V. T. (1995). Ultimate criteria for materials with different properties in biaxial tension and compression: a micromechanical approach. *Materials Science and Engineering A*, 202(1-2):84–93.

[Fondrk et al., 1999a] Fondrk, M. T., Bahniuk, E. H., and Davy, D. T. (1999a). A damage model for nonlinear tensile behavior of cortical bone. *Journal of Biomedical Engineering*, 121:533–541.

[Fondrk et al., 1999b] Fondrk, M. T., Bahniuk, E. H., and Davy, D. T. (1999b). Inelastic strain accumulation in cortical bone during rapid transient tensile loading. *Journal of Biomechanical Engineering*, 121:616–621.

[Fondrk et al., 1988] Fondrk, M. T., Bahniuk, E. H., Davy, D. T., and Michaels, C. (1988). Some viscoplastic characteristics of bovine and human cortical bone. *Journal of Biomechanics*, 21(8):623–630.

[Fridez, 1996] Fridez, P. (1996). *Modélisation de l'adaptation osseuse externe*. PhD thesis, Ecole Polytechnique Fédérale de Lausanne (EPFL).

[Frost, 1963] Frost, H. M. (1963). *Bone remodeling dynamics*. Springfield, IL: Charles C. Thomas.

[Gao et al., 2003] Gao, H., Ji, B., Jäger, I. L., Arzt, E., and Fratzl, P. (2003). Materials become insensitive to flaws at nanoscale: lessons from nature. *Proceedings of the National Academy of Science*, 100(10):5597–5600.

[George and Vashishth, 2003] George, W. and Vashishth, D. (2003). Damage development in bone is dependent on type of loading. In *49th Annual Meeting of the Orthopaedic Research Society, New Orleans, Louisiana*.

[Germain, 1973] Germain, P. (1973). La méthode des puissances virtuelles en mécanique des milieux continus. *Journal de Mécanique*, 12(2):236–274.

[Germain, 1995] Germain, P. (1995). *Introduction à la mécanique des milieux continus*. Masson, 2e edition.

[Giraud-Guilles, 1988] Giraud-Guilles, M. M. (1988). Twisted plywood architecture of collagen fibrils in human compact bone osteons. *Calcified Tissue International*, 42:167–180.

[Goldstein et al., 1983] Goldstein, S. A., Wilson, D. L., Sonstergard, D. A., and Matthews, L. S. (1983). The mechanical properties of human tibial trabecular bone as a function of metaphyseal location. *Journal of Biomechanics*, 16:965–969.

[Green and Naghdi, 1965] Green, A. E. and Naghdi, P. M. (1965). A general theory of an elastic-plastic continuum. *Archive for Rational Mechanics and Analysis*, 18(4):251–281.

[Guo, 2001] Guo, X. E. (2001). *Mechanical properties of cortical bone and cancellous bone tissue*, chapter 10. S. C. Cowin.

[Halphen and Nguyen, 1974] Halphen, B. and Nguyen, Q. S. (1974). Plastic and visco-plastic materials with generalized potential. *Mechanics Research Communications*, 1(1):43–47.

[Halphen and Nguyen, 1975] Halphen, B. and Nguyen, Q. S. (1975). Sur les matériaux standards généralisés. *Journal de Mécanique*, 14(1):39–63.

[Hartmann and Haupt, 1993] Hartmann, S. and Haupt, P. (1993). Stress computation and consistent tangent operator using non-linear kinematic hardening models. *International Journal for Numerical Methods in Engineering*, 36:3801–3814.

[Hay et al., 1999] Hay, J. C., Bolshakov, A., and Parr, G. M. (1999). A critical examination of the fundamental relations used in the analysis of nanoindentation data. *Journal of Material Research*, 14(6):2296–2305.

[He and Curnier, 1994] He, Q.-C. and Curnier, A. (1994). On some one-to-one constitutive correspondences in plasticity. *Archives of Mechanics*, 46(6):989–1004.

[He and Curnier, 1995] He, Q. C. and Curnier, A. (1995). A more fundamental approach to damaged elastic stress-strain relations. *International Journal of Solids and Structures*, 32(10):1433–1457.

[Hengsberger, 2002] Hengsberger, S. (2002). *Mechanical characterization of bone from the tissue down to the lamellar level by means of nanoindentation*. PhD thesis, Ecole Polytechnique Fédérale de Lausanne (EPFL).

[Hengsberger et al., 2003] Hengsberger, S., Enstroem, J., Peyrin, F., and Zysset, P. K. (2003). How is the indentation modulus of bone tissue related to its macroscopic elastic response ? A validation study. *Journal of Biomechanics*, 36(10):1503–1509.

[Hengsberger et al., 2001] Hengsberger, S., Kullik, A., and Zysset, P. K. (2001). A combined atomic force microscopy and nanoindentation technique to investigate the elastic properties of bone structural units. *European Cells and Materials*, 1:12–17.

[Hengsberger et al., 2002] Hengsberger, S., Kullik, A., and Zysset, P. K. (2002). Nanoindentation discriminates the elastic properties of individual human bone lamellae under dry and physiological conditions. *Bone*, 30(1):178–184.

[Hill, 1950] Hill, R. (1950). *The mathematical theory of plasticity*. Oxford University Press, London.

[Hiriart-Urruty and Lemaréchal, 1996] Hiriart-Urruty, J. P. and Lemaréchal, C. (1996). *Convex analysis and minimization algorithms*, volume I and II. Springer Verlag, Heidelberg, 2nd edition.

[HKS, 2001] HKS (2001). *ABAQUS/Standard user's manual - volume III*. Hibbitt, Karlsson and Sorensen, Inc.

[Hodgskinson and Currey, 1992] Hodgskinson, R. and Currey, J. D. (1992). Young's modulus, density and material properties in cancellous bone over a large density range. *Journal of Material Science and Material Medicine*, 3:377.

[Hoffler et al., 2000a] Hoffler, C. E., Moore, K. E., Kozloff, K., Zysset, P. K., Brown, M. B., and Goldstein, S. A. (2000a). Heterogeneity of bone lamellar-level elastic moduli. *Bone*, 26(6):603–609.

[Hoffler et al., 2000b] Hoffler, C. E., Moore, K. E., Kozloff, K., Zysset, P. K., and Goldstein, S. A. (2000b). Age, gender, and bone lamellae elastic moduli. *Journal of Orthopaedic Research*, 18:432–437.

[Hoffman, 1967] Hoffman, O. (1967). The brittle strength of orthotropic materials. *Journal of Composite Materials*, 1:200.

[Homminga et al., 2004] Homminga, J., Van-Rietbergen, B., Lochmüller, E. M., Weinans, H., Heckstein, F., and Huiskes, R. (2004). The osteoporotic vertebral structure is well adapted to the loads of daily life, but not to infrequent "error" loads. *Bone*, 34:510–516.

[Houlsby and Puzrin, 2000] Houlsby, G. T. and Puzrin, A. M. (2000). A thermomechanical framework for constitutive models for rate-independent dissipative materials. *International Journal of Plasticity*, 16(9):1017–1047.

[Houlsby and Puzrin, 2002] Houlsby, G. T. and Puzrin, A. M. (2002). Rate-dependent plasticity models derived from potential functions. *Journal of Rheology*, 46(1):113–126.

[Hughes and Taylor, 1978] Hughes, T. J. R. and Taylor, R. L. (1978). Unconditionally stable algorithms for quasi-static elasto/viscoplastic finite element analysis. *Computers and Structures*, 8:169–173.

[Humphrey, 2003] Humphrey, J. D. (2003). Continuum biomechanics of soft biological tissues. *Proceedings [of the Royal Society of London A] : Mathematical, Physical and Engineering Sciences*, 459:3–46.

[Jäger and Fratzl, 2000] Jäger, I. and Fratzl, P. (2000). Mineralized collagen fibrils: a mechanical model with a staggered arrangement of mineral particles. *Biophysical Journal*, 79(4):1737–1746.

[Jepsen and Davy, 1997] Jepsen, K. J. and Davy, D. T. (1997). Comparison of damage accumulation measures in human cortical bone. *Journal of Biomechanics*, 30(9):891–894.

[Jundt et al., 2005] Jundt, G., Arnoux, P. J., Kayvantash, K., Chabrand, P., and Brunet, C. (2005). A behaviour law for bone to describe damage and fracture. In *Proceedings (485), Biomechanics*.

[Kachanov, 1958] Kachanov, L. M. (1958). Time rupture process under creep conditions. *Izv. A Rad. Nauk. SSSR otd Tekh. Nauk.*, 8:26–31.

[Kanatani, 1984] Kanatani, K.-I. (1984). Distribution of directional data and fabric tensors. *International Journal of Engineering Science*, 22(2):149–164.

[Kari, 1993] Kari, S. (Espoo 1993). *Viscous and elastic-plastic material model in the ABAQUS*. Technical Research Centre of Finland, VTT Publications 144. 54 p.

[Keaveny et al., 2001] Keaveny, T. M., Morgan, E. F., Niebur, G. L., and Yeh, O. C. (2001). Biomechanics of trabecular bone. *Annual Review of Biomedical Engineering*, 3:307–333.

[Keaveny et al., 1994] Keaveny, T. M., Wachtel, E. F., Ford, C. M., and Hayes, W. C. (1994). Differences between the tensile and compressive strengths of bovine tibial trabecular bone depend on modulus. *Journal of Biomechanics*, 27:1137–1146.

[Keaveny et al., 1999] Keaveny, T. M., Wachtel, E. F., and Kopperdahl, D. L. (1999). Mechanical behavior of human trabecular bone after overloading. *Journal of Orthopaedic Research*, 17:346–353.

[Kotha and Guzelsu, 2003] Kotha, S. P. and Guzelsu, N. (2003). Tensile damage and its effects on cortical bone. *Journal of Biomechanics*, 36(11):1683–1689.

[Krajcinovic, 1989] Krajcinovic, D. (1989). Damage mechanics. *Mechanics of Materials*, 8(2-3):117–197.

[Krajcinovic, 1998] Krajcinovic, D. (1998). Selection of damage parameter - art or science? *Mechanics of Materials*, 28(1-4):165–179.

[Krajcinovic, 2000] Krajcinovic, D. (2000). Damage mechanics: accomplishments, trends and needs. *International Journal of Solids and Structures*, 37(1-2):267–277.

[Krajcinovic et al., 1987] Krajcinovic, D., Trafimow, J., and Sumarac, D. (1987). Simple constitutive model for a cortical bone. *Journal of Biomechanics*, 20(8):779–784.

[Kuhl et al., 2001] Kuhl, E., Steinmann, P., and Carol, I. (2001). A thermodynamically consistent approach to microplane theory. Part II. Dissipation and inelastic constitutive modeling. *International Journal of Solids and Structures*, 38(17):2933–2952.

[Ladevèze, 1993] Ladevèze, P. (1993). On an anisotropic damage theory. In Boehler, J. P., editor, *Failure Critera of Structured Media*, pages 355–363. Balkema, Rotterdam.

[Lakes et al., 1979] Lakes, R. S., Katz, J. L., and Sternstein, S. S. (1979). Viscoelastic properties of wet cortical bone. I. Torsional and biaxial studies. *Journal of Biomechanics*, 12:657–678.

[Landis, 1995] Landis, W. J. (1995). The strength of a calcified tissue depends in part on the molecular structure and organization of its constituent mineral crystals in their organic matrix. *Bone*, 16:533–544.

[Lang, 1970] Lang, S. B. (1970). Ultrasonic method for measuring elastic coefficients of bone and results on fresh and dried bovine bones. *IEEE Transactions on Biomedical Engineering*, 17:101–105.

[Lemaitre, 1996] Lemaitre, J. (1996). *A course on damage mechanics*. Springer-Verlag, 2nd edition.

[Lemaitre and Chaboche, 1985] Lemaitre, J. and Chaboche, J. L. (1985). *Mécanique des matériaux solides*. Dunod, Paris.

[Lemaitre and Chaboche, 2001] Lemaitre, J. and Chaboche, J.-L. (2001). *Mécanique des matériaux solides*. Dunod, 2e edition.

[Leukart and Ramm, 2003] Leukart, M. and Ramm, E. (2003). A comparison of damage models formulated on different material scales. *Computational Materials Science*, 28(3-4):749–762.

[Liebschner et al., 2001] Liebschner, M. A. K., Kopperdahl, D. L., Rosenberg, W. S., and Keaveny, T. M. (2001). Contribution of cortical shell and endplate to vertebral body stiffness. In *BED-Vol. 50, 2001 Bioengineering Conference, ASME*.

[Lippuner et al., 1997] Lippuner, K., von Overbeck, J., Perrelet, R., Bosshard, H., and Jaeger, P. (1997). Incidence and direct medical costs of hospitalizations due to osteoporotic fractures in Switzerland. *Osteoporosis International*, 7:414–425.

[Lothe and Barnett, 1976] Lothe, J. and Barnett, D. M. (1976). On the existence of surface-wave solutions for anisotropic elastic half-spaces with free surface. *Journal of Applied Physics*, 47(2):428–433.

[Lubarda and Krajcinovic, 1993] Lubarda, V. A. and Krajcinovic, D. (1993). Damage tensors and the crack density distribution. *International Journal of Solids and Structures*, 30(20):2859–2877.

[Lubarda and Krajcinovic, 1995] Lubarda, V. A. and Krajcinovic, D. (1995). Some fundamental issues in rate theory of damage-elastoplasticity. *International Journal of Plasticity*, 11(7):763–797.

[Lubarda et al., 1994] Lubarda, V. A., Krajcinovic, D., and Mastilovic, S. (1994). Damage model for brittle elastic solids with unequal tensile and compressive strengths. *Engineering Fracture Mechanics*, 49(5):681–697.

[Mahnken et al., 2000] Mahnken, R., Tikhomirov, D., and Stein, E. (2000). Implicit integration scheme and its consistent linearization for an elastoplastic-damage model with application to concrete. *Computers & Structures*, 75(2):135–143.

[Martin and Burr, 1982] Martin, R. B. and Burr, D. B. (1982). A hypothetical mechanism for the stimulation of osteonal remodelling by fatigue damage. *Journal of Biomechanics*, 15:137–139.

[Matzenmiller et al., 1995] Matzenmiller, A., Lubliner, J., and Taylor, R. L. (1995). A constitutive model for anisotropic damage in fiber-composites. *Mechanics of Materials*, 20(2):125–152.

[Matzenmiller and Taylor, 1994] Matzenmiller, A. and Taylor, R. L. (1994). A return mapping algorithm for isotropic elastoplasticity. *International Journal for Numerical Methods in Engineering*, 37:813–826.

[Mauch et al., 1992] Mauch, M., Currey, J. D., and Sedman, A. J. (1992). Creep fracture in bones with different stiffnesses. *Journal of Biomechanics*, 25(1):11–16.

[Maugin, 1999] Maugin, G. A. (1999). *The thermomechanics of nonlinear irreversible behaviors - an introduction*, volume 27 of *A*. World Scientific Publishing Co. Pte. Ltd.

[McElhaney, 1966] McElhaney, J. H. (1966). Dynamic response of bone and muscle tissue. *Journal of Applied Physiology*, 21:1231–1236.

[Melton et al., 1992] Melton, L. J., Chrischilles, E. A., Cooper, C., Lane, A. W., and Riggs, B. L. (1992). Perspective: How many women have osteoporosis? *Journal of Bone Mineral Research*, 7:1005–1010.

[Mizrahi et al., 1993] Mizrahi, J., Silva, M. J., Keaveny, T. M., Edwards, W. T., and Hayes, W. C. (1993). Finite-element stress analysis of the normal and osteoporotic lumbar vertebral body. *Spine*, 18(14):2088–2096.

[Moreau, 1970] Moreau, J. (1970). Sur les lois de frottement, de viscosité et de plasticité. *C. R. Acad. Sci., Paris*, 271:608–611.

[Moreau, 1979] Moreau, J. J. (1979). Application of convex analysis to some problems of dry friction. In *Trends in Applications of Pure Mathematics to Mechanics*. H. Zorski, Ed. London, U.K.: Pitman, vol. 2, pp. 263-280.

[Noble and Daniel, 1988] Noble, B. and Daniel, J. (1988). *Applied linear algebra*. Prentice Hall, third edition.

[Old and Calvert, 2004] Old, J. L. and Calvert, M. (2004). Vertebral compression fractures in the elderly. *American Family Physician*, 69(1):111–116.

[Oliver and Pharr, 1992] Oliver, W. C. and Pharr, G. M. (1992). An improved technique for determining hardness and elastic modulus using load and displacement sensing indentation experiments. *Journal of Materials Research*, 7(6):1564–1583.

[Oller et al., 2003] Oller, S., Car, E., and Lubliner, J. (2003). Definition of a general implicit orthotropic yield criterion. *Computer Methods in Applied Mechanics and Engineering*, 192(7-8):895–912.

[Oller et al., 1996] Oller, S., Oñate, E., Miquel, J., and Botello, S. (1996). A plastic damage constitutive model for composite materials. *International Journal of Solids and Structures*, 33(17):2501–2518.

[Ortiz, 1985] Ortiz, M. (1985). A constitutive theory for the inelastic behavior of concrete. *Mechanics of Materials*, 4(1):67–93.

[Panagiotopoulos, 1981] Panagiotopoulos, P. D. (1981). Non-convex superpotentials in the sense of F.H. Clarke and applications. *Mechanics Research Communications*, 8(6):335–340.

[Pattin et al., 1996] Pattin, C. A., Caler, W. E., and Carter, D. R. (1996). Cyclic mechanical property degradation during fatigue loading of cortical bone. *Journal of Biomechanics*, 29(1):69–79.

[Piekarski et al., 2004] Piekarski, J., Kowalczyk-Gajewska, K., Waarsing, E., and Mazdziarz, M. (2004). Approximations of stiffness tensor of bone - determining and accuracy. In *XXI International Congress of Theoretical and Applied Mechanics, Warsaw, Poland*.

[Piekarski, 1973] Piekarski, K. (1973). Analysis of bone as a composite material. *International Journal of Engineering Science*, 11(6):557–558.

[Pietruszczak et al., 1999] Pietruszczak, S., Inglis, D., and Pande, G. N. (1999). A fabric-dependent fracture criterion for bone. *Journal of Biomechanics*, 32(10):1071–1079.

[Prandtl, 1924] Prandtl, L. (1924). Spannungsverteilung in plastischen Körpern. In Biezeno, C. B. and eds., J. M. B., editors, *Proceedings of the First International Congress for Applied Mechanics*, pages 43–54. Technische Boekhandel en Druckerij, J. Waltman Jr., Delft, 1924.

[Predey et al., 2002] Predey, T. A., Sewall, L. E., and Smith, S. J. (2002). Percutaneous vertebroplasty: new treatment for vertebral compression fractures. *American Family Physician*, 66:611–615.

[Press et al., 1992] Press, W. H., Flannery, B. P., Teukolsky, S. A., and Vetterling, W. T. (1992). *Numerical recipes in FORTRAN 77: The art of scientific computing*. Cambridge University Press, 2nd edition.

[Puzrin and Houlsby, 2001] Puzrin, A. M. and Houlsby, G. T. (2001). A thermomechanical framework for rate-independent dissipative materials with internal functions. *International Journal of Plasticity*, 17(8):1147–1165.

[Rakotomanana et al., 1991] Rakotomanana, R. L., Curnier, A., and Leyvraz, P. F. (1991). An objective anisotropic elastic plastic model and algorithm applicable to bone mechanics. *European Journal of Mechanics, A/Solids*, 10(3):327–342.

[Ramtani and Zidi, 2002] Ramtani, S. and Zidi, M. (2002). Damaged-bone adaptation under steady homogeneous stress. *Journal of Biomechanical Engineering*, 124(3):322–327.

[Reilly and Burstein, 1975] Reilly, D. T. and Burstein, A. H. (1975). The elastic and ultimate properties of compact bone tissue. *Journal of Biomechanics*, 8(6):393–396.

[Reuss, 1930] Reuss, A. (1930). Berücksichtigung der elastischen Formänderung in der Plastizitätstheorie. *Zeitschrift für angewandte Mathematik und Mechanik*, 10:266–274.

[Rho et al., 1993] Rho, J.-Y., Ashman, R. B., and Turner, C. H. (1993). Young's modulus of trabecular and cortical bone material: ultrasonic and microtensile measurements. *Journal of Biomechanics*, 26:111–119.

[Rho et al., 1995] Rho, J.-Y., Hobatho, M. C., and Ashman, R. B. (1995). Relations of density and CT numbers to mechanical properties for human cortical and cancellous bone. *Medical Engineering & Physics*, 17:347–355.

[Rho et al., 1998] Rho, J.-Y., Kuhn-Spearing, L., and Zioupos, P. (1998). Mechanical properties and the hierarchical structure of bone. *Medical Engineering & Physics*, 20(2):92–102.

[Rho et al., 1999a] Rho, J.-Y., Roy, M. E., Tsui, T. Y., and Pharr, G. M. (1999a). Elastic properties of microstructural components of human bone tissue as measured by nanoindentation. *Journal of Biomedical Materials Research*, 45(1):48–54.

[Rho et al., 1997] Rho, J.-Y., Tsui, T. Y., and Pharr, G. M. (1997). Elastic properties of human cortical and trabecular lamellar bone measured by nanoindentation. *Biomaterials*, 18(20):1325–1330.

[Rho et al., 1999b] Rho, J.-Y., Zioupos, P., Currey, J. D., and Pharr, G. M. (1999b). Variations in the individual thick lamellar properties within osteons by nanoindentation. *Bone*, 25(3):295–300.

[Rimnac et al., 1993] Rimnac, C. M., Petko, A. A., Santner, T. J., and Wright, T. M. (1993). The effect of temperature, stress and microstructure on the creep of compact bovine bone. *Journal of Biomechanics*, 26(3):219–221.

[Rincón, 2003] Rincón, L. (2003). *Identification of a multiaxial failure criterion for human trabecular bone*. PhD thesis, Ecole Polytechnique Fédérale de Lausanne (EPFL).

[Rincón et al., 2001] Rincón, L., Frossard, A., Curnier, A., and Zysset, P. K. (2001). A rate-dependent damage model for bovine trabecular bone. *Computer Methods in Biomechanics and Biomedical Engineering*, 3:161–166.

[Ritchie et al., 2004] Ritchie, R. O., Kruzlic, J. J., Muhlstein, C. L., Nalla, R. K., and Stach, E. A. (2004). Characteristic dimensions and the micromechanisms of fracture and fatigue in 'nano' and 'bio' materials. *International Journal of Fracture*, 128:1–15.

[Rockafellar, 1970] Rockafellar, R. T. (1970). *Convex Analysis*. Princeton University Press, Princeton.

[Rogers, 1987] Rogers, T. G. (1987). *Yield criteria, flow rules, and hardening in anisotropic plasticity*. Yielding, Damage, and Failure of Anisotropic

Solids (Boehler, ed.), Mechanical Engineering Publications, London, pp. 53-79.

[Rohl et al., 1991] Rohl, L., Larsen, E., Linde, F., Odgaard, A., and Jorgensen, J. (1991). Tensile and compressive properties of cancellous bone. *Journal of Biomechanics*, 24:1143–1149.

[Roy et al., 1999] Roy, M. E., J.-Y.Rho, Tsui, T. Y., Evans, N. D., and Pharr, G. M. (1999). Mechanical and morphological variation of the human lumbar vertebral cortical and trabecular bone. *Journal of Biomedical Materials Research*, 44(2):191–197.

[Seeman, 2002] Seeman, E. (2002). Pathogenesis of bone fragility in women and men. *The Lancet*, 359(9320):1841–1850.

[Silva et al., 1994] Silva, M., Keaveny, T. M., and Hayes, W. C. (1994). Direct and computed tomography thickness measurements of the human lumbar vertebral shell and endplates. *Bone*, 15:409–414.

[Silva et al., 1998] Silva, M. J., Keaveny, T. M., and Hayes, W. C. (1998). Computed tomography-based finite element analysis predicts failure loads and fracture patterns for vertebral sections. *Journal of Orthopaedic Research*, 16(3):300–308.

[Simo and Hughes, 1999] Simo, J. C. and Hughes, T. J. R. (1999). *Computational inelasticity*. Springer-Verlag, Berlin.

[Simo and Ju, 1987] Simo, J. C. and Ju, J. W. (1987). Strain- and stress-based continuum damage models-I. Formulation. *International Journal of Solids and Structures*, 23(7):821–840.

[Simo and Taylor, 1985] Simo, J. C. and Taylor, R. L. (1985). Consistent tangent operators for rate-independent elastoplasticity. *Computer Methods in Applied Mechanics and Engineering*, 48(1):101–118.

[Sneddon, 1965] Sneddon, I. N. (1965). The relation between load and penetration in the axisymmetric Boussinesq problem for a punch of arbitrary profile. *International Journal of Engineering Science*, 3(1):47–57.

[Sobotka, 1984] Sobotka, Z. (1984). *Rheology of materials and engineering structures*. Rheology Series. Elsevier, Amsterdam.

[Spencer, 1993] Spencer, A. J. M. (1993). *Yield conditions and hardening rules for fibre-reinforced materials*. Failure Criteria of Structured Media, Boehler (ed.), Balkema, Rotterdam, pp. 171-177.

[Stroh, 1962] Stroh, A. N. (1962). Steady state problem in anisotropic elasticity. *Journal of Mathematical Physics*, 41:77–103.

[Sutcliffe, 1992] Sutcliffe, S. (1992). Spectral decomposition of the elasticity tensor. *Journal of Applied Mechanics*, 59:762–773.

[Swadener and Pharr, 2001] Swadener, J. G. and Pharr, G. M. (2001). Indentation of elastically anisotropic half-spaces by cones and parabolae of revolution. *Philosophical Magazine A*, 81(2):447–466.

[Taylor et al., 2002] Taylor, M., Cotton, J., and Zioupos, P. (2002). Finite element simulation of the fatigue behaviour of cancellous bone. *Meccanica*, 37:419–429.

[Timoshenko, 1968] Timoshenko, S. (1968). *Résistance des matériaux*, volume 2. Dunod, Paris.

[Ting, 1996] Ting, T. C. T. (1996). *Anisotropic elasticity - Theory and applications*. Oxford University Press.

[Tsai and Wu, 1971] Tsai, S. W. and Wu, E. M. (1971). A general theory of strength of anisotropic materials. *Journal of Composite Materials*, 5:58–80.

[Turner et al., 1995] Turner, C. H., Chandran, A., and Pidaparti, R. M. V. (1995). The anisotropy of osteonal bone and its ultrastructural implications. *Bone*, 17(1):85–89.

[van Buskirk and Ashman, 1981] van Buskirk, W. C. and Ashman, R. B. (1981). The elastic moduli of bone. In *Mechanical properties of bone*, pages 131–143. S. C. Cowin (Colorado: American Society of Mechanical Engineers).

[van Buskirk et al., 1981] van Buskirk, W. C., Cowin, S. C., and Ward, R. N. (1981). Ultrasonic measurement of orthotropic elastic constants of bovine femoral bone. *Journal of Biomechanical Engineering*, 103:67–72.

[Vlassak and Nix, 1993] Vlassak, J. J. and Nix, W. D. (1993). Indentation modulus of elastically anisotropic half spaces. *Philosophical Magazine A*, 67(5):1045–1056.

[Voyiadjis and Deliktas, 2000] Voyiadjis, G. Z. and Deliktas, B. (2000). A coupled anisotropic damage model for the inelastic response of composite materials. *Computer Methods in Applied Mechanics and Engineering*, 183(3-4):159–199.

[Voyiadjis and Thiagarajan, 1995] Voyiadjis, G. Z. and Thiagarajan, G. (1995). An anisotropic yield surface model for directionally reinforced metal-matrix composites. *International Journal of Plasticity*, 11(8):867–894.

[Wang et al., 2001] Wang, X., Bank, R. A., TeKoppele, J. M., and Agrawal, C. M. (2001). The role of collagen in determining bone mechanical properties. *Journal of Orthopaedic Research*, 19(6):1021–1026.

[Weiner et al., 1999] Weiner, S., Traub, W., and Wagner, H. D. (1999). Lamellar bone: structure-function relations. *Journal of Structural Biology*, 126(3):241–255.

[Wilkins, 1964] Wilkins, M. L. (1964). *Calculation of elastic-plastic flow*, volume 3. ADLER B. et al. Eds., Academic Press, New York.

[Wolff, 1892] Wolff, J. (1892). *Das Gestz der Transformation der Knochen*. A. Hirschwald, Berlin.

[Zhu and Cescotto, 1995] Zhu, Y. Y. and Cescotto, S. (1995). A fully coupled elasto-visco-plastic damage theory for anisotropic materials. *International Journal of Solids and Structures*, 32(11):1607–1641.

[Ziegler, 1983] Ziegler, H. (1983). *An introduction to thermomechanics*. North-Holland Publishing Company, second edition.

[Ziegler et al., 1974] Ziegler, H., Nänni, J., and Wehrli, C. (1974). Zur Konvexität der Dissipationsflächen. *Journal of Applied Mathematics and Physics (ZAMP)*, 25:76–82.

[Zioupos, 2002] Zioupos, P. (2002). Personal communication.

[Zioupos and Casinos, 1998] Zioupos, P. and Casinos, A. (1998). Cumulative damage and the response of human bone in two-step loading fatigue. *Journal of Biomechanics*, 31(9):825–833.

[Zioupos et al., 1996] Zioupos, P., Wang, X. T., and Currey, J. D. (1996). The accumulation of fatigue microdamage in human cortical bone of two different ages in vitro. *Clinical Biomechanics*, 11(7):365–375.

[Zysset, 1994] Zysset, P. K. (1994). *A constitutive law for trabecular bone*. PhD thesis, Ecole Polytechnique Fédérale de Lausanne (EPFL).

[Zysset, 2002] Zysset, P. K. (2002). A standard generalized materials approach to model the viscoelastic and rate-dependent damage behaviour of bone. In *13th Conference of the European Society of Biomechanics, Wroclaw, Poland*.

[Zysset, 2003] Zysset, P. K. (2003). A review of morphology-elasticity relationships in human trabecular bone: theories and experiments. *Journal of Biomechanics*, 36:1469–1485.

[Zysset, 2005] Zysset, P. K. (2005). Personal communication.

[Zysset and Curnier, 1995] Zysset, P. K. and Curnier, A. (1995). An alternative model for anisotropic elasticity based on fabric tensors. *Mechanics of Materials*, 21(4):243–250.

[Zysset et al., 1998] Zysset, P. K., Guo, X. E., Hoffler, C. E., Moore, K. E., and Goldstein, S. A. (1998). Mechanical properties of human trabecular bone lamellae quantified by nanoindentation. *Technology and Health Care*, 6:429–432.

[Zysset et al., 1999] Zysset, P. K., Guo, X. E., Hoffler, C. E., Moore, K. E., and Goldstein, S. A. (1999). Elastic modulus and hardness of cortical and trabecular bone lamellae measured by nanoindentation in the human femur. *Journal of Biomechanics*, 32:1005–1012.

[Zysset and Rincón, 2005] Zysset, P. K. and Rincón, L. (2005). An alternative fabric based yield and failure criterion for trabecular bone. *In Press*.

Curriculum Vitæ

David Garcia

Personnel

Adresse:	Avenue du Mont d'Or 13
	CH-1007 Lausanne
Naissance :	le 16 janvier 1976 à Lausanne
Origine :	Lausanne, Vaud
Etat civil	Marié

Formation

1991-1994:	Maturité, type C
	Gymnase cantonal de la Cité, Lausanne
1994-2000 :	Diplôme d'ingénieur physicien EPFL
	Ecole Polytechnique Fédérale de Lausanne

Activités

2000:	Ecole Polytechnique Fédérale de Zürich
	Assistant, Institut de Mécanique, ETHZ
2001 :	Centre Suisse de Calcul Scientifique, Manno
	Stage en visualisation scientifique, CSCS
2001-2005 :	Ecole Polytechnique Fédérale de Lausanne
	Laboratoire de Mécanique Appliquée
	Assistant-doctorant

Abstracts

D. Garcia, A. Curnier and P. K. Zysset. A constitutive law for bone tissue damage under tensile and compressive loading. *Proc. IV International Symposium on Computer Simulation in Biomechanics, The University of Sydney*, 2003. Winner of the Andrzej J. Komor New Investigator Award.

D. Garcia, A. Curnier and P. K. Zysset. A rate-dependent damage constitutive law for cortical bone tissue. *Proc. ESB 2004, S'Hertogenbosch, The Nederlands*, 2004.